THE HONG KONG
POLYTECHNIC UNIVERSITY
香港理工大學
Pao Yue-kong Library
包玉剛圖書館

Copyright Undertaking

This thesis is protected by copyright, with all rights reserved.

By reading and using the thesis, the reader understands and agrees to the following terms:

1. The reader will abide by the rules and legal ordinances governing copyright regarding the use of the thesis.

2. The reader will use the thesis for the purpose of research or private study only and not for distribution or further reproduction or any other purpose.

3. The reader agrees to indemnify and hold the University harmless from and against any loss, damage, cost, liability or expenses arising from copyright infringement or unauthorized usage.

IMPORTANT

If you have reasons to believe that any materials in this thesis are deemed not suitable to be distributed in this form, or a copyright owner having difficulty with the material being included in our database, please contact lbsys@polyu.edu.hk providing details. The Library will look into your claim and consider taking remedial action upon receipt of the written requests.

DYNAMIC BEHAVIOR AND STABILITY ANALYSIS OF ELECTROSTATIC MEMS RESONATORS AND ELECTROMAGNETIC-TRIBOELECTRIC ENERGY HARVESTING SYSTEMS

XIN YANG

PhD

The Hong Kong Polytechnic University

2021

The Hong Kong Polytechnic University

Department of Civil and Environmental Engineering

Dynamic Behavior and Stability Analysis
of Electrostatic MEMS Resonators
and Electromagnetic-Triboelectric Energy Harvesting Systems

Xin Yang

A Thesis Submitted in Partial Fulfillment of the Requirements
for the Degree of Doctor of Philosophy

July 2020

CERTIFICATE OF ORIGINALITY

I hereby declare that this thesis is my own work and that, to the best of my knowledge and belief, it reproduces no material previously published or written, nor material that has been accepted for the award of any other degree or diploma, except where due acknowledgement has been made in the text.

_____(Signed)

_____ Xin YANG _____(Name of student)

ABSTRACT

Stemming from rapid urbanization leads to smarter cities that can improve the quality of life through advanced micro-electronic technologies. To realize the concept of Internet of Things (IoT) for smart cities, different types of sensors and devices (e.g., micro-electro-mechanical systems (MEMS)) are used to gain data to manage urban services and resources in a smart manner. With the continuous development of wireless sensor networks, the need for sustainable mobile power supplies is of paramount importance. These wireless sensors and devices can be powered by electrochemical batteries that are limited in lifespan and required periodic charging. To enable the vast deployment of sensors everywhere, one promising and feasible alternative is to directly harness energy from our environment (e.g., omnipresent vibration energy from ambient sources) that can allow a better self-autonomy.

From the perspective of mechanics, in MEMS devices and vibration-based energy harvesting technologies, nonlinear dynamic oscillations have been a topic to intensive research for recent years. In this research, the following four major topics are investigated to offer a better understanding of nonlinear dynamical behavior in MEMS resonators and energy harvesting systems. They are: (i) the nonlinear free and forced vibration of electrostatically actuated MEMS resonators; (ii) the nonlocal dynamic effect of micro-/nano-scale structures; (iii) the quantitative and qualitative analysis of a tri-stable nonlinear non-natural system; and (iv) the theoretical and experimental studies of a magnetic levitation-based electromagnetic-triboelectric energy harvesting technique governed by a tri-stable nonlinear mechanism.

In general, fully-clamped microbeams are one of the major structural components in most MEMS devices. This work aims to construct accurate and simple lower-order analytical approximation solutions for the free and forced vibration of electrostatically actuated MEMS resonators, in which geometrical and material nonlinearities are induced by the mid-plane stretching, dynamic pull-in characteristics, electrostatic forces and other intrinsic properties. First, the free vibration of a doubly-clamped microbeam suspended on an electrode due to a suddenly applied DC voltage is considered. Based on the Euler–Bernoulli beam theory and the von Karman type nonlinear kinematics, the dynamic motion of the microbeam is further discretized by the Galerkin method to an autonomous system with general nonlinearity, which can be solved analytically by using the Newton harmonic balance method. In addition to large-

amplitude free vibration, the primary resonance response of a doubly-clamped microbeam driven by two symmetric electrodes is also investigated, where the microbeam is actuated by a bias DC voltage and a harmonic AC voltage. Following the same decomposition approach, the governing equation of a harmonically forced beam model can be transformed to a non-autonomous system with odd nonlinearity only. Then, lower-order analytical approximation solutions are derived to analyze the steady-state resonance response of such a problem under a combination of various DC and AC voltage effects. Finally, the analytical approximation results of both cases are validated and they are in good agreement with those obtained by the standard Runge-Kutta method.

Micro-/nano-scale structures are widely used in the design of MEMS/NEMS resonators. Nonlocal elasticity theory is one of the most popular theoretical approaches to investigate the intrinsic scale effect of micro-/nano-structures, it incorporates long range interactions between points in a continuum model. From the point of view of physics, the coupling of an internal characteristic length and a material parameter can be regarded as a nonlocal scale parameter. The range of this non-dimensional scale parameter is from zero up to different values previously. The zero nonlocal scale parameter refers to a situation without any nonlocal effect. However, the determination of a peak value for the nonlocal scale parameter is still uncertain. In this research, the nano-structural dependence of nonlocal dynamical behavior is investigated to present the existence of an upper limit for the nonlocal scale parameter through a dynamical analysis of nanorods, nanobeams and nanoplates. It is not only beneficial to the refinement of the nonlocal theory of elasticity, and also useful for the exploration of similar theories in nano-mechanics.

In nonlinear energy harvesting technologies, multi-stable oscillating mechanisms are an effective approach to achieve a lower excitation threshold for inter-well motions. The intrinsic behavior of triple-well nonlinear oscillators can be illustrated by Duffing-type equations. To study such nonlinear problems, the large-amplitude oscillation of a triple-well non-natural system is investigated, covering both qualitative and quantitative analysis. By varying the governing parameters, the system is changed from a mono-stable behavior to a tri-stable one (having three stable states). In terms of qualitative analysis, various classifications for the equilibrium points and its trajectories of the system are provided. As exact solutions for this problem expressed in terms of an implicit integral form must be solved numerically, an

analytical approximation method based on the NHB method is used to construct lower-order accurate solutions to the oscillation around the stable equilibrium points of this system.

Making use of the tri-stable nonlinearity, a magnetic levitation-based electromagnetic-triboelectric energy harvester is designed and investigated. The hybrid generator not only enhances the power output through resonant inter-well oscillation behavior, and also offers a wide and highly efficient operating bandwidth under low-frequency (<10 Hz) and broadband sources. Although many vibration-based energy harvesters are resonant in nature, they have difficulty going into high-energy orbits under random low-level excitations to limit their output power density. To overcome this deficiency, the integration of a slider-driven electromagnetic generator and a sliding-mode triboelectric nanogenerator allows more energy to be harvested from a single motion, which can further improve the power density. Besides, the implementation of magnetic levitation can reduce the possibility of mechanical contact and impact damage to enhance a long-term durability in practical uses. In this study, both theoretical and experimental investigations are presented to verify this new design, in which only four outer magnets are required on a plane to establish a triple-well nonlinear behavior. In the theoretical analysis, the magnetic force of this harvester is calculated by the magnetizing current method and the formation mechanism of this tri-stability is verified by a bifurcation analysis. While for the experimental work, a battery-shaped prototype is fabricated and tested by an electrodynamic shaker to evaluate its working performance.

The research findings are expected to be useful for designing MEMS-driven devices and vibration-based energy harvesting systems that can advance the development of current cutting-edge IoT technology.

LIST OF PUBLICATIONS

Journal Papers

- **X. Yang**, C. Wang and S.K. Lai, A magnetic levitation-based tristable hybrid energy harvester for scavenging energy from low-frequency structural vibration, *Engineering Structures*, 221, 110789, 2020.

- S.K. Lai, **X. Yang** and F.B. Gao, Analysis of large-amplitude oscillations in triple-well non-natural systems, *Journal of Computational and Nonlinear Dynamics-Transactions of the ASME*, 14, 091002, 2019.

- S.K. Lai, **X. Yang**, C. Wang and W.J. Liu, An analytical study for nonlinear free and forced vibration of electrostatically actuated MEMS resonators, *International Journal of Structural Stability and Dynamics*, 19(7), 1950072, 2019.

- C. Li, S.K. Lai and **X. Yang**, On the nano-structural dependence of nonlocal dynamics and its relationship to the upper limit of nonlocal scale parameter, *Applied Mathematical Modelling*, 69, 127–141, 2019.

Conference Papers

- C. Wang, **X. Yang** and S.K. Lai, Nonlinear dynamics and performance enhancement of multi-stable wideband energy harvesting: Theoretical analysis, *Proceedings of The 2nd International Conference on Modeling in Mechanics and Materials*, Suzhou, China, 29–31 March 2019. (Published in IOP Conference Series: Materials Science and Engineering, Vol. 531, 012040, 2019.)

- **X. Yang**, S.K. Lai and F.B. Gao, Nonlinear vibration of stringer shells: Qualitative and quantitative analysis, *Proceedings of Cross-Strait Symposium on Dynamical Systems and Vibration*, Hong Kong, 10–17 Dec 2017.

ACKNOWLEDGEMENTS

CONTENTS

LIST OF FIGURES

LIST OF TABLES

LIST OF SYMBOLS

The main symbols used in this thesis are listed below:

Chapter 3

L	Microbeam length
b	Microbeam width
h	Microbeam thickness
d	Initial gap between the microbeam and the electrode
x	Length coordinate
y	Width coordinate
z	Thickness coordinate
w	Deflection in the z-direction
υ	Poisson ratio
ρ	Material density
ε_0	Permittivity of the gap medium
$V(t)$	Actuation voltage
V_{dc}	DC voltage
V_{ac}	Amplitude of the excited AC voltage
$\tilde{f}$	Frequency of the excited AC voltage
$\tilde{c}$	Linear damping per unit length
I	Moment of inertia of the cross section about the y-axis
E	Effective Young's modulus
E'	Young's modulus
N_i	Initial axial load due to the residual stress
$\bar{t}$	Dimensionless time
W	Dimensionless beam deflection
ξ	Longitudinal coordinate
c	Damping parameter
f	AC voltage frequency
$\phi(\xi)$	Assumed deflection shape function
$q(\bar{t})$	Mid-point deflection of the microbeam
$g(u)$	General function of u
$F(u),\ G(u)$	Odd functions of u
ω_1	First-order approximate angular frequency
T_1	First-order approximate period
$u_1(t)$	First-order approximate periodic solution

ω_2	Second-order approximate frequency
T_2	Second-order approximate period
$u_2(t)$	Second-order approximate periodic solution
ω_2^*	Improved second-order approximate frequency
T_2^*	Improved second-order approximate period
$u_2^*(t)$	Improved second-order approximate periodic solution
$\phi(\xi)$	Assumed deflection shape function
$f(u)$	Odd function of u
$h(v)$	Odd function of v
$\tilde{A}$	Amplitude of steady-state response
Δu_1	Periodic function of $\tilde{\tau}$ with a period of 2π

Chapter 4

$\mathbf{t}$	Nonlocal stress tensor
$\boldsymbol{\sigma}$	Classical (local) stress tensor
∇^2	Laplacian operator
e_0	Material parameter
a	Internal characteristic length
ρ	Axially vibrating nanorod with a mass density
A	Cross-sectional area
u	Axial displacement
x	Axial coordinate
t	Time
E	Young's modulus
σ_{ii}, τ_{ij}	Stress
ε_{ii}, γ_{ij}	Strain
ω_n	Circular frequencies for the axial vibration of nanorods with mode numbers n
L	Length of nanorod
τ	Non-dimensional nonlocal scale parameter
θ	Torsional angle
$\bar{t}_m$	Distributed torsional load per unit length
$\bar{T}$	Dimensionless twisting moment
M	Bending moment
w	Transverse displacement
I	Area moment of inertia

L_a	Plate length
L_b	Plate width
h	Plate thickness
μ	Poisson's ratio
q	Transverse load per unit area
m, n	Half-wave numbers

Chapter 5

x	Dimensionless displacement
t	Time variables
E	Total energy level
$\varepsilon_1, \varepsilon_2$	Real parameters
A	Oscillation amplitude
$x(\tau)$	Displacement
Ω	Frequency
$\Delta x_{a1}(\tau)$	Small increment of $x_{a1}(\tau)$
$\Delta\Omega_{a1}$	Small increment of Ω_{a1}
$a_i, b_i, \cdots, f_i$	Fourier series coefficients
$\omega_{a1}(A)$	First-order approximate frequency
$x_{a1}(t)$	First-order approximate periodic solution
$\omega_{a2}(A)$	Second-order approximate frequency
$x_{a2}(t)$	Second-order approximate periodic solution
λ	Coordinate value of the corresponding equilibrium point
T_{a1}	First-order approximate period
T_{a2}	Second-order approximate period
$V(\bullet)$	Potential energy of the system (5.1)
$\omega_{e1}(B)$	Exact frequency of the corresponding system (5.51)
$\omega_{e2}(B')$	Exact frequency of the corresponding system (5.52)

Chapter 6

$\vec{K}_m$	Surface current density of the magnet A
$\vec{B}_{ext-B}$	External magnetic flux densities of the magnets B1, B2, B3 and B4
$\vec{B}_{ext-C}$	External magnetic flux densities of the magnets C1 and C2
S	Surface area of the magnet A

$\vec{m}_A$	Magnetization of the magnet A
$\vec{n}$	Unit vector in the outward direction of the surface
$\vec{B}$	Magnetic flux density of an isotropic medium
μ_0	Magnetic permeability
$\vec{H}$	Magnetic field strength
M_0	Uniform magnetization
F	Gaussian hypergeometric function
s	Relative displacement between the slider and the tube
F_r	Restoring force
F_g	Force of gravity
R_B	Distance between the centers of the four outer magnets (B1, B2, B3 and B4) and the coordinate origin
R_C	Radius of the cylindrical magnets (C1 and C2)
R_A	Radius of the moving magnet A
l_B, w_B, h_B	Length, width and height of the four outer magnets (B1, B2, B3 and B4)
h_C	Height of the cylindrical magnets (C1 and C2)
h_A	Height of the moving magnet A
d	Distance between the centers of both cylindrical magnets (C1 and C2)
m	Proof mass
c	Total damping coefficient (including mechanical and electrical damping)
g	Gravitational constant
$\vec{f}_d$	Dry friction between Al and PTFE films
$\ddot{z}_b$	Input base acceleration
x	Relative displacement of the moving magnet
V_{oc-EMG}	Open-circuit voltage
I_{sc-EMG}	Short-circuit current
N	Number of coil turns
ϕ	Magnetic flux through the area enclosed by coils
R_l	Total internal coil resistance of coils
$V_{oc-TENG}$	Open-circuit voltage
$I_{sc-TENG}$	Short-circuit current
Q_{sc}	Short-circuit transferred charge
C	Capacitance between two electrodes
σ	Surface charge density on the slider
ΔS	Change of contact area

LIST OF ABBREVIATIONS

AC	Alternating Current
Al	Aluminum
CNT	Carbon Nanotubes
Cu	Copper
DC	Direct Current
EMG	Electromagnetic Generator
HAM	Homotopy Analysis Method
HPM	Homotopy Perturbation Method
IoT	Internet of Things
LP	Lindstedt–Poincaré
MEMS	Micro-Electro-Mechanical Systems
NEMS	Nano-Electro-Mechanical Systems
NHB	Newton Harmonic Balance
PEG	Piezoelectric Generator
PTFE	Polytetrafluoroethylene
PVC	Polyvinyl Chloride
PVDF	Polyvinylidene Fluoride
PZT	Lead Zirconate Titanate Piezoelectric Ceramics
SDOF	Single-Degree-of-Freedom
SECE	Synchronous Electric Charge Extraction
SSHI	Synchronous Switching Harvesting on Inductor
TENG	Triboelectric Nanogenerator

Chapter 1

INTRODUCTION

1.1 Background

Rising population and accelerating urbanization are leading to the rapid growth of urban cities. Although urbanization is not exclusively a modern phenomenon, industrialization and modernization have expedited urban development. The level of urbanization is expected to reach 66% of the world's population by 2050 from 54% in 2014 (McNicoll, 2005). Rapid population growth introduces high demands and challenges for urban resources and services. A viable way to address this problem is the development of "*smart cities*" that use innovative and renewable technologies to reduce the resource consumption of cities and optimize the efficiency of operations and services in a smart manner. Nonetheless, the smart city market has not yet taken off due to several current technical and financial barriers.

The Internet of Things (IoT) plays a critical role in the implementation of smart cities by reshaping working styles to integrate intelligent systems for process optimization and empowering users to interact with new technologies (Jawhar et al., 2018; Samih, 2019). IoT systems create large intertwined networks between computing devices, mechanical/digital machines, and people, and offer the unique ability to transfer data over a network without requiring human-to-human or human-to-computer interaction. The IoT paradigm represents ongoing technology development in that any object and environment can be connected to the Internet or local area networks using embedded devices (e.g., micro-electro-mechanical systems (MEMS) or nano-electro-mechanical systems (NEMS)). Such devices, including those for sensor reading and actuation tasks, can transform a physical object into an information source or receiver with the potential to communicate with all other things in the network. The IoT is made increasingly promising by recent advancements in miniaturization and integration of devices with higher computational capacity and lower energy consumption. IoT applications and services can cover many areas, including industrial automation, traffic management, consumer electronics, environmental monitoring, healthcare systems, and energy grids based on the advancement of MEMS technologies. IoT systems can also provide a network of

connected devices with high autonomy and low manpower expense to improve industrial processes, energy efficiency, and the quality of services and life.

MEMS include small devices that combine mechanical and electrical components to describe an emerging research field (Pelesko and Bernstein, 2003). The functional working elements of MEMS are miniaturized structures, sensors, actuators, and microelectronics. MEMS technology focuses on the miniaturization of existing devices and tool development for efficient operations in a micro-world. However, some undesirable consequences may result from the continuous reduction of device size. For example, MEMS resonators (microelectromechanical oscillating structures that define stable frequencies) operate near their pull-in voltage and may lead to pull-in instability, thereby deteriorating MEMS components. MEMS-driven devices have gained tremendous attention over a wide range of engineering applications, such as microphones in portable smartphones, bio-MEMS devices in medical and health technologies, signal filtering techniques for data smoothing, chemical and mass sensors, and high-precision temperature-compensated resonators in real-time clocks (Li et al., 2003; Ng et al., 2008; Choudhary and Iniewski, 2017).

Nevertheless, powering the tremendous amount of embedded devices in the IoT presents a grand challenge. In many IoT applications, a wireless power supply is required due to mobility requirements and network size. In these situations, traditional electrochemical batteries are typically used as power resources. A long device lifetime is of prominent need in many IoT applications; for example, devices deployed in high-rise buildings and civil infrastructure for monitoring purposes are expected to work for decades and regular battery replacement and maintenance are infeasible. Moreover, the exceedingly high number of discarded batteries adversely impacts the environment and limits the expansion of IoT applications. More than 3 billion batteries are discarded in the USA every year (Jayakumar et al., 2014), leading to serious problems of chemical waste disposal and environmental pollution.

Energy harvesting techniques have been extensively explored to address this dilemma as a permanent and environmental-friendly alternative for powering IoT systems (Shirvanimoghaddam et al., 2019). The rapid development of various energy harvesting techniques has therefore become a popular research challenge because the capture of renewable energy from the ambient environment offers a promising platform to support the explosive growth of a wide range of demands. The principle of energy harvesting techniques is to convert

energy in the ambient environment (e.g., thermal, vibration, solar, radio-frequency signal energy) into electrical energy. Among these, vibrational energy is highly sustainable in urban surroundings (e.g., high-rise buildings, long-span bridges, railway vehicles, industrial machines, and human bodies), which are also the main areas for IoT applications. Vibrational energy possesses a high power density (up to 100 W/m^3). For example, a large number of sensors and actuators can be embedded in a long-span bridge to monitor its structural integrity under environmental excitation (e.g., wind load, moving vehicles) during its life cycle. In this case, wireless sensors and controllers that should ideally be self-powered are used for real-time monitoring, prognosis, detection, and signal transmission. In this respect, the pursuit of a scalable solution of energy harvesting for power supply is an imperative issue. Innovative vibration-based energy harvesting techniques can therefore prolong the lifetime and improve the application range of wireless sensors.

Theoretically, all vibrational energy that can be converted into electrical energy is renewable and sustainable in the ambient environment, and the intent is mostly aimed to power wireless sensors and monitoring systems. Various vibration-based energy harvesting techniques are capable of performing vibration-to-electric energy conversion (e.g., electromagnetic, electrostatic, piezoelectric and triboelectric transduction mechanisms) (Priya and Inman, 2009; Spreemann and Manoli, 2012; Elvin and Erturk, 2013; Wang et al., 2016a). Due to the limitations and deficiencies of a single working mechanism under low-amplitude, low-frequency, and time-varying vibration sources, a hybrid mechanical design has emerged as a new trend to enhance the working performance of vibration-driven energy harvesting. By coupling multiple transduction mechanisms, more electrical energy can be converted from vibrational motion and the advantages of different transduction mechanisms can be compacted into a single hub.

1.2 Problem Statements

From the perspective of applied mechanics, nonlinear dynamics (Daqaq et al., 2014; Comi et al., 2020) in MEMS devices and vibration-based energy harvesting technologies is an important and intensive research topic in recent years and some critical topics must be further investigated for better understanding nonlinear dynamical behavior in MEMS resonators and vibration-driven energy harvesting systems. This work is divided into four major parts to summarize the following research problems:

(i)   nonlinear free and forced vibration of electrostatically actuated MEMS resonators;

3

(ii) nonlocalized scaling effects of micro-/nano-scale structures to account for long-range forces between atoms and molecules;

(iii) quantitative and qualitative analysis of a tri-stable nonlinear non-natural system (i.e., the kinetic energy of this system is not purely a quadratic function of velocity); and

(iv) theoretical and experimental analysis of a magnetic levitation-based electromagnetic-triboelectric energy harvesting technique governed by tri-stable nonlinearity.

Fully clamped microbeams are one of the major structural components in MEMS resonating systems. Geometrical and material nonlinearities in electrically driven MEMS resonators under dynamical motion are caused by mid-plane stretching, dynamic pull-in behavior, electrostatic forces, and material properties. Among these, the electrostatic force is a major parameter that is inversely proportional to the square of the distance between the microbeam and actuated electrode in a MEMS resonator. Induced by strong excitation levels, the electrostatic force can cause large-amplitude microbeam deformation, resulting in axial residue stress and a damping effect. Pull-in instability is also a common detrimental effect in MEMS devices. To study these effects, approximate analytical solutions are constructed for both free and forced vibrations of doubly clamped MEMS resonators under electrostatic forces, which can offer an all-encompassing view of the system nature in response to parameter changes that concern nonlinearity. Because such dynamic problems are strongly nonlinear, exact solutions are scarce and unavailable except under very limited circumstances. Dynamic models of such cases can be derived using Kirchhoff's hypothesis and von Kármán nonlinear kinematics (Chia, 1980). Analytically solving the dynamic problems allows a coupling of Newton's method with the harmonic balancing (NHB) approach (Wu et al., 2006; Lai, 2007; Wu et al., 2017) to be applied for formulating lower-order approximate analytical solutions, which can provide accurate results for the primary resonance responses of systems subjected to various bias DC and harmonic AC voltage levels. The pull-in phenomenon of the MEMS resonators is also investigated for stability analysis.

Micro-/nano-scale structures are widely used in the design of MEMS/NEMS resonators due to the rapid development of nanotechnology and their unique properties, such as high strength and low density. Unfortunately, classical continuum theories cannot accurately interpret the dynamical behavior of micro-/nano-structures because they do not account for the interaction between atoms and molecules. Nonlocal elasticity theory (Eringen and Edelen, 1972; Eringen, 1983) is a generalized continuum mechanics theory that can be used to explain long-

4

range forces between atoms and molecules. This theory has been extended to various nano-scale structures (e.g., beams, rods, arches, shells) (Reddy, 2007; Wang et al., 2007a; Reddy, 2008; Hu et al., 2008; Lim, 2010a; Wang et al., 2012a). It is assumed that the stress at a specific point is a function of strain at all points in the continuum. To reflect the contribution of strains at other points to the stress at a specific point, nonlocal constitutive relations introduce a relevant kernel function that can be used for scaling effects to handle the distance between other points and the specific point. Owing to the kernel function and the internal characteristic length, nonlocal theory can capture nonlocal scaling effects that are ignored in classical continuum theory. Previous studies have shown that nonlocal results are in good agreement with those obtained from molecular dynamics simulations and experiments. Nonlocal elasticity theory can also be transformed into classical theory following the assumption of a long-wavelength limit, and to atomic lattice dynamics following the assumption of a short wavelength limit (Li et al., 2019). The coupling of an internal characteristic length and material parameter can be regarded as a nonlocal scaling parameter. This non-dimensional scaling parameter ranges from zero to various values without a rigorous explanation. In this study, the nano-structural dependence of nonlocal dynamical behavior is studied to verify the presence of a peak nonlocal scale parameter value through the dynamical analysis of nano-scale structures (i.e., nanorods, nanobeams, nanoplates).

The application of multi-stable nonlinearity-enhanced mechanisms (Erturk and Inman, 2011; Daqaq et al., 2014; Wang et al., 2018; Wang et al., 2019a) in nonlinear energy harvesting technology plays a crucial role in improving the working performance of vibration-based energy harvesters under a low excitation threshold via inter-well motions. The tri-stable nonlinear approach is useful for these purposes. The intrinsic behavior of triple-well nonlinear oscillators can be illustrated by Duffing-type equations (Nayfeh and Mook, 1995; Kovacic and Brennan, 2011). To study such nonlinear problems, the large-amplitude oscillation of a triple-well non-natural system is selected for investigation. The nonlinear system is governed by a quadratic dependence term on the velocity and an odd-parity restoring force with cubic and quintic nonlinearities. A variety of mathematical models in mechanical and structural engineering applications can give rise to this nonlinear problem. By varying the governing parameters, the system changes from a mono-stable state (with a single fixed point) to a tri-stable state (with three stable points). In terms of qualitative analysis, various classifications for the equilibrium points and its motion trajectories of the system are provided. Because exact solutions for this problem expressed in the form of an implicit integral must be solved

numerically, an analytical approximation method based on the NHB method is used to construct accurate lower-order solutions to the oscillation around the stable equilibria of this system.

Making use of the tri-stable nonlinearity, a magnetic levitation-based electromagnetic-triboelectric energy harvester has been designed and investigated. The hybrid generator not only enhances power output through resonant inter-well oscillation behavior but also offers a wide and highly efficient operating bandwidth under low-frequency (<10 Hz) and broadband sources. Many vibration-based energy harvesters are resonant types but high-energy orbits are difficult to reach under random low-level excitation levels, which restricts their output power density. To resolve this problem, the integration of a slider-driven electromagnetic generator and sliding-mode triboelectric nanogenerator can allow more energy to be harnessed from a single motion, which further improves the power density. The implementation of magnetic levitation can reduce the possibility of mechanical contact and impact damage to enhance long-term durability in practical use. In this work, both theoretical and experimental investigations are presented to test this new energy harvesting design, in which only four outer magnets are required on a plane to establish triple-well nonlinear behavior. In the theoretical analysis, the magnetic force of this energy harvester is calculated by the magnetizing current method (Agashe and Arnold, 2008) and the formation mechanism of the tri-stability is verified through bifurcation analysis. In the experimental study, a fabricated prototype is tested by an electrodynamic shaker to evaluate its working performance.

1.3 Research Objectives

The major objectives of this thesis are twofold. The first objective is to investigate nonlinear dynamic oscillations in MEMS resonators using the NHB method. An elegant and interesting trait of analytical approximation methods is their ability to solve nonlinear dynamical systems in many different applications rather than being restricted to a simple nonlinear system with a small perturbed parameter and oscillation amplitude (Lai, 2007). This goal is achieved by constructing approximate analytical solutions for both free and forced vibrations of doubly clamped MEMS resonators under electrostatic forces, which offer an all-encompassing view of the system nature in response to changes of system parameters that concern nonlinearity. Because micro-/nano-scale structures are involved in the design of MEMS resonators, the nonlocal dynamic effect of micro-/nano-scale structures is also investigated. Specifically, the tasks related to this objective are summarized as follows:

- modeling of nonlinear free and forced vibration of electrostatically actuated MEMS resonators based on the Euler–Bernoulli beam theory and von Kármán strain-displacement assumptions;

- construction of approximate analytical solutions for both models by coupling Newton's method with the harmonic balancing approach; and

- presentation of the existence of an upper limit for the nonlocal scale parameter through dynamical analysis of various nano-scale structures.

The second objective is to investigate the tri-stable oscillating mechanisms in vibration-based energy harvesting technologies. The intrinsic behavior of triple-well nonlinear oscillators can be illustrated by Duffing-type equations. To study such nonlinear problems, the large-amplitude oscillation of a triple-well non-natural system is investigated. To achieve this objective, the following tasks are addressed:

- qualitative and quantitative analysis of the large-amplitude oscillation of a triple-well non-natural system;

- development of a magnetic levitation-based electromagnetic-triboelectric energy harvester with tri-stable nonlinearity; and

- verification of the new design by both theoretical and experimental investigations.

This hybrid vibration-based energy generator enhances the power output through resonant inter-well oscillations and also offers a wider and highly efficient operating bandwidth under low-frequency (<10 Hz) and broadband vibration sources. The proposed energy harvester can perform symmetric oscillations in a horizontal position when the restoring force is only caused by a magnetic force. Upon placing the device in a vertical orientation, the oscillating system becomes asymmetric under the effects of both magnetic forces and gravity. Besides, the application of magnetic levitation can increase the durability of this device in practical engineering environments because mechanical contact and impact collisions are both reduced.

1.4 Research Methodology

Both quantitative and qualitative analyses of the nonlinear dynamic oscillations of MEMS resonators and large-amplitude oscillation of triple-well nonlinear systems are presented in this study. In the quantitative analysis, the NHB approach is used to formulate approximate analytical solutions of these nonlinear systems. This method yields an extended scope of

applicability and simplicity in applications and is also valid for solving nonlinear dynamical problems governed by large governing parameters and oscillation amplitudes compared with other conventional asymptotic approaches. Unlike traditional perturbation and classical harmonic balance methods, this approach formulates a set of linear algebraic equations depending only on initial conditions and does not require numerical integration. In the qualitative analysis, the existence of equilibria and their stability analysis are examined and classified.

Nonlocal elasticity theory is one of the most popular theoretical approaches to investigate the intrinsic scaling effects of micro-/nano-scale structures. The coupling of internal characteristic length and a material parameter can be regarded as a nonlocal scale parameter in nano-meters. There is no doubt that the zero nonlocal scale parameter corresponds to a situation without nonlocal effects (i.e., classical dynamic behavior). Nevertheless, the determination of critical value for the scaling parameter is a fundamental problem that remains uncertain. Different maximum values have been selected without rigorous verification. In this work, the nano-structural dependence of nonlocal dynamical behavior is investigated to verify the existence of an upper bound of the nonlocal scale parameter.

In addition, a comprehensive study involving both theoretical and experimental investigations is presented for a newly designed electromagnetic-triboelectric energy harvesting technique. This work exploits the relative motion between a coil and a magnet produced by low-frequency mechanical vibrations to induce an electrical voltage in the coil. The magnetizing current method is used to calculate magnetic forces, and bifurcation and chaotic analyses are applied to verify the formation mechanism of the tri-stable nonlinearity.

1.5 Thesis Outline

The thesis is organized into seven chapters. A brief framework of the thesis is given as follows.

- Chapter 1 introduces the present work and states the research objectives and methodologies.
- Chapter 2 reviews the relevant literature on MEMS devices, nonlocal elasticity theory, vibration-based energy harvesting techniques, various analytical approximation methods, and multi-stable nonlinear oscillating mechanisms.

- Chapter 3 presents derivations of accurate analytical approximation solutions for the nonlinear free vibration of an electrostatically actuated MEMS resonator with a one-sided electrode and investigates the resonance response of an electrostatically actuated MEMS resonator with two-sided electrodes under bias DC voltage and harmonic AC voltage.

- Chapter 4 discusses the nano-structural dependence of nonlocal dynamical behavior for verifying the existence of an upper limit of the nonlocal scale parameter through a dynamical analysis of nanorods, nanobeams, and nanoplates.

- Chapter 5 describes the qualitative and quantitative investigations of large-amplitude oscillation of a triple-well non-natural system, which is governed by a quadratic damping term and odd-parity restoring force with cubic and quantic nonlinearities.

- Chapter 6 presents the development of a novel magnetic levitation-based electromagnetic-triboelectric energy harvester governed by the tri-stable nonlinear mechanism. In terms of theoretical analysis, the magnetic force of this energy harvester is calculated by the magnetizing current method and the formation mechanism of this tri-stable nonlinearity is confirmed by bifurcation analysis. An experimental prototype is also fabricated to examine the effectiveness of the present design under low-frequency structural vibration sources.

- Chapter 7 summarizes all major findings of the research, discusses its advantages and limitations, and provides recommendations for the directions of future research.

Chapter 2
LITERATURE REVIEW

Nonlinear dynamic problems occur in many MEMS devices and vibration-based energy harvesting techniques. This chapter presents a comprehensive review of the following topics:

- dynamic behavior and responses of MEMS resonators;
- nonlocal elasticity theory in continuum mechanics;
- vibration-based energy harvesting techniques; and
- multi-stable nonlinearity-enhanced mechanisms.

2.1 Dynamic Behavior and Responses of MEMS Resonators

With the rapid development of current technologies, miniaturized structures with micro-scale features can be precisely manufactured and applied in MEMS devices. Elastic beams or plates of micro-scale thickness are most popular in these systems. In addition to the load-bearing capability, they can also be used as sensors and detectors to measure the interaction of certain molecules on their surface. Establishing an accurate relationship between dynamic behavior and deformation is thus a key issue for analysis. In such systems, MEMS resonators are mechanically resonating micro-structures that are electrically brought into resonance (Abdolvand et al., 2006). Since first proposed in the 1960s (Nathanson et al., 1967), MEMS resonators have been used in a wide range of applications within engineering, including signal filtering techniques, chemical and mass sensors, and probe-based microscopy (Younis and Alsaleem, 2009; Zhao et al., 2009; Rhoads et al., 2010). It is worth noting that mechanical nonlinearities in MEMS resonators can considerably affect the pull-in behavior and dynamic characteristics. The following comprehensively reviews the role of nonlinearities in MEMS resonators, as well as various analytical approximation approaches that extensively used to solve nonlinear problems.

2.1.1 Nonlinearities and Common Phenomena in MEMS Resonators

Among various actuation methods, electrostatic actuation is the most prevalent mechanism due to its associated advantages, such as simple micro-machining processes, small electrode size, and low power consumption (Zand, 2012). For electrostatically actuated MEMS resonators, force nonlinearity mainly comes from electrostatic and intermolecular forces,

which are nonlinearly related to the displacement that softens the device (Jia et al., 2012). The electrostatic force results from an electrostatic charge induced by an electrical potential difference between the electrodes accompanying the electric load. Intermolecular interactions between two electrodes become significant in the design of resonators with the miniaturization of such devices (Serry et al., 1998). The geometric nonlinearity is mainly caused by nonlinear stretching, which stiffens the device. For a doubly clamped microbeam, mid-plane stretching accompanies its transverse vibration.

The fringing field effect should be taken into account when modeling the electric field force. Several different formulae for computing fringing fields are presented in the literature; most notable are those proposed by Palmer (1937), Chang (1976; 1977), van der Meijs and Fokkema (1984), and Batra et al. (2006). Among these fringing field models, Palmer's formula can rapidly compute the capacitance with sufficiently small errors (Leus and Elata, 2004). Residual stress results from micro-machining processes and thermal expansion mismatch between different elements of MEMS devices (Madou, 1997), for which there is no unified measurement method. Some approaches are based on measuring its effect on the crystallographic structure of the material (Constable et al., 2004), measuring its effect on the micro-test structures subjected to mechanical loads (Ziebart et al., 1998; Denhoff, 2003), measuring the voltage and deflection at the pull-in state in electrostatically actuated MEMS devices (Osterberg and Senturia, 1997).

Additionally, typical long-range forces in MEMS devices involve van der Waals forces and Casimir forces, both of which are mainly due to spectrum alternation of the zero-point vacuum electromagnetic field in and around the space occupied by material bodies. Such forces can induce nonlinearity in the dynamic motions of a micro-structural element even if the deformation is small. Because of this complexity, the study of the elastic responses of structural elements coupled with long-range forces remains a challenging topic (e.g., stiction instabilities). Most previous studies used either elastic beam theory (De Boer and Michalske, 1999) or simple lumped electromechanical models consisting of a linear spring, a mass, and a parallel-plate capacitor (Osterberg and Senturia, 1997).

Furthermore, dynamic pull-in instabilities can lead to the deterioration of MEMS components, which is undesirable in MEMS resonators. This phenomenon has been extensively studied. Nayfeh et al. (2007) investigated the dynamic pull-in instability in a doubly

clamped microbeam and addressed the need for its consideration in MEMS design. Krylov (2007) studied the influence of various parameters on the dynamic pull-in instability of a microbeam based on the Lyapunov exponent criterion. Alsaleem et al. (2009; 2010) theoretically and experimentally investigated dynamic pull-in in MEMS resonators. Lakrad and Belhaq (2010) studied the effect of a high-frequency AC voltage on the pull-in instability of a MEMS device. Seleim et al. (2012) investigated the bifurcation and chaos of a closed-loop electrostatic MEMS resonator. Fang and Li (2013) accurately determined the dynamic pull-in voltage and pull-in position of microbeams using two analytical approximate models.

2.1.2 Theoritical Analysis for Nonlinear Problems

Nonlinear dynamic systems are commonly investigated both experimentally and theoretically. In theoretical research, both qualitative and quantitative analyses are involved. The qualitative analysis mainly refers to the phase plane method, which can represent all possible motions of the vibration system on the phase plane so that some properties of the system can be studied without specifically determining a solution (e.g., type and stability of singularities, existence, and stability of limit cycles). This information contributes to further study of the system but does not provide a quantitative solution. Because exact analytical solutions for nonlinear systems are rarely obtained owing to the existence of nonlinear terms, quantitative analysis mainly includes numerical methods and approximate analytical methods.

Numerical methods are well-developed tools for studying nonlinear dynamical problems. By adopting the time integration method to solve differential equations, numerical methods can provide accurate displacement, velocity, and acceleration values of the nonlinear dynamical system at certain moments. Some approaches, such as the Runge–Kutta method, are well developed with excellent accuracy and can also be used to verify the accuracy of other methods. However, numerical methods have intrinsic limitations. For example, they can only give discrete numerical solutions to nonlinear dynamical systems but not an overview of the system solutions. Hence, it is impossible to analyze the global properties of nonlinear dynamical systems using numerical methods.

Approximate analytical methods provide analytical expressions of solutions, which can be used to study the motion law of a nonlinear dynamical system, as well as the relationships between the motion characteristics of the system and system parameters, which thereby

facilitates parameter control of the system. However, compared with numerical methods, many approximate analytical methods involve tedious derivations and extensive computations. Some of the common approximate analytical methods are introduced here.

Perturbation-based methods are generally only suitable for problems with weakly nonlinear parameters (i.e., a small parameter). In principle, solutions and desired quantities are expanded into a power series of this small parameter. Based on the power of the small parameter, the governing differential equation of the nonlinear dynamical system can be discretized into a set of linear equations, which can be solved. The Lindstedt–Poincaré (LP) method, the averaging method, and the multiple scales method are common perturbation-based methods (Nayfeh and Mook, 1995). The LP method is a classical perturbation method initially introduced by Lindstedt in the 1880s. The basic idea is to expand the solution and frequency in a power series of a small parameter and then substitute them into the original differential equation for further calculation. Poincaré (1892) proved that the Lindstedt series is asymptotic in nature. Burton (1984) developed a modified version of the LP method, which was later modified for strongly nonlinear systems.

The method of averaging, originally developed in the 1930s (Krylov and Bogoliubov, 1937), can obtain both transient and steady-state responses by using small perturbations of corresponding linear oscillators. A detailed treatment of this method shows that it applies not only to time-varying periodic differential equations but also to those that do not necessarily exhibit time-periodic behavior (Sanders and Verhulst, 1985). In this case, the coefficients of the resultant averaged equations are then averaged over an infinitely long time interval. This idea was extended to obtain higher-order solutions for quasi-periodic differential equations (Perko, 1968) and non-periodic systems (Saenz, 1991). Leung and Zhang (1998) demonstrated the link between higher-order averaging and the Poincaré normal form of dynamical systems. This method was later used to study fractional oscillators (Li et al., 2001; Pankaj and Anindya, 2004; Shen et al., 2012a) where an averaging procedure is performed over an infinite time interval.

The method of multiple scales is another classical method that is applicable to a vast range of problems. The basic idea of this method is to consider the solution and time to be an expansion of multiple time scales, and then substitute them into the original differential

equation to collect the terms of various scales. These scales are identified by various orders of a smaller parameter, which are generally required in perturbation methods. A major advantage of this method is that the evolution equations yielded on slow time scales can be used to conduct stability analysis of the periodic solutions, which is scarce among perturbation methods and makes this method very popular for weakly nonlinear systems. The method of multiple scales covers nearly all of the areas accessible by perturbation methods and has been widely used in the literature (Nayfeh and Hassan, 1971; Asfar and Nayfeh, 1983; Hanagud et al., 1985; Janowicz, 2003; Shivamoggi, 2003; Luongo and Egidio, 2005; Alijani et al., 2011).

The classical harmonic balance method is also applicable to both weakly and strongly nonlinear problems. This is a special case of the Galerkin method with a trigonometric series as base functions. The periodic solution is expanded into a Fourier series with a certain number of harmonic terms depending on the accuracy requirement and then substituted into the governing differential equations to obtain a set of nonlinear algebraic equations by setting the corresponding harmonic coefficients to zero. Urabe et al. (1965; 1966) provided mathematical theories on the existence, convergence, error bound, and stability analysis of solutions of this method. Kelley and Mukundan (1993) defined the convergence of this method under more restrictive assumptions. However, the nonlinear algebraic equations are usually excessively complicated, which makes it particularly difficult to obtain high-order approximate solutions. A new approach is therefore required to overcome the shortcomings of the harmonic balance method.

The homotopy analysis method (HAM) is a semi-analytical technique for solving nonlinear problems. The rationale of the HAM originated from the concept of homotopy from topology to generate convergent series solutions for nonlinear systems. It was first proposed by Liao (1992; 2003) and further modified to introduce a non-zero auxiliary parameter to construct homotopy in a differential system in a general form and has been used to solve various nonlinear problems, including fluid flow between vertical porous plates (Abdulaziz et al., 2009), limited cycle flutter of airfoils (Chen and Liu, 2008), unsymmetrically laminated composite beams on a nonlinear elastic foundation (Talookolaei et al., 2011), flow of a power-law fluid film on an unsteady stretching surface (Wang and Pop, 2006), and the strongly nonlinear vibration of an elastically restrained beam with a lumped mass (Qian et al., 2011).

Many other methods have been developed for solving strong nonlinear systems based on perturbation-type and harmonic balancing-based methods. For example, Cheung et al. (1991) proposed a modified LP method by introducing a new parameter that remains small regardless of the magnitude of the original parameter. This allows a strongly nonlinear system to be changed into weakly non-linear using the new parameter and solved by the LP method. However, this method requires a non-zero linear part of the restoring force. Lau and Cheung (1981) proposed the incremental harmonic balance method, which linearizes the set of nonlinear ordinary differential equations along an incremental path to obtain a set of linear algebraic equations at a given time. This is a semi-analytical method that can be applied to analyze various nonlinear systems but cannot independently provide an initial solution. Leung et al. (2010) proposed the residue harmonic balance method to solve strongly nonlinear ordinary differential equations with fractional-order derivatives that represent the viscoelastic damping (Leung and Guo, 2011a), as well as the limit cycle of nonlinear jerk equations (Leung and Guo, 2011b). This method begins with an initial approximation obtained by solving the nonlinear algebraic equations resulting from a one-term Fourier series substitution into the ordinary differential equations. The residues resulting from the truncation of the Fourier series can be iteratively minimized by solving the linear algebraic equations. This approach was later used to solve a nonlinear system with inertia and static nonlinearities (Ju and Xue, 2015), a Duffing-type equation (Ju, 2015), and a restrained cantilever beam (Qian et al., 2017).

2.1.3 Nonlinear Free Vibration of Electrostatically Actuated MEMS Resonators

Fully clamped microbeams are one of the major structural forms used in the design and analysis of MEMS, due to their simplicity and applicability. In the literature, numerous studies have investigated the nonlinear dynamic behavior of various microbeam structures. Initially, the dynamic performance of microbeams was studied experimentally (Zook et al., 1992; Ayela and Fournier, 1998). In addition, both physical and mathematical models have been formulated to describe the dynamic behavior of MEMS resonators. In the theoretical analysis, a single-degree-of-freedom (SDOF) beam model is typically adopted to study the nonlinear response of microbeams (e.g., Tilmans and Legtenberg, 1994; Kuang and Chen, 2004; Mestrom et al., 2008; Kacem et al., 2009). Using the SDOF model assumption, the dynamic characteristics of MEMS resonators can be described by a nonlinear dynamic system. As exact closed-form solutions for complicated nonlinear dynamic systems are often not available, numerical and analytical methods are commonly used for theoretical analysis.

Making use of numerical-based approaches, Kuang and Chen (2004) examined the dynamic characteristics of shaped micro-actuators via the differential quadrature method. Wang et al. (2007b) characterized the dynamic responses of fixed micro-switches subjected to various voltage levels via a mesh-free method. Alsaleem et al. (2009) considered the nonlinear resonance and dynamic pull-in instability of MEMS resonators using the finite-difference method. Jia et al. (2010) carried out a numerical analysis for the free vibration of geometrically nonlinear micro-switches subjected to both electrostatic and Casimir forces. Ghayesh et al. (2013) investigated the nonlinear behavior of electrically actuated MEMS resonators by means of a pseudo-arclength continuation technique. On the basis of the classical Runge–Kutta method, Dantas and Gusso (2018) extended an investigation to the chaotic behavior of doubly clamped beam MEMS resonators, and Li et al. (2018) also considered the effect of thermal fields on the dynamic response of microbeams.

Although numerical methods can accurately predict the dynamic responses of MEMS resonators, they are not able to provide an all-encompassing view for analyzing the intrinsic nature and characteristics of complicated nonlinear dynamic systems. Hence, the concentration of analytical approximations for nonlinear dynamic systems has become more important. Using a variety of methods such as the multiple scale, harmonic balance, and perturbation-based approaches, many problems have been solved analytically. For example, Younis and Nayfeh (2003) formulated analytical expressions for the dynamic response of resonators. Zhang and Meng (2007) conducted a nonlinear dynamic analysis of MEMS sensors under parametric excitations. Elshurafa et al. (2011) studied the nonlinear dynamic behavior of folded-MEMS comb-drive resonators. Rezazadeh et al. (2012) analyzed the parametric oscillation of a microbeam. Moreover, Caruntu and Knecht (2011) and Caruntu and Taylor (2014) investigated the nonlinear response of micro-resonators under a near-half natural frequency and presented steady-state solutions for MEMS cantilever resonators, respectively. Qian et al. (2012) derived periodic solutions for a higher-order nonlinear oscillator that often arises in MEMS. Han et al. (2015a, 2015b) predicted the existence of chaotic motions in a fully clamped MEMS resonating device having two symmetrically actuated electrodes. Li and Zhang (2017) further gained deeper insights into the bistable effect of microbeam systems. More recently, Saadatmand and Shooshtari (2018) also performed a forced nonlinear vibration analysis of circular micro-plates in two-sided MEMS capacitive systems.

To analytically study the problem of electrostatically actuated MEMS resonators, the Newton harmonic balance (NHB) method is used in this study. This approach combines Newton's method and the classical harmonic balance method. It is conducted by first linearizing governing equations through Newton's method and then imposing the harmonic balance method, such that a set of linear algebraic equations can be derived instead of coupled and complicated nonlinear algebraic equations. This enables the complexity of the classical harmonic balance method to be greatly simplified. Specifically, only Fourier series expansions of some known functions are required, and the NHB method can be used to derive accurate lower-order analytical approximate solutions for a whole range of oscillation amplitudes. Furthermore, the accuracy of this method is unconstrained by the presence of large governing parameters.

This method was initially proposed by Wu et al. (2006) to derive accurate approximate solutions for large-amplitude oscillations of conservative SDOF systems with odd nonlinearity. Subsequently, it was extended to derive analytical approximations for general strongly nonlinear conservative oscillators by introducing two new oscillating systems with odd nonlinearity (Sun and Wu, 2008; Lai et al., 2009b). This method has been successfully generalized to deal with various strongly nonlinear problems in structural and mechanical engineering, such as the nonlinear jerk equation (Wu et al., 2006), the double sine-Gordon equation (Lim et al., 2007), large post-buckling deformation of elastic rings under a uniform hydrostatic pressure (Wu et al., 2007a), a double-well Duffing oscillator (Wu et al., 2007b), a mass oscillation system attached to a stretched elastic wire (Sun et al., 2007), a large hydrothermal buckling deformation of beams (Yu et al., 2008), a nonlinear vibration of a constant-tension string (Lai et al., 2008), a nonlinear cubic-quintic Duffing oscillator (Lai et al., 2009a), a large-amplitude vibration of simply-supported laminated plates (Lai et al., 2009b), a nonlinear oscillation of a current-carrying wire in magnetic fields (Sun et al., 2009), and a strongly nonlinear damped oscillator (Wu and Sun, 2010).

In the past decade, following the NHB method, Yu et al., (2012; 2013a; 2013b; 2017) investigated a post-buckling deformation of MEMS beams, a large-amplitude vibration of spring-hinged beams, a post-buckling deformation of sandwich beams, and a large-amplitude free vibration of cantilever tapered beams resting on a nonlinear elastic foundation. Sun et al. (2015) analyzed the instability behavior of a drill string in a horizontal well. Liu et al. (2017a) considered a free vibration problem of electrostatically actuated MEMS resonators.

Furthermore, Lai et al. (2017) studied the dynamic behavior of a structural system with a pair of irrational nonlinearities. Tang et al. (2017) extended the method to the nonlinear free vibration of dielectric elastomer balloons.

In addition, Wu et al. (2017) further modified the NHB method for solving strongly nonlinear conservative oscillators by implementing the second-order Newton iteration procedure and the harmonic balance method. This modified version not only retains the salient features of the original NHB method but also includes information on the second-order derivative, thereby resulting in a faster convergence rate. More recently, Liu et al. (2019) extended the method to derive analytical approximate solutions for asymmetric conservative oscillators. Soon after, Wu et al. (2018b) further extended the NHB method to yield accurate approximate solutions to study the resonance responses of harmonically forced nonlinear oscillating systems.

2.1.4 Nonlinear Forced Vibration of Electrostatically Actuated MEMS Resonators

Forced nonlinear oscillation systems have attracted a great deal of research attention because they are common in many structural and mechanical components working under periodic loadings and cyclic excitations. These systems are much more intricate than free oscillation systems, as they exhibit both resonance and nonlinear effects. Different methods are available for obtaining analytical approximate solutions of harmonically forced nonlinear oscillation problems, each with their own limitations. As mentioned above, various perturbation-based methods have been widely used for the analysis of weakly nonlinear oscillation systems; these require the presence of small physical parameters in governing equations for analytically expanding the solution in a power series of that parameters. Such methods are likely to be inefficient for accurately solving strongly forced nonlinear systems, which do not have small parameters. Moreover, even when small parameters do exist, the analytical representations of perturbation-based methods are generally limited to a small range of validity.

A general review of some studies relevant to forced nonlinear oscillation problems in the past few decades is given as follows. Burton (1984) proposed a modified version of the LP method that is applicable for the steady-state response of strongly nonlinear vibration systems under weak harmonic excitations. Burton and Rahman (1986) developed a modified version of the multiple-scale method to construct lower-order approximate solutions of strongly nonlinear

forced oscillators. They further used this method to investigate the large-amplitude primary- and super-harmonic resonances in the Duffing oscillator (Rahman and Burton, 1986). Later, Rahman and Burton (1989) compared two different higher-order multi-scale expansion methods with the LP method to investigate the steady-state response of forced nonlinear vibration systems. In the 1990s, Hassan (1994a, 1994b) applied the higher-order multi-scale method with reconstitution to determine the periodic steady-state periodic response of harmonically excited nonlinear oscillators. Xu and Cheung (1994) extended the average method using a generalized harmonic function to solve strongly forced nonlinear vibration problems. This extended method can obtain good results in the primary resonance region, but the error in the region remote from the primary resonance tends to become dominant. Chen and Cheung (1996) further developed a modified approach of the LP method for a strongly nonlinear system with quadratic and cubic nonlinearities. Nayfeh and Lacarbonara (1997) identified a first-order modal approximation for the primary and subharmonic resonances of a parameter distribution system with even nonlinearity under periodic excitations. The approximate results were highly consistent with the numerical results, but the higher-order modal approximate solution of this method may not be consistent with the numerical solutions.

Furthermore, Waluya and van Horssen (2003) approximated the first integral for strongly nonlinear forced oscillators using a perturbation method based on integrating factors. Azrar et al. (2002) studied the nonlinear forced vibration of elastic thin plates under various types of harmonic excitations using an asymptotic-numerical method. Sze et al. (2005) extended the incremental harmonic balance method to investigate the forced response of axially moving beams with the internal resonance between the first two transverse modes. Yang and Chen (2006) performed an analysis of the nonlinear forced vibration of axially moving viscoelastic beams excited by a supporting foundation. Yao and Zhang (2007) proved the existence of Shilnikov-type multi-pulse orbits in the dynamic response of rectangular thin plates under parametric excitations. In addition, Avramov (2008) proposed coupling of the Rausher method and nonlinear modes to analyze the forced vibration of shallow arch structures. Abdoun et al. (2009) also presented an asymptotic analysis for the forced harmonic vibration of viscoelastic structures.

In the past decade, Kovacic and Brennan (2011) reviewed various methods for solving different types of forced Duffing-type equations. Ghayesh and Amabili (2012) analyzed the internal resonance effect on the nonlinear response of axially moving beams. Bekhoucha et al.

(2013) dealt with the forced nonlinear vibration problem of rotating anisotropic beams with uniform cross-sections. Jiang et al. (2015) made various comparisons of the use of the LP, multi-scale, averaging, and harmonic balance methods for solving nonlinear forced oscillators under weak and strong external excitations. The results showed that the harmonic balance method is superior to other methods for solving the forced harmonic vibration of nonlinear oscillators. Tajaddodianfar et al. (2015; 2017) adopted the homotopy analysis method to analyze the dynamic responses of doubly clamped micro-structures under combined DC and AC actuation. Chakraverty and Mall (2017) generalized an artificial neural network method to solve the forced vibration equation of Duffing-type problems. More recently, Liang et al. (2018) considered the forced vibration of gyroscopic structures in terms of nonlinear normal modes and using an iterative approach. To refine the accuracy of analytical approximations to nonlinear forced-type problems, Wu et al. (2018b) devised an improved version of the NHB method to establish accurate lower-order approximate solutions for harmonically forced nonlinear oscillation systems.

2.2 Nonlocal Scaling Effect in Micro-/Nano-scale Structures

As mentioned in the previous section, micro-/nano-scale structures are widely used in MEMS/NEMS devices. The development trends and perspectives of MEMS/NEMS in various engineering applications can be referred to Fig. 2.1 (Zhu et al., 2020). In recent decades, rapid advances in nanoscience and nanotechnology further make these devices more compact and ingenious. The miniaturization of structures allows more functionality in a given hub. MEMS/NEMS resonators are often simplified as beam- or plate-type structures in mechanical design, having length scales in the range of 10–10^4 μm and feature sizes on the order of a few nanometers (Rhoads et al., 2010). At such micro-/nano-scale structures, the influence of material length scales in the study of mechanics of solid structures cannot be ignored. For example, a sensor can act as a detector or device that measures a physical quantity and converts it into a signal, which can be read by an instrument; an actuator is a motor that operates using an energy source for controlling a mechanism or system. Examples of sensors are thermocouples and pressure transducers (Goh et al., 2018), whereas examples of actuators are micro-/nano-probes and biochemical sensing materials (Yew et al., 2007; Goh et al., 2019). The effects of surface stress are not taken into consideration in most practical sensor and actuator designs. The omission of surface stress is acceptable for sensors and actuators on the large scale, while the neglect of surface stress on the micro- to nano-scale can cause significant

response underestimation, resulting in undesirable performance, unwanted behaviors, or even design failure.

Experimental studies allow direct observation of micro-/nano-scale structures, but it is comparatively restricted to advanced equipment and state-of-the-art facilities for molecular and atomic experimentation. In the theoretical analysis, using the classical elasticity theory fails to give a surface stress-deformation relation, because it lacks an intrinsic length scale and cannot capture the size-dependence of deformation, as observed experimentally from micro-/nano-scale structures (Wong et al., 1997; Ramesh, 2009). Hence, a vast number of research studies, using different analytical models, have been devoted to investigating the size-dependent structural behavior of nanostructures, e.g., vibration, bending, and buckling. Since the large body of literature has come into existence in the last two decades, only a general review on recent studies relevant to micro-/nano-scale structures based on different theories (e.g., strain gradient, modified couple stress, and nonlocal elasticity theories) is presented herein.
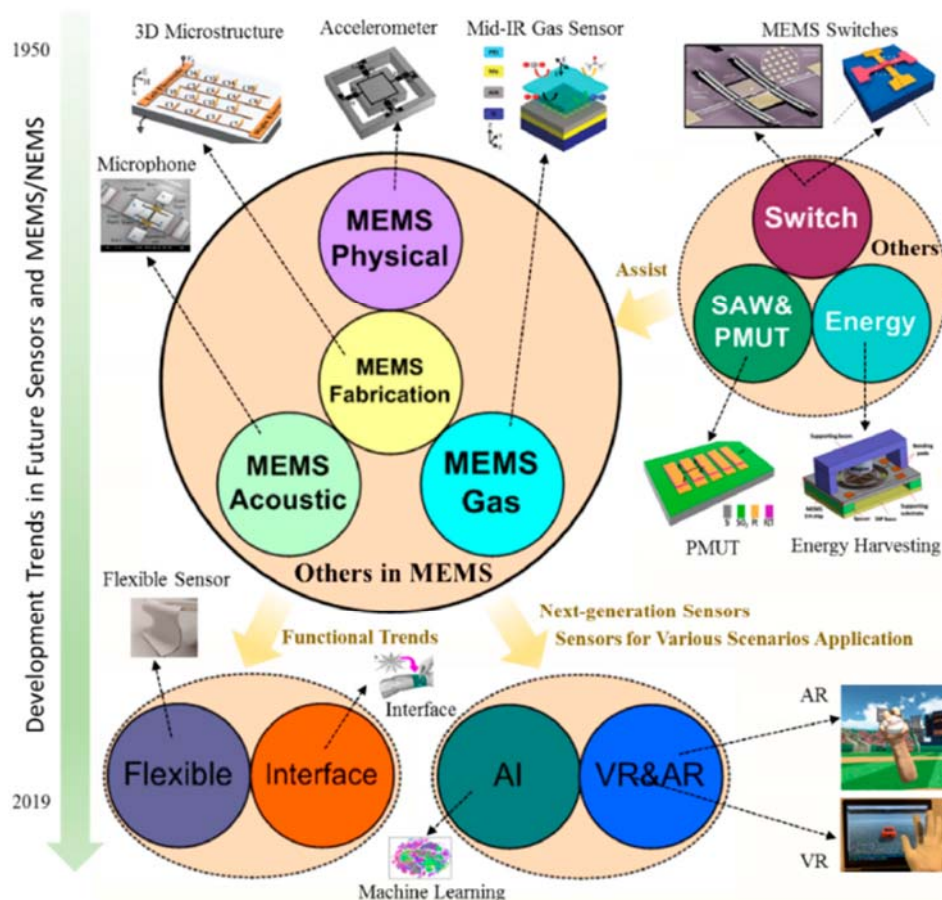
Fig. 2.1: Development trends and perspectives of MEMS/NEMS in various engineering applications (Zhu et al., 2020).

21

Among various nano-based structures, Reddy (2010) analyzed the nonlinear bending of nanobeams and nanoplates. Shen et al. (2010b) made use of a nonlocal shear deformable shell model to study the thermal post-buckling of axially compressed double-walled nanotubes. Xiang et al. (2010) presented an investigation on the dynamic instability of cantilevered nanorods subjected to an end follower force. Wang et al. (2012a) developed a generic governing equation for the bifurcation buckling of nano-arches. Ke et al. (2015) considered the free vibration problem of piezoelectric nanoplates. To characterize the mechanical properties of single-layered graphene nanosheets, the dynamic and stability analyses of such problems were performed (Zhang et al., 2015a; Zhang et al., 2015b, Zhang et al., 2016a; Zhang et al., 2016b).

In addition, Wang et al. (2016b) derived new analytical solutions for the elastic buckling of nonlocal columns with allowance for self-weight. Ganapathi and Polit (2017) examined the dynamic characteristics of curved nanobeams. Aya and Tufekci (2017) attempted to analyze the out-of-plane behavior of curved nanobeams. Polit et al. (2018) carried out the elastic stability analysis of curved nanobeams. Furthermore, Liu et al. (2018) discussed the nonlinear vibration problem of piezoelectric nanoplates. Arefi et al. (2019) extended their study to the bending of curved nanobeams reinforced by graphene platelets. More recently, Mao et al. (2020) also evaluated the small-scale effect on the linear and nonlinear vibrations of functionally graded graphene-reinforced piezoelectric composite microplates.

Employing the strain gradient elasticity theory, Lim et al. (2015) solved the dynamic equations of motion for wave propagation in nanobeams. Subsequently, Ebrahimi and Barati (2017; 2018) investigated the buckling and vibration of functionally graded curved nanobeams. Sahmani and Aghdam. (2017; 2018) analyzed the nonlinear dynamic instability of functionally graded multilayer graphene-reinforced nanoshells. They also considered the nonlinear bending problem of functionally graded graphene-reinforced porous nanobeams. On the other hand, Karami et al. (2019) investigated the dynamics of porous doubly-curved nanoshells. She et al. (2019a; 2019b) examined the snap-buckling mechanism and large-amplitude bending deformation of functionally graded porous curved nanobeams. Moreover, Sobhy and Abazid (2019) presented a study on the dynamic and instability of functionally graded graphene-reinforced curved nanobeam structures.

Generalizing the concept of the modified couple stress theory (Yang et al., 2002), Dehrouyeh-Semnani et al. (2017a; 2017b) recently investigated the nonlinear vibration and stability of fluid-conveying micropipes. Ghayesh and Farokhi (2017; 2018) conducted a parametric analysis for the nonlinear dynamics of doubly curved shallow micro shells. They also (Farokhi and Ghayesh 2018a; 2018b) investigated the mechanical behavior of various typical micro-structures. Ghayesh et al. (2018; 2019) further studied the nonlinear oscillation of functionally graded microplates and the viscoelastic dynamics of axially functionally graded microbeams. Taati et al. (2018) analyzed the buckling and post-buckling behavior of functionally graded microbeams. Soon after, Karami et al. (2019) also investigated the vibration of functionally graded curved microbeams.

Concurrent to the above studies, the widespread use of nonlocal continuum elastic stress field theory (Eringen, 1972; 1983) makes it one of the hottest research areas in nanomechanics. Eringen (1972; 1983; 2002) and Eringen and Edelen (1972) developed a constitutive relation from nonlocal continuum mechanics by specifying the stress state at a given point to be a function of the strain states at all points in that body. Nonlocal elasticity theory has been used to study dislocation mechanics, fracture mechanics, lattice dispersion of elastic waves, wave propagation in composites, and surface tension fluids (Peddieson et al., 2003; Sudak, 2003; Wang, 2005; Zhang et al., 2005; Wang and Varadan, 2006; Xu, 2006; Hu et al., 2008; Lim et al., 2015; Tong et al., 2018). This theory also accounts for small-length-scale effects considered in dynamic problems. Based on nonlocal continuum mechanics, there are two kinds of nonlocal elasticity models, i.e., the nonlocal softening model (e.g., Assadi and Farshi, 2011; Civalek and Demir, 2011; Rahmani and Pedram, 2014; Ansari et al., 2016; Li et al., 2017a; Liu et al., 2017b; Li et al., 2017c; Ebrahimi and Barati, 2018) and the nonlocal hardening model (e.g., Li et al., 2011c; Huang, 2012; Lim, 2010a; 2010b; Li, 2014a). The first model is derived from the nonlocal differential constitutive relations and the classical equilibrium equations. In other words, the commonly used governing equations for classical macro-scale materials/structures using the classical continuum theory are still valid at nano-scales, but those classical equations must be modified based on the connotation of the nonlocal theory. Hence, the use of classical elasticity analysis for nanostructures is coupled to the nonlocal softening model. The nonlocal differential intension can then be implanted into a classical framework.

On the other hand, the hardening one is formulated by the nonlocal variational principle or the long-range interaction among atoms. The nonlocal stresses can be determined directly

from the nonlocal differential constitutive equations or the physically-based nonlocal models. Various nonlocal internal forces in a new form can also be calculated. The nonlocal strain potential energy, external work, and/or kinetic energy of nanostructures are derived. The principle of virtual work or the Hamilton principle can then be employed to obtain the nonlocal governing equations. Nevertheless, it is strange to find that some reversed conclusions are found from the nonlocal softening and hardening models. There are many research studies to examine and validate their correctness. The controversial argument is related to the nano-structural stiffness predicted by the nonlocal theory, it is reduced or strengthened by comparing with those predicted via the classical continuum theory. Generally, it is reduced in the nonlocal softening model while strengthened in the hardening model. Hence, the nonlocal deformation is higher and the nonlocal natural frequencies (or wave velocities) are lower than that of the classical counterparts in the softening model, but opposite results can be obtained in the hardening model. Consider this paradox, Li (2014b) and Li et al. (2015) proved that the nonlocal softening and hardening models are both correct, the major reason depends on different types of surface stress effects, namely the long-range attractive (compressive surface stress) or repulsive (tensile surface stress) interactions.

Specifically, the following section presents a review of nonlocal elasticity theory according to its applications in three major micro-/nano-scale structures.

2.2.1 Nonlocal Scaling Effect of Nanorods

Carbon nanotubes (CNTs) are a hotspot in the field of nanotechnology due to their extraordinary physical properties such as high stiffness-to-weight and strength-to-weight ratios and enormous electrical and thermal conductivities compared with other known materials (Lim et al., 2012). Continuum modeling is intensively used as the main approach to analyze nanotubes. Because nano-scale effects should be taken into account in nanostructures, classical continuum models have been extended by introducing spatial integrals that consider the local stress contribution of all other points in the domain. Based on nonlocal continuum elastic stress field theory, many CNT studies (e.g., Li and Kardomatas, 2007; Tounsi et al., 2007; Lim, 2009; 2010a) have directly extended classical models where the nano-scale effect is considered as an additional axial force. In these studies, the model is derived as a mixture of classical and nonlocal models and is therefore called a partial nonlocal stress model.

Based on nonlocal continuum mechanics, Lim (2008) proposed an exact nonlocal model where infinite higher-order boundary conditions were derived and classified as soft and hard cases (Lim, 2010b) instead of classical boundary conditions. Because higher-order nonlocal terms are neglected in the strain energy density of the partial nonlocal stress model, equations of equilibrium/motion of this model have no higher-order nonlocal terms, and governing differential equations with higher-order nonlocal terms have opposite signs. Hence, the equilibrium condition constructed from a partial nonlocal stress model does not describe a nonlocal nanostructure in a true state of equilibrium. Based on the exact nonlocal stress model, Lim and coworkers subsequently investigated thermal buckling and torsion (Lim et al., 2012; Li et al., 2011a) of nanotubes. He also pointed out that the presence of a nonlocal nano-scale in the non-local stress model tends to increase nanostructure stiffness (Lim, 2010b). By applying Eringen's nonlocal elasticity theory, Wang et al. (2009) and Xiang et al. (2010) investigated the post-buckling behavior of cantilevered nanorods under an end-concentrated load and the dynamic instability of nanorods subjected to an end-follower force, respectively.

2.2.2 Nonlocal Scaling Effect of Nanobeams

Because beam-type elements are widely used in micro-scale systems such as MEMS/NEMS, many previous studies have investigated nanobeams based on nonlocal elasticity theory. Peddieson et al. (2003) first used the nonlocal elasticity theory to develop an Euler−Bernoulli nanobeam model and illustrated the magnitude of predicted nonlocal effects by solving some representative problems. Numerous subsequent investigations of nonlocal nanobeams have been reported (e.g., Lu et al., 2006; Xu, 2006; Lu, 2007; Reddy, 2007; Maranganti and Sharma, 2007; Wang et al., 2007a; Wang et al., 2008; Liu et al., 2008; Challamel and Wang, 2008; Aydogdu, 2009; Wang, 2009; Kiani and Mehri, 2010; Lim et al., 2010a; Murmu and Adhikari, 2010; Phadikar and Pradhan, 2010; Civalek and Akgöz, 2010; Liu and Rajapakse, 2010; Li et al., 2010; Fu et al., 2010). For instance, Lu et al. (2006) established a nonlocal Euler−Bernoulli nanobeam model based on the nonlocal theory with several typical boundary conditions and found that the obtained dynamic properties differed substantially from those predicted by classical elasticity theory. Reddy (2007) used nonlocal theory on Euler−Bernoulli, Timoshenko, Reddy, and Levinson beams and investigated the effect of nonlocal behavior on deflections, buckling loads, and natural frequencies. It is noteworthy that the above studies all used the partial nonlocal stress model.

Several other investigations (Lim et al., 2009; Niu et al., 2009; Lim et al., 2010; Li et al., 2011b; Lim and Yang, 2010) have been conducted on nonlocal nanobeams based on the exact nonlocal model. The results of this model show that nonlocal nano-scale effects cause an increase of structural stiffness, whereas the results of the partial nonlocal stress model show that nonlocal nano-scale effects decrease the structural stiffness.

2.2.3 Nonlocal Scaling Effect of Nanoplates

Nanoplates have also received considerable research interest in the modeling of graphene sheets. Duan and Wang (2007) developed exact solutions for axisymmetric bending of micro/nano-scale circular plates based on nonlocal theory. Aghababaei and Reddy (2009) applied nonlocal third-order shear deformation nanoplate theory to the bending and vibration of plates. Pradhan and Phadikar (2009) presented a nonlocal elasticity theory for nanoplate vibration. Artan and Lehmann (2009) obtained exact solutions for a rotationally symmetric bending problem of elastic annular plates based on nonlocal plate theory using the initial values method. Murmu and Pradhan (2009a, 2009b) studied the buckling and vibration behavior of biaxially compressed orthotropic nanoplates. Niu et al. (2010) constructed an analytical model for bending analysis of unconstrained nonlocal higher-order nanoplates. Jomehzadeh and Saidi (2011) decoupled the nonlocal elasticity equations for three-dimensional vibration analysis of nanoplates. There have also been some studies involving graphene sheets (Murmu and Pradhan, 2009d; Pradhan and Murmu, 2009; Pradhan, 2009; Pradhan and Kumar, 2010; Ansari et al., 2010). However, aside from all of the previous studies mentioned here, further investigation of nanoplates and graphene sheets is required, especially for exact nonlocal models of nanoplates.

2.3 Vibration-based Energy Harvesting Techniques

Vibration-based energy harvesting is the technique of converting kinetic energy to electrical energy. This is an attractive and interesting topic, but many energy harvesting techniques have still limited to low efficiency and poor environmental adaptability. A viable way to improve the holistic performance of such energy harvesters can resort to hybrid energy scavenging modes and multi-stable nonlinear mechanisms. The following section presents a basic overview of recent research achievements of vibration-based energy harvesting technology in terms of different transduction mechanisms and the multi-stable nonlinear mechanisms are presented in the next section.

The three most commonly used conversion techniques are piezoelectric, electromagnetic, and triboelectric approaches. As shown in Table 2.1, these three kinds of transduction mechanisms have their own merits and possible practical limitations (Wang, 2017; Park et al., 2019).

Table 2.1: A comparison of various energy harvesting technologies using EMG, TENG and PEG (Wang, 2017; Park et al., 2019).

Energy Harvesting Technique	Electromagnetic Generator (EMG)	Triboelectric Nanogenerator (TENG)	Piezoelectric Generator (PEG)
Working Principle	Electromagnetic induction	Contact electrification and electrostatic induction	Piezoelectric effect and electrostatic induction
Impedance Type	Resistive	Capacitive	Capacitve
Advantages	- High output current and power - High efficiency - Easy to scale up - High durability - Low output impedance	- High output voltage - Simple fabrication process - Low weight	- Simple structure on a small scale - Easy to scale down to nanoscale - High coupling coefficient - Easy to rectify the output voltage
Disadvantages	- Low output voltage - Heavy weight - Affected by electromagnetic field - Difficult to rectify the voltage	- Low output current - High device impedance - Pulsed output - Low durability	- High device impedance - Pulsed output - Low efficiency - Brittle - Low strain limit
Potential Applications	- Rotational system - Windmill	- Wearable - Healthcare - Blue energy harvesting - Self-powered sensors	- Flexible - Implantable

2.3.1 Piezoelectric Energy Harvesting Techniques

A piezoelectric generator (PEG) elicits the piezoelectric effect of piezoelectric materials, i.e., an electric potential can be induced at the terminals of a piezoelectric material due to the polarization of ions in the crystal when strains are produced in the material. In PEGs, strains can be induced by environmental excitations and the electric potential can be used to create a current through innovative designs, thus accomplishing energy conversion. Piezoelectric

energy harvesting technology is considered a promising method for replacing batteries to power microsystems due to merits including high energy density, simple structure, and long lifetime. A wide range of PEGs with different mechanical structures and functions have been developed to achieve this goal.

Antaki et al. (1995) proposed a piezoelectric array within the midsole of a shoe to power artificial organs. The device consisted of two longitudinal barrel-house cylindrical piezoelectric stacks excited by a passive hydraulic pulse device. Shenck and Paradiso (2001) developed a piezoelectric energy harvester to harvest the walking energy of the human body, dubbed the extraction piezoelectric insole. PZT (lead zirconate titanate) ceramic and PVDF (polyvinylidene fluoride) piezoelectric materials are used in the heel and toe parts of the insole, respectively. Kim (2002) proposed a diaphragm-structured piezoelectric energy harvester in his doctoral dissertation. Kim et al. (2004) developed a cymbal transducer consisting of a piezoelectric ceramic disk sandwiched between two concave-shaped metal end-caps.

In addition to these various mechanical structures, a cantilever structure is also commonly used in the design of piezoelectric energy harvesters due to its simplicity, low rigidity, and high efficiency under low vibration frequencies, e.g., a typical example is given in Fig. 2.2. There are two primary types of cantilever structures: unimorph and bimorph. The unimorph cantilever structure mainly consists of a substrate and single piezoelectric sheet, whereas the bimorph cantilever structure consists of a substrate sandwiched between two piezoelectric sheets. Cho et al. (2005) established a theoretical model of piezoelectric energy harvesting using a unimorph structure. A unimorph cantilever PEG using macro fiber composite materials was proposed by Yang et al. (2009a). Roundy and co-workers (2003; 2004) developed a bimorph cantilever PEG based on PZT ceramic and added a mass at the free end of the beam to reduce the resonant frequency of the system. Sodano et al. (2004) developed a bimorph cantilever PEG with improved flexibility by embedding PZT ceramic in epoxy resin. All of these cantilever PEGs adopted rectangular-shaped cantilevers. The effective strain of the piezoelectric layer in the device has been shown to be concentrated near the fixed end of the cantilever beam under external vibration. Therefore, to make the strain of the piezoelectric layer evenly distributed in the length direction for improving output performance, Baker et al. (2005) used a triangular-shaped cantilever instead of a rectangle in the PEG. The experimental results showed that the output power can be increased by 30%. In addition, to reduce the device stiffness and operating frequency and improve its output performance, Berdy et al. (2009) proposed an energy

harvester with a piezoelectric cantilever spring structure. Daqaq et al. (2014) discussed the role of nonlinearities in piezoelectric-based energy harvesting techniques. Yang et al., (2017) conducted a survey to study the energy efficiency of various piezoelectric energy harvesters. Recently, Lai et al. (2019) further devised a compact nonlinear multi-stable piezo-magneto-elastic energy harvester array that can scavenge energy from low-amplitude (< 3 m/s^2) and low-frequency (< 20 Hz) vibration sources.
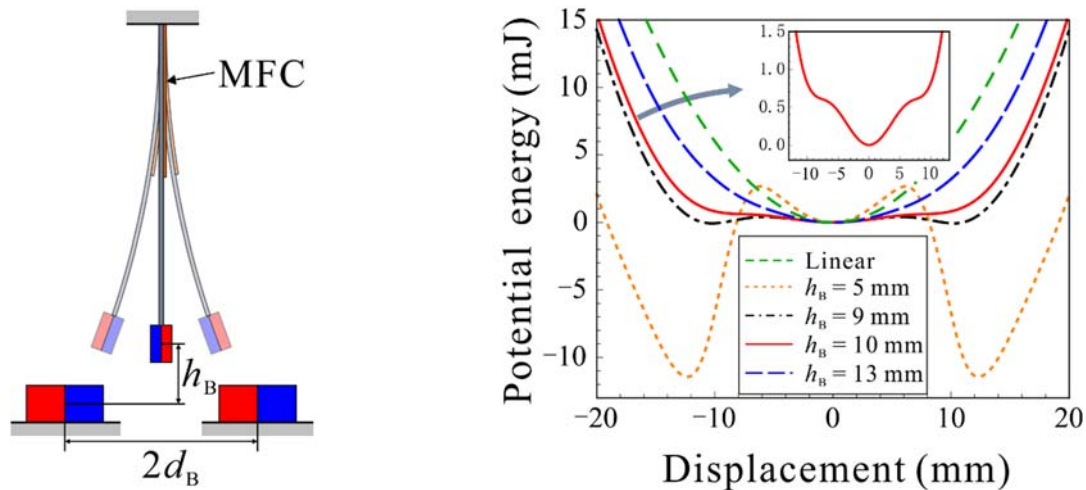
Fig. 2.2: Typical example of a piezoelectric energy harvesting technique (Lai et al., 2019).

In addition to the above macro-scale PEGs, an increasing number of PEGs have been proposed and fabricated based on MEMS technology for integration with microdevices for micro-scale applications. PEGs are compatible with MEMS processing technology. Jeon et al. (2003; 2005) proposed a MEMS generator with a transverse mode thin-film PZT. Renaud et al. (2007) proposed a piezoelectric MEMS generator with an integrated mass. Kok et al. (2008) fabricated a PEG without a supporting layer. Marinkovic and Koser (2009) developed a MEMS energy harvester consisting of a large center clamped at its corner to four tethers. Additional piezoelectric MEMS generators have been proposed and fabricated (e.g., Tvedt et al., 2010; Nguyen et al., 2010; Miki et al., 2010).

2.3.2 Electromagnetic Energy Harvesting Techniques

An electromagnetic generator (EMG) generally consists of coils and magnets. Under external excitations, the relative motion between the coil and magnet causes a change of the rate of the magnetic flux through the coil, thus developing an inductive electromotive force in the coil in accordance with Faraday's law, a fundamental law of electromagnetism. The EMG

technique offers a highly efficient way of converting physical vibrational energy into usable electrical power and also facilitates low-frequency device operation owing to its simple resonator composition. Like PEGs, both micro- and macro-scale EMGs have been developed by numerous research groups. A popular electromagnetic coupling architecture of EMGs involves a cylindrical magnet oscillating inside a coil. Ching et al. (2002) proposed a multi-modal resonating power transducer. Serre et al. (2008) reported a silicon micro-machined transducer with a discrete magnet. Another silicon micro-scale transducer with a discrete magnet was proposed by Lai et al. (2008). Macro-scale EMGs of this architecture have also been proposed (Cheng et al., 2007; Cao et al., 2007).

Naumann (2003) developed a modification of the previous coupling architecture in which a linear-supported magnet oscillates between two repulsive arranged magnets. This modified coupling architecture has also been used by other research groups to design electromagnetic transducers on the macro-scale (Saha et al., 2008; Domme, 2008; Hatipoglu and Urey, 2010) and micro-scale (Park and Lee, 2002; Wang and Arnold, 2009). Another commonly used coupling architecture (often used in micro-scale transducers) is that of a magnet that oscillates toward a coil without immersion. Wang et al. (2009b) presented a prototype device of this architecture, which has also been applied in a transducer-based on a multi-frequency acrylic beam structure (Yang et al., 2009). Further developments using this architecture can be found in Williams and Yates (1996) and Hoffmann et al. (2009). The coupling architecture based on oppositely polarized cylindrical magnets as oscillating mass was used by Takahara et al. (2004) and Zuo et al. (2010). Ruellan et al. (2005) used a similar architecture with ring magnets instead of cylindrical magnets and oscillating coils instead of oscillating magnets. In addition, Halim et al. (2016) also proposed a battery-like electromagnetic energy harvester that can use two flux-guided magnet stacks to harness energy from human motions, see Fig. 2.3.

The oscillation direction in the above-mentioned examples is parallel to the coil symmetry axis. However, there are also examples where the oscillation direction is perpendicular to the coil symmetry axis, which can be found in Koukharenko et al. (2006), Beeby et al. (2007), Soliman et al. (2008), Niu et al. (2008), Zhu et al. (2010), and Hadas et al. (2010). The output performances of the presented examples vary significantly from one another, which mainly results from the different transducer designs. For example, different electromagnetic coupling architectures have different output performance capability, and different component

dimensions can influence the output performance. Hence, substantial research is still required for proposing proper transducers for different applications.
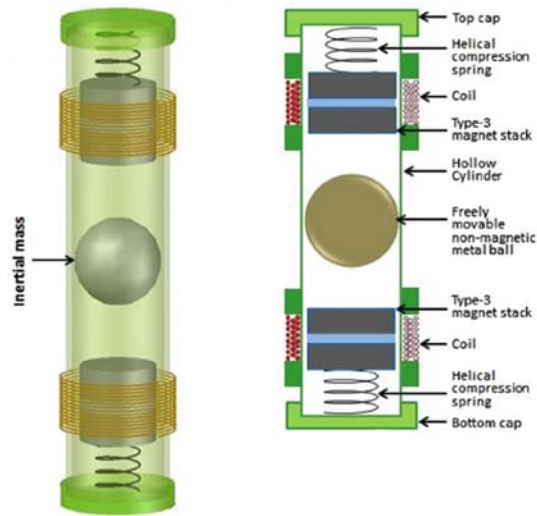
Fig. 2.3: A miniaturized electromagnetic energy harvesting (Halim et al., 2016).

Recently, using the electromagnetic-triboelectric mechanism, Jin et al. (2016) designed a double-deck structure to integrate generator units together for energy harvesting. Seol et al. (2016) proposed an oscillator-based vibration energy harvester, in which the floating oscillator consisted of a core magnet and polymer clothes. Gupta et al. (2017) devised a multi-modal energy harvester using polymer springs with nonlinear stiffness. Zhu et al. (2017b) used a multi-impact approach to achieve good energy harvesting efficiency under a frequency bandwidth of 10–45 Hz. In addition, Salauddin et al. (2018) integrated a dual Halbach magnet array and a magnetically floated approach to convert human-induced motions to electrical energy. Saadatnia et al. (2018) further applied a linear tubular system in conjunction with a grating structure to harness the clean energy from water waves.

Embedding the magnetic levitation technique, Zhu and Zu (2012) investigated a magnetoelectric harvester and presented the vibration amplitudes and energy output responses of the system. Mann and his associates (Mann and Sims, 2009; Mann and Owens, 2010) not only provided the theoretical design of a magnetically levitated energy harvester, and also presented a bi-stable electromagnetic-induction energy generator via magnetic levitation oscillations. Soares dos Santos et al. (2016) introduced a nonlinear model to study the energy transduction effect of a magnetic levitation-based electromagnetic energy harvesting technique. More recently, Gao et al. (2018) presented an electromagnetic-induction energy harvester by

31

using the magnetic levitation effect. Wang et al. (2019) conducted a parametric analysis of using magnetic levitation for energy harvesting. Furthermore, Tan et al. (2019) proposed a battery-like hybrid module based on magnetic levitation to harness energy from human motions.

Consider the effect of magnetic levitation, magnetic forces can be calculated using different analytical methods. The method of magnetic dipoles (Li et al., 2016; Zhu et al., 2017a; Wang et al., 2017a) is commonly used to consider all permanent magnets as point dipoles when the size of such magnets is sufficiently small compared to the separation interval of that magnets. To consider the geometry and size of magnets, the magnetizing current method was used (Agashe and Arnold, 2008) to calculate magnetic forces acting on permanent magnets in the presence of external magnetic fields. This method enables us to calculate the magnitude of magnetic forces, where the calculation model can be obtained by replacing those magnets with a suitable distribution of magnetizing currents. Employing this method, the dynamic behavior of piezoelectric cantilever energy harvesting systems with a bistable potential well (Tan et al., 2015) and a tri-stable potential well (Leng et al., 2017) under magnetic fields can be calculated analytically. To compare with the method of magnetic dipoles, this calculation method is more applicable for different magnet intervals.

2.3.3 Triboelectric Energy Harvesting Techniques

A triboelectric nanogenerator (TENG) stems from the triboelectric effect, i.e., that a material can become electrically charged through friction. Since the first triboelectric nanogenerator (TENG) invented in 2012 (Wang et al., 2012b; 2012c; 2012d), there has been a tremendous amount of work in several engineering applications proposed by Wang's group (Wang et al., 2016a; Wang et al., 2017b; Wu et al., 2019; Wang, 2020; and references therein) due to the unique merits of high efficiency, low weight, and low fabrication cost. Four fundamental modes of the TENG can be used to classify its research achievements.

The first invented operation mode is the vertical contact-separation mode (see Fig. 2.4(a)) where the mechanical motion direction is perpendicular to the surface of the two dielectric films. This type of mechanical motion has been achieved by structural designs, such as arch-shaped (Wang et al., 2012b), spring-supported (Zhu et al., 2012), zig-zag (Bai et al., 2013a), and cantilever-based (Yang et al., 2013a) designs. This mode can be used to harvest energy from finger typing (Zhong et al., 2013a), engine vibration (Chen et al., 2013), human walking

(Zhu et al., 2013; Yang et al., 2013b; Hou et al., 2013), and biomedical systems (Zhang et al., 2013).

The second operation mode is an in-plane sliding mode, see Fig. 2.4(b). Triboelectric charges in this mode are generated due to the relative sliding between the two surfaces of two dielectric films, which makes generation much more effective than that in contact-separation mode. This mode excels in harvesting energy from planar motions (Jing et al., 2014), disk rotations (Zhang et al., 2014a), and cylindrical rotations (Bai et al., 2013b).

The third operation mode is a single-electrode mode, see Fig. 2.4(c). With only one electrode, TENGs of this mode can harvest energy from arbitrary, free-moving objects because one of the triboelectric layers can move freely without restriction. Due to this characteristic, this mode has been used in applications to harvest energy from airflow (Yang et al., 2013c), rotating tires (Zhang et al., 2014b), raindrops (Liang et al., 2015), and the turning of book pages (Zhong et al., 2013b).

The fourth operation mode is a free-standing triboelectric-layer mode, see Fig. 2.4(d). TENGs of this mode are also capable of harvesting energy from mechanical motion without an attached electrode. TENGs of this type have been proposed for scavenging energy from vibration (Wang et al., 2014a), rotation motions (Guo et al., 2015a), computer mouse operation (Guo et al., 2015b), airflow (Guo et al. 2014), and a walking human or moving automobile (Xie et al., 2014; Wang et al., 2014b).
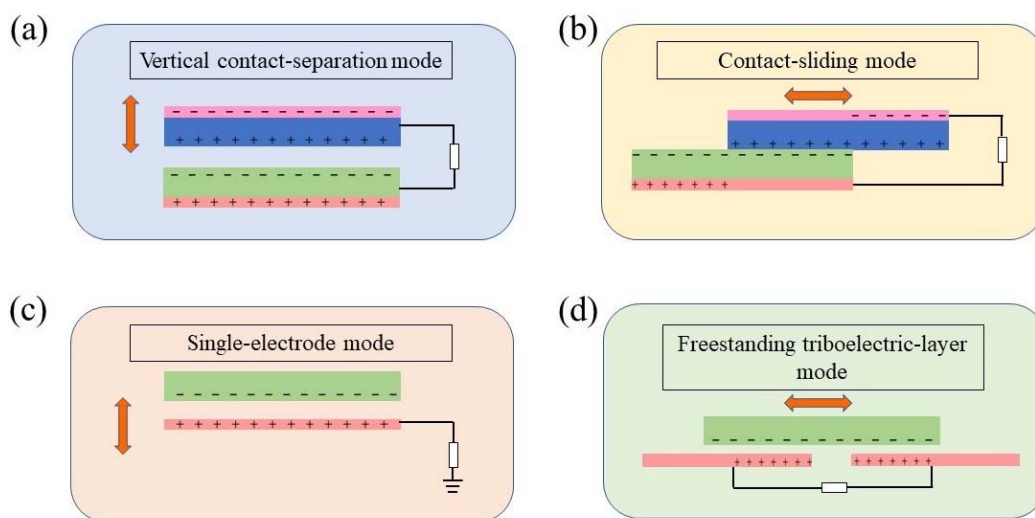
Fig. 2.4: Four fundamental modes of the triboelectric mechanism (Wang et al., 2016a).

2.3.4 Hybrid Energy Harvesting Techniques

At present, many energy harvesters can only function in a restricted range of dynamical situations. For example, many energy harvesters can only work under laboratory conditions or specified application scenarios. When the scenarios are not in accordance with the expected conditions (e.g., a change of gravity direction, a large change of vibration frequency), the energy harvesters typically fail. To enhance the performance of energy harvesters and make up for the reduced output power caused by the miniaturization and integration of the generator structure, many small generators adopt various coupling mechanisms, such as piezoelectric-electromagnetic (Rawnak and Mehmet, 2017; Javed and Abdelkefi, 2018; Sriramdas and Pratap, 2018; Fan et al., 2018; Toyabur et al., 2018), electromagnetic-triboelectric (Gupta et al., 2017; Quan et al., 2015; Seol et al., 2016; Zhu et al., 2017b; Salauddin et al., 2017; Saadatnia et al., 2018), piezoelectric-triboelectric (Karumuthil et al., 2017; Guo et al., 2018; Li et al., 2018), and even triboelelectic-thermoelectric (Kim et al., 2016; Wu et al., 2018a) to harness more electrical energy under a single mechanical motion.

By hybridizing two transduction mechanisms, the advantages of different transduction mechanisms can be combined in a single hub. He et al. (2017) first proposed a piezoelectric-electromagnetic-triboelectric hybrid vibration energy harvester with a complex structural design. To simplify the hybrid design for working well in real applications under low-frequency, low-amplitude, and time-varying sources, Wang et al. (2019a) invented a novel tri-hybrid energy harvester that can enhance the output performance of the frequency up-conversion via inter-well motions and also offers a wider operating bandwidth at low acceleration via the combination of resonant inter-well oscillation behavior and non-resonant behavior.

2.4 Multi-stable Nonlinearity-enhanced Mechanisms
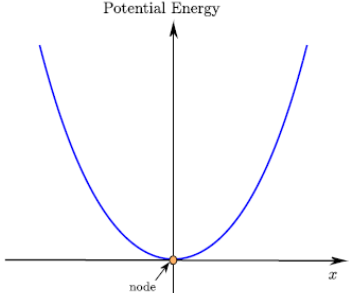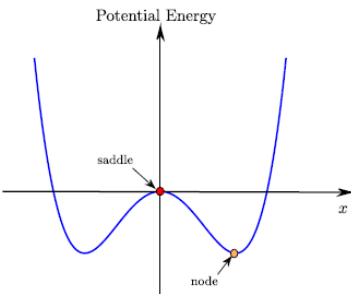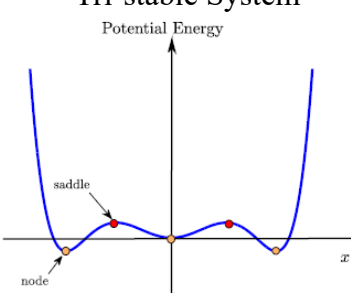
In the field of vibration-based energy harvesting techniques, earlier efforts mainly focused on linear dynamic harvesters, which can only work well in a very narrow bandwidth (i.e., when an external excitation must be nearly equal to the fundamental frequency of such dynamic systems). Under real-world engineering conditions, ambient structural vibration sources are often broadband and time-varying in nature. Because external operating frequencies shift away from the resonant frequency, the performance of these harvesters rapidly degrades. Moreover, structural vibration sources are also low-amplitude (<1 g) and low-frequency (<10 Hz) in nature, e.g., power line aeolian vibration, wind turbine dynamics, and train-track interaction.

Hence, conventional linear-type energy harvesters, covering a narrow frequency bandwidth, are not capable of working functionally.

To address this problem, nonlinear energy harvesting techniques have been introduced to broaden the usable bandwidth of linear counterparts by using external design means so that the magnitude and nature of the nonlinearity can be purposefully controlled. The most common approach is to use magnetic or mechanical forces to introduce a nonlinear restoring force with mono-, bi-, or multi-stability (Daqaq et al., 2014). For example, in a typical piezoelectric system, nonlinearity can be formed by introducing magnetic restoring forces to the system. Previous studies showed that the exploitation of nonlinear stiffness of a doubly-clamped MEMS resonator can achieve more than one order of magnitude improvement in both bandwidth and power density, as compared to a typical linear device (Hajati and Kim, 2011). A comparison of multi-stable nonlinearity-enhanced mechanisms is presented in Table 2.2 (Panyam and Daqaq, 2017).

In particular, low-frequency oscillators are still required in multi-stable mechanisms for the sake of low-frequency energy scavenging. Most multi-stable energy harvesters can only enhance the voltage generation by enlarging the amplitude of oscillation (Harne and Wang, 2013; Pellegrini et al., 2013; Kim and Seok, 2014; Zhou et al., 2014), it implies that they have the same working performance in power density as the conventional low resonant frequency counterpart in essence. Unfortunately, low resonant frequency harvesters often suffer from the problem of low power density. A major reason is the power generation of a vibration-based energy harvester decreases cubically with its vibration frequency (Cook-Chennault et al., 2008). Another one lies in the fact that, for a given mass, large mechanical displacements are required to permit the increasingly compliant springs resonating at lower frequencies, leading to an extra space consumption (Gu and Livermore, 2011).

Table 2.2: A comparison of multi-stable nonlinearity-enhanced mechanisms.

Mechanism	Advantages	Disadvantages
Mono-stable System	- Increased bandwidth when compared with equivalent linear systems for harmonic excitations - Frequency of peak response can be shifted away from the resonant frequency	- Poor performance under random excitation - Unable to perform well in real applications
Bi-stable System	- Improved performance for random excitations - Inter-well dynamics results in high amplitude responses	- Inter-well oscillations require high excitation levels - Design requires prior knowledge of excitation levels
Tri-stable System	- Shallower potential wells can be achieved when comparing to bistable harvesters - Inter-well dynamics can be triggered more easily	More complex configurations and layouts

2.4.1 Mono-stable Dynamical Systems

The effect of inherent nonlinearities on the performance of energy harvesters was considered in the early research on monostable energy harvesters. Hu et al. (2006) presented the influence of inherent geometric and material nonlinearities due to large deformation on the response behavior of PEGs. Quinn et al. (2007) investigated a kinetic energy harvester with essential nonlinearities and demonstrated that nonlinearity improves the performance of energy harvesting. Beeby et al. (2007) proposed a micro-EMG and observed nonlinear behavior in experiments.

Burrow and Clare (2007) and Barton et al. (2010) were among the first to intentionally introduce nonlinearities to energy harvesting by proposing an electromagnetic cantilever beam-type generator with a tip magnet attached to the cantilever beam and experimentally test the performance. Other mechanisms have been proposed to introduce nonlinearities into monostable energy harvesters. For instance, Mann and Sims (2008) proposed a magnetically levitated inductive harvester using two outer magnets to levitate a suspending central magnet. Stanton et al. (2010a) and Sebald et al. (2011a, 2011b) proposed a piezoelectric cantilever beam-type energy harvester with a tip magnet and two fixed external magnets. Masana and Daqaq (2011) proposed a clamped-clamped axially loaded piezoelectric beam harvester. For micro-scale applications, Marinkovic and Koser (2009) proposed a micro-PEG with geometric hardening nonlinearity that can broaden the steady-state bandwidth of the harvester. Tvedt et al. (2010) proposed and tested an electrostatic MEMS harvester that also produces a hardening influence. Miki et al. (2010) proposed a MEMS electret generator with monostable Duffing-type behavior. Le Van Quyen et al. (2010) proposed and tested a electrostatic micropower generator with softening nonlinearity. From an excitation viewpoint, investigations have been conducted on the performance of monostable energy harvesters under different types of excitations including harmonic excitations (Nguyen et al., 2010; Masana and Daqaq, 2011; Quinn et al., 2011; Sebald et al., 2011a; 2011b), random excitations (Gammaitoni et al., 2009; Lee et al., 2010; Nguyen et al., 2010; Daqaq, 2010; Nguyen and Halvorsen, 2011; Daqaq, 2011; Green et al., 2012; Halvorsen, 2013; He and Daqaq, 2013), parametric excitations (Daqaq et al., 2009; Ma et al., 2010; Daqaq and Bode, 2011; Abdelkefi et al., 2012), and impulsive loads (Quinn et al., 2007; Quinn et al., 2011).

2.4.2 Bi-stable Dynamical Systems

For bi-stable energy harvesting, McInnes et al. (2008) first theoretically investigated bi-stability in energy harvesters. Cottone et al. (2009) and Erturk et al. (2009) proposed two different bi-stable piezoelectric cantilever beam-type energy harvesters with two different kinds of magnet arrangements. Gammaitoni et al. (2009) also created a bi-stable restoring force using magnets. Away from the use of magnetoelastic potential to create bi-stability, other methods have also been proposed to create bi-stability. For instance, Arietta et al. (2010) created a bi-stable restoring force without an external force or magnetic field on the condition that certain laminations of carbon-fiber-epoxy plates result in buckling due to different thermal expansion coefficients at room temperature. Mann and Owens (2010) created bi-stability using a smart arrangement of magnets instead of the buckling of elastic structures. Ando et al. (2010)

fabricated a MEMS energy harvester using magnetoelastic buckling to demonstrate bi-stability. Nguyen et al. (2013) fabricated and tested a MEMS electrostatic energy harvester with curved springs to create bi-stability.

A number of theoretical and experimental investigations have also been reported on bi-stable energy harvesting under stochastic or deterministic excitations (Masana and Daqaq, 2009; Mann and Owens, 2010; Stanton et al., 2010b; Arietta et al., 2010; Ando et al., 2010; Litak et al., 2010; Ferrari et al., 2010; Sneller et al., 2011; Daqaq, 2011; Ferrari et al., 2011; Cammarano et al., 2011; Ali et al., 2011; Masana and Daqaq, 2012; Nguyen et al., 2013). Most of these efforts reported improved performance of the bi-stable energy harvesters compared with their counterparts.

2.4.3 Multi-stable Dynamical Systems

Compared with bi-stable energy harvesters, multi-stable (e.g. tri-stable, quad-stable) energy harvesters provide shallower potential wells and result in a lower excitation threshold for inter-well motions. The design of multi-stable energy harvesters is therefore of particular interest. Zhou et al. (2014) first proposed a tri-stable energy harvester consisting of a cantilever beam with a tip magnet and two external magnets, and its performance was superior to that of its bi-stable counterpart. Kim et al. (2015) numerically investigated a tri-stable oscillator constructed around a cantilever-based magnetically coupled system. Oumbé et al. (2015) proposed a tri-stable energy harvesting system with fractional-order viscoelastic materials. Panyam and Daqaq (2017) characterized the effective bandwidth of a tri-stable energy harvester. Previous studies on tri-stable systems mainly focused on the effect of potential well depth, mechanical impacts to induce inter-well oscillations, and the device's sensitivity to system parameters (Zhou et al., 2015; Zhou et al., 2016).

Kim and Seok (2014) theoretically investigated a bi-morph cantilever harvester that could be arranged from monostable to penta-stable. Zhou et al. (2017) presented a broadband quad-stable energy harvester and verified its advantages over a bi-stable harvester. Wang et al. (2017a) proposed a wideband quintuple-well potential piezoelectric-based vibration energy harvester using combined nonlinearity (i.e., magnetic nonlinearity and piecewise linearity produced by mechanical impact). More recently, Wang et al. (2019a) proposed a septuple-stable energy harvester that performs better than other recently proposed hybrid energy harvesters.

2.5 Remarks

In this work, in order to better understanding nonlinear dynamical behavior in MEMS resonators, both free and forced nonlinear vibration of doubly clamped MEMS microbeams are investigated. The effects of the mid-plane stretching, axial residual stress, and electrostatic force are considered. Specifically, we derive the analytical approximate solutions to the nonlinear free vibration of a doubly clamped microbeam with a one-sided electrode resulting from the sudden change of DC voltage, based on which we examine the dynamic pull-in voltage and natural frequency of the system. The current model is different from the previous work (Liu et al., 2017a) as the fringing field effect is also taken into consideration. Building upon the Euler–Bernoulli beam theory and von Kármán-type nonlinear kinematics (Chia, 1980), the equation of motion can be further converted to a nonlinear ordinary differential equation by the Galerkin method and then solved by the NHB method. In addition, we develop analytical approximations of the resonance behavior of a fully clamped MEMS resonator with two-sided electrodes actuated by DC voltage and harmonic AC voltage. Following the same decomposition principle, the governing equation is also converted to an ordinary differential equation with odd nonlinearity.

For nonlocal elasticity theory, although such a nonlocal theory is useful for capturing the small-scale effects of micro-/nano-scale structures, there is still an unsolved question about the extent of the nonlocal scale effect in such structures, or the existence of an upper bound in the nonlocal scale parameter, i.e., its magnitude. This is a critical issue because the nonlocal scale parameter can act as a connector between the classical and nonlocal theories, but different ranges of the nonlocal scale parameter can be found in the literature without rigorous explanation. This question is still puzzled to the selection of the nonlocal scale parameter in nanometers. To make this issue clear, the physical nonlocal scale parameter "$e_0 a$" was hidden by a dimensionless quantity $\tau = e_0 a / l$ in most research studies, where l is an external characteristic length scale (e.g., wavelength, crack length), but the dimensionless quantity τ was only chosen roughly. Some of the ranges about this dimensionless quantity τ are presented in Table 2.3. Given the above descriptions, we aim to determine an upper limit of the nonlocal scale parameter through dynamic analysis for various nano-structures including the axial vibration of nano-rods, transverse vibration of nano-beams, and free vibration of nano-plates.

Table 2.3: Various ranges of the dimensionless quantity (τ) in the literature.

Dimensionless Quantity (τ)	References
$0 - 0.02$	Lim, 2010a
$0 - 0.05$	Li et al., 2017a
$0 - 0.06$	Wang et al., 2008
$0 - 0.1$	Yu and Lim, 2014; Ansari et al., 2016; Liu et al., 2017b
$0 - 0.15$	Wang et al., 2018
$0 - 0.2$	Lim, 2010b; Xiang et al., 2010; Li et al., 2012; Lim et al., 2015; Xu et al., 2017
$0 - 0.3$	Yang and Lim, 2012
$0 - 0.4$	Wang and Duan, 2008
$0 - 0.6$	Lu, 2007
$0 - 0.7$	Wang et al., 2007
$0 - 0.8$	Murmu and Pradhan, 2009b; Guo and Yang, 2012
$0 - 1.0$	Lu et al., 2006 and 2007; Murmu et al., 2013

For energy harvesting technology, we propose a novel magnetic levitation-based electromagnetic-triboelectric energy harvester that can work well under low-frequency and low-amplitude sources. This harvester governed by the tri-stable nonlinearity-enhanced mechanism is realized by a simple arrangement of using four outer magnets on a plane. The tri-stable nonlinearity with resonant inter-well oscillations in a magnetically levitated structure can make the hybrid device possess a higher working efficiency and a wider operating bandwidth at low frequencies. The magnetizing current method is applied to calculate the magnetic forces of this model to reveal the triple-well nonlinear phenomenon. The formation mechanism of the tri-stable nonlinear behavior is also investigated by bifurcation analysis. To verify the theoretical model, a prototype of the harvester is fabricated for experimental studies. Under electrodynamical shaking tests, the output performance of the fabricated prototype is studied.

Theoretically, there are no general tools for characterizing the performance of energy harvesters with different transduction mechanisms under different excitations. In general, lower potential barriers are associated with lower-level excitations required to induce inter-well oscillations. Multi-stable energy harvesters are mainly used to harvest energy under low-frequency excitations resulting in low natural frequency of the device. However, when the implementation of nonlinearity in dynamical systems yields a triple-well potential function, it may induce complex response behavior and require ingenious mechanical designs. For

example, the variation of governing parameters may lead to the occurrence of bifurcation and chaotic motions. Such complicated behavior can strongly affect the performance of energy harvesters. Moreover, inter-well oscillations induce more space consumption, which limits the improvement of the device's power density. Hence, further study is, therefore, necessary on the design of energy harvesters. On one hand, behind complex nonlinear behavior, there is always a subtle order that governs the complexity way. On the other hand, the steady-state frequency response of such nonlinear energy harvesters under harmonic excitation is an important performance metric to indicate the transduction capabilities of the energy harvesters. Therefore, a global analysis of the fundamental mechanism causing periodic and chaotic behavior of tri-stable nonlinear systems subjected to external excitations not only sheds light on the selection of an appropriate frequency bandwidth in energy harvesting but also provides relevant information on the design of adaptive circuits to modulate power output.

Chapter 3

NONLINEAR FREE AND FORCED VIBRATION OF ELECTROSTATICALLY ACTUATED MEMS RESONATORS

3.1 Introduction

This chapter presents investigations on both nonlinear free and forced vibration of doubly clamped MEMS microbeams. It is organized as follows. In Section 3.2, a nonlinear dynamic model is formulated for the beam-type MEMS resonator with a one-sided electrode. The electrostatic force is expressed by a Taylor series around the stable equilibrium position. In addition, a general SDOF model that describes the nonlinear dynamics of a beam-based resonator with two-sided electrodes is also formulated. In Section 3.3, the NHB method for both free and harmonically forced nonlinear dynamic systems is briefly described. In Section 3.4, the accuracy of the present solutions for both models is verified in contrast to the results obtained from the Runge-Kutta method. Finally, conclusions are drawn in the last section.

3.2 Problem Definition and Formulation

Two schematic diagrams for a doubly clamped microbeam model are shown in Fig. 3.1. In these diagrams, one microbeam is suspended on a rigid electrode, whereas the other one is sandwiched by two symmetric rigid electrodes. We consider the microbeam of length L, width b and thickness h. The initial gap between the microbeam and the electrode is d. The coordinates x, y, and z are along the beam length, width and thickness, respectively. We assume that the actuation voltage is $V(t) = V_{dc} + V_{ac} \cos\left(2\pi \tilde{f} t\right)$, where V_{dc} is the DC voltage, and V_{ac} and $\tilde{f}$ are the amplitude and frequency of the excited AC voltage, respectively. From the perspective of physics, the bias DC voltage and the excited AC voltage are connected in series. This form of excitation can provide a pathway for tuning various effects on MEMS resonators (Younis and Alsaleem, 2009).

Employing the classical beam theory and the von Kármán nonlinearity (Chia, 1980), the transverse deflection of the microbeam with a one-sided electrode or two-sided electrodes can be expressed as follows

$$\rho b h \frac{\partial^2 w}{\partial t^2} + \tilde{c} \frac{\partial w}{\partial t} + EI \frac{\partial^4 w}{\partial x^4} - \left[N_i + \frac{Ebh}{2L} \int_0^L \left(\frac{\partial w}{\partial x} \right)^2 dx \right] \frac{\partial^2 w}{\partial x^2} = F_e \qquad (3.1)$$

where w is the deflection in the z-direction, $\tilde{c}$ is the linear damping per unit length, I is the moment of inertia of the cross-section about the y-axis, E is the effective Young's modulus of the beam $(= E' / (1 - \upsilon^2)$ with $E' =$ Young's modulus and $\upsilon =$ Poisson ratio), ρ is the beam material density, N_i is the initial axial load due to the residual stress on the beam, F_e is the electric force per unit length, and t is time. When the microbeam is suspended on an electrode, we consider

$$F_e = \frac{1}{2} \frac{b \varepsilon_0 V^2(t)}{(d-w)^2} \left[1 + \beta \frac{(d-w)}{b} \right] \qquad (3.2)$$

In another case, when the microbeam is suspended between two symmetric electrodes, the electrostatic force becomes

$$F_e = \frac{1}{2} \varepsilon_0 b \left\{ \frac{\left[V_{dc} + V_{dc} \cos(2\pi \tilde{f} t) \right]^2}{(d-w)^2} - \frac{V_{dc}^2}{(d+w)^2} \right\} \qquad (3.3)$$

where ε_0 is the permittivity of the gap medium.

In Eq. (3.2), $\beta (=0.65)$ is a parameter that is used to account for the "*fringing field effect*" due to the finite width of the microbeam. The fringing field effect for a doubly clamped microbeam with two-sided electrodes is much smaller than that with a one-sided electrode due to the symmetric configuration of the electrodes, leading to the partial cancellation of the effect, so we can ignore the fringing field effect in Eq. (3.3).
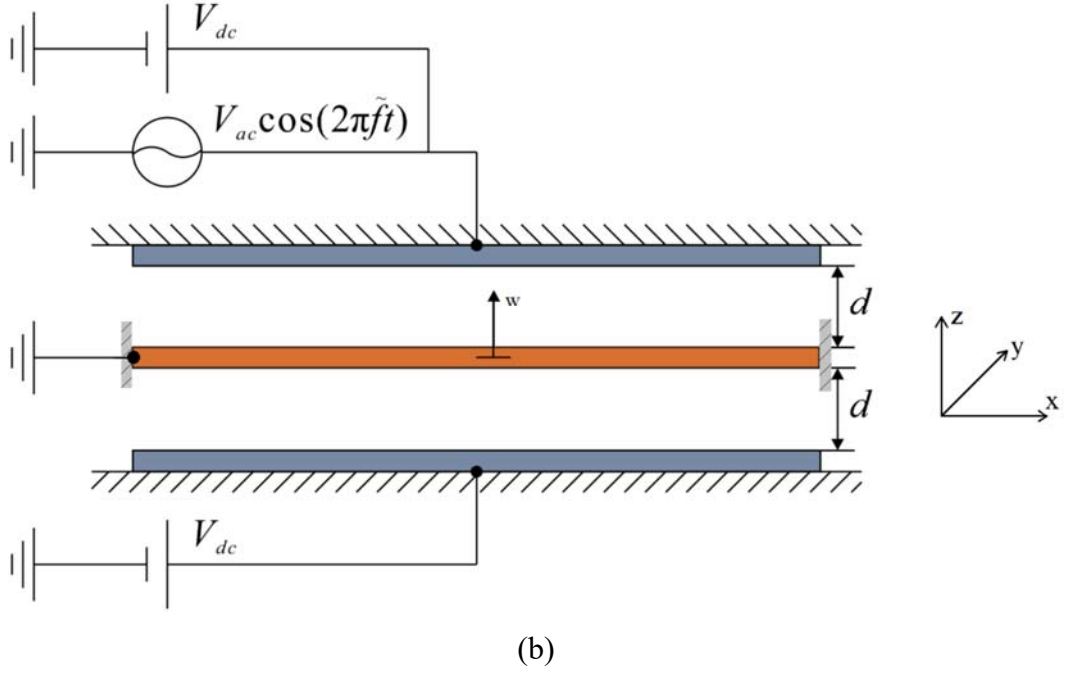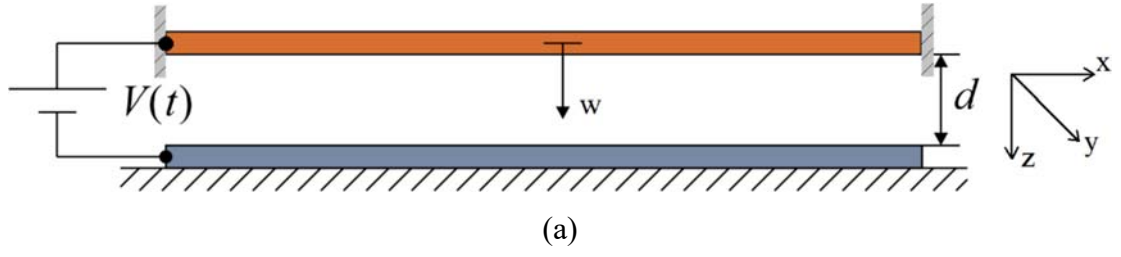
Fig. 3.1: (a) Schematic of a doubly-clamped microbeam with a one-sided electrode and (b) schematic of a doubly-clamped microbeam with two-sided electrodes.

For a doubly clamped microbeam, the following boundary conditions are imposed as

$$w(0,t) = 0, \quad \frac{\partial w(0,t)}{\partial x} = 0 \tag{3.4}$$

$$w(L,t) = 0, \quad \frac{\partial w(L,t)}{\partial x} = 0 \tag{3.5}$$

Before the electrostatic actuation, the initial conditions are

$$w(x,0) = 0, \quad \frac{\partial w(x,0)}{\partial t} = 0 \tag{3.6}$$

For convenience and brevity, the dimensionless quantities are defined as follows

$$\bar{t} = \sqrt{\frac{EI}{\rho bhL^4}}\,t\,,\ W = \frac{w}{d}\,,\ \xi = \frac{x}{L}\,,\ c = \frac{\tilde{c}L^2}{\sqrt{\rho EIbh}}\,,\ f_i = \frac{N_i L^2}{EI}\,,\ \alpha = 6\left(\frac{d}{h}\right)^2,$$

$$\lambda^2 = \frac{24\varepsilon_0 L^4}{Eh^3 d^3}\,,\ \gamma = \frac{d}{b}\,,\ f = \sqrt{\frac{\rho bhL^4}{EI}}\,\tilde{f}$$

(3.7)

where $\bar{t}$, W, ξ, c and f are the dimensionless time, beam deflection, longitudinal coordinate, damping parameter, and AC voltage frequency, respectively. By utilizing Eq. (3.7), the dimensionless equation of motion for Eq. (3.1) is re-written as

$$\frac{\partial^2 W}{\partial \bar{t}^2} + c\frac{\partial W}{\partial \bar{t}} + \frac{\partial^4 W}{\partial \xi^4} - \left[f_i + \alpha\int_0^1 \left(\frac{\partial W}{\partial \xi}\right)^2 d\xi\right]\frac{\partial^2 W}{\partial \xi^2} = F_{es}$$

(3.8)

in which

$$F_{es} = \frac{\lambda^2 V^2(t)}{4(1-W)^2}[1 + \gamma\beta(1-W)]$$

(3.9)

for the microbeam with one-sided electrode and

$$F_{es} = \lambda^2 V_{dc}^2 \frac{W}{(1-W^2)^2} + \frac{1}{4}\lambda^2\left[\frac{2V_{dc}V_{ac}\cos(2\pi f\bar{t}) + V_{ac}^2\cos^2(2\pi f\bar{t})}{(1-W)^2}\right]$$

(3.10)

for the microbeam with two-sided electrodes. The corresponding dimensionless boundary conditions are

$$W(0,\bar{t}) = 0\,,\ \frac{\partial W(0,\bar{t})}{\partial \xi} = 0$$

(3.11)

$$W(1,\bar{t}) = 0\,,\ \frac{\partial W(1,\bar{t})}{\partial \xi} = 0$$

(3.12)

and the dimensionless initial conditions are

$$W(\xi,0) = 0\,,\ \frac{\partial W(\xi,0)}{\partial \bar{t}} = 0$$

(3.13)

As we only investigate the first-mode natural frequency and primary resonance of doubly clamped microbeams in this work, the deflection function of the microbeam can be approximated as a product of two functions with a sustainable error in accordance with the Galerkin method. The deflection function is expressed as

$$W(\xi,\bar{t}) = \phi(\xi)q(\bar{t})$$

(3.14)

45

where $\phi(\xi)$ is the assumed deflection shape function that corresponds to the first-mode shape and satisfies the boundary conditions given in Eqs. (3.11) and (3.12). $q(\bar{t})$ is the mid-point deflection of the microbeam. A reasonable deflection shape function for the first-mode shape of Eq. (3.8) is (Moghimi and Ahmadian, 2009)

$$\phi(\xi) = \cosh(\lambda_1 \xi) - \cos(\lambda_1 \xi) - \frac{\cosh(\lambda_1) - \cos(\lambda_1)}{\sinh(\lambda_1) - \sin(\lambda_1)} \left[\sinh(\lambda_1 \xi) - \sin(\lambda_1 \xi) \right] \quad (3.15)$$

in which $\lambda_1 = 4.730040745$.

Case 1: Asymmetric vibration of a doubly clamped microbeam with a one-sided electrode due to a suddenly applied DC voltage

Consider the MEMS device in Fig. 3.1(a), the electrostatic actuation (i.e., DC voltage) makes the microbeam deflect to an equilibrium configuration, and then it vibrates asymmetrically around the equilibrium position due to the DC voltage. For free and undamped vibration, we first compute the natural frequencies of the microbeam. In this case, the damping term and the AC voltage in Eqs. (3.8) and (3.9) can be set to zero. Substituting Eq. (3.15) into Eq. (3.8) and applying the Galerkin procedure, the governing partial differential equation can be converted to a nonlinear ordinary differential equation as follows

$$\frac{d^2 q}{d\bar{t}^2} + \alpha_1 q + \alpha_2 q^3 + \frac{\lambda^2 V_{dc}^2}{4} \int_0^1 \frac{\phi}{(1 - q\phi)^2} [1 + \gamma\beta(1 - q\phi)] d\xi = 0 \quad (3.16)$$

with the following initial conditions

$$q(0) = 0, \quad \frac{dq(0)}{d\bar{t}} = 0 \quad (3.17)$$

where $\alpha_1 = \int_0^1 \left(\frac{d^4 \phi}{d\xi^4} - f_i \frac{d^2 \phi}{d\xi^2} \right) \phi d\xi$ and $\alpha_2 = -\alpha \int_0^1 \left(\frac{d\phi}{d\xi} \right)^2 d\xi \int_0^1 \frac{d^2 \phi}{d\xi^2} \phi d\xi$. It is noted that analytical approximate solutions for the free vibration of the nonlinear system (3.16) cannot be directly obtained by the NHB method, as the electrostatic force term is not able to be integrated analytically. To deal with this issue, instead of approximating it using a Taylor series expansion around the initial configuration $q = 0$, it is performed to expand this term around the equilibrium position. This is because the free vibration of the microbeam occurs around its equilibrium position (i.e., $q = q_0$) rather than its initial position (i.e., $q = 0$). The accuracy of the two approximation methods can be verified below.

Incorporating a Taylor series expansion (Liu et al., 2017a), we expand the integral part in Eq. (3.16) up to fourth-order terms around the initial position and the equilibrium position of the microbeam in Eqs. (3.18) and (3.19), respectively, we have

$$\frac{d^2q}{dt^2} + \alpha_1 q + \alpha_2 q^3 + \sum_{n=0}^{4} L_n q^n = 0 \tag{3.18}$$

$$\frac{d^2q}{dt^2} + \alpha_1 q + \alpha_2 q^3 + \sum_{n=0}^{4} K_n (q-q_0)^n = 0 \tag{3.19}$$

where $L_n = -\frac{\lambda^2}{4} \int_0^1 (n+1+\gamma\beta)\phi^{n+1} d\xi$ and $K_n = -\frac{\lambda^2}{4} \int_0^1 \frac{[n+1+\gamma\beta(1-q_0\phi)]\phi^{n+1}}{(1-q_0\phi)^{n+2}} d\xi$. The exact value of the equilibrium position can be calculated iteratively according to the principle that the restoring force of the microbeam at the equilibrium position in Eq. (3.16) is zero, i.e.,

$$\alpha_1 q_0 + \alpha_2 q_0^3 + \int_0^1 \frac{\lambda^2 \phi}{4(1-q_0\phi)^2} [1 + \gamma\beta(1-q_0\phi)] d\xi = 0 \tag{3.20}$$

As a case study, numerical calculations are performed for the dynamic analysis of a microbeam with the geometrical and material parameters given in Table 3.1. Fig. 3.2 shows the values of the equilibrium position of the microbeam under various electrostatic actuation levels, i.e., V_{dc}.

Table 3.1: Geometrical and material parameters of the microbeam (Younis and Nayfeh, 2003).

Variables	Symbol	Values
Beam length	L	210 μm (for Case 1[*])
		310 μm (for Case 2[*])
Beam width	b	100 μm
Beam thickness	h	1.5 μm
Initial gap width	d	1.18 μm
Young's modulus	E'	151 GPa
Poisson ratio	υ	0.3
Beam material density	ρ	2332 kg/m³
Initial axial load	N_i	0.0009N
Dielectric constant of the gap medium	ε_0	8.854×10^{-12} F/m
Quality factor	Q	197

Notes: *Cases 1 and 2 correspond to a doubly clamped microbeam with one-sided electrode and two-sided electrodes, respectively. Only the beam length is different, other parameters are the same in both cases.

For comparison, we refer the systems (3.16), (3.18), and (3.19) as models 1, 2, and 3, respectively. Indeed, the use of a Taylor series expansion around the initial position $q = 0$ has been used for analysis by using the homotopy analysis method (Moghimi and Ahmadian, 2009). By only changing the length of the microbeam, values of the dynamic pull-in voltage of the microbeam for the three models are calculated in accordance with the principle of energy conservation. Note that the dynamic pull-in instability occurs when there is no solution to the deflection q in the range of $(0, 1)$ where has the same energy level as the initial conditions. In Table 3.2, it is obvious that the results of model 3 are much closer to that of model 1 than that of model 2 under different beam lengths from 210 μm to 510 μm. Among various cases in Table 3.2, the maximum relative error of the dynamic pull-in voltage values between model 1 and model 3 is only 0.7% for $L = 210$ μm, but it is up to 4.3% between model 1 and model 2. Besides, the results for the restoring force of the three models under an input voltage of 25 V are depicted in Fig. 3.3. The circle dots represent the exact solution, while the dashed line and solid line correspond to the two approximation models, respectively, i.e., Eqs. (3.18) and (3.19). It is observed that the results of the three models have an excellent agreement with each other when the deflection is small. For $q > 0.2$, there is a significant discrepancy. Specifically, the solid line is much closer to the circle dots than the dashed line, it refers that the integral term in Eq. (3.16) approximated by a Taylor series at the equilibrium position has greater accuracy than that at the initial position. Hence, the system (3.19) is used for the subsequent analysis.
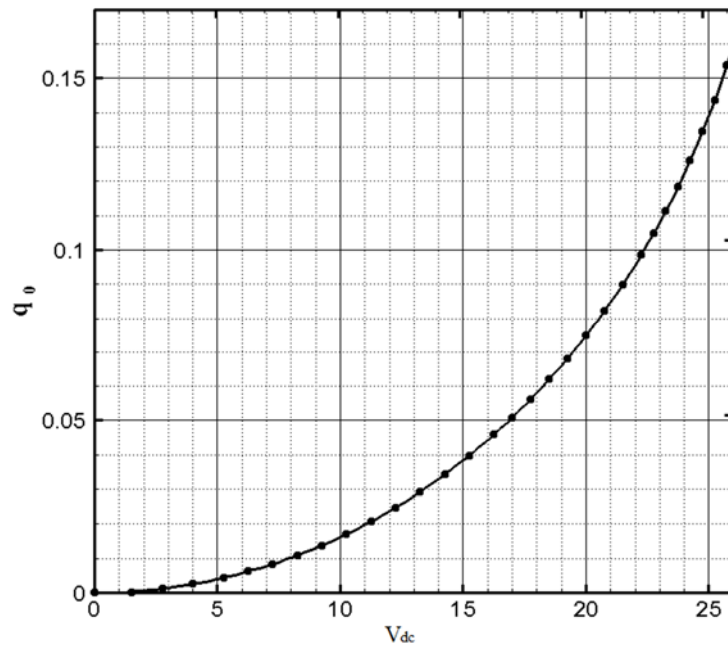
Fig. 3.2: Values of the equilibrium position q_0 for various electrostatic actuation levels V_{dc}.

Table 3.2: A comparison between values of dynamic pull-in voltage of different models.

Length of beam (μm)	DC dynamic pull-in voltage (V)		
	Model 1 (Eq. 3.16)	Model 2 (Eq. 3.18)	Model 3 (Eq. 3.19)
210	25.84	26.96	26.02
310	12.94	13.46	13.03
410	8.18	8.49	8.23
510	5.87	6.08	5.90
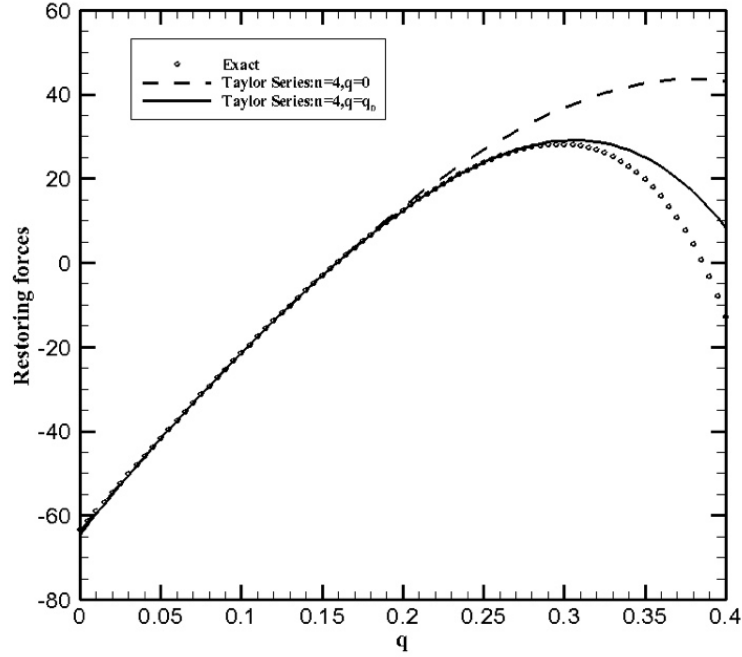
Fig. 3.3: Comparison of the restoring forces of three models under an input voltage of 25V.

To address the problem (3.19), a new variable is introduced as follows

$$u = q - q_0 \tag{3.21}$$

Then, we obtain

$$\frac{d^2u}{dt^2} + g(u) = 0 \tag{3.22}$$

with

$$u(0) = -q_0 , \quad \frac{du}{dt}(0) = 0 \tag{3.23}$$

The restoring force function of Eq. (3.22) is $g(u) = \beta_1 u + \beta_2 u^2 + \beta_3 u^3 + \beta_4 u^4$, in which

$\beta_1 = \alpha_1 + 3\alpha_2 q_0^2 + K_1$, $\beta_2 = 3\alpha_2 q_0 + K_2$, $\beta_3 = \alpha_2 + K_3$ and $\beta_4 = K_4$. In this system, the

potential energy is given by

$$V(u) = \frac{1}{2}\beta_1 u^2 + \frac{1}{3}\beta_2 u^3 + \frac{1}{4}\beta_3 u^4 + \frac{1}{5}\beta_4 u^5 \tag{3.24}$$

The system (3.22) can be solved analytically in accordance with Section 3.3. For brevity and convenience, the dimensionless time "$\bar{t}$" in Eq. (3.22) is simplified to "t" in the following analysis.

Case 2: Resonance response of a doubly clamped microbeam with two-sided electrodes actuated by a bias DC voltage and an AC harmonic voltage

Consider the MEMS model in Fig. 3.1(b), the initial position is a stable equilibrium position for the microbeam. In this case, the DC voltage is acted as a bias one and the microbeam is driven by the AC voltage to vibrate symmetrically around its initial position. Here, we focus on the investigation of resonance responses when the actuating frequency is near the first natural frequency of the microbeam. For a small AC voltage ($V_{ac} << V_{dc}$), we can neglect the term with V_{ac}^2, Eq. (3.8) can be simplified as

$$\frac{\partial^2 W}{\partial \bar{t}^2} + c\frac{\partial W}{\partial \bar{t}} + \frac{\partial^4 W}{\partial \xi^4} - \left[f_i + \alpha \int_0^1 \left(\frac{\partial W}{\partial \xi} \right)^2 d\xi \right] \frac{\partial^2 W}{\partial \xi^2} - \lambda^2 V_{dc}^2 W (1 + 2W^2 + 3W^4)$$

$$= \frac{1}{2}\lambda^2 V_{dc} V_{ac} \cos(2\pi f \bar{t}) \tag{3.25}$$

By means of a Taylor series expansion, the electrostatic force term is generally expanded up to the fifth-order term near the initial position $q = 0$ and the higher-order terms are ignored.

Substituting Eq. (3.14) into (3.25) and applying the Galerkin procedure, the nonlinear governing equation of motion can be written as

$$\frac{d^2 q}{d\bar{t}^2} + f(q) + h\left(\frac{dq}{d\bar{t}} \right) = F_0 \cos(\tilde{\omega}\bar{t}) \tag{3.26}$$

where

$$f(q) = (\beta_1 + \alpha_1)q + (\beta_2 + \alpha_2)q^3 + \alpha_3 q^5$$

$$h(p) = cp \quad (p = dq/d\bar{t})$$

$$F_0 = \frac{1}{2}\lambda^2 V_{dc} V_{ac} \int_0^1 \phi d\phi \tag{3.27}$$

$$\tilde{\omega} = 2\pi f$$

$$\beta_1 = \int_0^1 \left(\frac{d^4\phi}{d\xi^4} - f_i \frac{d^2\phi}{d\xi^2} \right) \phi d\phi$$

$$\beta_2 = \int_0^1 \left[-\alpha \frac{d^2\phi}{d\xi^2} \int_0^1 \left(\frac{d\phi}{d\xi} \right)^2 d\xi \right] \phi d\phi$$

$$\alpha_i = -i\lambda^2 V_{dc}^2 \int_0^1 \phi^{2i} d\phi \quad (i = 1, 2, 3)$$

The main interest of this section is to seek the amplitude-frequency responses of Eq. (3.26) using the solution approach described in Section 3.3. For brevity and convenience, the dimensionless time "$\bar{t}$" in Eq. (3.26) is simplified to "t" in the following analysis. We also set the mid-point deflection of the microbeam "q" to "u" for easy reference.

3.3 Solution Approaches

In this section, the solution methodologies of the NHB method and its improved version for symmetric nonlinear conservative oscillators (Wu et al., 2006; 2017), the NHB method for asymmetric nonlinear conservative oscillators (Wu and Lim, 2004), and the NHB method for symmetric nonlinear oscillating systems under an external harmonic force (Wu et al., 2018b) are mentioned in the following sections.

3.3.1 NHB Method for Symmetric Nonlinear Conservative Oscillations

Consider an SDOF nonlinear oscillator governed by

$$\frac{d^2u}{dt^2} + f(u) = 0, \quad u(0) = A, \quad \frac{du}{dt}(0) = 0 \tag{3.28}$$

where $f(u)$ is an odd function (i.e., $f(-u) = -f(u)$) and satisfies $uf(u) > 0$ for $u \in [-A, A]$, $u \neq 0$. It is obvious that $u = 0$ is the equilibrium position and the system oscillates between symmetric limits $[-A, A]$. The period and corresponding periodic solution depend on the oscillation amplitude A.

By introducing a new independent variable $\tau = \omega t$, Eq. (3.28) can be rewritten as

$$\Omega u'' + f(u) = 0, \quad u(0) = A, \quad u'(0) = 0 \tag{3.29}$$

where $\Omega = \omega^2$. ω is the corresponding angular frequency of nonlinear oscillations and a prime denotes differentiation with respect to τ. It is obvious that the solution to Eq. (3.29) is a periodic function of τ with a period of 2π. Because the restoring force function $f(u)$ is an

odd function of u, the periodic solution $u(\tau)$ can be represented by a Fourier series containing only odd multiples of τ, i.e.,

$$u(\tau) = \sum_{i=1}^{\infty} h_i \cos[(2i-1)\tau] \tag{3.30}$$

Following the single-term harmonic balance approximation, we first set

$$u_1(\tau) = A\cos\tau \tag{3.31}$$

which satisfies the initial conditions in Eq. (3.29). Based on the odd function assumption $f(-u) = -f(u)$, the function $f(u_1(\tau))$ can be expanded in a Fourier series as

$$f(u_1(\tau)) = \sum_{i=1}^{\infty} a_{2i-1} \cos[(2i-1)\tau] \tag{3.32}$$

where

$$a_{2i-1} = \frac{4}{\pi} \int_0^{\pi/2} f(u_1(\tau)) \cos[(2i-1)\tau] d\tau, \quad i = 1, 2, \dots \tag{3.33}$$

Substituting Eqs. (3.31) and (3.32) into Eq. (3.29) and setting the coefficient of $\cos\tau$ to zero lead to

$$a_1 - A\Omega = 0 \tag{3.34}$$

which can be solved for Ω as a function of A as

$$\Omega(A) = \Omega_1(A) = \frac{a_1}{A} \tag{3.35}$$

Therefore, the first-order approximate period of the nonlinear system (3.28) is

$$T_1(A) = 2\pi \sqrt{\frac{A}{a_1}} \tag{3.36}$$

and the corresponding approximate periodic solution is

$$u_1(t) = A\cos\tau, \quad \tau = \sqrt{\Omega_1(A)}\, t \tag{3.37}$$

Next, the combination of Newton's method and the harmonic balance method is formulated to solve Eq. (3.29). First, applying Newton's procedure, the periodic solution and the squared angular frequency of Eq. (3.29) can be expressed as

$$u = u_1 + \Delta u_1, \quad \Omega = \Omega_1 + \Delta\Omega_1 \tag{3.38}$$

where Δu_1 and $\Delta\Omega_1$ are small increments of the first-order approximations u_1 and Ω_1, respectively. Δu_1 is a periodic function of τ of period 2π. Substituting Eq. (3.38) into Eq. (3.29) and linearizing with respect to the correction terms Δu_1 and $\Delta\Omega_1$, we have

$$\Omega_1 u_1'' + f(u_1) + \Delta\Omega_1 u_1'' + \Omega_1 \Delta u_1'' + f_u(u_1)\Delta u_1 = 0, \quad \Delta u_1(0) = 0, \quad \Delta u_1'(0) = 0 \qquad (3.39)$$

where the subscript u in $f_u(u_1)$ denotes the derivative of $\Delta\Omega_1$ with respect to u.

Then, the harmonic balance method can be applied to solve Eq. (3.39) for Δu_1 and $\Delta\Omega_1$. Since $f(-u) = -f(u)$, $f_u(u_1(\tau))$ can be expanded into the following Fourier series:

$$f_u(u_1(\tau)) = \frac{b_0}{2} + \sum_{i=1}^{\infty} b_{2i}\cos(2i\tau) \qquad (3.40)$$

where

$$b_{2(i-1)} = \frac{4}{\pi}\int_0^{\pi/2} f_u(u_1(\tau))\cos[2(i-1)\tau]d\tau, \quad i = 1, 2, \dots \qquad (3.41)$$

For the second-order approximate solution, we set $\Delta u_1(\tau)$ in Eq. (3.39) as

$$\Delta u_1(\tau) = x_1(\cos\tau - \cos 3\tau) \qquad (3.42)$$

Substituting Eqs. (3.31), (3.32), (3.40), and (3.42) into Eq. (3.39), expanding the resulting expression in a trigonometric series and setting the coefficients of $\cos\tau$ and $\cos 3\tau$ to zero, we obtain

$$2a_1 - 2A\Omega_1 + (b_0 - b_4 - 2\Omega_1)x_1 - 2A\Delta\Omega_1 = 0 \qquad (3.43)$$

$$(b_2 + b_4 - b_0 - b_6 + 18\Omega_1)x_1 + 2a_3 = 0 \qquad (3.44)$$

Solving Eqs. (3.43) and (3.44) yields

$$x_1(A) = -\frac{2a_3 A}{(b_2 + b_4 - b_0 - b_6)A + 18a_1} \qquad (3.45)$$

$$\Delta\Omega_1(A) = -\frac{a_3[(b_0 - b_4)A - 2a_1]}{A[(b_2 + b_4 - b_0 - b_6)A + 18a_1]} \qquad (3.46)$$

Therefore, the second-order approximate period and the corresponding approximate periodic solution of the nonlinear system (3.28) are

$$T_2(A) = \frac{2\pi}{\sqrt{\Omega_2(A)}}, \quad \Omega_2(A) = \Omega_1(A) + \Delta\Omega_1(A) \qquad (3.47)$$

and

$$u_2(t) = u_1(\tau) + \Delta u_1(\tau) = (A)\cos\tau + x_1(A)(\cos\tau - \cos 3\tau), \quad \tau = \sqrt{\Omega_2(A)}t \qquad (3.48)$$

As shown above, it is clear how the procedure works for constructing higher-order approximate solutions. For example, for the kth-order analytical approximation, we set

$$\Delta u_{k-1}(\tau) = \sum_{i=1}^{k-1} x_i \{\cos[(2i-1)\tau] - \cos[(2i+1)\tau]\} \tag{3.49}$$

3.3.2 Improved NHB Method for Symmetric Nonlinear Conservative Oscillations

To improve the convergence of the NHB method, the one-dimensional nonlinear oscillator governed by Eq. (3.28) is reconsidered and the first-order approximate solutions are obtained in the same way as presented in Section 3.3.1. For the second-order approximate solutions, applying Newton's procedure, the periodic solution and the squared angular frequency of Eq. (3.29) are also expressed as (Wu et al. 2017)

$$u = u_1 + \Delta u_{1s}, \quad \Omega = \Omega_1 + \Delta \Omega_{1s} \tag{3.50}$$

where Δu_{1s} and $\Delta \Omega_{1s}$ are small increments of the first-order approximations u_1 and Ω_1, respectively. Δu_{1s} is a periodic function of τ with a period of 2π, and $\Delta \Omega_{1s}$ is a constant. Then, the second-order Taylor expansion by retaining the second-order power term is applied, that is, substituting Eq. (3.50) into Eq. (3.29), expanding in a Taylor series about u_1 and Ω_1, and neglecting the third-order and higher-order degree terms in Δu_{1s} and $\Delta \Omega_{1s}$, we have

$$\Omega_1 u_1'' + f(u_1) + \Omega_1 \Delta u_{1s}'' + \Delta \Omega_{1s} u_1'' + \Delta \Omega_{1s} \Delta u_{1s}'' + f_u(u_1) \Delta u_{1s} + \frac{1}{2} f_{uu}(u_1)(\Delta u_{1s})^2 = 0,$$
$$\Delta u_{1s}(0) = 0, \quad \Delta u_{1s}'(0) = 0 \tag{3.51}$$

Since Eq. (3.51) is nonlinear in nature, the solving procedures are required to divide into the following two steps. First, we linearize Eq. (3.51) with respect to Δu_{1s} and $\Delta \Omega_{1s}$, leading to a linear equation that can be solved by the harmonic balance method. This linear equation is identical to Eq. (3.39), we omit the procedures and use the results of $\Delta \Omega_1$ and Δu_1 derived in Section 3.3.1 in the next step. That is, replacing $\Delta \Omega_{1s}$ in $\Delta \Omega_{1s} \Delta u_{1s}$ with $\Delta \Omega_1$ and one of two Δu_{1s} terms in $\frac{1}{2} f_{uu}(u_1)(\Delta u_{1s})^2$ with Δu_1 in Eq. (3.51), respectively, this can formulate a linear equation in terms of Δu_{1s} and $\Delta \Omega_{1s}$ as follows

$$\Omega_1 u_1'' + f(u_1) + (\Omega_1 + \Delta \Omega_1) \Delta u_{1s}'' + \Delta \Omega_{1s} u_1'' + \left[f_u(u_1) + \frac{1}{2} f_{uu}(u_1) \Delta u_1 \right] \Delta u_{1s} = 0,$$
$$\Delta u_{1s}(0) = 0, \quad \Delta u_{1s}'(0) = 0 \tag{3.52}$$

In Eq. (3.52), the function $f_{uu}(u_1(\tau))$ can be expanded by using a Fourier series as follows

$$f_{uu}(u_1(\tau)) = \sum_{i=1}^{\infty} c_{2i-1} \cos[(2i-1)\tau] \tag{3.53}$$

where

$$c_{2i-1} = \frac{4}{\pi} \int_0^{\pi/2} f_{uu}(u_1(\tau)) \cos[(2i-1)\tau]d\tau, \quad i = 1, 2, \ldots \tag{3.54}$$

and $\Delta u_{1s}(\tau)$ can be expressed as

$$\Delta u_{1s}(\tau) = x_{1s}(\cos\tau - \cos 3\tau) + x_{2s}(\cos 3\tau - \cos 5\tau) \tag{3.55}$$

Inserting Eqs. (3.31), (3.32), (3.40), (3.42), (3.45), (3.46), (3.53) and (3.55) into Eq. (3.52), expanding the resulting expression in a trigonometric series and setting the coefficients of $\cos\tau$, $\cos 3\tau$ and $\cos 5\tau$ to zero, we get

$$\begin{cases} M_1 x_{1s} + N_1 x_{2s} - A\Delta\Omega_{1s} = 0 \\ M_2 x_{1s} + N_2 x_{2s} + a_3 = 0 \\ M_3 x_{1s} + N_3 x_{2s} + a_5 = 0 \end{cases} \tag{3.56}$$

where

$$M_1 = \frac{1}{8}\left[\frac{-8a_1}{A} - 8\Delta\Omega_1 + 4b_0 - 4b_4 + x_1(3c_1 - 3c_3 - c_5 + c_7)\right] \tag{3.57}$$

$$N_1 = \frac{1}{8}\left[4b_2 - 4b_6 + x_1(2c_3 - 2c_5 - c_7 + c_9)\right] \tag{3.58}$$

$$M_2 = \frac{1}{8}\left[\frac{72a_1}{A} + 72\Delta\Omega_1 - 4b_0 + 4b_2 + 4b_4 - 4b_6 + x_1(-3c_1 + 5c_3 - c_5 - 2c_7 + c_9)\right] \tag{3.59}$$

$$N_2 = \frac{1}{8}\left[-\frac{72a_1}{A} - 72\Delta\Omega_1 + 4b_0 - 4b_2 + 4b_6 - 4b_8 + x_1(2c_1 - 4c_3 + 3c_5 - 2c_9 + c_{11})\right] \tag{3.60}$$

$$M_3 = \frac{1}{8}\left[-4b_2 + 4b_4 + 4b_6 - 4b_8 - x_1(c_1 + c_3 - 4c_5 + c_7 + 2c_9 - c_{11})\right] \tag{3.61}$$

$$N_3 = \frac{1}{8}\left[\frac{200a_1}{A} + 200\Delta\Omega_1 - 4b_0 + 4b_2 + 4b_8 - 4b_{10} + x_1(-2c_1 + 3c_3 - 2c_5 + 2c_7 - 2c_{11} + c_{13})\right] \tag{3.62}$$

in which x_1 and $\Delta\Omega_1$ are given in Eqs. (3.45) and (3.46), respectively. The solutions to Eq. (3.56) are

$$x_{1s}(A) = \frac{-N_3 a_3 + N_2 a_5}{M_2 N_3 - M_3 N_2} \tag{3.63}$$

$$x_{2s}(A) = \frac{M_3 a_3 - M_2 a_5}{M_2 N_3 - M_3 N_2} \tag{3.64}$$

$$\Delta\Omega_{1s}(A) = \frac{a_3(M_3N_1 - M_1N_3) + a_5(M_1N_2 - M_2N_1)}{A(M_2N_3 - M_3N_2)} \tag{3.65}$$

Therefore, the improved second-order analytical approximations of the nonlinear system (3.28) are

$$T_{2s}(A) = \frac{2\pi}{\sqrt{\Omega_{2s}(A)}}, \quad \Omega_{2s}(A) = \Omega_1(A) + \Delta\Omega_{1s}(A) \tag{3.66}$$

and

$$\begin{aligned} u_{2s}(t) &= u_1(\tau) + \Delta u_{1s}(\tau) \\ &= A\cos\tau + x_{1s}(A)(\cos\tau - \cos 3\tau) + x_{2s}(A)(\cos 3\tau - \cos 5\tau), \quad \tau = \sqrt{\Omega_{2s}(A)}t. \end{aligned} \tag{3.67}$$

Higher-order analytical approximate solutions can be constructed by using the last approximations u_{2s} and Ω_{2s} in place of u_{1s} and Ω_{1s}, respectively, and implementing similar procedures as aforementioned.

3.3.3 NHB Method for Asymmetric Nonlinear Conservative Oscillations

Consider an SDOF nonlinear oscillator governed by

$$\frac{d^2u}{dt^2} + g(u) = 0, \quad u(0) = A, \quad \frac{du}{dt}(0) = 0 \tag{3.68}$$

where $g(u)$ is a general function of u, i.e., $g(-u) \neq -g(u)$ with odd and even nonlinearities. Let $V(u) = \int g(u)du$ be the potential energy of the system and suppose that it reaches its minimum at $u = u_0$, called a center. We assume $u_0 = 0$, the system will thus oscillate between the asymmetric bounds $[-B, A]$ where both $-B$ ($B > 0$) and A have the same energy level, i.e.,

$$V(-B) = V(A) \tag{3.69}$$

in which B can be analytically expressed as a function of A.

To solve such a non-odd system, two new odd nonlinear systems should be introduced (Wu and Lim, 2004), as illustrated below:

$$\frac{d^2u}{dt^2} + F(u) = 0, \quad u(0) = A, \quad \frac{du}{dt}(0) = 0 \tag{3.70}$$

$$\frac{d^2u}{dt^2} + G(u) = 0, \quad u(0) = B, \quad \frac{du}{dt}(0) = 0 \tag{3.71}$$

where

$$F(u) = \begin{cases} g(u) & \text{if} \quad u \geq 0 \\ -g(-u) & \text{if} \quad u < 0 \end{cases} \tag{3.72}$$

$$G(u) = \begin{cases} -g(-u) & \text{if} \quad u > 0 \\ g(u) & \text{if} \quad u \leq 0 \end{cases} \tag{3.73}$$

In Eqs. (3.70) and (3.71), both of $F(u)$ and $G(u)$ are odd functions of u. Hence, Eqs. (3.70) and (3.71) are two oscillating systems with odd nonlinearity and therefore can be solved independently by the NHB method described in Section 3.3.1 or Section 3.3.2. Then, the approximate analytical solutions for Eq. (3.68) can be constructed. The first-order approximate angular frequency ω_1, the first-order approximate period T_1 and the corresponding approximate periodic solution $u_1(t)$ are given by

$$\omega_1(A) = \frac{2\omega_{1F}\omega_{1G}}{\omega_{1F} + \omega_{1G}}, \quad T_1(A) = \frac{T_{1F}(A) + T_{1G}(B)}{2} \tag{3.74}$$

and

$$u_1(t) = \begin{cases} u_{1F}(t), & \text{for} \ \ 0 \leq t \leq \dfrac{T_{1F}(A)}{4} \\[2mm] u_{1G}\left(t - \dfrac{T_{1F}(A)}{4} + \dfrac{T_{1G}(B)}{4}\right), & \text{for} \ \ \dfrac{T_{1F}(A)}{4} \leq t \leq \dfrac{T_{1F}(A)}{4} + \dfrac{T_{1G}(B)}{2} \\[2mm] u_{1F}\left(t + \dfrac{T_{1F}(A)}{2} - \dfrac{T_{1G}(B)}{2}\right), & \text{for} \ \ \dfrac{T_{1F}(A)}{4} + \dfrac{T_{1G}(B)}{2} \leq t \leq \dfrac{T_{1F}(A)}{2} + \dfrac{T_{1G}(B)}{2} \end{cases} \tag{3.75}$$

where the subscripts "1F" and "1G" of ω, T and u denote the first-order analytical solutions for the systems (3.70) and (3.71), respectively.

The second-order approximate frequency ω_2, the second-order approximate period T_2 and the corresponding approximate periodic solution $u_2(t)$ are

$$\omega_2(A) = \frac{2\omega_{2F}\omega_{2G}}{\omega_{2F} + \omega_{2G}}, \quad T_2(A) = \frac{T_{2F}(A) + T_{2G}(B)}{2} \tag{3.76}$$

and

$$u_2(t) = \begin{cases} u_{2F}(t), & \text{for} \ \ 0 \leq t \leq \dfrac{T_{2F}(A)}{4} \\[2mm] u_{2G}\left(t - \dfrac{T_{2F}(A)}{4} + \dfrac{T_{2G}(B)}{4}\right), & \text{for} \ \ \dfrac{T_{2F}(A)}{4} \leq t \leq \dfrac{T_{2F}(A)}{4} + \dfrac{T_{2G}(B)}{2} \\[2mm] u_{2F}\left(t + \dfrac{T_{2F}(A)}{2} - \dfrac{T_{2G}(B)}{2}\right), & \text{for} \ \ \dfrac{T_{2F}(A)}{4} + \dfrac{T_{2G}(B)}{2} \leq t \leq \dfrac{T_{2F}(A)}{2} + \dfrac{T_{2G}(B)}{2} \end{cases} \tag{3.77}$$

where the subscripts "2F" and "2G" of ω, T and u denote the second-order analytical solutions for the systems (3.70) and (3.71), respectively.

Applying the improved NHB method in Section 3.3.2, the second-order approximate frequency ω_2^*, the second-order approximate period T_2^* and the corresponding approximate periodic solution $u_2^*(t)$ can also be expressed as

$$\omega_2^*(A) = \frac{2\omega_{2s-F}\omega_{2s-G}}{\omega_{2s-F} + \omega_{2s-G}}, \quad T_2^*(A) = \frac{T_{2s-F}(A) + T_{2s-G}(B)}{2} \tag{3.78}$$

and

$$u_2^*(t) =$$

$$\begin{cases} u_{2s-F}(t), & \text{for} \quad 0 \le t \le \frac{T_{2s-F}(A)}{4} \\ u_{2s-G}\left(t - \frac{T_{2s-F}(A)}{4} + \frac{T_{2s-G}(B)}{4}\right), & \text{for} \quad \frac{T_{2s-F}(A)}{4} \le t \le \frac{T_{2s-F}(A)}{4} + \frac{T_{2s-G}(B)}{2} \\ u_{2s-F}\left(t + \frac{T_{2s-F}(A)}{2} - \frac{T_{2s-G}(B)}{2}\right), & \text{for} \quad \frac{T_{2s-F}(A)}{4} + \frac{T_{2s-G}(B)}{2} \le t \le \frac{T_{2s-F}(A)}{2} + \frac{T_{2s-G}(B)}{2} \end{cases} \tag{3.79}$$

where the subscripts "2s−F" and "2s−G" of ω, T and u denote the improved second-order analytical approximations (obtained from Eqs. (3.66) and (3.67) in Section 3.3.2) for the systems (3.70) and (3.71), respectively.

3.3.4 NHB Method for Symmetric Nonlinear Oscillations under an External Harmonic Force

Consider the following SDOF nonlinear oscillating system governed by (Wu et al., 2018b)

$$\frac{d^2u}{dt^2} + f(u) + h\left(\frac{du}{dt}\right) = F_0 \cos(\tilde{\omega}t) \tag{3.80}$$

where $f(u)$ and $h(v)(v = du/dt)$ are odd functions of u and v (i.e., $f(-u) = -f(u)$ and $h(-v) = -h(v)$), respectively. It is noted that this method is to derive steady-state responses that can match with the excitation period. Both sub-harmonic and super-harmonic oscillations are not considered herein.

First, by introducing a new independent variable $\tilde{\tau} = \tilde{\omega}t$, Eq. (3.80) can be rewritten as

$$\tilde{\omega}^2 u'' + f(u) + h(\tilde{\omega}u') = F_0 \cos(\tilde{\tau} + \theta) \tag{3.81}$$

58

where a prime denotes the differentiation with respect to $\tilde{\tau}$. A phase θ is added in the force excitation so that we can construct a response with phase zero. For the steady-state response of Eq. (3.81), the periodic conditions for both displacement and velocity are given by

$$u(0) = u(2\pi) = \tilde{A}, \ u'(0) = u'(2\pi) = 0 \tag{3.82}$$

where $\tilde{A}$ is the amplitude of the steady-state response.

For the first-order approximation to $u(\tilde{\tau})$, $\tilde{A}$ and θ, following the single-term harmonic balance method, we assume

$$u(\tilde{\tau}) = u_1(\tilde{\tau}) = \tilde{A}_1 \cos \tilde{\tau} \tag{3.83}$$

Based on the odd function assumption $f(-u) = -f(u)$ and $h(-v) = -h(v)$, $f(u_1(\tilde{\tau}))$ and $h(\tilde{\omega}u_1'(\tilde{\tau}))$ can be expanded in a Fourier series as

$$f(u_1(\tilde{\tau})) = \sum_{i=1}^{\infty} \tilde{a}_{2i-1} \cos(2i-1)\tilde{\tau} \tag{3.84}$$

$$h(\tilde{\omega}u_1'(\tilde{\tau})) = \sum_{i=1}^{\infty} \tilde{c}_{2i-1} \sin(2i-1)\tilde{\tau} \tag{3.85}$$

where

$$\tilde{a}_{2i-1} = \frac{1}{\pi} \int_0^{2\pi} f(\tilde{A}_1 \cos \tilde{\tau}) \cos(2i-1)\tilde{\tau} d\tilde{\tau}, \quad (i = 1, 2, \ldots) \tag{3.86}$$

$$\tilde{c}_{2i-1} = \frac{1}{\pi} \int_0^{2\pi} h(-\tilde{\omega}\tilde{A}_1 \sin \tilde{\tau}) \sin(2i-1)\tilde{\tau} d\tilde{\tau}, \quad (i = 1, 2, \ldots) \tag{3.87}$$

Incorporating Eqs. (3.83)–(3.85) into Eq. (3.81) and setting the coefficients of $\cos \tilde{\tau}$ and $\sin \tilde{\tau}$ to zero, we have

$$\left(-\tilde{\omega}_1^2 \tilde{A}_1 + \tilde{a}_1\right)^2 + \tilde{c}_1^2 = F_0^2 \tag{3.88}$$

and

$$\tan \theta_1 = \frac{\tilde{c}_1}{\tilde{\omega}_1^2 \tilde{A}_1 - \tilde{a}_1} \tag{3.89}$$

Then, the first-order approximation to the amplitude, frequency and phase of the resonance response is expressed as

$$\tilde{A} = \tilde{A}_1, \quad \tilde{\omega} = \tilde{\omega}_1, \quad \theta = \theta_1 \tag{3.90}$$

and the corresponding periodic solution is

$$u_1(t) = \tilde{A}_1 \cos \tilde{\tau}, \quad \tilde{\tau} = \tilde{\omega}_1 t \tag{3.91}$$

Subsequently, the second-order approximation to $u(\tilde{\tau})$, $\tilde{A}$, $\tilde{\omega}$ and θ is expressed by adding increments to the first-order approximation, i.e.,

$$u_2 = u_1 + \Delta u_1, \quad \tilde{A}_2 = \tilde{A}_1 + \Delta \tilde{A}_1, \quad \tilde{\omega}_2 = \tilde{\omega}_1 + \Delta \tilde{\omega}_1, \quad \theta_2 = \theta_1 + \Delta \theta_1 \tag{3.92}$$

where Δu_1 is a periodic function of $\tilde{\tau}$ with a period of 2π. Substituting Eq. (3.92) into Eq. (3.81) and linearizing with respect to the correction terms Δu_1, $\Delta \tilde{\omega}_1$, $\Delta \theta_1$ and $\Delta \tilde{A}_1$, we achieve

$$\begin{aligned}
&\tilde{\omega}_1^2 u_1'' + f(u_1) + h(\tilde{\omega}_1 u_1') + \tilde{\omega}_1^2 \Delta u_1'' + 2\tilde{\omega}_1 \Delta \tilde{\omega}_1 u_1'' + f_u(u_1)\Delta u_1 \\
&+ h_v(\tilde{\omega}_1 u_1')(\Delta \tilde{\omega}_1 u_1' + \tilde{\omega}_1 \Delta u_1') = F_0 \cos(\theta_1 + \tilde{\tau}) - F_0 \sin(\theta_1 + \tilde{\tau})\Delta \theta_1, \\
&\Delta u_1(0) = \Delta u_1(2\pi) = \Delta \tilde{A}_1, \quad \Delta u_1'(0) = \Delta u_1'(2\pi) = 0
\end{aligned} \tag{3.93}$$

where the subscripts u and v denote the derivatives of $f(u)$ and $h(v)$ with respect to u and v, respectively.

Then, the harmonic balance method will be applied to solve Eq. (3.93) for Δu_1, $\Delta \tilde{\omega}_1$, $\Delta \theta_1$ and $\Delta \tilde{A}_1$. Since $f(-u) = -f(u)$ and $h(-v) = -h(v)$, $f_u(u_1(\tilde{\tau}))$ and $h_v(\tilde{\omega} u_1'(\tilde{\tau}))$ can be expanded into the following Fourier series:

$$f_u(u_1(\tilde{\tau})) = \frac{\tilde{b}_0}{2} + \sum_{i=1}^{\infty} \tilde{b}_{2i} \cos(2i)\tilde{\tau} \tag{3.94}$$

$$h_v(\tilde{\omega} u_1'(\tilde{\tau})) = \frac{\tilde{d}_0}{2} + \sum_{i=1}^{\infty} \tilde{d}_{2i} \cos(2i)\tilde{\tau} \tag{3.95}$$

where

$$\tilde{b}_{2i} = \frac{1}{\pi} \int_0^{2\pi} f_u(u_1(\tilde{\tau})) \cos(2i)\tilde{\tau} d\tilde{\tau}, \quad i = 0, 2... \tag{3.96}$$

$$\tilde{d}_{2i} = \frac{1}{\pi} \int_0^{2\pi} h_v(\tilde{\omega} u_1'(\tilde{\tau})) \cos(2i)\tilde{\tau} d\tilde{\tau}, \quad i = 0, 2... \tag{3.97}$$

For the second-order approximate solution, we set $\Delta u_1(\tilde{\tau})$ as

$$\Delta \tilde{u}_1 = \Delta \tilde{A}_1 \cos \tilde{\tau} + C_1(\cos \tilde{\tau} - \cos 3\tilde{\tau}) + S_1 \left(\frac{\sin 3\tilde{\tau}}{3} - \frac{\sin 5\tilde{\tau}}{5} \right) \tag{3.98}$$

which satisfies the boundary conditions in Eq. (3.93). Substituting Eqs. (3.84), (3.85), (3.90), (3.91), (3.94), (3.95) and (3.98) into Eq. (3.93), expanding the resulting expression in a

trigonometric series and setting the coefficients of $\cos\tilde{\tau}$, $\sin\tilde{\tau}$, $\cos 3\tilde{\tau}$ and $\sin 3\tilde{\tau}$ to zero, we get

$$K_1 \cdot z_1 = e_1 \cdot \Delta\theta_1 + f_1 \tag{3.99}$$

where

$$K_1 = \begin{pmatrix} K_{11} & K_{12} & K_{13} & K_{14} \\ K_{21} & K_{22} & K_{23} & K_{24} \\ K_{31} & K_{32} & K_{33} & K_{34} \\ K_{41} & K_{42} & K_{43} & K_{44} \end{pmatrix} \tag{3.100}$$

$$z_1 = (\Delta\tilde{\omega}_1, \ \Delta\tilde{A}_1, \ C_1, \ S_1)^T \tag{3.101}$$

$$e_1 = (-F_0\sin\theta_1, \ -F_0\cos\theta_1, \ 0, \ 0)^T \tag{3.102}$$

$$f_1 = (0, \ 0, \ -\tilde{a}_3, \ -\tilde{c}_3)^T \tag{3.103}$$

where

$$K_{11} = -2\tilde{A}_1\tilde{\omega}_1, \ K_{12} = (-2\tilde{\omega}_1^2 + \tilde{b}_0 + \tilde{b}_2)/2, \ K_{13} = (-2\tilde{\omega}_1^2 + \tilde{b}_0 - \tilde{b}_4)/2,$$

$$K_{14} = \tilde{\omega}_1(\tilde{d}_2 - \tilde{d}_6)/2, \ K_{21} = \tilde{A}_1(-\tilde{d}_0 + \tilde{d}_2)/2, \ K_{22} = \tilde{\omega}_1(-\tilde{d}_0 + \tilde{d}_2)/2,$$

$$K_{23} = \tilde{\omega}_1(-\tilde{d}_0 + 4\tilde{d}_2 + 3\tilde{d}_4)/2, \ K_{24} = \tilde{\omega}_1(5\tilde{b}_2 - 8\tilde{b}_4 + 3\tilde{b}_6)/30, \ K_{31} = 0,$$

$$K_{32} = (\tilde{b}_2 + \tilde{b}_4)/2, \ K_{33} = (18\tilde{\omega}_1^2 - \tilde{b}_0 + \tilde{b}_2 + \tilde{b}_4 - \tilde{b}_6)/2, \tag{3.104}$$

$$K_{34} = \tilde{\omega}_1(\tilde{d}_0 - \tilde{d}_2 + \tilde{d}_6 - \tilde{d}_8)/2, \ K_{41} = \tilde{A}_1(-\tilde{d}_2 + \tilde{d}_4)/2, \ K_{42} = \tilde{\omega}_1(-\tilde{d}_2 + \tilde{d}_4)/2,$$

$$K_{43} = \tilde{\omega}_1(3\tilde{d}_0 - \tilde{d}_2 + \tilde{d}_4 - 3\tilde{d}_6)/2, \ K_{44} = (-90\tilde{\omega}_1^2 + 5\tilde{b}_0 - 3\tilde{b}_2 - 5\tilde{b}_6 + 3\tilde{b}_8)/30$$

Eq. (3.99) is an underdetermined system and will be solved in a least-squares sense to ensure the rationality of linearization in Eq. (3.93), Solving Eq. (3.99) for z_1 yields

$$z_1 = \Delta\theta_1 \cdot g_1 + h_1, \quad g_1 = K_1^{-1}e_1, \quad h_1 = K_1^{-1}f_1 \tag{3.105}$$

Making use of Eq. (3.105) leads to

$$\|X_1\|^2 = \Delta\tilde{\omega}_1^2 + \Delta\tilde{A}_1^2 + C_1^2 + S_1^2 + \Delta\theta_1^2 = (g_1^T g_1 + 1)\Delta\theta_1^2 + 2(g_1^T h_1)\Delta\theta_1 + h_1^T h_1 \tag{3.106}$$

Subsequently, it can be deduced from the expression above that when

$$\Delta\theta_1 = -\frac{g_1^T h_1}{g_1^T g_1 + 1} \tag{3.107}$$

the norm $\|X_1\|^2$ will arrive at its minimum. The least-norm solution to Eq. (3.99) is therefore given by Eqs. (3.106) and (3.107). Finally, the second-order approximation to the amplitude, frequency and phase of the resonance response can be written as

$$\tilde{A} = \tilde{A}_2, \quad \tilde{\omega} = \tilde{\omega}_2, \quad \theta = \theta_2 \tag{3.108}$$

and the corresponding periodic solution is

$$u_2(t) = (\tilde{A}_1 + \Delta\tilde{A}_1)\cos\tilde{\tau} + C_1(\cos\tilde{\tau} - \cos 3\tilde{\tau}) + S_1\left(\frac{\sin 3\tilde{\tau}}{3} - \frac{\sin 5\tilde{\tau}}{5}\right),$$

$$\tilde{\tau} = (\tilde{\omega}_1 + \Delta\tilde{\omega}_1)t$$

(3.109)

In a similar manner, higher-order analytical approximations can be constructed by using the approximations u_2, $\tilde{A}_2$, $\tilde{\omega}_2$ and θ_2 in place of u_1, $\tilde{A}_1$, $\tilde{\omega}_1$ and θ_1, respectively, and repeating the similar procedures as mentioned above.

3.4 Results and Discussion

Case 1: Asymmetric vibration of a doubly clamped microbeam with one-sided electrode due to a suddenly applied DC voltage

In this section, analytical approximate solutions obtained by the NHB method for the proposed system are presented and compared with those results from the Runge–Kutta method. The geometrical and material parameters of the microbeam can be referred to Table 3.1. For reference, the exact frequency of the nonlinear system (3.68) is given by

$$\omega_e = \frac{2\omega_{e1}\omega_{e2}}{\omega_{e1} + \omega_{e2}}$$

(3.110)

where

$$\omega_{e1} = \pi / \int_0^{\frac{\pi}{2}} \frac{\sqrt{2}A\sin\theta}{\sqrt{V(A) - V(A\cos\theta)}}d\theta \quad \text{and} \quad \omega_{e2} = \pi / \int_0^{\frac{\pi}{2}} \frac{\sqrt{2}B\sin\theta}{\sqrt{V(B) - V(B\cos\theta)}}d\theta$$

(3.111)

The equilibrium points as well as the first-, second- and improved second-order initial frequencies obtained by the NHB method and the exact frequencies under different input voltages are listed in Table 3.3. It is observed that the vibration amplitude increases with an increase of the input voltage, while the frequency declines. When the input voltage is low, the first-order (ω_1), second-order (ω_2) and improved second-order (ω_2^*) frequencies all agree well with the exact solution (ω_e). When the input voltage is near the DC dynamic pull-in voltage, the higher-order initial frequencies are still in good agreement with the exact solution.

To further illustrate and verify the accuracy for the NHB method, the time-history responses of the microbeam mid-point deflection for the first-, second- and improved second-order approximate solutions and the Runge–Kutta results are presented in Figs. 3.4(a) and

3.5(a), and the corresponding absolute errors between $q_1(\bar{t})$, $q_2(\bar{t})$, $q_2^*(\bar{t})$ and $q_{num}(\bar{t})$ are shown in Figs. 3.4(b) and 3.5(b). When the value of V_{dc} is close to the DC dynamic pull-in voltage, the improved second-order approximation is still in good agreement with the Runge–Kutta results. However, the first-order approximation is not sufficiently good, see Fig. 3.5(b).

Table 3.3: Equilibrium points and initial frequencies under different input voltage levels.

V	Equilibrium point	ω_1	ω_2	ω_2^*	ω_e
2	0.0006	24.5815	24.5815	24.5815	24.5815
5	0.0039	24.4768	24.4768	24.4768	24.4768
8	0.0102	24.2969	24.2969	24.2969	24.2969
12	0.0237	23.8758	23.8758	23.8758	23.8758
14	0.0330	23.5950	23.5950	23.5950	23.5950
16	0.0443	23.3545	23.3545	23.3545	23.3545
18	0.0580	22.9785	22.9785	22.9785	22.9785
20	0.0748	22.1461	22.1461	22.1461	22.1461
22	0.0955	21.2774	21.2770	21.2770	21.2770
24	0.1222	19.8367	19.8339	19.8430	19.8430
25	0.1389	18.4935	18.4806	18.4811	18.4810
25.5	0.1485	13.3114	12.5159	12.4416	12.3925
26	0.1593	13.2852	12.5064	12.4346	12.3827
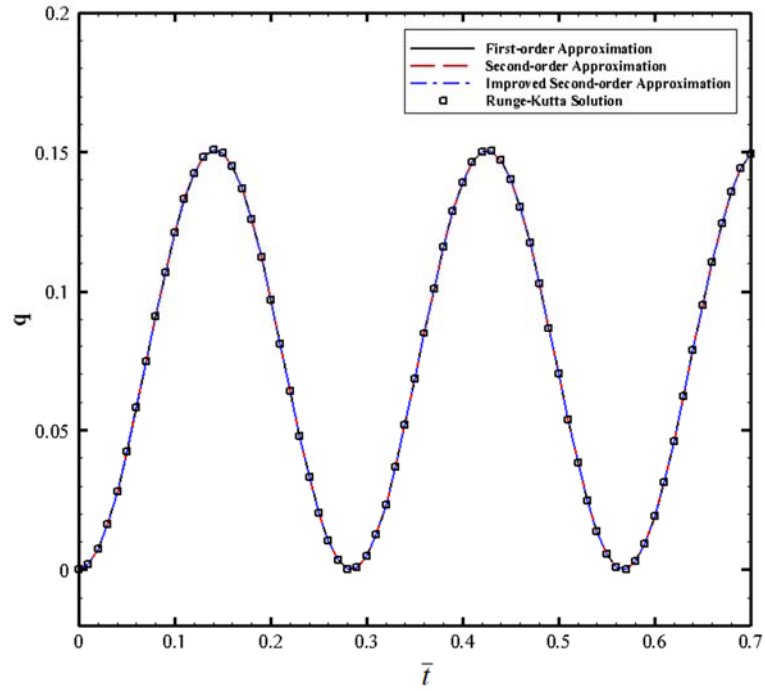
(a)
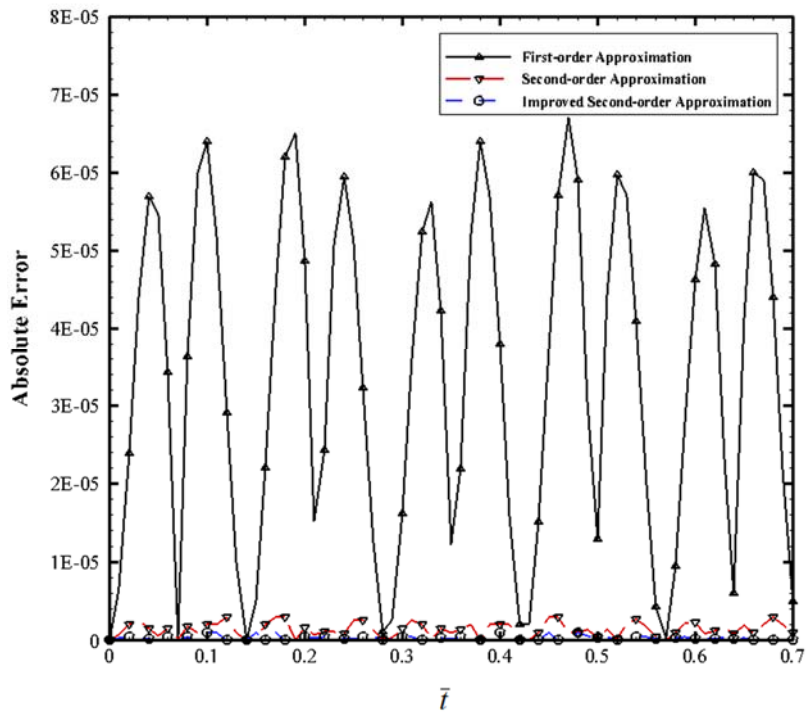
(b)

Fig. 3.4: (a) Time-history responses for $V_{dc} = 20$; (b) Comparison of the absolute errors between the approximate and numerical solutions in this case.
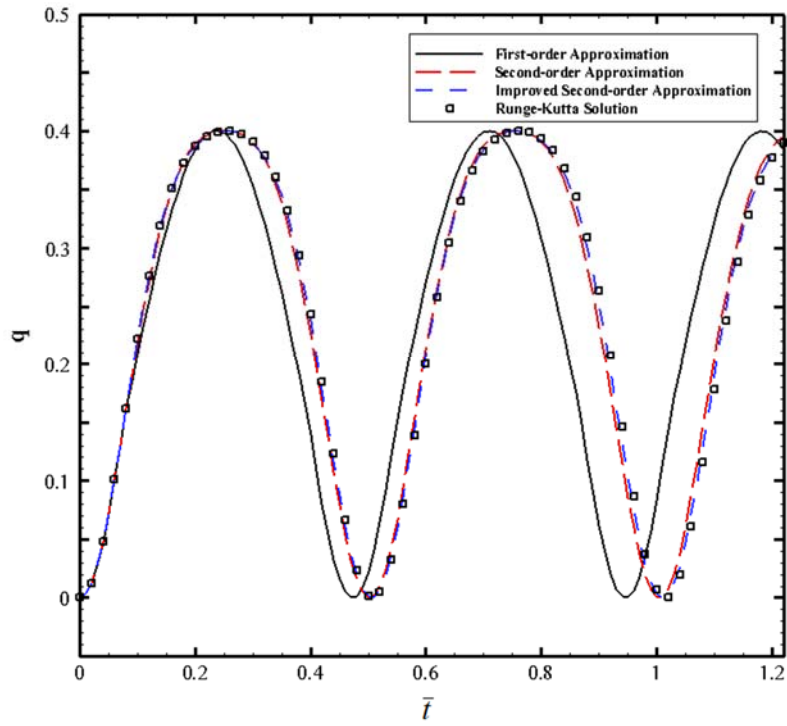
(a)
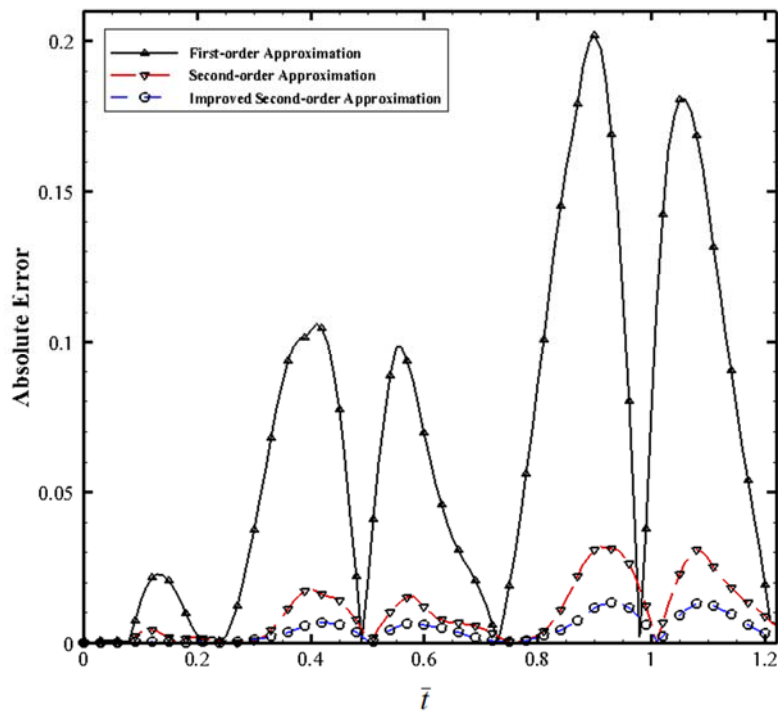
(b)

Fig. 3.5: (a) Time-history responses for $V_{dc} = 25.5$; (b) Comparison of the absolute errors

between the approximate and numerical solutions in this case.

65

Case 2: Resonance response of a doubly clamped microbeam with two-sided electrodes actuated by a bias DC voltage and an AC harmonic voltage

In this section, a case study of the doubly-clamped microbeam with two-sided electrodes actuated by a DC voltage and a harmonic AC voltage is presented. The geometrical and material parameters of the microbeam are given in Table 3.1. The frequency-amplitude curves derived by the NHB and Runge–Kutta methods for three different sets of electric loads, i.e., (i) $V_{dc} = 8$ V and $V_{ac} = 0.2$ V; (ii) $V_{dc} = 12$ V and $V_{ac} = 0.07$ V; and (iii) $V_{dc} = 16$ V and $V_{ac} = 0.01$ V, are depicted to show the accuracy of the proposed analytical method and investigate the steady-state dynamic behavior of the microbeam. Based on these three examples, we obtain the corresponding normalized parameters as follows:

(i) $\tilde{c} = 0.123511$, $\beta_1 = 728.474$, $\beta_2 = 561.989$, $\alpha_1 = -136.442$, $\alpha_2 = -505.355$, $\alpha_3 = -1581.48$, $F_0 = 1.41706$.

(ii) $\tilde{c} = 0.104213$, $\beta_1 = 728.474$, $\beta_2 = 561.989$, $\alpha_1 = -306.996$, $\alpha_2 = -1137.05$, $\alpha_3 = -3558.33$, $F_0 = 0.743957$.

(iii) $\tilde{c} = 0.0686132$, $\beta_1 = 728.474$, $\beta_2 = 561.989$, $\alpha_1 = -545.77$, $\alpha_2 = -2021.42$, $\alpha_3 = -6325.92$, $F_0 = 0.141706$.

Consider the present three cases, a comparison of the first- and second-order approximate frequency-amplitude responses $q_1(\omega)$ and $q_2(\omega)$ and the numerical results $q_{num}(\omega)$ given by the Runge–Kutta method is presented in Figs. 3.6–3.8, respectively. Note that ω here is the external forcing frequency $\tilde{\omega}$ as stated in Eq. (3.27). Here, the stable and unstable solutions, determined by the Floquet theory (Nayfeh and Mook, 1995), are represented by the solid and dashed lines, respectively. The red and blue lines, respectively, denote to the first- and second-order analytical approximations of the frequency-amplitude responses, while the black circle dots represent the Runge–Kutta results. In Figs 3.6–3.8, the analytical approximation and numerical solutions are mainly consistent in the whole frequency range near the resonant frequency. In order to get a closer investigation, Figs. 3.6(c), 3.7(c), and 3.8(c) respectively depict the corresponding absolute errors between $q_1(\omega)$, $q_2(\omega)$, and $q_{num}(\omega)$ in each case between two jumping points. These figures clearly indicate that the second-order analytical approximation provides better solutions to the numerical results. The primary resonant response of the nonlinear system is examined by varying the frequency of excitation around the first linear natural frequency of the system. It is noted that the first natural frequency of the

microbeam decreases with increasing the DC voltage. We observe from these figures that the first non-dimensional natural frequencies of the microbeam for the three cases are 24.33, 20.53, and 13.52, respectively.

In this model, two factors, i.e., electrostatic force and geometrical nonlinearity, are considered. The nonlinear electrostatic force tends to yield a softening behavior while the geometrical nonlinearity tends to yield a hardening behavior. It can be observed that nonlinearity caused by the electrostatic force is dominant in these three cases since the nonlinear resonance peaks are all bent to the left-hand side. Besides, the amplitude of the microbeam mid-point increases as the excitation frequency decreases from a value larger than the corresponding first linear frequency until reaching to point A, i.e., nonlinear resonance. At this point, the motion becomes unstable via a limited point bifurcation, thereby causing the system to jump to the lower-amplitude stable branch, as indicated by the black arrows. The system shows different dynamic responses as the excitation frequency increases from a low value. In this case, instability occurs at point B due to a limited point bifurcation. The system then jumps to the upper-amplitude stable branch as indicated by the black arrows.
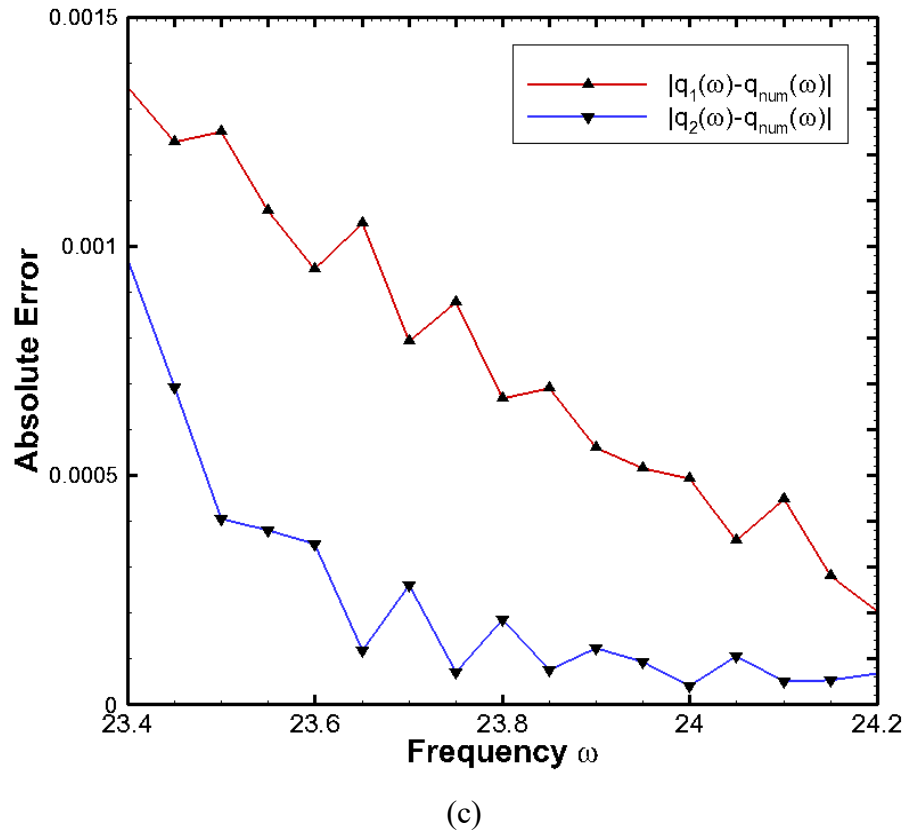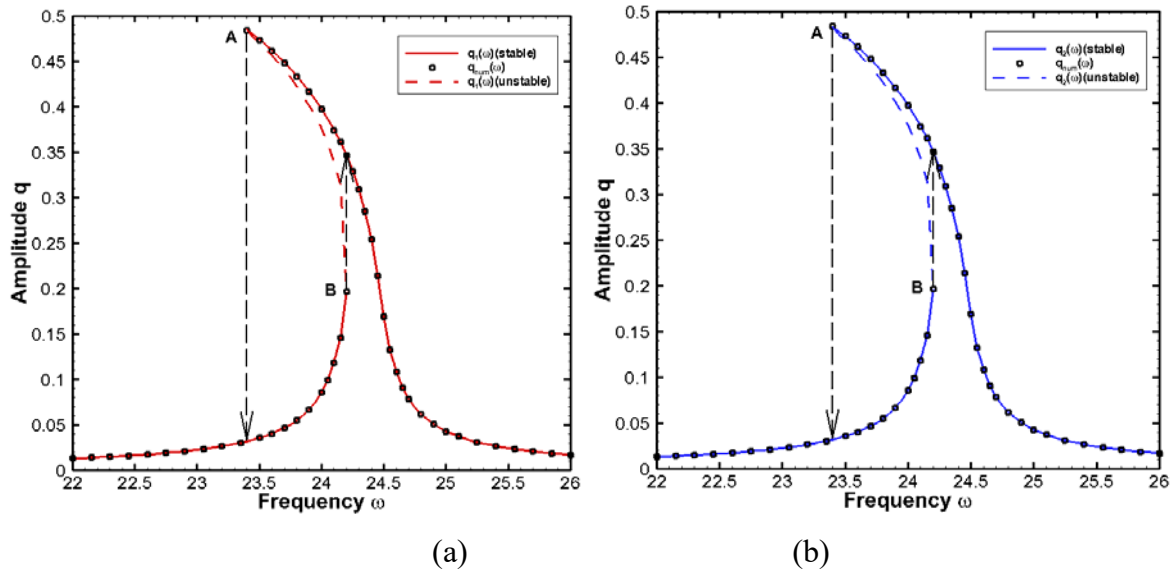
Fig. 3.6: (a) First-order approximate frequency-amplitude response for V_{dc} = 8 V and V_{ac} = 0.2 V; (b) Second-order approximate frequency-amplitude response for V_{dc} = 8 V and V_{ac} = 0.2 V; and (c) Comparison of the absolute errors between the approximate and numerical solutions. (Note that ω is the external forcing frequency $\tilde{\omega}$ as stated in Eq. (3.27).)

(a)

(b)

(c)
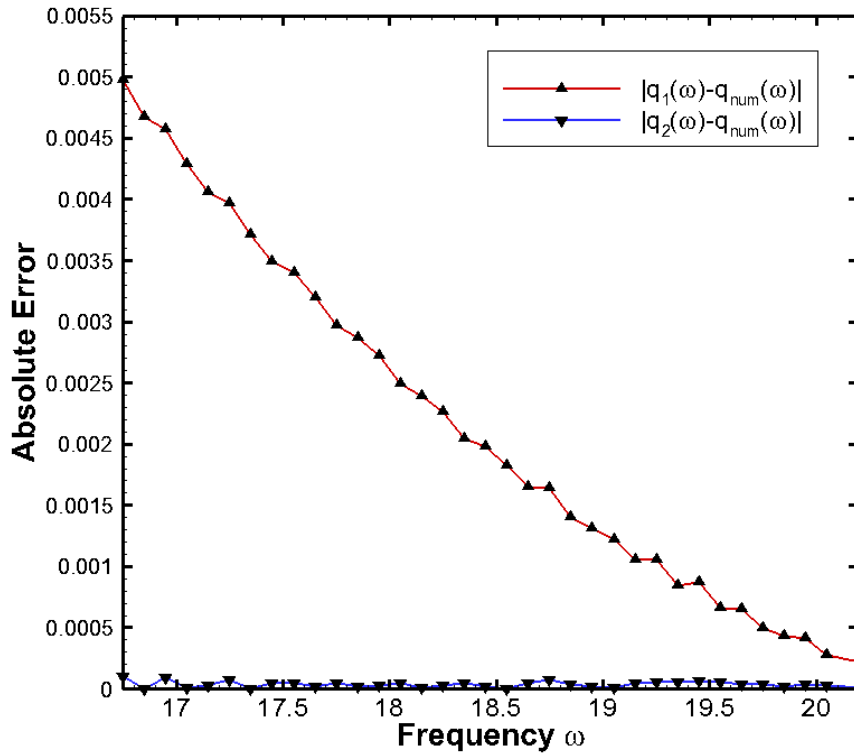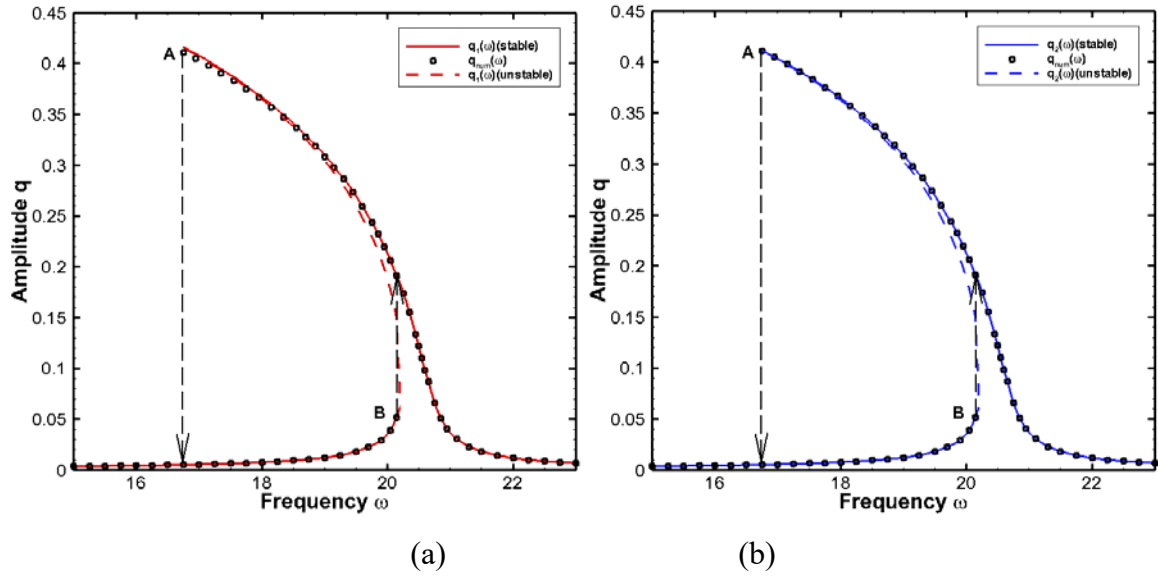
Fig. 3.7: (a) First-order approximate frequency-amplitude response for $V_{dc} = 12$ V and $V_{ac} = 0.07$ V; (b) Second-order approximate frequency-amplitude response for $V_{dc} = 12$ V and $V_{ac} = 0.07$ V; and (c) Comparison of the absolute errors between the approximate and numerical solutions. (Note that ω is the external forcing frequency $\tilde{\omega}$ as stated in Eq. (3.27).)

69

(a)   (b)

(c)
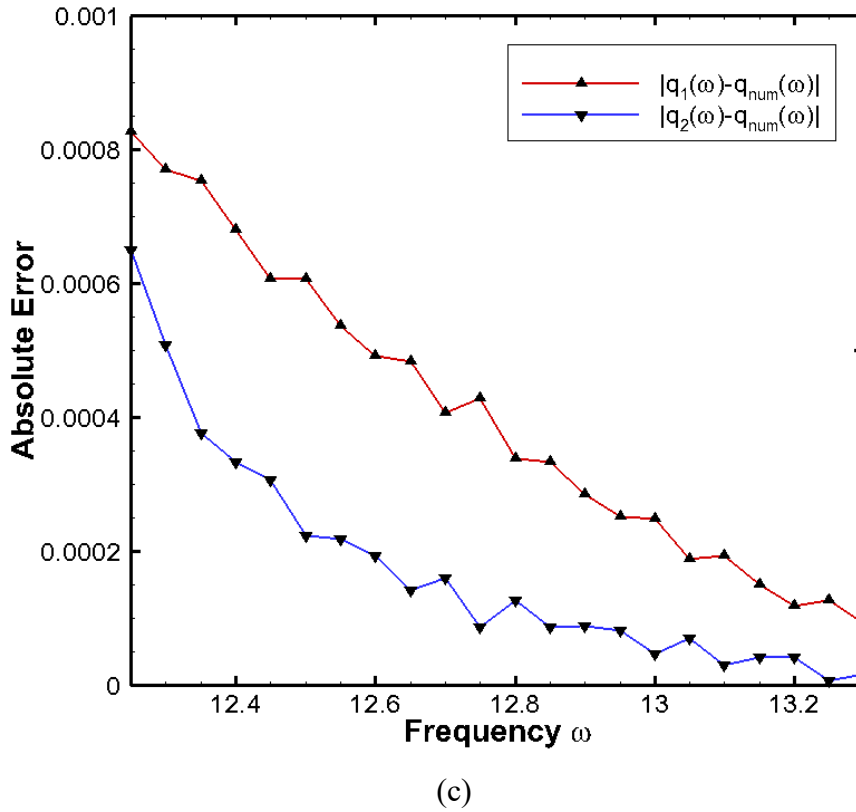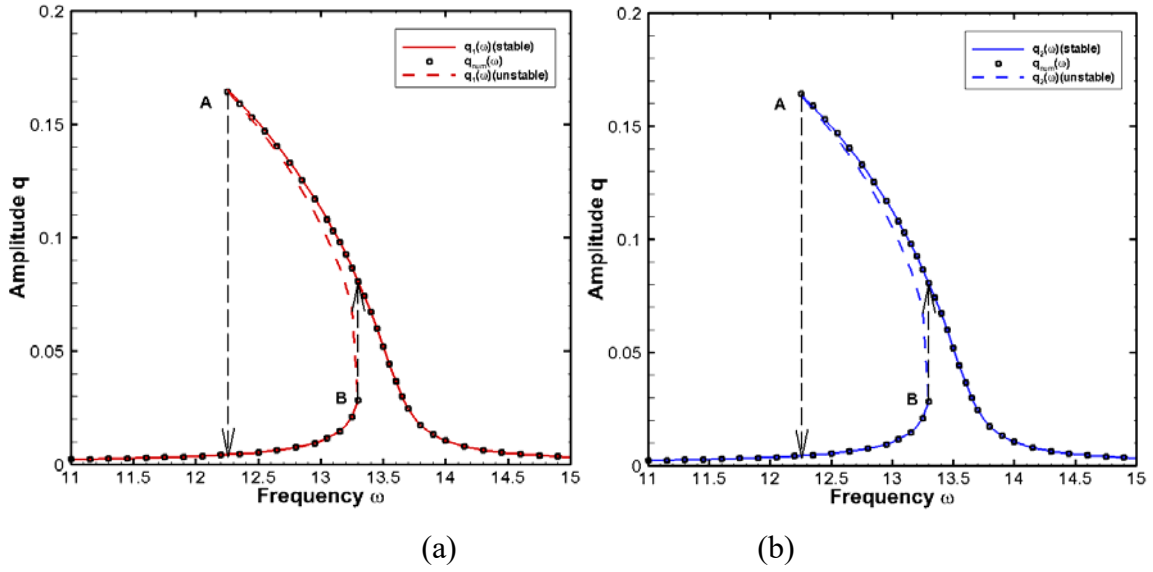
Fig. 3.8: (a) First-order approximate frequency-amplitude response for $V_{dc} = 16$ V and $V_{ac} =$ 0.01 V; (b) Second-order approximate frequency-amplitude response for $V_{dc} = 16$ V and $V_{ac} = 0.01$ V ; and (c) Comparison of the absolute errors between the approximate and numerical solutions. (Note that ω is the external forcing frequency $\tilde{\omega}$ as stated in Eq. (3.27).)

3.5 Concluding Remarks

In this chapter, the nonlinear free and forced vibration responses of MEMS microbeams are studied. We mainly focus on the development of lower-order analytical approximation solutions based on the NHB method for such problems, in which simple and accurate analytical expressions can be obtained. On the one hand, the asymmetric vibration of a doubly clamped microbeam with a one-sided electrode due to a suddenly applied DC voltage is investigated. The integral-differential governing equation of this beam model is transformed into a second-order ordinary differential equation having odd and even nonlinearities through the Galerkin method. As the electrostatic force term of this nonlinear system is not able to be integrated analytically, such that it is expanded by using a Taylor series around the equilibrium position of this system instead of the initial position of the system in regard to accuracy. The resultant nonlinear equation can then be solved by the NHB method. The analytical results are in excellent agreement with the numerical results obtained by the standard Runge–Kutta method for the whole stable regime, even when V_{dc} is extremely near the DC dynamic pull-in voltage. The accuracy of the second-order NHB method has therefore been verified for the strongly nonlinear system. By increasing the input voltage, the results show that the vibration amplitude increases as the frequency decreases.

On the other hand, the primary resonance effect of a doubly-clamped microbeam with two-sided symmetric electrostatic actuation as well as harmonically electrostatic loads on one side is also investigated. Accurate frequency-amplitude responses near the first natural frequency of the system are derived by means of the analytical approach. Consider various electrostatic loads, the relationship between the vibration amplitude and natural frequency of the microbeam is established. It is found that a softening effect due to the nonlinear electrostatic force is dominant in this case. Based on the present approach, this offers an efficient and reliable avenue to further analyze the nonlinear dynamics of complex MEMS resonators subjected to various external excitation levels.

Chapter 4

NANO-STRUCTURAL DEPENDENCE OF NONLOCAL DYNAMICAL BEHAVIOR

4.1 Introduction

As mentioned in the previous study, the effect of material length scales in the study of structures at micro-/nano-scales cannot be ignored and the nonlocal continuum elastic stress field theory is used to capture the small-scale effects of micro-/nano-scale structures. This chapter will focus on determining the upper limit of this nonlocal scale parameter through a dynamic analysis for various nanostructures. In Section 4.2, the nonlocal elasticity theory is briefly reviewed. In Section 4.3, three illustrative cases, the axial vibration of nanorods, transverse vibration of nanobeams, and free vibration of nanoplates, are used to determine the upper limit of the nonlocal scale parameter. In Section 4.4, the present results are discussed and confirmed by the previous studies. Finally, the key findings of this work are drawn in the last section.

4.2 Nonlocal Elasticity Theory

In generalized continuum mechanics, the nonlocal elasticity theory is used to predict the mechanical properties of nanomaterials by introducing the size-dependent constitutive parameters that can consider the intrinsic scale effect. The fundamental constitutive equation of the nonlocal elasticity theory in a differential form is given by (Eringen, 1983)

$$\left[1 - \left(e_0 a \right)^2 \nabla^2 \right] \mathbf{t} = \boldsymbol{\sigma} \tag{4.1}$$

where $\mathbf{t}$ is the nonlocal stress tensor, $\boldsymbol{\sigma}$ is the classical (local) stress tensor determined by the classical continuum mechanics theory, ∇^2 is the Laplacian operator, e_0 is a material parameter and a is an internal characteristic length. The nonlocal differential constitutive relation (4.1) can be reduced to the classical one when the parameter $e_0 a$ tends to zero. Therefore, nonlocal stress is identical to the classical one under the condition of $e_0 a = 0$. Actually, the classical theory is one of the simplified versions in generalized continuum mechanics and it can be treated as a special case of the nonlocal elasticity theory.

Based on a nonlocal framework, the product of e_0a was introduced as the nonlocal scale parameter by Eringen (1983), aimed at forming a nonlocal kernel function and measuring the contribution of the strains at other points to the stress at a specific point. With increasing the distance between other points and the specific point, the influence of the strains at other points will be weakened. The nonlocal scale parameter is used to determine a domain where the scale effect must be taken into consideration, while it can be neglected outside this parameter regime. For classical materials/structures at macro-scales, the nonlocal scale effect can be neglected. However, the scale effect should be considered for nanomaterials/structures when the external characteristic scale is at the same level as the internal characteristic scale. Under such circumstances, the nonlocal scale parameter plays a crucial role to quantify the length scale effect.

The differential constitutive equation has been extensively applied to study the size-dependent effect of nanostructures under various scenarios, including static deformation, buckling, vibration, wave propagation, dislocation, and damage mechanics. Indeed, nanomaterials can be modeled by different structural forms, such as nanowires, nanorods, nanotubes, nanobeams, nanoplates, and nanoshells. The present work is concerned with the upper limit of the nonlocal scale parameter. For this purpose, we investigate the scale range in dynamical behavior by taking three nanostructures for illustration. The nonlocal dynamics of nanostructures may differ from each other, implying the structural dependence of nonlocal dynamical behavior. Nevertheless, the effect of dynamic behavior is attributed to the factor of different structural characteristics, rather than the nonlocal scale effect. Consider various nanostructures made of the same material, the nonlocal scale effect has a commonality. This is the motivation of the present study, in which the upper limit of the nonlocal scale parameter can be determined according to the nonlocal softening mechanism.

4.3 Dynamic Analysis of Structural Elements
4.3.1 Axial Vibration of Nanorods

To show the characteristics of the nonlocal softening model, the formulations of the equation of motion for the axial vibration of nanorods based on the nonlocal differential constitutive relation and the classical equation of motion are presented herein. For a uniform, axially vibrating nanorod with a mass density ρ and a cross-sectional area A, we consider an element dx of the nanorod. The internal forces (i.e. axial force) on both sides of the element are

N and $N + \partial N / \partial x\, dx$, respectively. Hence, the classical equation of motion in an axial direction can be written as

$$\rho A dx \frac{\partial^2 u}{\partial t^2} = \left(N + \frac{\partial N}{\partial x} dx \right) - N \tag{4.2}$$

where u is the axial displacement, x is the axial coordinate and t is time. In fact, Eq. (4.2) can be treated as an equilibrium equation with the inertial force $-\rho A dx\, \partial^2 u / \partial t^2$ according to the dynamic-static method.

Consider the one-dimensional expression of Eq. (4.1) for nanorods, we can multiply A on both sides of the one-dimensional nonlocal constitutive equation, and then we obtain

$$N - (e_0 a)^2 \frac{\partial^2 N}{\partial x^2} = EA\varepsilon \tag{4.3}$$

where $N = \sigma A$ and $\sigma = E\varepsilon$ are adopted, in which E is the Young's modulus, σ is stress and ε is strain. The first partial derivative of Eq. (4.3) with respect to x is given by

$$\frac{\partial N}{\partial x} - (e_0 a)^2 \frac{\partial^3 N}{\partial x^3} = EA \frac{\partial^2 u}{\partial x^2} \tag{4.4}$$

in which the classical relation between the strain and the displacement (geometric equation) $\varepsilon = \partial u / \partial x$ is used. From Eq. (4.2) we obtain

$$\frac{\partial N}{\partial x} = \rho A \frac{\partial^2 u}{\partial t^2} \tag{4.5}$$

$$\frac{\partial^3 N}{\partial x^3} = \rho A \frac{\partial^4 u}{\partial x^2 \partial t^2} \tag{4.6}$$

Substitution of Eqs. (4.5) and (4.6) into Eq. (4.4) yields the nonlocal softening based governing equation of motion for nanorods as

$$\rho \frac{\partial^2 u}{\partial t^2} - \rho (e_0 a)^2 \frac{\partial^4 u}{\partial x^2 \partial t^2} = E \frac{\partial^2 u}{\partial x^2} \tag{4.7}$$

It is found that the nonlocal softening model is developed by combining the nonlocal constitutive relation with the classical equation of motion (or equilibrium equation). It is noted that the same result with Eq. (4.7) was derived by Aydogdu (2009). The solution to Eq. (4.7) can be obtained via the method of separation of variables as

$$u_n(x,t) = \left[C_{1n} \sin\left(\sqrt{\frac{\rho \omega_n^2}{E - \rho(e_0 a)^2 \omega_n^2}} x \right) + C_{2n} \cos\left(\sqrt{\frac{\rho \omega_n^2}{E - \rho(e_0 a)^2 \omega_n^2}} x \right) \right] e^{i\omega_n t} \tag{4.8}$$

where ω_n ($n=1,2,3,\ldots$) are circular frequencies for the axial vibration of nanorods with mode numbers n, and C_{1n} and C_{2n} are undetermined coefficients.

If the axial displacement related to the circular frequency of each mode is obtained, the general solution for the axial displacement of nanorods can be achieved after the superposition of each mode. Consider a fixed boundary constraint at both ends of a nanorod, we have

$$u\big|_{x=0,L} = 0 \tag{4.9}$$

where L is the length of the nanorod. The circular frequencies can then be determined analytically by combining Eq. (4.8) with (4.9), as

$$\omega_n = \sqrt{\frac{n^2\pi^2 E}{\rho L^2 + n^2\pi^2\rho(e_0 a)^2}} \tag{4.10}$$

This implies that the circular frequencies decrease with an increase in the nonlocal scale parameter, and the scale parameter may increase all the time mathematically. By choosing the parameters $L=10$ nm, $E=1.06$ TPa, $\rho=2250$ kg/m^3, we can plot the effect of the circular frequency against the nonlocal scale parameter numerically in Fig. 4.1. It is observed that the circular frequencies of an axially vibrating nanorod decrease slowly at the beginning of increasing the nonlocal scale parameter. Subsequently, the frequencies decrease rapidly when the nonlocal scale parameter reaches a certain value (e.g., $e_0 a > 0.2$ nm). Although the frequency curves decline all the time, they remain smooth in general. Based on this case, it is hard to conclude that there exists an upper limit of the nonlocal scale parameter for the axial vibration of nanorods because an infinity value is meaningless from a physical perspective.

The procedures of how to derive the governing equation using the nonlocal softening model are given above. It should be mentioned that the classical equilibrium equation or equation of motion is also available for the nonlocal hardening model. Therefore, not only the softening model but also the hardening model can be derived from the classical equations. The major difference is the expressions of relevant physical quantities used in two nonlocal models. When we still consider the axial vibration of nanorods, the expressions of the nonlocal stress in the softening and hardening models are, respectively (Lim, 2010b)

$$t_{xx} = E\sum_{m=0}^{\infty}(e_0 a)^{2m}\,\varepsilon_{xx}^{\langle 2m\rangle} \tag{4.11}$$

$$t_{xx} = E \sum_{m=0}^{\infty} (e_0 a)^{2m} \varepsilon_{xx}^{\langle 2m \rangle} - 2E \sum_{m=0}^{\infty} \sum_{n=1}^{\infty} (e_0 a)^{2(m+n)} \varepsilon_{xx}^{\langle 2(m+n) \rangle} \tag{4.12}$$

where the superscript $\langle 2m \rangle$ denotes the $(2m)^{\text{th}}$-order derivative with respect to the axial coordinate. The classical stress $\sigma_{xx} = E\varepsilon_{xx}$ is recovered in case of vanishing the nonlocal scale parameter in Eqs. (4.11) and (4.12).
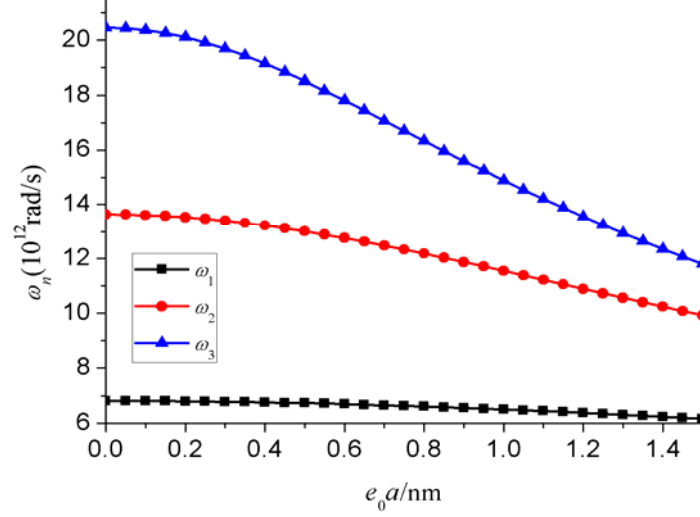
Fig. 4.1: Effect of the nonlocal scale parameter on the circular frequencies of a clamped nanorod.

Taking another example for the torsion of nanorods, the dimensionless twisting moment based on the nonlocal softening model is expressed as (Li, 2014a)

$$\overline{T} = \sum_{n=1}^{\infty} \tau^{2n-2} \theta^{\langle 2n-1 \rangle} \tag{4.13}$$

where τ is the non-dimensional nonlocal scale parameter, θ is the torsional angle. In the nonlocal hardening model, it should be replaced by (Li, 2014a)

$$\overline{T} = -\sum_{n=0}^{\infty} (2n-1)\tau^{2n} \theta^{\langle 2n+1 \rangle} \tag{4.14}$$

which was derived through the variational principle (Li, 2014a). For both models, the same equilibrium equation $\overline{T}^{\langle 1 \rangle} = -\overline{t}_m$ can be used, where $\overline{t}_m$ is a distributed torsional load per unit length. Nevertheless, the expression of the twisting moment $\overline{T}$ for the nonlocal hardening model is different from that of the softening model.

4.3.2 Transverse Vibration of Nanobeams

Based on the nonlocal softening model, we further investigate the transverse vibration of nanobeams. First, the classical equation of motion for the transverse vibration of nanobeams is given by

$$\frac{\partial^2 M}{\partial x^2} - \rho A \frac{\partial^2 w}{\partial t^2} = 0 \qquad (4.15)$$

where M is the bending moment, w is the transverse displacement, A is the rectangular cross-sectional area of the nanobeam (= breadth (b) × height (h)). To consider the one-dimensional expression of Eq. (4.1) for nanobeams, we multiply A on both sides of the one-dimensional nonlocal constitutive equation and then obtain

$$M - (e_0 a)^2 \frac{\partial^2 M}{\partial x^2} = -EI \frac{\partial^2 w}{\partial x^2} \qquad (4.16)$$

where $I = \int_A y^2 dA$ is the area moment of inertia, $M = \int_A y t_{xx} dA$ and $\sigma = E\varepsilon = -Ey \frac{\partial^2 w}{\partial x^2}$.

From Eqs. (4.15) and (4.16), we get

$$\frac{\partial^2 M}{\partial x^2} = \rho A \frac{\partial^2 w}{\partial t^2} \qquad (4.17)$$

$$\frac{\partial^4 M}{\partial x^4} = \rho A \frac{\partial^4 w}{\partial x^2 \partial t^2} \qquad (4.18)$$

$$\frac{\partial^2 M}{\partial x^2} - (e_0 a)^2 \frac{\partial^4 M}{\partial x^4} = -EI \frac{\partial^4 w}{\partial x^4} \qquad (4.19)$$

Substituting Eqs. (4.17) and (4.18) into (4.19), one derives the following equation of motion of a nanobeam as

$$\rho A \frac{\partial^2 w}{\partial t^2} - \rho A (e_0 a)^2 \frac{\partial^4 w}{\partial x^2 \partial t^2} + EI \frac{\partial^4 w}{\partial x^4} = 0 \qquad (4.20)$$

It is also found that the governing equation (4.20) is constructed by the one-dimensional nonlocal differential constitutive relation and classical equations. This accords with the basic derivation procedures of the nonlocal softening model. A similar governing equation was derived by Lim and his associates (Lim et al., 2010b). In this case, a simply-supported boundary condition is applied at both ends of the nanobeam, that is

$$w\big|_{x=0,L} = 0; \quad \frac{\partial^2 w}{\partial x^2}\bigg|_{x=0,L} = 0 \qquad (4.21)$$

Consider Eqs. (4.20) and (4.21), the following displacement form is assumed as

$$w_n(x,t) = W_n \sin\frac{n\pi x}{L} e^{i\omega_n t} \tag{4.22}$$

where $n = 1,2,3,\ldots$ and it satisfies the boundary conditions above. The general form of the transverse displacement can be obtained by superposing all the vibration modes and circular frequencies, given by

$$w(x,t) = \sum_{n=1}^{\infty} W_n \sin\frac{n\pi x}{L} e^{i\omega_n t} \tag{4.23}$$

Substituting the trial solution of Eq. (4.22) into Eq. (4.20) yields

$$\omega_n = \sqrt{\frac{EI}{\rho A} \frac{\left(\dfrac{n\pi}{L}\right)^4}{\left[1+\left(e_0 a\right)^2 \left(\dfrac{n\pi}{L}\right)^2\right]}} \tag{4.24}$$

To demonstrate the relationship between the circular frequency and the nonlocal scale parameter for a rectangular nanobeam, the following parameters are selected: $E=1.06$ TPa, $\rho=2250$ kg/m^3, and $L=10$ nm. The dimensions of the rectangular section are taken as $b=1.5$ nm, $h=0.34$ nm, $A=0.51$ nm^2, and $I=4.913\times10^{-3}$ nm^4. Relevent numerical results are presented in Fig. 4.2.
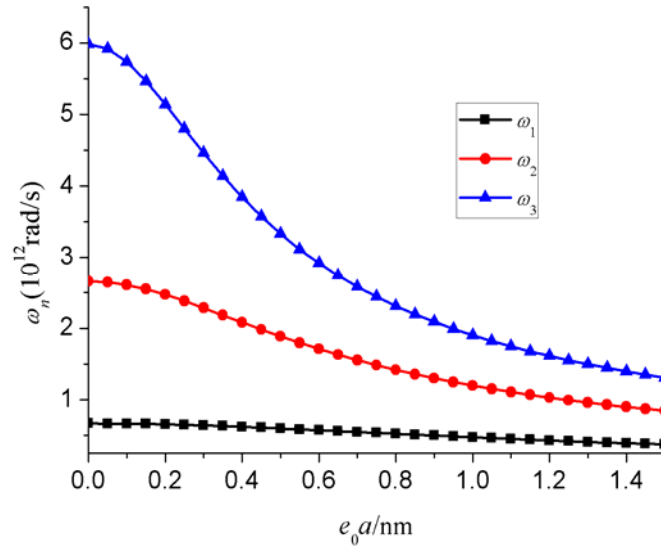
Fig. 4.2: Effect of the nonlocal scale parameter on the circular frequencies of a simply-supported nanobeam.

The pattern shown in Fig. 4.2 is similar to the axial vibration of nanorods in Fig. 4.1. In this case, the circular frequencies decrease with increasing the nonlocal scale parameter for a

simply-supported nanobeam. However, the slope of the frequency curves or the frequency decrease rate is different from that of a nanorod. The circular frequencies decrease rapidly at an early stage of increasing the nonlocal scale parameter from zero. After that, the frequency decrease rate slows down gradually. In Eq. (4.24), it seems that the nonlocal scale parameter may increase continuously in theory, similar to that of the axial vibration of nanorods. Nevertheless, it is difficult to understand why the nonlocal scale parameter can be chosen arbitrarily. What is the physical meaning of an infinite nonlocal scale parameter, and how to explain the principle for selection of the nonlocal scale parameter? We believe there is an upper bound for the nonlocal scale parameter in the vibration of nanorods and nanobeams but not shown in those examples. Therefore, we consider the free vibration of nanoplates in the next section, as there is no essential difference in the nonlocal softening dynamics of nanorods, nanobeams, and nanoplates.

Although the nonlocal dynamical behavior reveals the nano-structural dependence due to different structural properties, the mechanism of the nonlocal scale effect appeared in nanorods and nanobeams should coincide with that of nanoplates. This is because different nanostructures with the same material can be converted to each other. For example, a carbon nanotube and a graphene nano-ribbon can be produced from a graphene sheet as shown in Fig. 4.3, where the carbon nanotube, graphene nano-ribbon, and graphene sheet can be modeled as structures of a nanorod, a nanobeam, and a nanoplate, respectively. The nonlocal scale effect of such nanostructures should be qualitatively consistent with that of graphene sheet because the nonlocal scale effect is reflected by the nonlocal scale parameter $e_0 a$, which completely depends on the properties of specific materials.

In fact, we can explain the reason why the upper limit of the nonlocal scale parameter disappears in the previous examples. In the abovementioned calculations, it is convenient to insert Eq. (4.22) rather than the summation Eq. (4.23) into Eq. (4.20), resulting in a simple expression (4.24). If we consider the nonlocal differential constitutive relation (4.1) and transform it into the nonlocal differential equation for a bending moment, we can acquire the bending moment by solving the nonlocal differential equation. Then, substituting the nonlocal bending moment into the classical equation of motion yields

$$\rho A \frac{\partial^2 w}{\partial t^2} - \rho A (e_0 a)^2 \frac{\partial^4 w}{\partial x^2 \partial t^2} + EI \sum_{m=0}^{\infty} (e_0 a)^{2m} \frac{\partial^{2m+4} w}{\partial x^{2m+4}} = 0 \qquad (4.25)$$
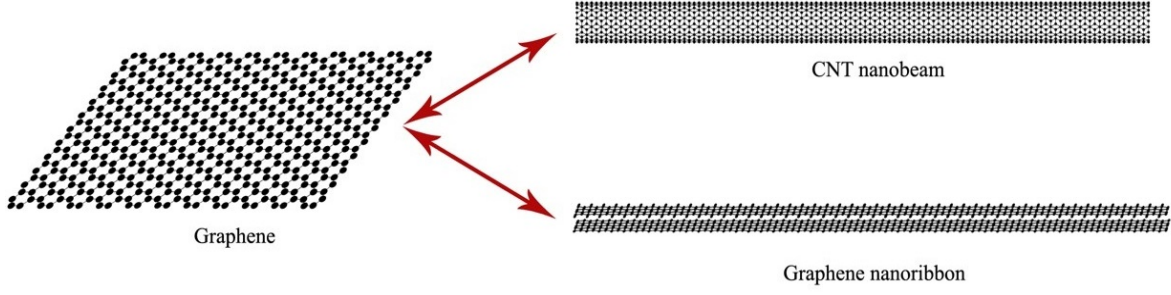
Fig. 4.3: Conversion between graphene sheet, carbon nanotube, and graphene nano-ribbon.

Equation (4.25) includes higher-order nonlocal terms, this is the exact version of the nonlocal governing equation for nanobeams. Some different results can be obtained from Eq. (4.25), and the upper limit of the nonlocal scale parameter may arise in the solution procedures. Similarly, the modified governing equation for the axial vibration of nanorods can be derived as

$$\rho\frac{\partial^2 u}{\partial t^2} - \rho\left(e_0 a\right)^2 \frac{\partial^4 u}{\partial x^2 \partial t^2} = E\sum_{m=0}^{\infty}\left(e_0 a\right)^{2m}\frac{\partial^{2m+2} u}{\partial x^{2m+2}} \tag{4.26}$$

4.3.3 Free Vibration of Nanoplates

In this section, we further consider the free vibration of nanoplates. As shown in Fig. 4.4, L_a, L_b, and h are length, width, and thickness of a nanoplate, respectively. Consider the nonlocal two-dimensional differential constitutive relations, one obtains

$$\sigma_{xx} - \left(e_0 a\right)^2 \nabla^2 \sigma_{xx} = \frac{E}{1-\mu^2}\left(\varepsilon_{xx} + \mu\varepsilon_{yy}\right)$$

$$\sigma_{yy} - \left(e_0 a\right)^2 \nabla^2 \sigma_{yy} = \frac{E}{1-\mu^2}\left(\varepsilon_{yy} + \mu\varepsilon_{xx}\right) \tag{4.27}$$

$$\tau_{xy} - \left(e_0 a\right)^2 \nabla^2 \tau_{xy} = \frac{E}{2\left(1+\mu\right)}\gamma_{xy}$$

where $\sigma_{ii}\left(i = x, y\right)$ and $\tau_{ij}\left(i, j = x, y\right)$ are stresses, $\varepsilon_{ii}\left(i = x, y\right)$ and $\gamma_{ij}\left(i, j = x, y\right)$ are strains, and μ is the Poisson's ratio.
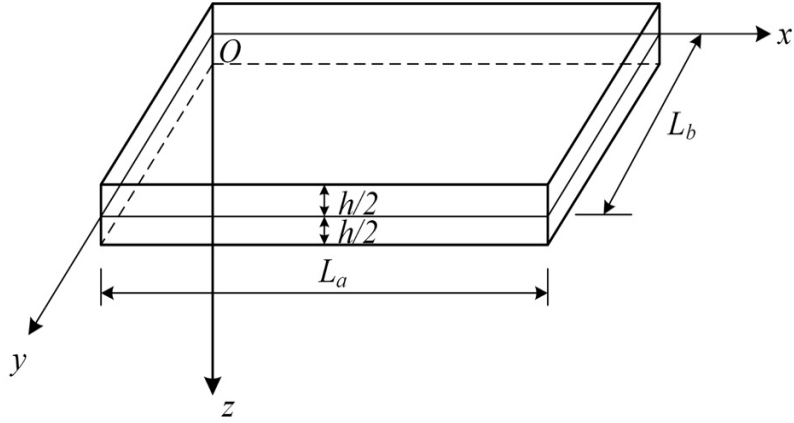
Fig. 4.4: Schematic of a simple nanoplate.

According to the geometric equations of a plane problem in classical, we can derive the nonlocal constitutive equations for nanoplates by ignoring the in-plane displacements at the neutral plane in x and y directions, as follows

$$\sigma_{xx} - \left(e_0 a\right)^2 \nabla^2 \sigma_{xx} = \frac{-Ez}{1-\mu^2}\left(\frac{\partial^2 w}{\partial x^2} + \mu \frac{\partial^2 w}{\partial y^2}\right)$$

$$\sigma_{yy} - \left(e_0 a\right)^2 \nabla^2 \sigma_{yy} = \frac{-Ez}{1-\mu^2}\left(\frac{\partial^2 w}{\partial y^2} + \mu \frac{\partial^2 w}{\partial x^2}\right) \tag{4.28}$$

$$\tau_{xy} - \left(e_0 a\right)^2 \nabla^2 \tau_{xy} = \frac{-Ez}{1+\mu}\frac{\partial^2 w}{\partial x \partial y}$$

Besides, the correlation between the nonlocal bending moment and the displacement can be expressed as (Murmu and Pradhan, 2009b)

$$M_{xx} - \left(e_0 a\right)^2 \nabla^2 M_{xx} = -D\left(\frac{\partial^2 w}{\partial x^2} + \mu \frac{\partial^2 w}{\partial y^2}\right)$$

$$M_{yy} - \left(e_0 a\right)^2 \nabla^2 M_{yy} = -D\left(\frac{\partial^2 w}{\partial y^2} + \mu \frac{\partial^2 w}{\partial x^2}\right) \tag{4.29}$$

$$M_{xy} - \left(e_0 a\right)^2 \nabla^2 M_{xy} = -D\left(1-\mu\right)\frac{\partial^2 w}{\partial x \partial y}$$

where $D = Eh^3/12(1-\mu^2)$ is the bending rigidity defined in classical elasticity mechanics. The nonlocal bending moment relations in Eq. (4.29) can be reducible to the classical counterparts when the nonlocal scale parameter is set to zero. The components of the nonlocal bending moment per unit length can be obtained by solving Eq. (4.29), given by

$$M_{xx} = -D \sum_{k=0}^{\infty} (e_0 a)^{2k} \nabla^{2k} \left(\frac{\partial^2 w}{\partial x^2} + \mu \frac{\partial^2 w}{\partial y^2} \right)$$

$$M_{yy} = -D \sum_{k=0}^{\infty} (e_0 a)^{2k} \nabla^{2k} \left(\frac{\partial^2 w}{\partial y^2} + \mu \frac{\partial^2 w}{\partial x^2} \right) \qquad (4.30)$$

$$M_{xy} = -D(1-\mu) \sum_{k=0}^{\infty} (e_0 a)^{2k} \nabla^{2k} \frac{\partial^2 w}{\partial x \partial y}$$

Employing the classical theory of elasticity, the equilibrium equation for a thin-plate in terms of the internal force (bending moment) can be expressed as

$$\frac{\partial^2 M_{xx}}{\partial x^2} + 2 \frac{\partial^2 M_{xy}}{\partial x \partial y} + \frac{\partial^2 M_{yy}}{\partial y^2} + q = 0 \qquad (4.31)$$

where q is the transverse load per unit area. Substituting Eq. (4.30) into Eq. (4.31) yields the nonlocal governing differential equation for the free vibration of nanoplates (Liu et al., 2016)

$$D \sum_{k=0}^{N} (e_0 a)^{2k} \nabla^{2k} \left(\frac{\partial^4 w}{\partial x^4} + 2 \frac{\partial^4 w}{\partial x^2 \partial y^2} + \frac{\partial^4 w}{\partial y^4} \right) = \frac{1}{12} \rho h^3 \left(\frac{\partial^4 w}{\partial x^2 \partial t^2} + \frac{\partial^4 w}{\partial y^2 \partial t^2} \right) - \rho h \frac{\partial^2 w}{\partial t^2} \qquad (4.32)$$

where $N=1,2,3,\ldots,\infty$. Note that inertia forces are contained in the transverse load by considering the translation and rotation motions. Besides, only the first few terms of the infinite series in Eq. (4.32) are taken into account in most previous studies (e.g., Lim, 2010a; Anjomshoa et al., 2014), other higher-order terms can be neglected. It is not clear whether the higher-order items should be abandoned. Unlike the previous studies, we consider all the higher-order terms of Eq. (4.32) in the present work. For simplicity, a simply-supported condition is applied to all plate edges as an example, we can write the boundary conditions as

$$w\big|_{x=0,\,L_a} = 0; \quad \frac{\partial^2 w}{\partial x^2}\bigg|_{x=0,\,L_a} = 0$$

$$\qquad (4.33)$$

$$w\big|_{y=0,\,L_b} = 0; \quad \frac{\partial^2 w}{\partial y^2}\bigg|_{y=0,\,L_b} = 0$$

Assume that the displacement of a nanoplate is expressed as

$$w(x,y,t) = W_{mn} \sin \frac{m\pi x}{L_a} \sin \frac{n\pi y}{L_b} e^{i\omega_{mn}t} \qquad (4.34)$$

where m, $n=1,2,3,\ldots$ are half-wave numbers. It is obvious the assumed displacement function can satisfy the boundary conditions in Eq. (4.33).

Making use of the Rayleigh-Ritz method (Thorby, 2008), the circular frequencies for the free vibration of simply-supported nanoplates can be obtained as

$$\omega_{mn} = \sqrt{\dfrac{D\left\{\displaystyle\sum_{k=0}^{N}(-1)^k (e_0 a)^{2k}\left[\left(\dfrac{m\pi}{L_a}\right)^2+\left(\dfrac{n\pi}{L_b}\right)^2\right]^k\right\}\left[\left(\dfrac{m\pi}{L_a}\right)^2+\left(\dfrac{n\pi}{L_b}\right)^2\right]^2}{\dfrac{\rho h^3}{12}\left[\left(\dfrac{m\pi}{L_a}\right)^2+\left(\dfrac{n\pi}{L_b}\right)^2\right]+\rho h}}$$

(4.35)

We found that there is an upper limit of the nonlocal scale parameter in the free vibration of nanoplates. For this purpose, the infinite series in Eq. (4.35) is considered gradually. When $N=0$, the nonlocal circular frequencies become the classical counterparts, and it is independent of the nonlocal scale parameter. When $N=1$, it must satisfy

$$1-(e_0 a)^2\left[\left(\dfrac{m\pi}{L_a}\right)^2+\left(\dfrac{n\pi}{L_b}\right)^2\right] > 0$$

(4.36)

Hence, one obtains

$$e_0 a < \sqrt{\dfrac{L_a^2 L_b^2}{(m\pi L_b)^2+(n\pi L_a)^2}}$$

(4.37)

When $N=2$, we get

$$1-(e_0 a)^2\left[\left(\dfrac{m\pi}{L_a}\right)^2+\left(\dfrac{n\pi}{L_b}\right)^2\right]+(e_0 a)^4\left[\left(\dfrac{m\pi}{L_a}\right)^2+\left(\dfrac{n\pi}{L_b}\right)^2\right]^2 \geq 0$$

(4.38)

The admissibility of Eq. (4.38) is satisfied naturally for selecting the nonlocal scale parameter arbitrarily. Furthermore, it is easily proved that the requirement of the nonlocal scale parameter in the case of $N=2s+1$ is identical to the case with $N=1$, while the case of $N=2s$ is the same as $N=2$, i.e., no upper limit of $e_0 a$ is required when $N=2s$ in Eq. (4.35). It seems that the required condition of the nonlocal scale parameter is only summarized in Eq. (4.37), as Eq. (4.38) makes no demand. Under this circumstance, the ratio of the geometrical sequence in the brace of Eq. (4.35) is less than 1. Consequently, the circular frequencies can be written as

$$\omega_{mn} = \sqrt{\dfrac{D\left[\left(\dfrac{m\pi}{L_a}\right)^2+\left(\dfrac{n\pi}{L_b}\right)^2\right]^2}{\left\{\dfrac{\rho h^3}{12}\left[\left(\dfrac{m\pi}{L_a}\right)^2+\left(\dfrac{n\pi}{L_b}\right)^2\right]+\rho h\right\}\left\{1+(e_0 a)^2\left[\left(\dfrac{m\pi}{L_a}\right)^2+\left(\dfrac{n\pi}{L_b}\right)^2\right]\right\}}}$$

(4.39)

According to Eq. (4.39), the nonlocal scale effect on the free vibration of nanoplates is plotted in Fig. 4.5. Note that the upper limit of the nonlocal scale parameter can be calculated from Eq. (4.37) with the following parameters: $L_a=L_b=10$ nm, $h=0.34$ nm, $E=1.06$ TPa, $\mu=0.25$ and $\rho=2250$ kg/m^3 (Shen et al., 2012b). It shows that the circular frequencies decrease slowly at the beginning of increasing the nonlocal scale parameter. When the nonlocal scale parameter arrives at a certain value, the decrease rate of the circular frequency curves becomes faster. There is a common upper limit for the nonlocal scale parameter in Fig. 4.5 and it is the minimum one determined from Eq. (4.37).

In Fig. 4.5, the analysis is not fully correct because the nonlocal scale parameter in Eq. (4.38) cannot be chosen freely. The tenability of the inequality (4.38) is always valid with the arbitrary parameter e_0a mathematically. There is a sudden increase for the circular frequencies caused by arbitrarily choosing the nonlocal scale parameter, thereby causing a contradictory to the nonlocal softening model. We can explain it as follows. By selecting different terms in the infinite series of Eq. (4.35), we show some numerical examples for the effect of the nonlocal scale parameter on vibration frequencies, where the parameters (Shen et al., 2012b) are still adopted. It is noted that the Galerkin method was used to solve the natural frequencies of nanoplates in (Shen et al., 2012b). When different terms of the infinite series are taken (e.g., $N=1$, 2, and 20), the first four order modes are presented in Fig. 4.6, Fig. 4.7 and Table 4.1. As mentioned, there are two nonlocal elasticity models. In this study, we use the nonlocal softening model, the equivalent stiffness of nanostructures should decrease as compared with the stiffness predicted directly by the classical continuum theory. In other words, the vibration frequencies based on the nonlocal theory are smaller than that of the classical elasticity theory.

Using Eq. (4.37) and the parameters listed above (Shen et al., 2012b), we can calculate the limit values of the nonlocal scale parameter e_0a as nm for $m=n=1$ (ω_{11}), nm for $m=1$ and $n=2$, or $m=2$ and $n=1$ (ω_{12} or ω_{21}), nm for $m=n=2$ (ω_{22}), respectively. Hence, the common upper limit of the nonlocal scale parameter for the first four order modes with $N=1$ is nm. Accordingly, the effect of the nonlocal scale parameter on the first four order modes is shown in Fig. 4.6 for $N=1$, where the upper limit of the nonlocal scale parameter is utilized for the range of the horizontal axis. It is seen that the nonlocal circular frequencies ($e_0a>0$) are smaller than of the classical ones ($e_0a=0$). This is consistent with the viewpoint of the nonlocal softening model. As aforementioned, the case of odd number terms $N=2s+1$ is the same as $N=1$. In the present

work, we only consider the first four order modes, which can reflect some fundamental and remarkable findings.
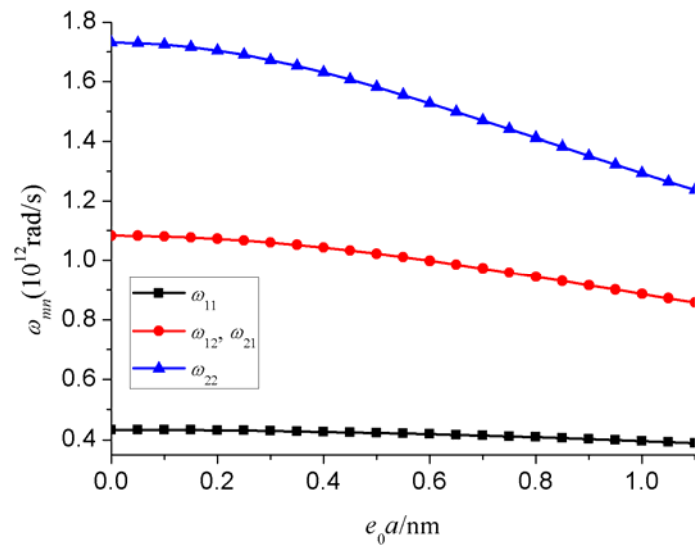
Fig. 4.5: Effect of the nonlocal scale parameter on the circular frequencies of a simply-supported nanoplate.
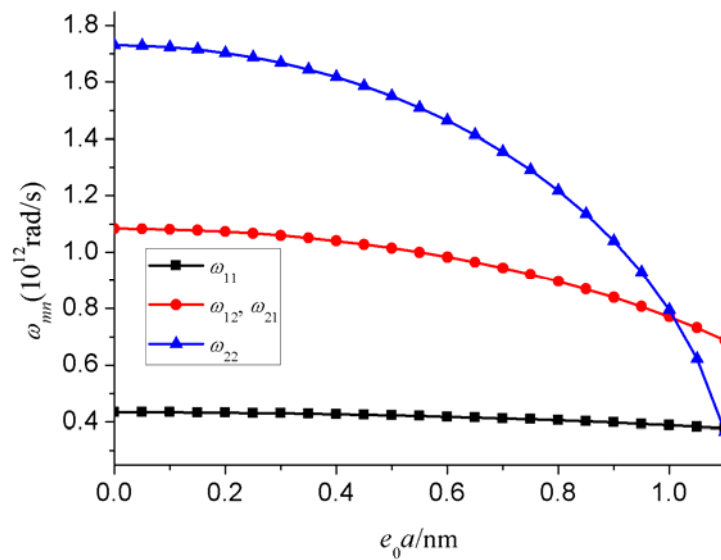
Fig. 4.6: Variation of circular frequencies with respect to nonlocal scale parameter for $N=1$.

Unlike the cases of $N=1$ and $N=2s+1$, the calculation results of $N=2$ show that the nonlocal circular frequencies decrease with increasing the nonlocal scale parameter, and so the nonlocal frequencies are smaller than the corresponding classical counterparts involving $e_0a=0$ when the nonlocal scale parameter is not too large, as illustrated in Fig. 4.7. When the nonlocal scale parameter exceeds a certain critical value, a reversed relationship between the circular frequency and the nonlocal scale parameter occurs, i.e., the nonlocal circular frequencies increase with an increase in the nonlocal scale parameter, as illustrated in Fig. 4.7(a) where only ω_{11} with a relatively larger range of nonlocal scale parameter is taken as an example. Obviously, it opposes the mechanism of the nonlocal softening model adopted in this work. Consequently, the upper limit of the nonlocal scale parameter can be determined accordingly, that is, the critical value of the nonlocal scale parameter that causes an opposite performance of the circular frequencies is the upper limit of that nonlocal scale parameter.

(a)

(b)

(c)
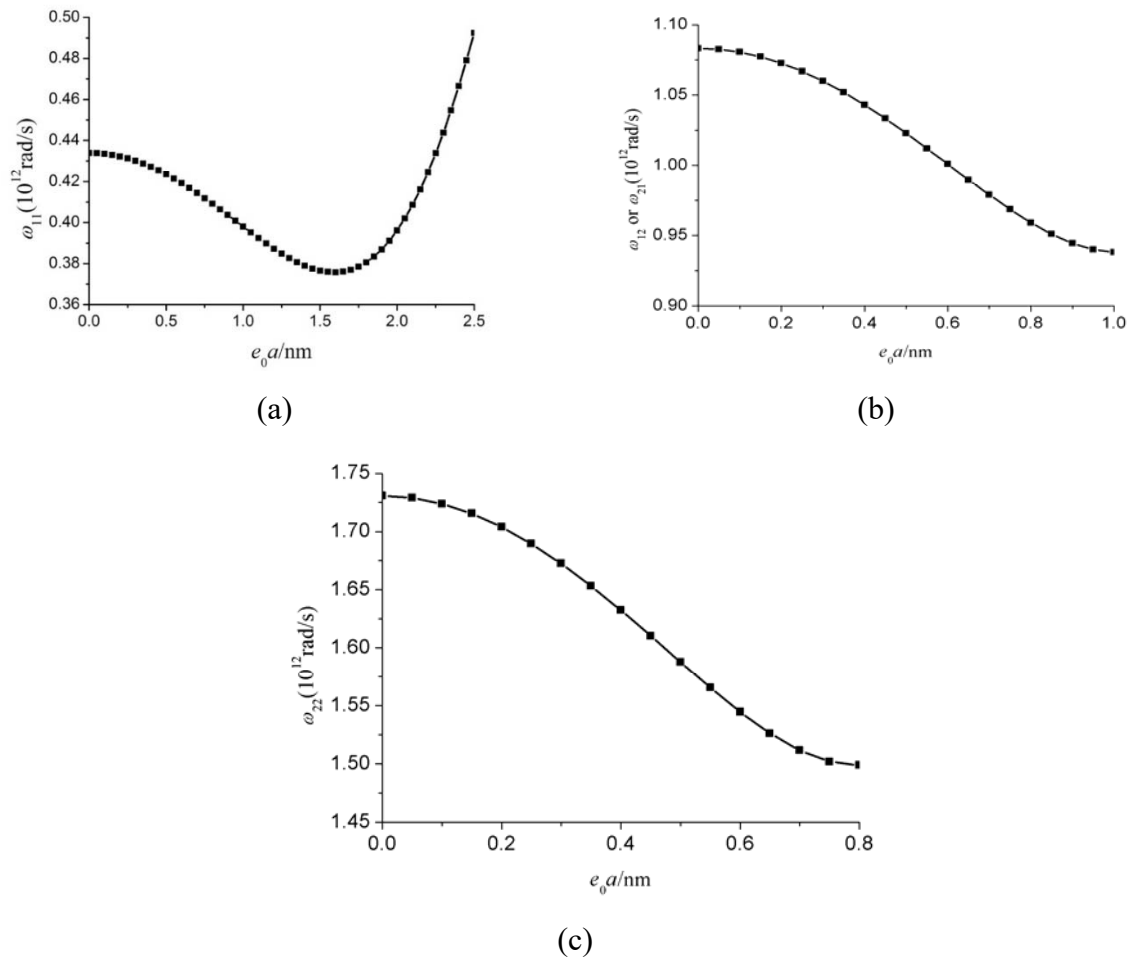
Fig. 4.7: Variation of circular frequencies with respect to the nonlocal scale parameter for $N=2$.

Table 4.1: Variation of circular frequencies with respect to the nonlocal scale parameter for $N=20$.

e_0a (nm)	ω_{11} ($\times 10^{12}$ rad/s)	ω_{12} or ω_{21} ($\times 10^{12}$ rad/s)	ω_{22} ($\times 10^{12}$ rad/s)
0	0.43389	1.08319	1.73065
0.2	0.43219	1.07265	1.70395
0.4	0.42720	1.04280	1.63071
0.6	0.41925	0.99815	1.52716
0.8	0.40884	0.94429	1.41057
1.0	0.39652	0.88635	1.29822
1.2	0.38288	0.82850	4.70856
1.4	0.36843	0.94479	106.27974
1.6	0.35364	8.40973	1611.47657
1.8	0.33887	92.76365	17616.03573
2.0	0.32548	792.50489	148927.27052
2.2	0.36496	5494.30464	1.02349×10^6

Although the nonlocal scale parameter seems to be chosen freely when $N=2$ from Eq. (4.38), the upper limits of the nonlocal scale parameter in the first four order modes should be 1.6 nm, 1.0 nm, 0.8 nm, respectively, in Figs. 4.7(a)–(c), in order to confirm the physical implication of the nonlocal softening phenomenon. Hence the common upper limit of the nonlocal scale parameter in these cases is 0.8 nm. In addition, the nonlocal material parameter e_0 can also be determined by considering the magnitude of the internal characteristic length a. For a carbon material (the nanoplate model corresponds to a graphene sheet), $a=0.142$ nm, and hence $e_0=5.63$ is obtained. Because the actual value is unknown, e_0 was usually assumed as a range of 0~14 (Murmu and Pradhan, 2009c; Liang and Han, 2014) or 0~19 (Duan et al., 2007) in numerical examples. The present value $e_0=5.63$ falls within these intervals.

In Table 4.1, the results for $N=20$ are presented. The first four order modes decrease with increasing the nonlocal scale parameter first, but the trend changes and the circular frequencies increase dramatically. For example, increasing the nonlocal scale parameter from 1.0 nm to 2.2 nm, the first four order modes surge from 0.14 THz ($\omega_{12} = 0.88635 \times 10^{12}$ rad/s) and 0.21 THz ($\omega_{22} = 1.29822 \times 10^{12}$ rad/s) to 874.45 THz ($\omega_{12} = 5494.30464 \times 10^{12}$ rad/s) and even 1.63×10^5 THz ($\omega_{22} = 1.02349 \times 10^{18}$ rad/s), respectively. There is an enormous change in the order of magnitude of circular frequencies inconceivably. On one hand, the nonlocal softening model requires the reduction of the frequency or the stiffness. On the other hand, it is difficult to

explain the great leap of circular frequencies from a physical perspective. Therefore, the common upper limit of the nonlocal scale parameter for the first four order modes is 1.0 nm when N=20. A similar conclusion can be achieved for even number terms N=2s. Although specific values of the upper limit may be different in even numbers, the change is relatively small. That means the upper limit of the scale parameter e_0a or the material parameter e_0 is related to the selected number of terms N and the frequency orders m and n, but such effects do not affect the qualitative conclusion in this study.

Having determined the upper limit of the scale parameter, we conclude that the circular frequencies would reduce with increasing the scale parameter, which coincides with the point of the nonlocal softening model. In addition, the degree of change is not identical for different modes. For example, with an increase of e_0a from 0 to 0.8 nm in Table 4.1, the decrease percentages are 5.77%, 12.82%, and 18.49% for ω_{11}, ω_{12} (ω_{21}), and ω_{22}, respectively. Consequently, the extent of variation becomes dominant for higher modes. In fact, the higher circular frequencies correspond to shorter wavelengths, resulting in higher energy. The energy loss is more significant for higher energy in vibration due to various physical factors, including both nonlocal and classical contributions. Hence, the nonlocal scale parameter makes the higher circular frequencies decline more obviously.

We also calculate the natural frequencies with N=0, which are f_{11}=433.89/2π GHz, f_{21}=f_{12}=1083.19/2π GHz, and f_{22}=1730.65/2π GHz. These are exactly the classical results for the free vibration of simply supported plates without a nonlocal scale effect using the parameters listed above. They are in good agreement with the previous studies (Shen et al., 2012b; Pradhan and Kumar, 2011). However, there are no research studies concerned with the upper limit of the nonlocal scale parameter previously, and the similar form of Eq. (4.39) was derived and utilized in most studies. As indicated earlier, Eq. (4.39) is actually not correct because the upper limit of the nonlocal scale parameter is not considered and involved appropriately. Besides, the classical natural frequencies f_{mn} are identical to the results under the condition of e_0a=0 in Fig. 4.6, Fig. 4.7 and Table 4.1. This confirms the present models and calculations.

4.4 Results and Discussion

In the previous section, an upper bound of the nonlocal scale parameter is obtained. Consider various nano-based structures, the nonlocal scale parameter indicates different effects

on structural dynamical behavior. Hence, it appears the structure-dependent property of nonlocal dynamics. For the axial vibration of nanorods and the transverse vibration of nanobeams, the circular frequencies always decrease with increasing the nonlocal scale parameter, but the decrease rates are different. While for the free vibration of nanoplates, the frequencies decrease first and then increase abruptly with increasing the nonlocal scale parameter. The behavior of nonlocal dynamics may be different for different nanostructures, but the trend of the nonlocal scale effect must be the same due to the same concept of the nonlocal theory. Therefore, there exists an upper bound of the nonlocal scale parameter according to the physical implication of the nonlocal softening model. This upper limit should be common for various nano-based structures because the nonlocal scale effect in nano-mechanics is identical. We can take 0~0.8 nm as a range of e_0a while studying the nonlocal scale effect in the dynamical behavior of nanostructures. The physical meaning of this range is that one has to account for the scale effect if the structural external characteristic length scale is at the same level as the nonlocal scale parameter, i.e., $l \approx Ne_0a \approx 0.8N$ where $N<10$.

The present analysis can be confirmed by the previous studies, Lim (2010b), Li (2014), and Liu et al. (2016) derived the nonlocal stress from the nonlocal differential constitutive relation in Eq. (4.1) for nanobeams, nanorods, and nanoplates, respectively. The unified form of solutions can be written as $\mathbf{t} = \mathbf{C} : \sum_{n=0}^{\infty} (e_0a)^{2n} \nabla^{2n} \boldsymbol{\varepsilon}$, where $\mathbf{C}$ is the elastic coefficient tensor and $\boldsymbol{\varepsilon}$ is the strain tensor. The boundness of the nonlocal scale parameter can also be implied from the solution in order to ensure the convergence of the nonlocal stress. Wang et al. (2011) concluded that the nonlocal scale effect is related to the surface effect for the vibration of nanoplates. The wavelengths in x and y directions are $\lambda_x = 2L_a/m$ and $\lambda_y = 2L_b/n$, respectively. An equivalent wavelength is defined as $\lambda = \lambda_x \eta / \sqrt{\eta^2 + 1}$ where $\eta = \lambda_y / \lambda_x$. After that, a critical equivalent wavelength $\lambda_{cr} = 19.12(e_0a)$ for a significant nonlocal scale effect is determined. Because the equivalent wavelength cannot be lower than its critical value, i.e. $\lambda \geq \lambda_{cr}$, otherwise the scale effect is so weak that one can ignore it. The range of e_0a is in the order of magnitude 0~0.74 nm for the fundamental frequency via $\lambda \geq \lambda_{cr}$. Although the nonlocal scale parameter was not involved in the work by Wang et al. (2011), the upper limit of the nonlocal scale parameter derived from the work is basically in accordance with the results suggested in the present study.

On the other hand, Liang and Han (2014) also investigated the nonlocal scale parameter for graphene sheets and proposed a formulation $(e_0 a)^2 = R^2/8$ where R is the radius of a nonlocal influence domain. Until recently, the area of the nonlocal influence domain is still not clear. Because the nonlocal scale effect stems from the long-range interactions between atoms, we can consider how long the distance from other points to a specified point (i.e. the center of the nonlocal influence circle) is, with significant long-range interactions. Edelen (1976) pointed out that the long-range interaction for electrostatic forces between non-adjacent atoms in crystal materials can arrive at the order of magnitude of tenfold lattice distance. At a nano-scale, such an acting distance can be considered to be of a long-range. If the radius of a nonlocal influence circle is selected as $R=15a$, this is no longer valid for the nonlocal long-range interaction as the radius exceeds $15a$. Hence, we can deduce that the range of $e_0 a$ is in the order of magnitude 0~0.75 nm. This result supports the claim of this study again.

Moreover, Wang et al. (2008) evaluated the nonlocal scale parameter for achiral and chiral single-walled carbon nanotubes (SWCNTs). The value of $e_0 a=0.7$ *nm* was recommended for the application of the nonlocal theory in the estimation of the stiffness of CNTs. Such a result was verified through comparison studies using molecular dynamics (MD). Ansari et al. (2011) further investigated the nonlocal scale parameter for double-walled carbon nanotubes (DWCNTs) with different aspect ratios and boundary conditions. The solutions of a nonlocal shell model are consistent with the results of MD simulations, in terms of predicting the vibration behavior of various armchair and zigzag DWCNTs. Specifically, the range of $e_0 a$ (about 0~0.92 nm) was proposed for different types of chirality and boundary conditions. This further verify the correctness of the present study.

4.5 Concluding Remarks

In this study, we discussed the approach to determine the upper bound of the nonlocal scale parameter, which is used to account for the influence of material length scales in the study of mechanics of solid structures at micro-/nano-scales. The size-dependence of nonlocal dynamic behavior is demonstrated. According to the present analysis, we can take 0~0.8 nm as a range of $e_0 a$ for studying the nonlocal scale effect in the dynamical behavior of nanostructures. The results are compared with the available solutions to confirm its validity. The puzzling question is solved accordingly, and the present work provides a basis for the choice of a nonlocal scale range when studying the mechanical properties of nanostructures by using the nonlocal elasticity theory. Building upon the nonlocal partial-differential constitutive framework, three

nanostructure models are investigated herein, i.e., the axial vibration of nanorods, transverse vibration of nanobeams, and free vibration of nanoplates. The physical meaning of the scale upper limit is explained through these illustrative cases and it is conducive to the estimation of the structural external characteristic scale at which the nonlocal scale effect should be considered. Compared with the previous studies, the present work is simple and easy for the determination of a size-dependent range in micro-/nano-scale structures.

Chapter 5

LARGE-AMPLITUDE OSCILLATION OF A TRIPLE-WELL NON-NATURAL SYSTEM

5.1 Introduction

Making use of the tri-stable mechanism, a new electromagnetic-triboelectric energy harvesting technique is proposed in this work. Prior to introducing this new energy harvester, we will first consider a triple-well non-natural system that exhibits heteroclinic and homoclinic orbits under different equilibrium states in this chapter. Particular emphasis on this problem can gain deeper insights into the tri-stable nonlinear behavior. Besides, many mathematical models in mechanical and structural engineering applications can give rise to this nonlinear problem. In qualitative analysis, the fixed points and their trajectories of the nonlinear system in response to changes in the governing parameters are studied. In addition, the NHB method (Wu et al., 2006) is also employed to solve the nonlinear problem under symmetric and asymmetric oscillations. The structure of this chapter is organized as follows. Section 5.2 describes the triple-well non-natural system. The qualitative analysis and qualitative analysis are presented in Section 5.3 and section 5.4, respectively. Section 5.5 shows the accuracy of the present solutions for the system in contrast to the results obtained from the Runge-Kutta method. Finally, the major findings of the present work are summarized in Section 5.6.

5.2 Triple-well Non-natural System

Consider the following triple-well nonlinear problem

$$E(x)\frac{d^2x}{dt^2} + F(x)\left(\frac{dx}{dt}\right)^2 + G(x) = 0 \tag{5.1}$$

with the initial conditions

$$x(0) = A, \qquad \frac{dx}{dt}(0) = 0 \tag{5.2}$$

where $E(x) = 1 + \alpha_1 x^2$, $F(x) = \alpha_1 x$ and $G(x) = \alpha_2 x + \alpha_3 x^3 + \alpha_4 x^5$. x and t are dimensionless displacement and time variables, respectively. The governing parameters α_1, α_2, α_3 and α_4 in the functions $E(x)$, $F(x)$ and $G(x)$ are real constants. This system is

governed by a quadratic dependence term on the velocity (Pandey et al., 2017) and an odd-parity restoring force having cubic-quintic nonlinearities.

Integrating Eq. (5.1) yields

$$T + V = E \tag{5.3}$$

in which

$$T = \frac{1}{2}\left(1 + \alpha_1 x^2\right) y^2 \text{ and } V = \frac{1}{2}\alpha_2 x^2 + \frac{1}{4}\alpha_3 x^4 + \frac{1}{6}\alpha_4 x^6 \tag{5.4}$$

where $y = dx/dt$. In Eq. (5.3), the first term on the left-hand side is the kinetic energy and the second one is the potential energy. The constant value E is the total energy level that can be determined by the initial conditions in Eq. (5.2). Because the kinetic energy of this system is not purely a quadratic function of the velocity, it is thus called a "*non-natural*" system (Meirovitch, 1970; Nayfeh and Mook, 1995).

In Eq. (5.1), there is a quadratic dependence term on the velocity, but the nonlinear problem is a conservative system. A simple argument to show the existence of periodic motions with the presence of a quadratic dependence term on the velocity in dynamic problems is provided below (Lai and Chow, 2012). Consider a simple oscillator

$$\frac{d^2 x}{dt^2} + \varepsilon_1 \left(\frac{dx}{dt}\right)^2 + \varepsilon_2 x = 0 \tag{5.5}$$

where ε_1 and ε_2 are real parameters. Multiplying Eq. (5.5) by $y = \left(dx/dt\right)$ and integrating from 0 to t yield

$$\left[y^2 + \varepsilon_2 x^2\right]_0^t = -2\varepsilon_1 \int_0^t y^3 dt \tag{5.6}$$

If a periodic mode exists and t is the period, then the left-hand side of Eq. (5.6) is zero. For a cubic power on the right-hand side, it is plausible that the integral may vanish to form a close trajectory in the phase-space plane (x, y). However, the integral may not vanish for an even power of y. This is consistent with the fact that a classical damped harmonic oscillator (e.g., $d^2 x/dt^2 + c\left(dx/dt\right) + \omega_0^2 x = 0$) does not have a periodic motion.

There is always an inherent mechanism to provoke bifurcations and instabilities that can induce unpredictable responses in nonlinear dynamics. Generally, a local bifurcation would occur when there is a change of governing parameters and initial conditions, leading to the

instability of equilibrium states. Hence, various combinations of the governing parameters in Eq. (5.1) will generate diverse results. It is found that there exist both heteroclinic and homoclinic orbits under various equilibrium states. In a dynamical system, a heteroclinic orbit is a trajectory path in phase space where joins two different stable equilibrium points, while a homoclinic orbit is a trajectory path in phase space where connects a saddle point to itself, as shown in Fig. 5.1.
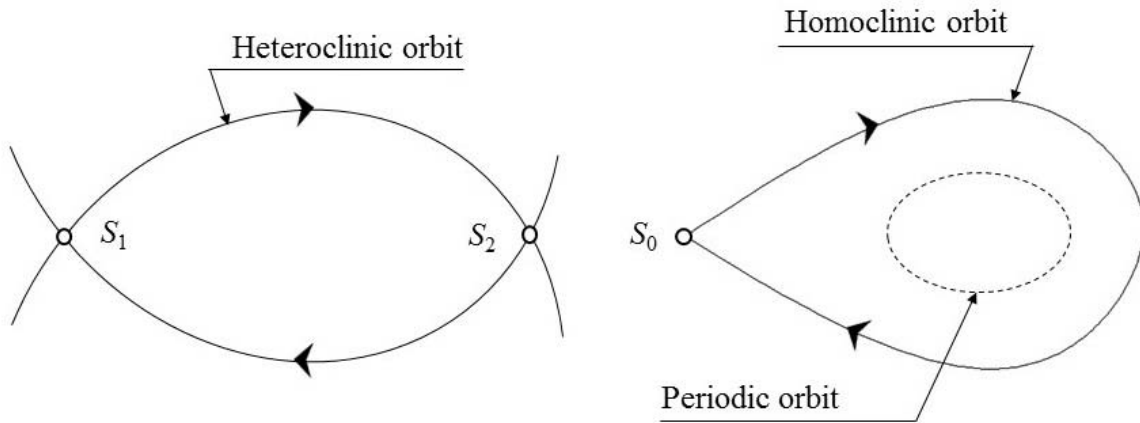
Fig. 5.1: Trajectories of heteroclinic and homoclinic orbits (Aslanov, 2017).

As aforementioned, various mathematical models in mechanical and structural engineering applications can give rise to the system (5.1). One example is the large-amplitude vibration of stringer cylindrical shells (Bayat and Pakar, 2013; Bayat et al., 2014; Pakar and Bayat, 2015), in which the studied parameters are restricted to all positive values $\left(\alpha_i > 0, \ i = 1 - 4 \right)$. Stringer cylindrical shells are tubular structures with supporting ribs situated along the length uniformly with a constant distance between them. In this case, there is only a single potential well in the system.

Other examples in engineering and physical models where the system (5.1) arises are:

- Absence of quadratic velocity and quintic nonlinearity (i.e., $\alpha_1 = 0$, $\alpha_2 \neq 0$, $\alpha_3 \neq 0$ and $\alpha_4 = 0$): this is a simple Duffing equation that can model the nonlinear vibration of beams, panels, and fluid-conveying pipes (Rao, 2003; Hui et al., 2011; Tang and Yang, 2018), the dynamic buckling problem of a drill string in a horizontal well (Sun et al., 2015) and the nonlinear cantilevered piezoelectric energy harvesters (Daqaq et al., 2014; Vakakis et al., 2009; Harne and Wang, 2013);

- Absence of quadratic velocity (i.e., $\alpha_1 = 0$, $\alpha_2 \neq 0$, $\alpha_3 \neq 0$ and $\alpha_4 \neq 0$): the problem becomes a cubic-quintic Duffing equation that can model the nonlinear dynamics of a slender elastica (Lenci et al., 1999), the large-amplitude vibration of a restrained uniform beam carrying intermediate lumped mass (Hamdan and Shhabaneh, 1997) and a rotating pendulum system as vibration absorbers and fly-ball governors (Lai et al., 2011);

- Absence of quintic nonlinearity (i.e., $\alpha_1 \neq 0$, $\alpha_2 \neq 0$, $\alpha_3 \neq 0$ and $\alpha_4 = 0$): the equation can be used to model the nonlinear dynamics of cantilever beams, flexible rotating beams and tapered beams (Hamdan and Dado, 1997; Jarrar and Hamdan, 2007; Guo and Zhang, 2016); and

- Absence of cubic and quintic nonlinear terms (i.e., $\alpha_1 \neq 0$, $\alpha_2 \neq 0$, $\alpha_3 = 0$ and $\alpha_4 = 0$): the equation can be used to model a physical particle on a rotating parabola (Nayfeh and Mook, 1995; Wu et al., 2003) and a non-polynomial oscillator (Mohanasubha and Senthilvelan, 2017).

Special cases of Eq. (5.1) have been treated in the literature, but the overall version of Eq. (5.1) has not yet been investigated. In Eq. (5.1), the pattern of equilibrium points is not related to the value of the parameter α_1, as there are no practical applications for $\alpha_1 < 0$. In Eq. (5.1), we only consider $\alpha_1 > 0$, $\alpha_2 \neq 0$, $\alpha_3 \neq 0$ and $\alpha_4 \neq 0$, including negative linear stiffness and cubic and quintic nonlinearities.

To establish a firm understanding of the dynamical behavior of the nonlinear system, a qualitative analysis is employed to discuss the pattern of equilibrium points in Section 5.3. The nature of each equilibrium state is determined due to the influence of the governing parameters. In Section 5.4, a quantitative analysis is presented to construct analytical approximate solutions for periodic motions around each stable equilibrium point by means of the NHB method. In Section 5.5, several cases of Eq. (5.1) with different parameters are presented to illustrate the accuracy and effectiveness of the NHB method. Finally, the key findings of this work are concluded in the last section.

5.3 Qualitative Analysis

This section aims to classify the triple-well nonlinear system in terms of their equilibria and stabilities and to provide solutions for various classifications of the system. Consider the following equation

$$\frac{dV(x_i)}{dx} = \alpha_2 x_i + \alpha_3 x_i^3 + \alpha_4 x_i^5 = 0 \tag{5.7}$$

and the stability of the equilibrium points can be determined by examining

$$\frac{d^2V(x_i)}{dx^2} = \alpha_2 + 3\alpha_3 x_i^2 + 5\alpha_4 x_i^4 \tag{5.8}$$

at the equilibrium points. The pattern of the roots of Eq. (5.7) varies with different values of the parameters. Table 5.1 lists all the cases according to different values of the parameters. The number of equilibrium points and the orbital characteristics around centers are also determined. Note that these cases correspond to three patterns of the roots, i.e., 1, 3, or 5 equilibrium points.

For cases that have only one equilibrium point, there are two situations. In cases 1 and 3, the system has a minimum potential energy level at where is a center. While in case 8, the system reaches a maximum potential energy level at where is a saddle point. The possible trajectories for these two cases are shown in Fig. 5.2.

On the other hand, there exist three equilibrium points x_1, x_2 and x_3 in the system and there are four situations. In cases 2 and 7, the potential energy levels have a local maximum at x_1 and two minima at x_2 and x_3. Hence, x_1 is a saddle point while x_2 and x_3 are centers. In cases 6 and 11, the potential energy levels have a local minimum at x_1 and two maxima at x_2 and x_3. Hence, x_1 now becomes a center and x_2 and x_3 are saddle points. In case 4, the potential energy level has a local minimum at x_1, and x_2 and x_3 are inflection points. Hence, x_1 is a center, and x_2 and x_3 are degenerate singular points. In case 9, the potential energy level has a local maximum value at x_1, and x_2 and x_3 are inflection points. Hence, x_1 is a saddle point, and x_2 and x_3 are degenerate singular points. The possible trajectories are presented in Fig. 5.3.

Table 5.1: Equilibrium states of the nonlinear system (5.1).

Case number	Governing parameters		Number of equilibrium points	Equilibrium points and orbital characteristics around centers
1	$\alpha_1 > 0$, $\alpha_2 > 0$, $\alpha_3 > 0$, $\alpha_4 > 0$		1	$x_1 = 0$ (center, symmetric orbit)
2	$\alpha_1 > 0$, $\alpha_2 < 0$, $\alpha_3 > 0$, $\alpha_4 > 0$		3	$x_1 = 0$ (saddle point) $x_{2,3} = \pm R3$ (center, asymmetric orbit)
3	$\alpha_1 > 0$,	$\alpha_3^2 - 4\alpha_2\alpha_4 < 0$	1	$x_1 = 0$ (center, symmetric orbit)
4	$\alpha_2 > 0$,	$\alpha_3^2 - 4\alpha_2\alpha_4 = 0$	3	$x_1 = 0$ (center, symmetric orbit) $x_{2,3} = \pm R1$ (degenerate singular point)
5	$\alpha_3 < 0$, $\alpha_4 > 0$	$\alpha_3^2 - 4\alpha_2\alpha_4 > 0$	5	$x_1 = 0$ (center, symmetric orbit) $x_{2,3} = \pm R2$ (saddle point) $x_{4,5} = \pm R3$ (center, asymmetric orbit)
6	$\alpha_1 > 0$, $\alpha_2 > 0$, $\alpha_3 > 0$, $\alpha_4 < 0$		3	$x_1 = 0$ (center, symmetric orbit) $x_{2,3} = \pm R2$ (saddle point)
7	$\alpha_1 > 0$, $\alpha_2 < 0$, $\alpha_3 < 0$, $\alpha_4 > 0$		3	$x_1 = 0$ (saddle point) $x_{2,3} = \pm R3$ (center, asymmetric orbit)
8	$\alpha_1 > 0$,	$\alpha_3^2 - 4\alpha_2\alpha_4 < 0$	1	$x_1 = 0$ (saddle point)
9	$\alpha_2 < 0$,	$\alpha_3^2 - 4\alpha_2\alpha_4 = 0$	3	$x_1 = 0$ (saddle point) $x_{2,3} = \pm R1$ (degenerate singular point)
10	$\alpha_3 > 0$, $\alpha_4 < 0$	$\alpha_3^2 - 4\alpha_2\alpha_4 > 0$	5	$x_1 = 0$ (saddle point) $x_{2,3} = \pm R3$ (center, asymmetric orbit) $x_{4,5} = \pm R2$ (saddle point)
11	$\alpha_1 > 0$, $\alpha_2 > 0$, $\alpha_3 < 0$, $\alpha_4 < 0$		3	$x_1 = 0$ (center, symmetric orbit) $x_{2,3} = \pm R2$ (saddle point)

Note: $R1 = \sqrt{\dfrac{-\alpha_3}{2\alpha_4}}$, $R2 = \sqrt{\dfrac{-\alpha_3 - \sqrt{\alpha_3^2 - 4\alpha_2\alpha_4}}{2\alpha_4}}$ and $R3 = \sqrt{\dfrac{-\alpha_3 + \sqrt{\alpha_3^2 - 4\alpha_2\alpha_4}}{2\alpha_4}}$.
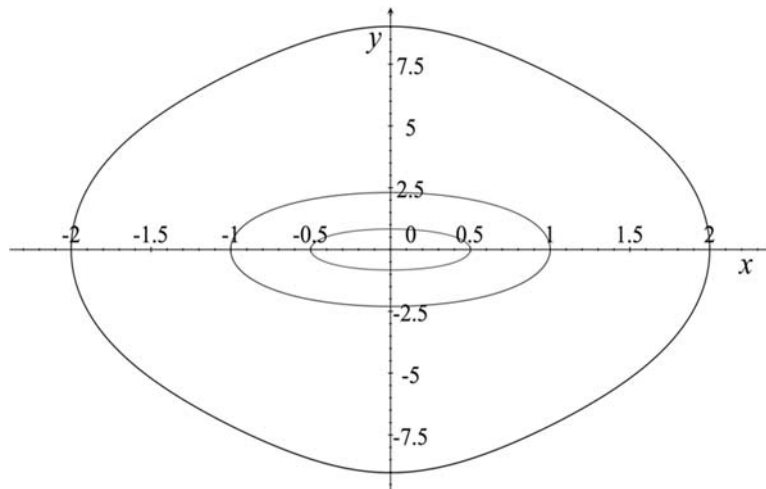
(a) Case 1 and Case 3
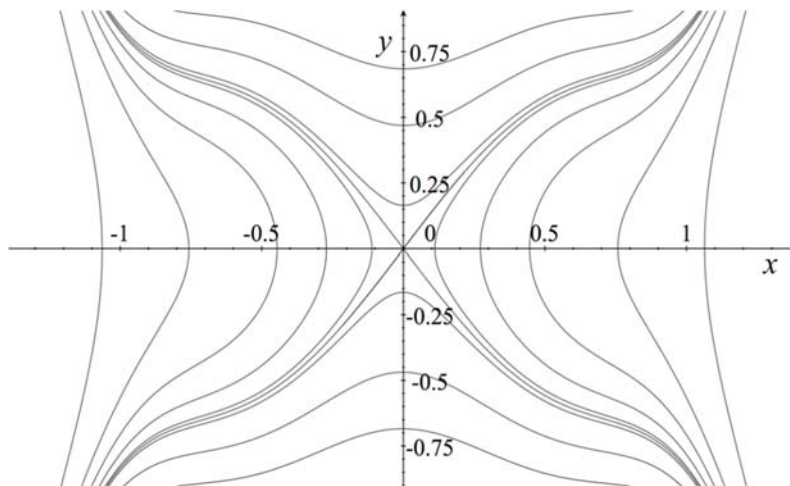
(b) Case 8

Fig. 5.2: Phase planes for the nonlinear system with one equilibrium point.
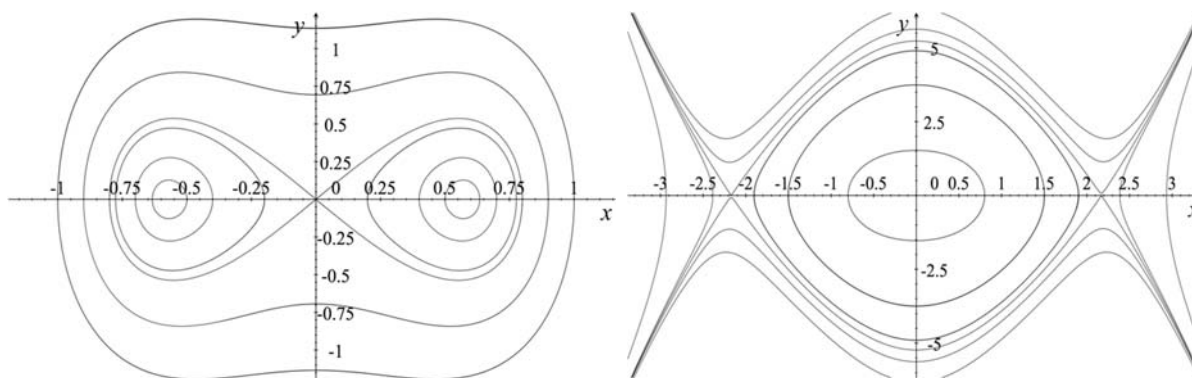
(a) Case 2 and Case 7

(b) Case 6 and Case 11
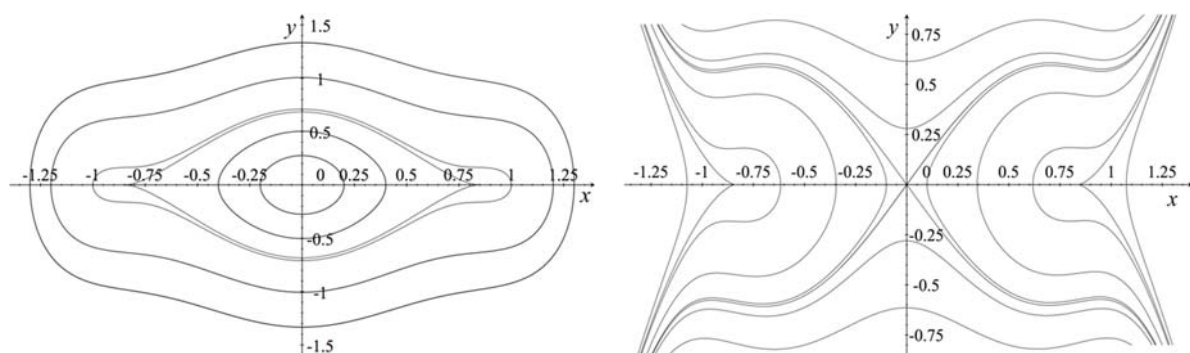
(c) Case 4

(d) Case 9

Fig. 5.3: Phase planes for the nonlinear system with three equilibrium points.

There are still two cases that possess five equilibrium points. In case 5, the system arrives its minimum potential energy levels at x_1, x_4 and x_5, and the maximum potential energy levels are at x_2 and x_3. Hence, x_1, x_4, and x_5 are centers, and x_2 and x_3 are saddle points. In case 10, the system arrives its minimum potential energy levels at x_2 and x_3, and the maximum potential energy levels at x_1, x_4, and x_5. In this case, x_2 and x_3 are centers, and x_1, x_4, and x_5 become saddle points. The possible trajectories of heteroclinic and homoclinic orbits are plotted in Fig. 5.4.
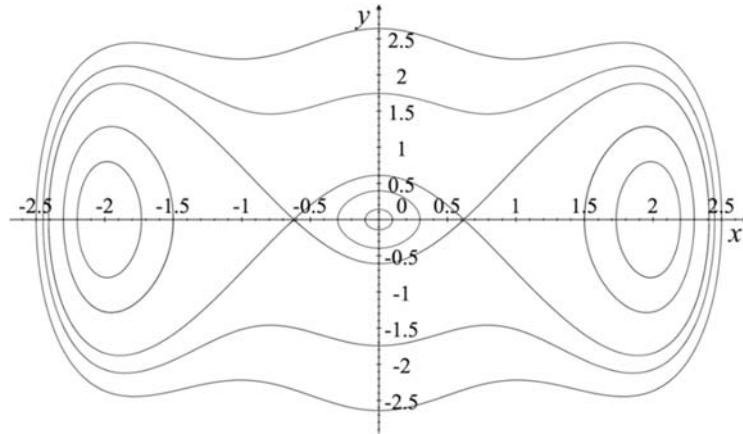
(a) Case 5
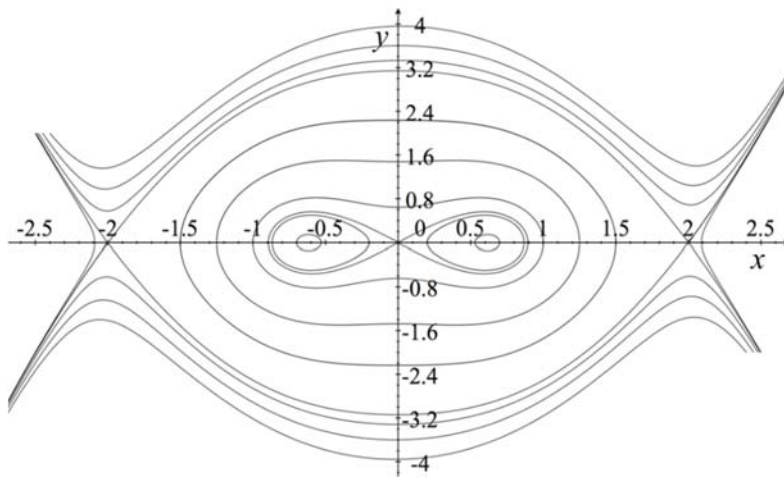
(b) Case 10

Fig. 5.4: Phase planes for the nonlinear system with five equilibrium points.

In Figs. 5.2–5.4, we clearly observe three different modes, corresponding to the mono-stable (case 1), bi-stable (case 2), and tri-stable (case 5) cases. Among them, cases 1, 2, and 5 have one, two, and three "*stable*" equilibrium points, respectively. To further investigate the effect of various parameters (α_1, α_2 and α_3) on the pattern of the roots in Eq. (5.7), two bifurcation diagrams are plotted in Figs. 5.5 and 5.6. Fig. 5.5 presents the relationship between the negative linear stiffness (α_2) and the cubic nonlinear term (α_3), and Fig. 5.6 shows the variation of the quadratic velocity term (α_1) and the cubic nonlinear term (α_3). In these two figures, we observe that a bifurcation of the system occurs when α_3 tends to become a negative value.

Fig. 5.5: Bifurcation behavior of the nonlinear system affected by the parameters α_2 and α_3.
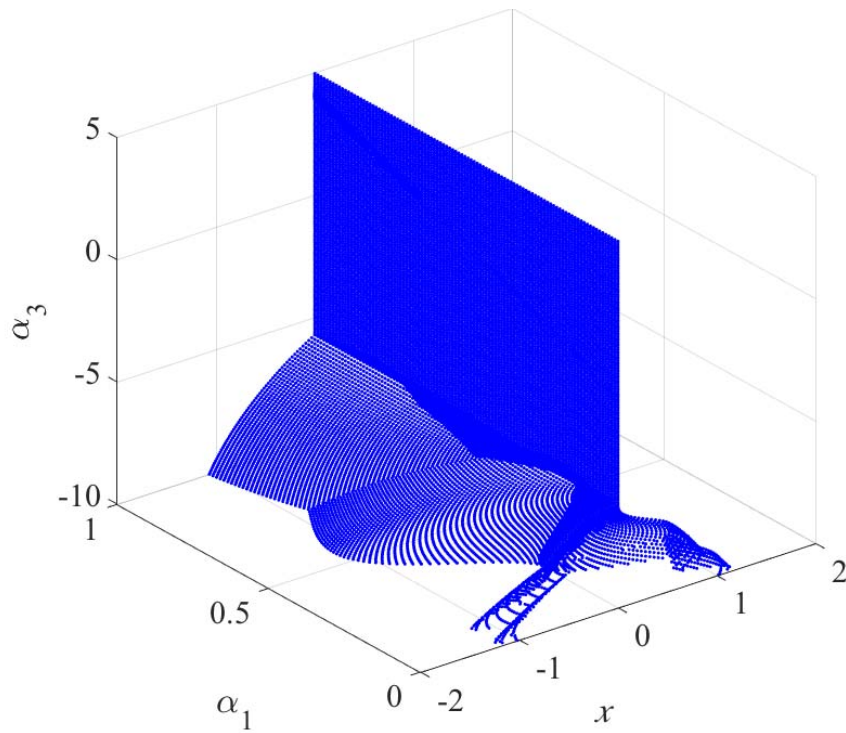
Fig. 5.6: Bifurcation behavior of the nonlinear system affected by the parameters α_1 and α_3.

101

According to the qualitative analysis for Eq. (5.1), the periodic motion of the non-natural system only occurs around centers, which depends on the parameter values and the initial amplitudes. In cases 1 and 3, the system oscillates periodically between a symmetric bound $[-A, A]$ and $0 < A < +\infty$. In cases 2 and 7, a periodic oscillation occurs around the stable equilibrium points x_2 (or x_3) and it is asymmetric about the equilibrium points. The oscillation amplitude A is subject to the region $0 < A < K \left(-K < A < 0 \right)$, where K is calculated by

$$K = \sqrt{-\frac{3\alpha_3}{4\alpha_4} + \frac{\sqrt{3\left(3\alpha_3^2 - 16\alpha_2\alpha_4\right)}}{4\alpha_4}} \qquad (5.9)$$

In cases 6 and 11, the presence of periodic motions will occur around the stable equilibrium point x_1 only, which is symmetric about this point and the oscillation amplitude should satisfy $0 < A < x_1$. In case 4, the system oscillates periodically around center x_1 between a symmetric bound $[-A, A]$ and $0 < A < x_2$. In case 5, the oscillation of the system may occur around the stable equilibrium point x_1 and it is symmetric about this point. The oscillation amplitude A is bounded by $0 < A < x_2$. Besides, the oscillation may also occur around the equilibrium point x_4 (or x_5) and it is asymmetric in nature. The oscillation amplitude should satisfy $x_2 < A < L$ (or $-L < A < x_3$), where L is given by

$$L = \sqrt{-\frac{\alpha_3}{2\alpha_4} + \frac{\sqrt{\alpha_3^2 - 4\alpha_2\alpha_4}}{4\alpha_4} + \frac{1}{4\alpha_4^2}\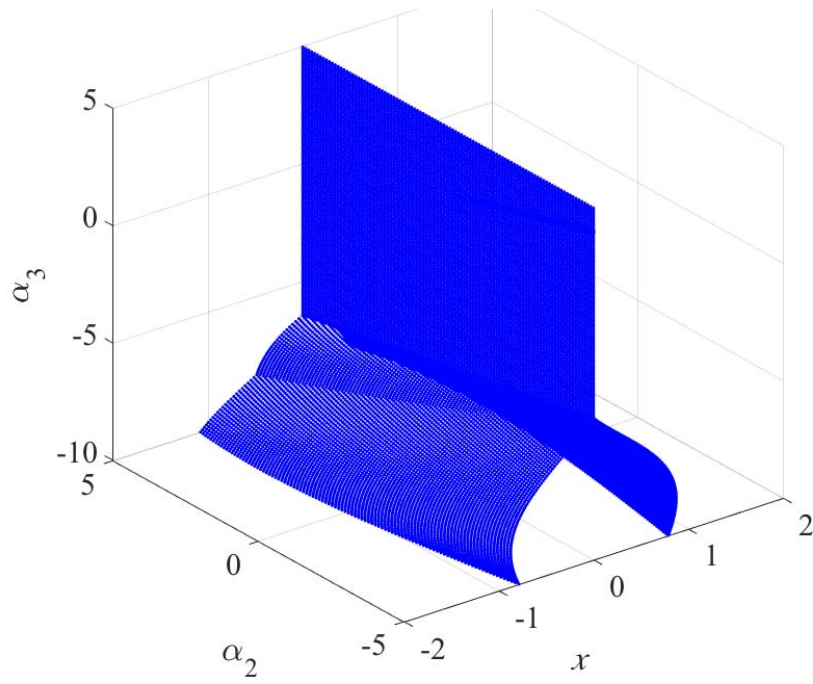left(\sqrt{8\alpha_3^2\alpha_4^2 - 32\alpha_2\alpha_4^3 + \alpha_4^2(\alpha_3^2 - 4\alpha_2\alpha_4)}\right)} \qquad (5.10)$$

In case 10, the oscillation occurs around the stable equilibrium point x_2 (or x_3), and it is asymmetric in nature. If $V(x_1) \leq V(x_4)$, the oscillation amplitude should satisfy $0 < A < K \left(-K < A < 0 \right)$. While for $V(x_1) > V(x_4)$, the oscillation amplitude should satisfy $M < A < x_4$ (or $x_5 < A < -M$), in which M is defined as

$$M = \sqrt{-\frac{\alpha_3}{2\alpha_4} + \frac{\sqrt{\alpha_3^2 - 4\alpha_2\alpha_4}}{4\alpha_4} + \frac{1}{4\alpha_4^2}\left(\sqrt{8\alpha_3^2\alpha_4^2 - 32\alpha_2\alpha_4^3 + \alpha_4^2(\alpha_3^2 - 4\alpha_2\alpha_4)}\right)} \qquad (5.11)$$

5.4 Quantitative Analysis

In this section, the NHB method (Wu et al., 2006) is employed to construct analytical approximate solutions to the system (5.1). As indicated in Section 5.3, there are two types of periodic motions, i.e., a symmetric oscillation with the stable equilibrium point x_1, and an asymmetric oscillation with the stable equilibrium points $x_2(x_3)$ or $x_4(x_5)$.

5.4.1 Analytical Approximations for Symmetric Oscillations

Following Section 3.3.1, the system (5.1) with odd nonlinearity can be analytically solved by the NHB method. By defining a new independent variable $\tau = \omega t$, Eq. (5.1) can be expressed as

$$\Omega \left[E(x)\ddot{x} + F(x)\dot{x}^2 \right] + G(x) = 0 \qquad (5.12)$$

and the initial conditions are

$$x(0) = A, \ \dot{x}(0) = 0 \qquad (5.13)$$

where $\Omega = \omega^2$ and a dot of x denotes differentiation with respect to τ.

Applying the Newton's procedure, the displacement $x(\tau)$ and the square of frequency Ω are written as

$$x(\tau) = x_{a1}(\tau) + \Delta x_{a1}(\tau) \qquad (5.14)$$

$$\Omega = \Omega_{a1} + \Delta \Omega_{a1} \qquad (6.15)$$

in which $\Delta x_{a1}(\tau)$ and $\Delta \Omega_{a1}$ are small increments of $x_{a1}(\tau)$ and Ω_{a1}, respectively. Substituting Eqs. (5.14) and (5.15) into Eq. (5.12), we have

$$\begin{aligned}(\Omega_{a1} + \Delta \Omega_{a1})\left[E(x_{a1} + \Delta x_{a1})(\ddot{x}_{a1} + \Delta \ddot{x}_{a1}) + F(x_{a1} + \Delta x_{a1})(\dot{x}_{a1} + \Delta \dot{x}_{a1})^2 \right] \\ + G(x_{a1} + \Delta x_{a1}) = 0 \end{aligned} \qquad (5.16)$$

Further linearizing Eq. (5.16) with respect to the correction terms $\Delta x_{a1}(\tau)$ and $\Delta \Omega_{a1}$ leads to

$$\begin{aligned}&\Omega_{a1}\left[E(x_{a1})\ddot{x}_{a1} + F(x_{a1})\dot{x}_{a1}^2 \right] + G(x_{a1}) + E(x_{a1})(\Omega_{a1}\Delta \ddot{x}_{a1} + \Delta \Omega_{a1}\ddot{x}_{a1}) + \\ &F(x_{a1})\dot{x}_{a1}(2\Omega_{a1}\Delta \dot{x}_{a1} + \Delta \Omega_{a1}\dot{x}_{a1}) + \Omega_{a1}\left[E_x(x_{a1})\ddot{x}_{a1} + F_x(x_{a1})\dot{x}_{a1}^2 \right]\Delta x_{a1} + \\ &G_x(x_{a1})\Delta x_{a1} = 0 \end{aligned} \qquad (5.17)$$

where the subscript x denote differentiation with respect to x. Making use of the Fourier series expansions gives

$$E(x_{a1})\ddot{x}_{a1} + F(x_{a1})\dot{x}_{a1}^2 = \sum_{i=0}^{\infty} a_{2i+1} \cos\left[(2i+1)\tau\right] \tag{5.18}$$

$$G(x_{a1}) = \sum_{i=0}^{\infty} b_{2i+1} \cos\left[(2i+1)\tau\right] \tag{5.19}$$

$$E(x_{a1}) = \sum_{i=0}^{\infty} c_{2i} \cos(2i\tau) \tag{5.20}$$

$$F(x_{a1})\dot{x}_{a1} = \sum_{i=0}^{\infty} d_{2(i+1)} \sin\left[2(i+1)\tau\right] \tag{5.21}$$

$$E_x(x_{a1})\ddot{x}_{a1} + F_x(x_{a1})\dot{x}_{a1}^2 = \sum_{i=0}^{\infty} e_{2i} \cos(2i\tau) \tag{5.22}$$

$$G_x(x_{a1}) = \sum_{i=0}^{\infty} f_{2i} \cos(2i\tau) \tag{5.23}$$

where a_i, b_i, c_i, d_i, e_i and f_i are Fourier series coefficients that can be determined by

$$a_{2i+1} = \frac{4}{\pi} \int_0^{\pi/2} \left[E(x_{a1})\ddot{x}_{a1} + F(x_{a1})\dot{x}_{a1}^2\right] \cos\left[(2i+1)\tau\right] d\tau, \quad i = 0,1,2.... \tag{5.24}$$

$$b_{2i+1} = \frac{4}{\pi} \int_0^{\pi/2} G(x_{a1}) \cos\left[(2i+1)\tau\right] d\tau, \quad i = 0,1,2.... \tag{5.25}$$

$$c_{2i} = \frac{4}{\pi} \int_0^{\pi/2} E(x_{a1}) \cos(2i\tau) d\tau, \quad i = 0,1,2.... \tag{5.26}$$

$$d_{2(i+1)} = \frac{8}{\pi} \int_0^{\pi/2} F(x_{a1})\dot{x}_{a1} \sin\left[2(i+1)\tau\right] d\tau, \quad i = 0,1,2.... \tag{5.27}$$

$$e_{2i} = \frac{4}{\pi} \int_0^{\pi/2} \left[E_x(x_{a1})\ddot{x}_{a1} + F_x(x_{a1})\dot{x}_{a1}^2\right] \cos(2i\tau) d\tau, \quad i = 0,1,2.... \tag{5.28}$$

$$f_{2i} = \frac{4}{\pi} \int_0^{\pi/2} G_x(x_{a1}) \cos(2i\tau) d\tau, \quad i = 0,1,2.... \tag{5.29}$$

For the first-order analytical approximation, we set

$$\Delta x_{a1}(\tau) = 0, \quad \Delta \Omega_{a1} = 0 \tag{5.30}$$

and

$$x_{a1}(\tau) = A \cos\tau \tag{5.31}$$

The above equation satisfies the initial conditions given in Eq. (5.13). Substituting Eqs. (5.18)–(5.23), (5.30) and (5.31) into Eq. (5.17), expanding the resulting expression into a trigonometric series and setting the coefficient of $\cos\tau$ to zero, we obtain

$$\Omega_{a1}(A) = -\frac{b_1}{a_1} \tag{5.32}$$

Hence, the first-order frequency $\omega_{a1}(A)$ and corresponding approximate periodic solution $x_{a1}(t)$ are

$$\omega_{a1}(A) = \sqrt{\Omega_{a1}(A)}, \quad x_{a1}(t) = A\cos\tau, \quad \tau = \omega_{a1}(A)t \tag{5.33}$$

For the second-order analytical approximation, we set

$$\Delta x_{a1}(\tau) = z_1(\cos\tau - \cos 3\tau) \tag{5.34}$$

Inserting Eqs. (5.18)–(5.23), (5.31) and (5.34) into Eq. (5.17), expanding the resulting expression in a trigonometric series and setting the coefficients of $\cos\tau$ and $\cos 3\tau$ to zero, we obtain

$$z_1(A) = -\frac{2C_1}{A_2 + B_2\Omega_{a1}} \tag{5.35}$$

$$\Delta\Omega_{a1}(A) = -\frac{2C_1(B_1 + A_1\Omega_{a1})}{a_1(B_2 + A_2\Omega_{a1})} \tag{5.36}$$

where

$$A_1 = \frac{1}{2}\left(-c_0 + 8c_2 + 9c_4 + 2d_2 + 3d_4 + e_0 - e_4\right) \tag{5.37}$$

$$B_1 = \frac{1}{2}(f_0 - f_4) \tag{5.38}$$

$$A_2 = -a_1 f_0 - a_3 f_0 + a_1 f_2 + a_1 f_4 + a_3 f_4 - a_1 f_6 \tag{5.39}$$

$$B_2 = 9a_1 c_0 + a_3 c_0 - a_1 c_2 - 8a_3 c_2 - a_1 c_4 - 9a_3 c_4 + 9a_1 c_6 + a_1 d_2 - 2a_3 d_2 - \\ a_1 d_4 - 3a_3 d_4 + 3a_1 d_6 - a_1 e_0 - a_3 e_0 + a_1 e_2 + a_1 e_4 + a_3 e_4 - a_1 e_6 \tag{5.40}$$

$$C_1 = a_3 b_1 - a_1 b_3 \tag{5.41}$$

Therefore, the second-order frequency $\omega_{a2}(A)$ and corresponding approximate periodic solution $x_{a2}(t)$ are

$$\omega_{a2}(A) = \sqrt{\Omega_{a2}(A)}$$

$$x_{a2}(t) = x_{a1}(\tau) + \Delta x_{a1}(\tau) = (A + z_1)\cos\tau - z_1\cos 3\tau, \quad \tau = \omega_{a2}(A)t \tag{5.42}$$

where

$$\Omega_{a2}(A) = \Omega_{a1}(A) + \Delta\Omega_{a1}(A)$$
$$= -\frac{b_1}{a_1} - \frac{2C_1\left[B_1 + A_1(-b_1/a_1)\right]}{a_1\left[B_2 + A_2(-b_1/a_1)\right]} \tag{5.43}$$

Based on the above equations, the analytical approximate solutions for the symmetric oscillation of the nonlinear system (5.1) around the stable equilibrium point x_1 can be derived.

5.4.2 Analytical Approximations for Asymmetric Oscillations

In addition, there exist heteroclinic orbits (Yao and Zhang, 2007; Algaba et al., 2013) where the nonlinear system (5.1) has more than one equilibrium point. Under this condition, the system can also oscillate around other stable equilibrium points with the asymmetric limits $[A', A]$ where A' and A have the same energy level in accordance with the principle of conservation of energy (Wu and Lim, 2004)

$$V(A) = V(A') \tag{5.44}$$

in which A' can be expressed as a function of A.

When the system oscillates asymmetrically, a new variable is introduced as follows:

$$u = x - \lambda \tag{5.45}$$

Eq. (5.1) can be derived as

$$\tilde{E}(u)\frac{d^2u}{dt^2} + \tilde{F}(u)\left(\frac{du}{dt}\right)^2 + \tilde{G}(u) = 0 \tag{5.46}$$

with the following initial conditions

$$u(0) = B = A - \lambda, \ \frac{du(0)}{dt} = 0 \tag{5.47}$$

in which

$$\tilde{E}(u) = 1 + \alpha_1\lambda^2 + 2\alpha_1\lambda u + \alpha_1 u^2 \tag{5.48}$$

$$\tilde{F}(u) = \alpha_1\lambda + \alpha_1 u \tag{5.49}$$

$$\tilde{G}(u) = \gamma_1 u + \gamma_2 u^2 + \gamma_3 u^3 + \gamma_4 u^4 + \gamma_5 u^5 \tag{5.50}$$

where $\gamma_1 = \alpha_2 + 3\alpha_3\lambda^2 + 5\alpha_4\lambda^4$, $\gamma_2 = 3\alpha_2\lambda + 10\alpha_4\lambda^3$, $\gamma_3 = \alpha_3 + 10\alpha_4\lambda^2$, $\gamma_4 = 5\alpha_4\lambda$ and $\gamma_5 = \alpha_4$. Note that λ is the coordinate value of the corresponding equilibrium point.

In Eq. (5.46), it is noted that $\tilde{E}(-u) \neq -\tilde{E}(u)$, $\tilde{F}(-u) \neq -\tilde{F}(u)$, $\tilde{G}(-u) \neq -\tilde{G}(u)$, and the system oscillates within asymmetric bound $[B', B]$ $(B' = A' - \lambda)$ around the stable equilibrium point $u = 0$. To solve such a mixed-parity nonlinear system, two newly odd nonlinear systems is introduced as follows (see Section 3.3.3, Wu and Lim, 2004):

$$H(u)\frac{d^2u}{dt^2} + I(u)\left(\frac{du}{dt}\right)^2 + J(u) = 0, \ u(0) = B, \ \frac{du(0)}{dt} = 0 \tag{5.51}$$

and

$$K(u)\frac{d^2u}{dt^2} + L(u)\left(\frac{du}{dt}\right)^2 + M(u) = 0, \ u(0) = -B'(B' < 0), \ \frac{du(0)}{dt} = 0 \tag{5.52}$$

where

$$H(u) = \begin{cases} \tilde{E}(u), & u \geq 0 \\ \tilde{E}(-u), & u < 0 \end{cases}, \ I(u) = \begin{cases} \tilde{F}(u), & u \geq 0 \\ -\tilde{F}(-u), & u < 0 \end{cases},$$

$$J(u) = \begin{cases} \tilde{G}(u), & u \geq 0 \\ -\tilde{G}(-u), & u < 0 \end{cases} \tag{5.53}$$

and

$$K(u) = \begin{cases} \tilde{E}(-u), & u > 0 \\ \tilde{E}(u), & u \leq 0 \end{cases}, \ L(u) = \begin{cases} -\tilde{F}(-u), & u > 0 \\ \tilde{F}(u), & u \leq 0 \end{cases},$$

$$M(u) = \begin{cases} -\tilde{G}(-u), & u > 0 \\ \tilde{G}(u), & u \leq 0 \end{cases} \tag{5.54}$$

Equations (5.51) and (5.52) can be solved independently by the NHB method as mentioned in Section 5.3.1. To consider the asymmetric oscillation of the system (5.1), the analytical approximations are mathematically formulated by combining the piecewise approximate solutions obtained from Eqs. (5.51) and (5.52).

According to Eqs. (5.51) and (5.52), the first-order approximate periodic solution ($x_{a1}(t)$) for the asymmetric oscillation of the nonlinear system (5.1) is

$$x_{a1}(t) = \begin{cases} u_{11}(t) + \lambda, & 0 \leq t \leq \dfrac{T_{11}(B)}{4} \\[2ex] u_{12}\left(t - \dfrac{T_{11}(B)}{4} + \dfrac{T_{12}(B')}{4}\right) + \lambda, & \dfrac{T_{11}(B)}{4} \leq t \leq \dfrac{T_{11}(B)}{4} + \dfrac{T_{12}(B')}{2} \\[2ex] u_{11}\left(t + \dfrac{T_{11}(B)}{2} - \dfrac{T_{12}(B')}{2}\right) + \lambda, & \dfrac{T_{11}(B)}{4} + \dfrac{T_{12}(B')}{2} \leq t \leq \dfrac{T_{11}(B) + T_{12}(B')}{2} \end{cases} \tag{5.55}$$

and the first-order approximate period (T_{a1}) and frequency ($\omega_{a1}(A)$) are

$$T_{a1}(A) = \frac{T_{11}(B) + T_{12}(B')}{2} \text{ and } \omega_{a1}(A) = \frac{2\pi}{T_{a1}(A)} \tag{5.56}$$

where the subscripts "11" and "12" of T and u denote the first-order approximate periods and the corresponding periodic solutions for the systems (5.51) and (5.52), respectively.

Besides, the second-order approximate periodic solution ($x_{a2}(t)$) for the asymmetric oscillation of the nonlinear system (5.1) is

$$x_{a2}(t) = \begin{cases} u_{21}(t) + \lambda, & 0 \leq t \leq \dfrac{T_{21}(B)}{4} \\[2ex] u_{22}\left(t - \dfrac{T_{21}(B)}{4} + \dfrac{T_{22}(B')}{4}\right) + \lambda, & \dfrac{T_{21}(B)}{4} \leq t \leq \dfrac{T_{21}(B)}{4} + \dfrac{T_{22}(B')}{2} \\[2ex] u_{21}\left(t + \dfrac{T_{21}(B)}{2} - \dfrac{T_{22}(B')}{2}\right) + \lambda, & \dfrac{T_{21}(B)}{4} + \dfrac{T_{22}(B')}{2} \leq t \leq \dfrac{T_{21}(B) + T_{22}(B')}{2} \end{cases} \tag{5.57}$$

and the second-order approximate period (T_{a2}) and frequency ($\omega_{a2}(A)$) are

$$T_{a2}(A) = \frac{T_{21}(B) + T_{22}(B')}{2} \text{ and } \omega_{a2}(A) = \frac{2\pi}{T_{a2}(A)} \tag{5.58}$$

where the subscripts "21" and "22" of T and u denote the second-order approximate periods and the corresponding periodic solutions for the systems (5.51) and (5.52), respectively.

5.5 Results and Discussion

In this section, the approximate solutions for various parameters α_1, α_2, α_3, and α_4 are presented to verify the accuracy of the NHB method with respect to the Runge–Kutta method and other methods, e.g., the homotopy perturbation method (HPM) (Pakar and Bayat, 2015; Neamaty et al., 2015). For symmetric oscillation, the exact frequency of the nonlinear problem (5.1) in terms of an implicit form is given by

$$\omega_e(A) = \pi / \int_0^{\frac{\pi}{2}} \sqrt{\frac{1 + \alpha_1(A\cos\theta)^2}{2[V(A) - V(A\cos\theta)]}} (-A\cos\theta) d\theta \tag{5.59}$$

where $V(\bullet)$ is the potential energy of the system (5.1). For an asymmetric oscillation, the exact frequency of the nonlinear system (5.1) can be constructed by

$$\omega_e(A) = \frac{2\omega_{e1}(B)\omega_{e2}(B')}{\omega_{e1}(B) + \omega_{e2}(B')} \tag{5.60}$$

where $\omega_{e1}(B)$ and $\omega_{e2}(B')$ are the exact frequencies of the corresponding systems (5.51) and (5.52), respectively.

Consider cases 1 and 3, the first-order and second-order approximate frequencies (i.e., ω_{a1} and ω_{a2}) of the NHB method are compared with the exact solution (ω_e) and the HPM solution (ω_{HPM}) in Tables 5.2–5.5. The first-order approximate frequencies derived from the NHB method are the same as those results of the HPM (Pakar and Bayat, 2015). They have good agreement with the corresponding exact solutions when the initial amplitude is small. When the initial amplitude A larger than 5, these two analytical approximations are not acceptable. However, the second-order approximate frequencies have good agreement with the exact results for small as well as large initial amplitudes. Figures 5.7 and 5.8 show the results of the first-order and second-order approximate periodic solutions (i.e., $x_{a1}(t)$ and $x_{a2}(t)$) obtained from the NHB method and the corresponding numerical solution ($x_e(t)$) obtained from the Runge–Kutta method. We clearly observe that the accuracy of the second-order approximate periodic solution is higher than the first-order approximate periodic solution.

On the other hand, the results of the other two examples for case 5 are given in Tables 5.6 and 5.7 for the asymmetric and symmetric oscillations around three stable equilibrium points, respectively. Both the first-order and second-order approximate frequencies are highly consistent with the exact solution due to a small initial deviation to the corresponding equilibrium points. The time history responses of the analytical approximate periodic solutions (i.e., $x_{a1}(t)$ and $x_{a2}(t)$) and numerical solution ($x_e(t)$) are depicted in Figs. 5.9–5.11. The absolute errors in Figs. 5.9–5.11 show that the accuracy of the second-order approximate periodic solution is still better than the first-order approximate periodic solution when compared with the numerical one.

Table 5.2: Comparison of approximate and exact frequencies for $\alpha_1 = 0.5$, $\alpha_2 = 2$, $\alpha_3 = 2$, and $\alpha_4 = 1.3$.

A	ω_{HPM} (Pakar and Bayat, 2015)	ω_{a1} Eq. (5.33)	ω_{a2} Eq. (5.42)	ω_e Eq. (5.59)
0.2	1.42860	1.42860	1.42860	1.42860
0.5	1.51099	1.51099	1.51091	1.51090
1.2	2.07308	2.07308	2.07268	2.07151
2	3.24037	3.24037	3.28111	3.27386
5	8.68858	8.68858	9.45407	9.39663
10	17.8432	17.8432	20.1124	20.0870
20	35.9595	35.9595	41.0192	41.2150
100	180.258	180.258	206.475	208.430

Table 5.3: Comparison of approximate and exact frequencies for $\alpha_1 = 0.5$, $\alpha_2 = 2$, $\alpha_3 = -2$, and $\alpha_4 = 1.3$

A	ω_{HPM} (Pakar and Bayat, 2015)	ω_{a1} Eq. (5.33)	ω_{a2} Eq. (5.42)	ω_e Eq. (5.59)
0.2	1.40554	1.40554	1.40555	1.40555
0.5	1.37654	1.37654	1.37689	1.37689
1.2	1.59706	1.59706	1.60129	1.59977
2	2.68328	2.68328	2.70640	2.69843
5	8.35474	8.35474	9.07751	9.02539
10	17.6635	17.6635	19.9041	19.8821
20	35.8686	35.8686	40.9120	41.1093
100	180.240	180.240	206.454	208.409

Table 5.4: Comparison of approximate and exact frequencies for $\alpha_1 = 0.1$, $\alpha_2 = 1$, $\alpha_3 = 0.5$, and $\alpha_4 = 0.27$.

A	ω_{HPM} (Pakar and Bayat, 2015)	ω_{a1} Eq. (5.33)	ω_{a2} Eq. (5.42)	ω_e Eq. (5.59)
0.2	1.00660	1.00660	1.00660	1.00660
0.5	1.04435	1.04435	1.04420	1.04419
1.2	1.32777	1.32777	1.32138	1.32091
2	2.08167	2.08167	2.04997	2.04623
5	7.17538	7.17538	7.25945	7.23658
10	16.9607	16.9607	18.2688	18.1618
20	35.9570	35.9570	40.3727	40.2831
100	183.549	183.549	210.094	211.840

Table 5.5: Comparison of approximate and exact frequencies for $\alpha_1 = 0.1$, $\alpha_2 = 1$, $\alpha_3 = -0.5$, and $\alpha_4 = 1.3$.

A	ω_{HPM} (Pakar and Bayat, 2015)	ω_{a1} Eq. (5.33)	ω_{a2} Eq. (5.42)	ω_e Eq. (5.59)
0.2	0.99162	0.99162	0.99161	0.99161
0.5	0.95157	0.95157	0.95139	0.95140
1.2	0.86921	0.86921	0.86940	0.86936
2	1.35401	1.35401	1.32931	1.32155
5	6.56908	6.56908	6.61769	6.59292
10	16.5881	16.5881	17.8510	17.7492
20	35.7578	35.7578	40.1412	40.0554
100	183.508	183.508	210.046	211.792

Table 5.6: Comparison of approximate and exact frequencies for $\alpha_1 = 0.5$, $\alpha_2 = 2$, $\alpha_3 = -5.7$, and $\alpha_4 = 1.3$.

A	Equilibrium point at	ω_{a1}, Eq. (5.33)	ω_{a2}, Eq. (5.42)	ω_e, Eq. (5.59)
0.1	$x_1 = 0$	1.39730	1.39728	1.39728

A	Equilibrium point at	ω_{a1}, Eq. (5.56)	ω_{a2}, Eq. (5.58)	ω_e, Eq. (5.60)
2.1	$x_4 = 2$	3.51270	3.51244	3.51264
−1.9	$x_5 = -2$	3.51882	3.51862	3.51877

Note: The system oscillates symmetrically around x_1, but asymmetrically around x_4 or x_5.

Table 5.7: Comparison of approximate and exact frequencies for $\alpha_1 = 0.1$, $\alpha_2 = 1$, $\alpha_3 = -1.5$, and $\alpha_4 = 0.27$.

A	Equilibrium point at	ω_{a1}, Eq. (5.33)	ω_{a2}, Eq. (5.42)	ω_e, Eq. (5.59)
0.1	$x_1 = 0$	0.99412	0.99412	0.99412

A	Equilibrium point at	ω_{a1}, Eq. (5.56)	ω_{a2}, Eq. (5.58)	ω_e, Eq. (5.60)
2.2865	$x_4 = 2.1865$	2.62193	2.62042	2.62161
−2.0865	$x_5 = -2.1865$	2.62691	2.62562	2.62665

Note: The system oscillates symmetrically around x_1, but asymmetrically around x_4 or x_5.

Fig. 5.7: Comparison of analytical approximate periodic solutions with numerical solution for $\alpha_1 = 0.5$, $\alpha_2 = 2$, $\alpha_3 = -0.2$, $\alpha_4 = 1.3$, and $A = 10$.
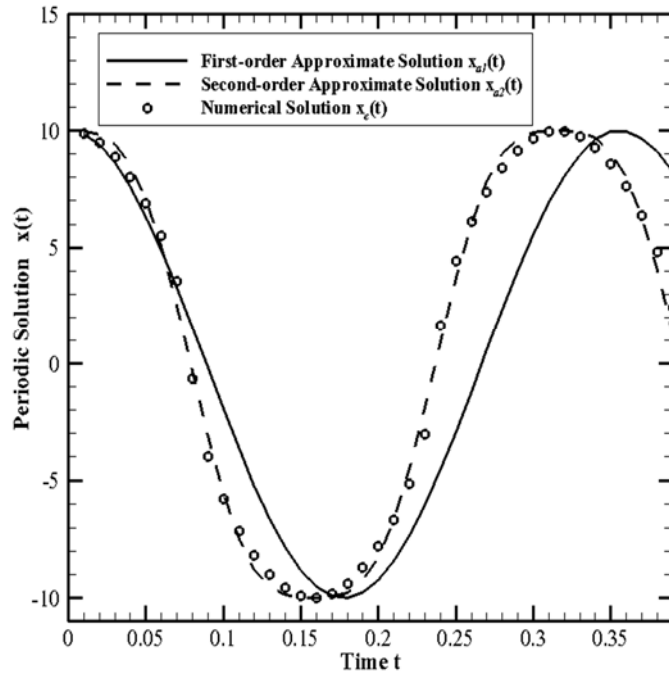

Fig. 5.8: Comparison of analytical approximate periodic solutions with numerical solution for $\alpha_1 = 0.1$, $\alpha_2 = 1$, $\alpha_3 = -1.5$, $\alpha_4 = 0.27$, and $A = 100$.

(a)

(b)

Fig. 5.9: (a) Comparison of analytical approximate periodic solutions with numerical solution for $\alpha_1 = 0.1$, $\alpha_2 = 1$, $\alpha_3 = -1.5$, $\alpha_4 = 0.27$, and $A = 0.1$; (b) Comparison of the absolute errors between the approximate and numerical solutions.

(a)

(b)

Fig. 5.10: (a) Comparison of analytical approximate periodic solutions with numerical solution for $\alpha_1 = 0.1$, $\alpha_2 = 1$, $\alpha_3 = -1.5$, $\alpha_4 = 0.27$, and $A = 2.2865$; (b) Comparison of the absolute errors between the approximate and numerical solutions.
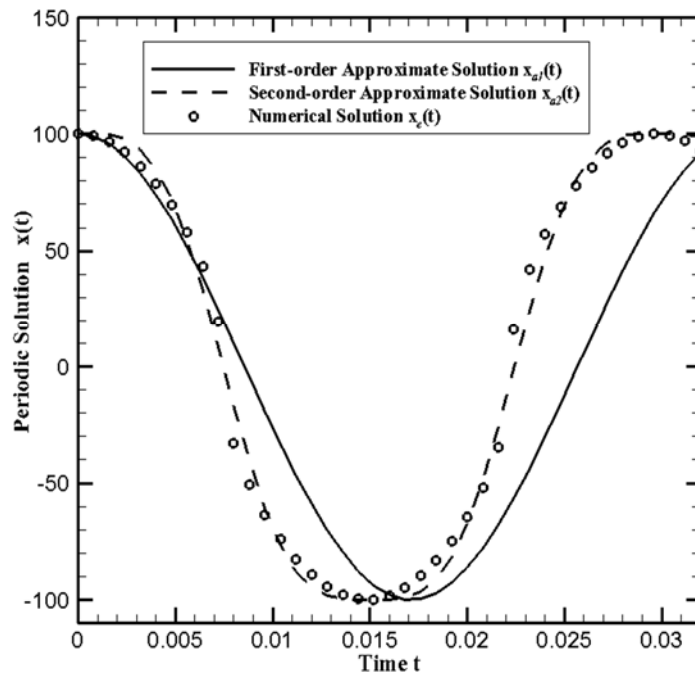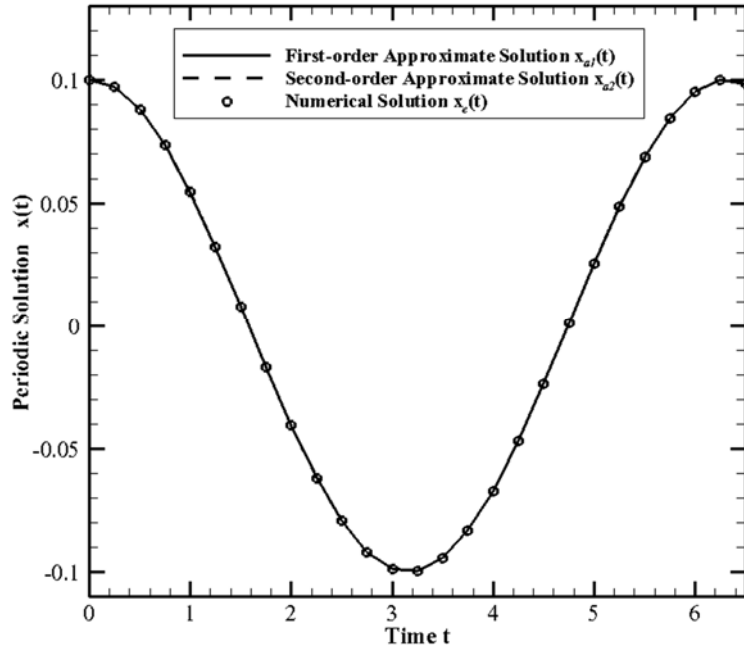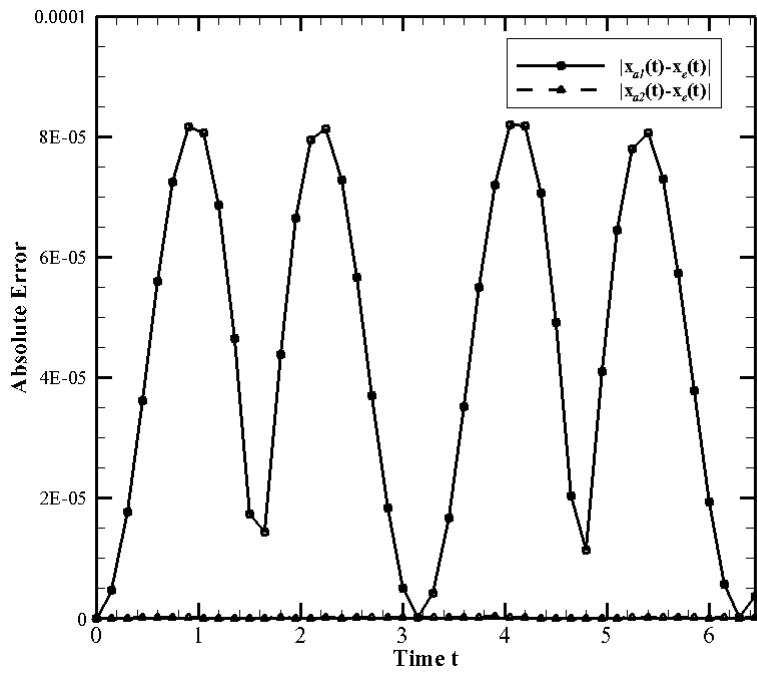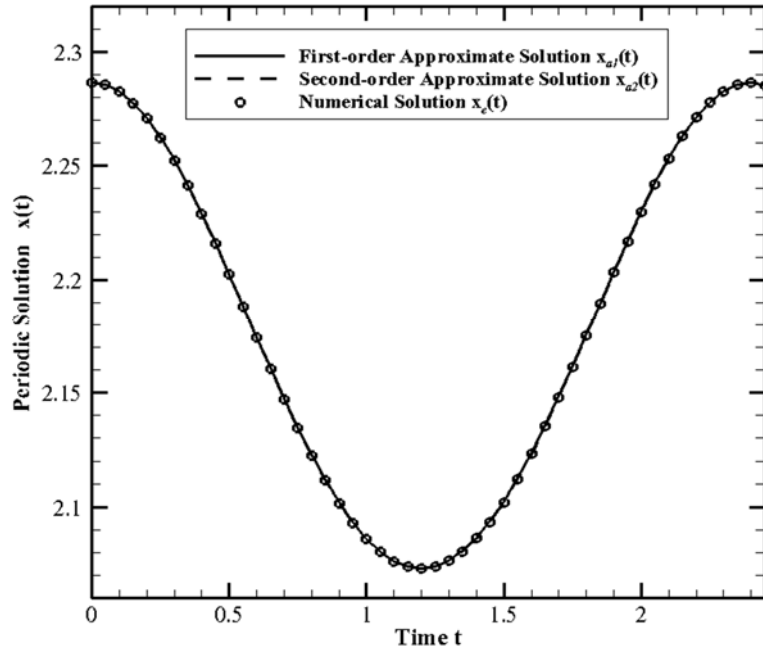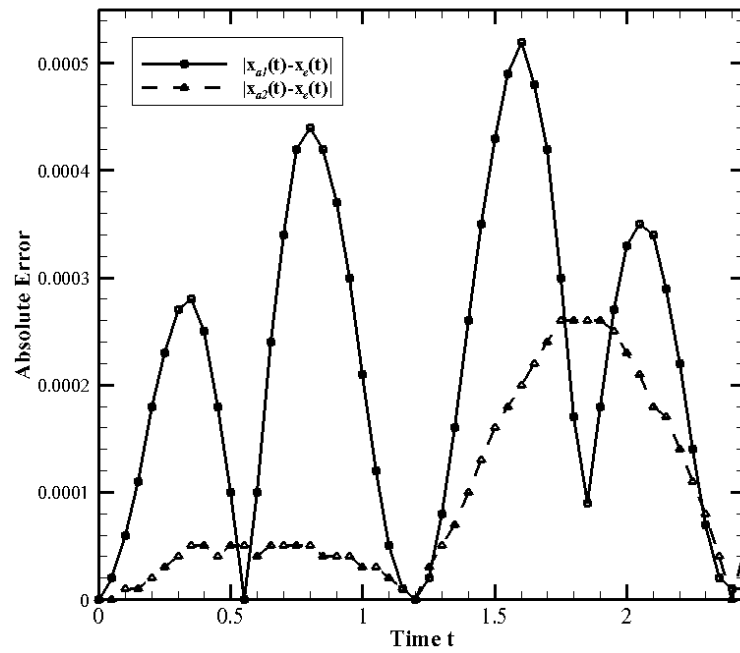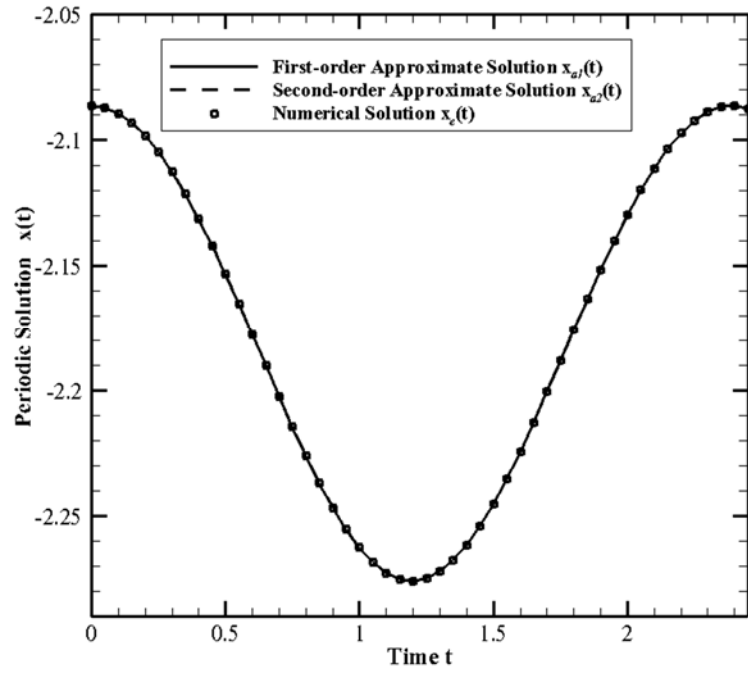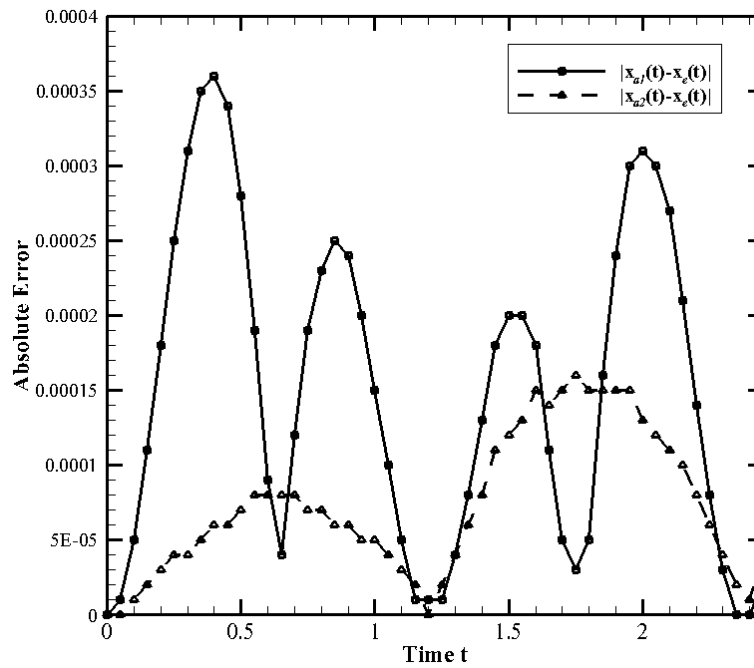
(a)

(b)

Fig. 5.11: (a) Comparison of analytical approximate periodic solutions with numerical solution for $\alpha_1 = 0.1$, $\alpha_2 = 1$, $\alpha_3 = -1.5$, $\alpha_4 = 0.27$, and $A = -2.2865$; (b) Comparison of the absolute errors between the approximate and numerical solutions.

5.6 Concluding Remarks

Presented herein is a global analysis to investigate a triple-well non-natural system, which is governed by a quadratic velocity term and an odd-parity nonlinearity. The equilibrium points and its trajectories of the nonlinear system due to the influence of various governing parameters are classified, including the effect of negative linear stiffness. All possible motions under different initial amplitudes and governing parameters are also depicted. Based on the qualitative analysis, it is found that there exist three different types of equilibrium points, i.e., a center, a saddle point, and a degenerate singular point. Intrinsic behavior of the non-natural system, from a mono-stable mode to a tri-stable state, can be controlled by the governing parameters. We also observe the interchange of heteroclinic and homoclinic orbits under different equilibrium states. In addition, the NHB method is applied to construct accurate lower-order analytical approximations for the nonlinear system. The analytical approximation results that are valid for large amplitudes of oscillation and governing parameters can achieve a sufficiently good agreement with the exact solution. Both symmetric and asymmetric oscillations around different equilibrium points are presented as well.

Chapter 6

A TRI-STABLE HYBRID ENERGY HARVESTER BASED ON MAGNETIC LEVITATION

6.1 Introduction

In this chapter, we propose a novel magnetic levitation-based electromagnetic-triboelectric energy harvester that can work well under low-frequency and low-amplitude sources. The structure of this chapter is organized as follows. Section 6.2 describes the design configuration, working principle, formation mechanism, and theoretical analysis of the proposed system. In Section 6.3, experimental results are presented to evaluate the working performance of this hybrid energy harvester. Finally, the major findings of the present work are summarized in Section 6.4.

6.2 System Design of a Tri-stable Hybrid Generator

6.2.1 Design Configuration

To design a tri-stable hybrid energy harvester, a slider-driven electromagnetic generator (EMG) and a sliding-mode triboelectric nanogenerator (TENG) were optimally integrated into a suspended structure via a magnetically levitated approach, as illustrated in Fig. 6.1. Two parallel stainless steel rods as the framework of this hybrid generator were fixed by three sets of fasteners made up of aluminum alloy.

In the present design, a cylindrical PVC tube (with a length of 37 mm) was attached to the middle fastener. Four cuboid neodymium magnets (NdFeB, $5mm \times 3mm \times 2mm$, N35 grade) were fixed to an outer sleeve around the PVC tube. The other two fasteners, each of them consisted of a micrometer and one NdFeB cylindrical magnet ($\phi 10mm \times 4mm$, N35 grade), were symmetrically placed at both sides of the PVC tube and separated by an adjustable distance from the tube. The micrometers can be used to fine-tune the design based on the theoretical analysis of this work to achieve a tri-stable nonlinear system. The EMG unit consisted of a series of copper coils and one NdFeB cylindrical magnet (moving magnet) ($\phi 12mm \times 18mm$, N35 grade) placed in the cylindrical PVC tube to restrain its motion in a single direction. The other two cylindrical magnets with their magnetic poles were oriented to

repel the moving magnet, thereby rendering the suspension of the moving magnet inside the tube.
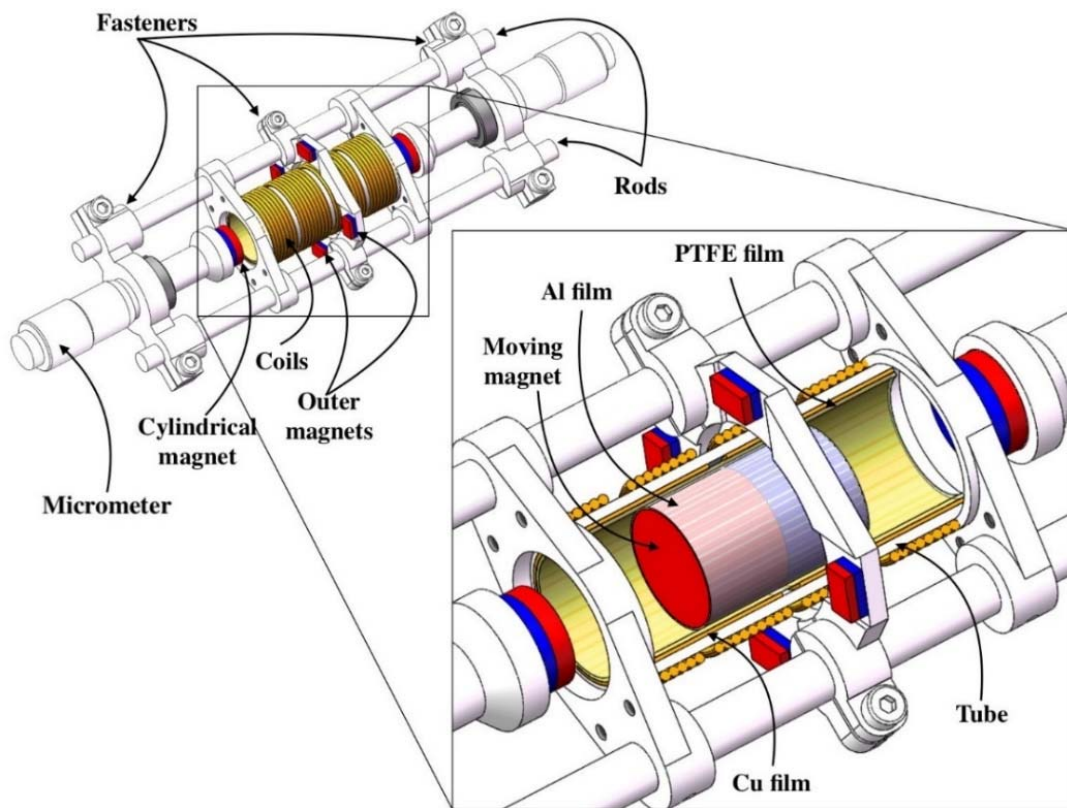
(a)
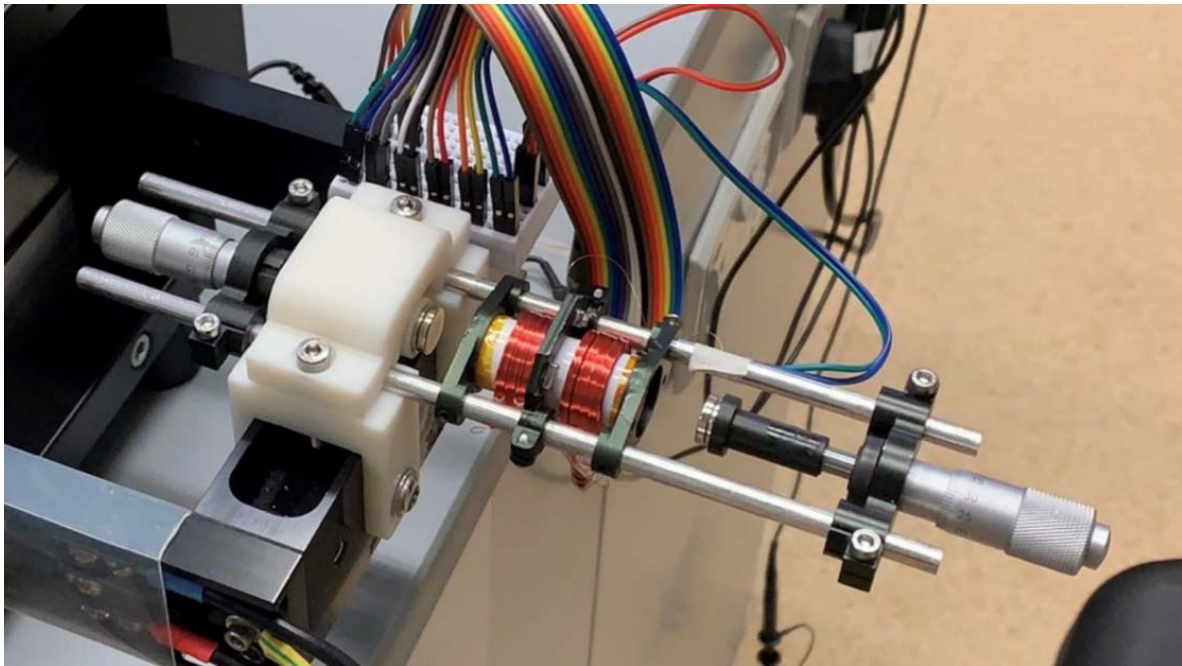
(b)

Fig. 6.1: (a) Schematic of a novel hybrid energy harvester; and (b) a fabricated prototype.

In addition, the resultant magnetic force, combined with the interaction between the moving magnet and the four outer magnets, can create a tri-stable potential well in the system. Eight ring-shaped coils (with a total number of 1900 turns) were connected in series and wrapped over the PVC tube. For the TENG unit, a 50-μm-thick aluminum (Al) film covered the curved surface of the moving magnet as a freestanding tribo-material. Two 50-μm-thick copper (Cu) films were attached on the inner surface of the PVC tube with a 0.1-mm gap between them, which can serve as back electrodes. A 50-μm-thick polytetrafluoroethylene (PTFE) film was aligned onto the surfaces of the back electrodes as another tribo-material.

6.2.2 Working Principle of the Hybrid Generator

When an external force is exerted on the hybridized system along the PVC tube, the moving magnet (as a proof mass) covered by an Al film can act as a slider to oscillate inside the tube. The sliding behavior can induce the coupling effect of the EMG and TENG units, as shown in Fig. 6.2. The EMG unit works on Faraday's law: the change of the rate of the magnetic flux through the coils develops an inductive electromotive force in the coils, as well as Lenz's law: the direction of the induced voltage in the coils opposes the change of magnetic fields produced by it (Spreemann and Manoli, 2012).

The electromagnetic output can be extracted directly from the coils. For the TENG unit, the Al electrode can generate friction during vibration modes. The internal surface of the tube was attached to a PTFE film with two Cu electrodes, which can be used to collect the power output. According to the triboelectric effect (Fan et al., 2012; Wang, 2013), PTFE has a higher electron affinity than Al, this results in negative triboelectric charges on the PTFE film surface and positive triboelectric charges on the Al surface during the direct contact of both surfaces.

Figure 6.3 shows a schematic diagram of the power generation process over a half cycle that can be divided into four stages. At the neutral position (stage (i)), the slider is at the center of the tube with equal negative charges on the two Cu electrodes. Once the slider moves to the right side of the tube (stage (ii)), the magnetic flux across the coils increases on the right side and decreases on the left. The current flow induced in the two coils by the electromagnetic induction is in opposite directions according to Lenz's law. Meanwhile, increasing the relative displacement between the slider and the PTFE film causes a different inductive potential between the two Cu electrodes, which drives inductive electrons to flow from the left electrode to the right one, forming a triboelectric current to the left. The electromagnetic and triboelectric

currents last until the slider reaches its maximum relative displacement (stage (iii)). The slider is then pushed back with decreasing the relative displacement by the restoring force of the system (stage (iv)).
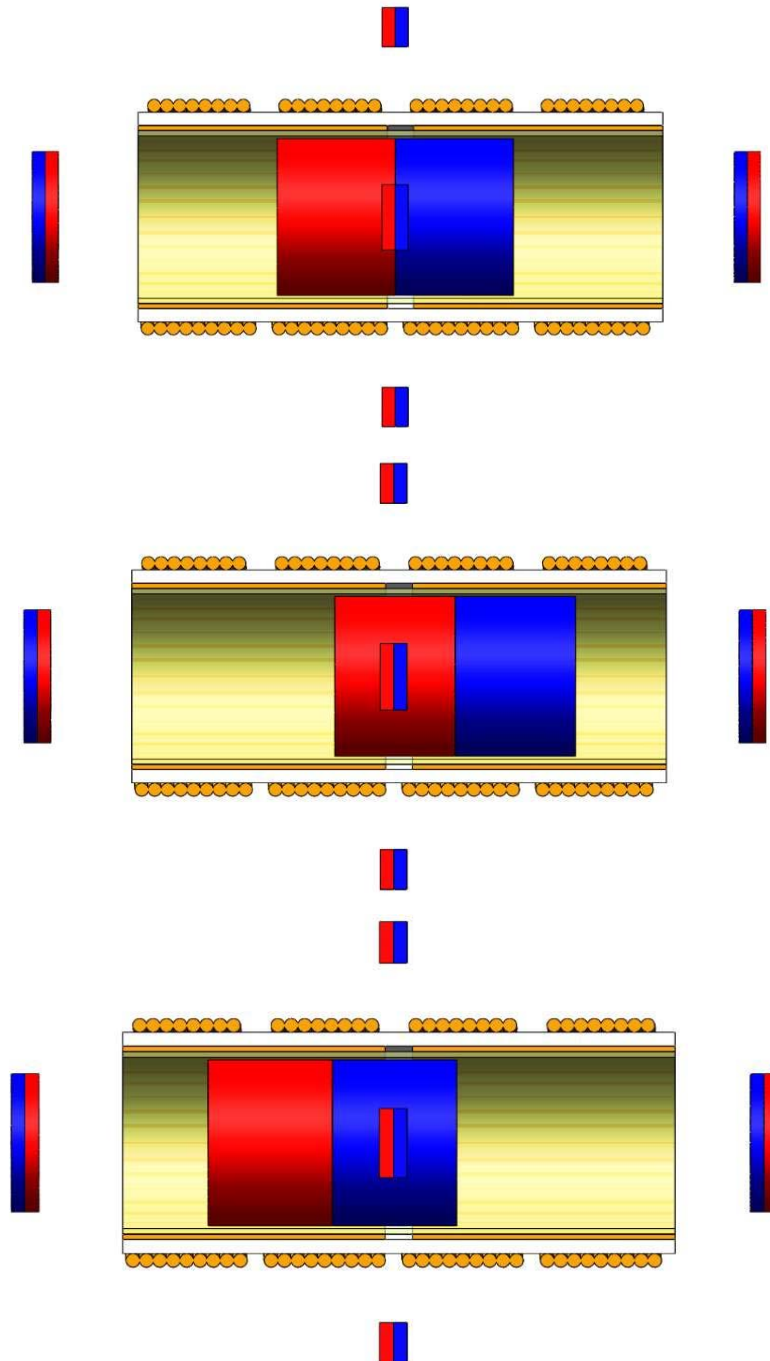
Fig. 6.2: Three stable equilibrium positions of the slider in a symmetric tri-stable state.
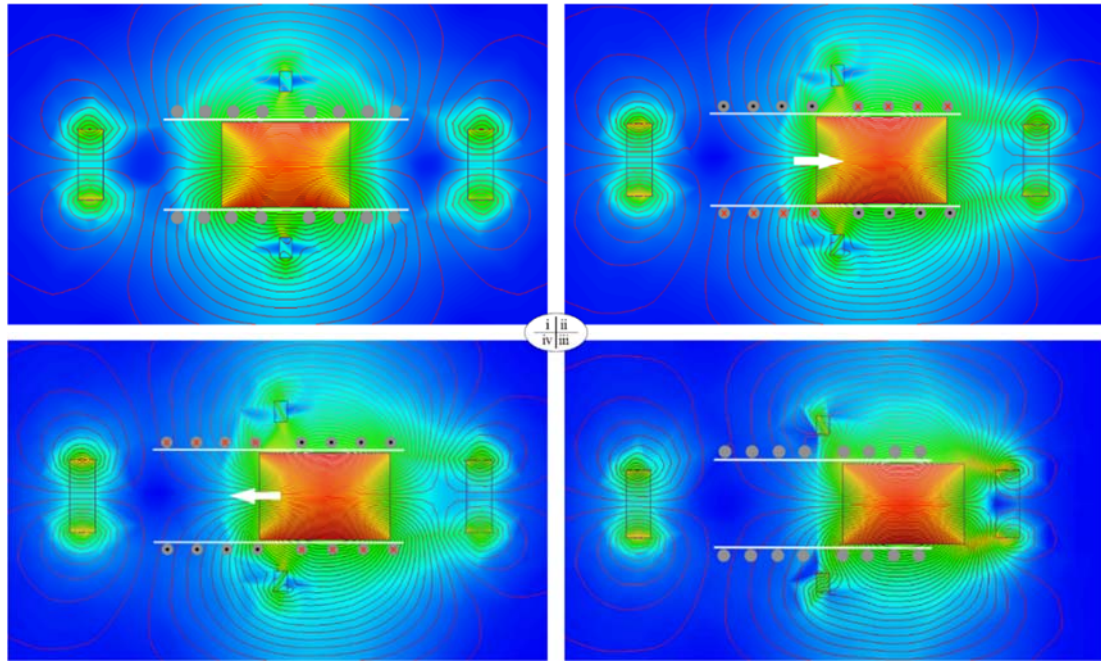
(a)
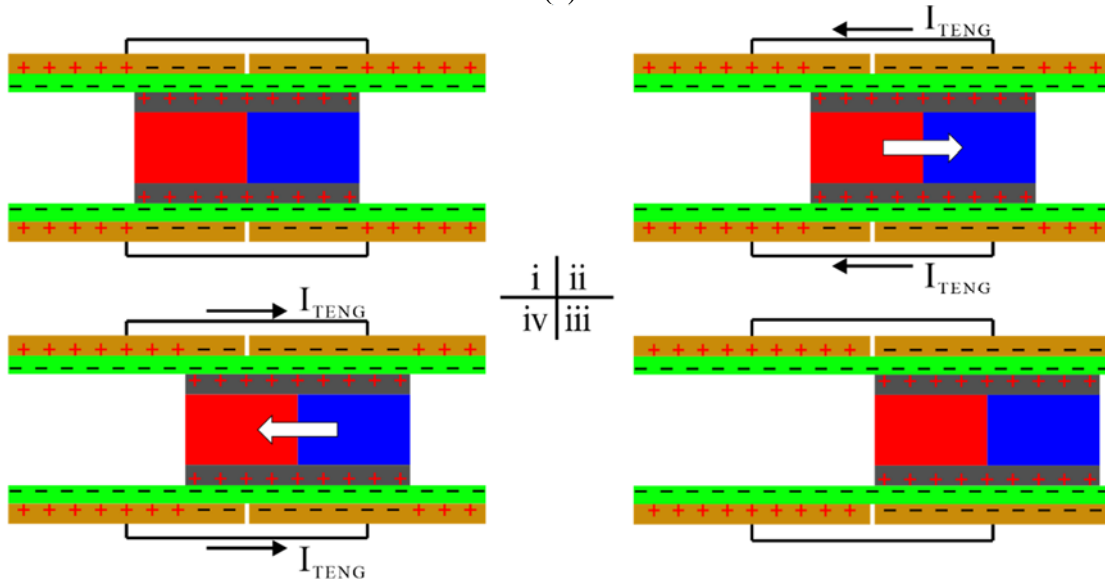
(b)

Fig. 6.3: Power generation process of (a) the EMG unit and (b) the TENG unit over a half cycle.

As the magnetic flux keeps changing across the coils, it can generate an EMG current opposite that of stage ii. Meanwhile, the potential difference between the two Cu electrodes decreases and the induced electrons flow back from the right electrode to the left one, generating a triboelectric current to the right. The slider then returns to the initial state and repeats the process on the other side. In this way, the electromagnetic and triboelectric currents can be constantly generated by the proposed system.

6.2.3 Formation of Tri-stable Nonlinear Behavior

A tri-stable nonlinear characteristic is designed in the proposed hybrid generator. This characteristic can be realized by magnetic interaction. Figure 6.4 shows the configuration and its associated geometric parameters of the magnets. Both rectangular and cylindrical coordinate systems are set and the origins of them are located at the center of the moving magnet A. Two static cylindrical magnets (i.e., C1 and C2) are placed on the z-axis. Four outer magnets, namely B1, B2, B3 and B4, are placed in the x-y plane. The magnetizing current method (Agashe and Arnold, 2008) is employed in the current magnet model. In this model, we concern the magnetic forces on the moving magnet (A) in the z-direction due to the magnetic fields produced by the four outer magnets (B1, B2, B3, and B4) and two static cylindrical magnets (C1 and C2). For simplicity and brevity, they are denoted by F_{B-z} and F_{C-z}, respectively.

According to the magnetizing current method, these two force components can be written as:

$$\vec{F}_{B-z} = \iint_S \vec{K}_m \times \vec{B}_{ext-B} dS \qquad (6.1)$$

$$\vec{F}_{C-z} = \iint_S \vec{K}_m \times \vec{B}_{ext-C} dS \qquad (6.2)$$

where $\vec{K}_m$ is the surface current density of the magnet A; $\vec{B}_{ext-B}$ and $\vec{B}_{ext-C}$ are the external magnetic flux densities of the outer magnets (B1, B2, B3, B4) and cylindrical magnets (C1, C2), respectively; S is the surface area of the magnet A; and $\vec{K}_m$ is given by

$$\vec{K}_m = \vec{m}_A \times \vec{n} \qquad (6.3)$$

where $\vec{m}_A$ is the magnetization of the magnet A and $\vec{n}$ is a unit vector in the outward direction of the surface. The magnetization of the magnet A is in the z-direction, so the magnetizing current densities $\vec{K}_m$ on the left and right surfaces of the magnet A are zero. On the curved surface of the magnet A, the direction of $\vec{K}_m$ is tangent to the cross-section of the magnet A. For simplicity, the magnetic forces can be calculated using the cylindrical coordinate system with an origin at the point O as shown in Fig. 6.4.

The magnetic flus density of an isotropic medium can be expressed by

$$\vec{B} = \mu \vec{H} \qquad (6.4)$$

122

where μ is the magnetic permeability and $\vec{H}$ is the magnetic field strength. According to Eqs. (6.1) and (6.2), it is not difficult to understand that only the magnetic field strength along the $\vec{r}$ direction needs to be considered in order to calculate the magnetic forces F_{B-z} and F_{C-z} in the z-direction.

For a cuboidal magnet (length (l) × width (w) × height (h)) with a uniform magnetization M_0 in the z-direction at the origin of the rectangular coordinate system, the x- and y-components of the magnetic field strength at a point (x_0, y_0, z_0) are given by (Agashe and Arnold, 2008):

$$H_{B-x}(x_0, y_0, z_0) = \frac{M_0}{4\pi} \cdot$$
$$\sum_{k,m,n=1}^{2} (-1)^{k+m+n} \ln\left\{ y_0 + (-1)^n \frac{l}{2} + \sqrt{\left[x_0 + (-1)^k \frac{w}{2}\right]^2 + \left[y_0 + (-1)^m \frac{l}{2}\right]^2 + \left[z_0 + (-1)^n \frac{h}{2}\right]^2} \right\} \quad (6.5)$$

$$H_{B-y}(x_0, y_0, z_0) = \frac{M_0}{4\pi} \cdot$$
$$\sum_{k,m,n=1}^{2} (-1)^{k+m+n} \ln\left\{ x_0 + (-1)^n \frac{w}{2} + \sqrt{\left[x_0 + (-1)^k \frac{w}{2}\right]^2 + \left[y_0 + (-1)^m \frac{l}{2}\right]^2 + \left[z_0 + (-1)^n \frac{h}{2}\right]^2} \right\} \quad (6.6)$$

For a cylindrical magnet (with a diameter of "$2a$" and a height of "$2t$") with a uniform magnetization M_0 in the z-direction at the origin, the r-component of the magnetic field strength at a point (ρ_0, θ_0, z_0) in the cylindrical coordinate system, using the Gaussian hypergeometric expression, is given by (Akoun and Yonnet, 1984):

$$H_{C-r}(\rho_0, \theta_0, z_0) =$$
$$-\frac{M_0}{8}\sqrt{\frac{a}{2\rho_0}}\left\{\left[\left(\frac{2a\rho_0}{(z_0 - 1.5t)^2 + \rho_0^2 + a^2}\right)^{3/2} F\left(\frac{5}{4}, \frac{3}{4}; 2; \left(\frac{2a\rho_0}{(z_0 - 1.5t)^2 + \rho_0^2 + a^2}\right)^2\right)\right]\right.$$
$$\left. -\left[\left(\frac{2a\rho_0}{(z_0 - 0.5t)^2 + \rho_0^2 + a^2}\right)^{3/2} F\left(\frac{5}{4}, \frac{3}{4}; 2; \left(\frac{2a\rho_0}{(z_0 - 0.5t)^2 + \rho_0^2 + a^2}\right)^2\right)\right]\right\} \quad (6.7)$$

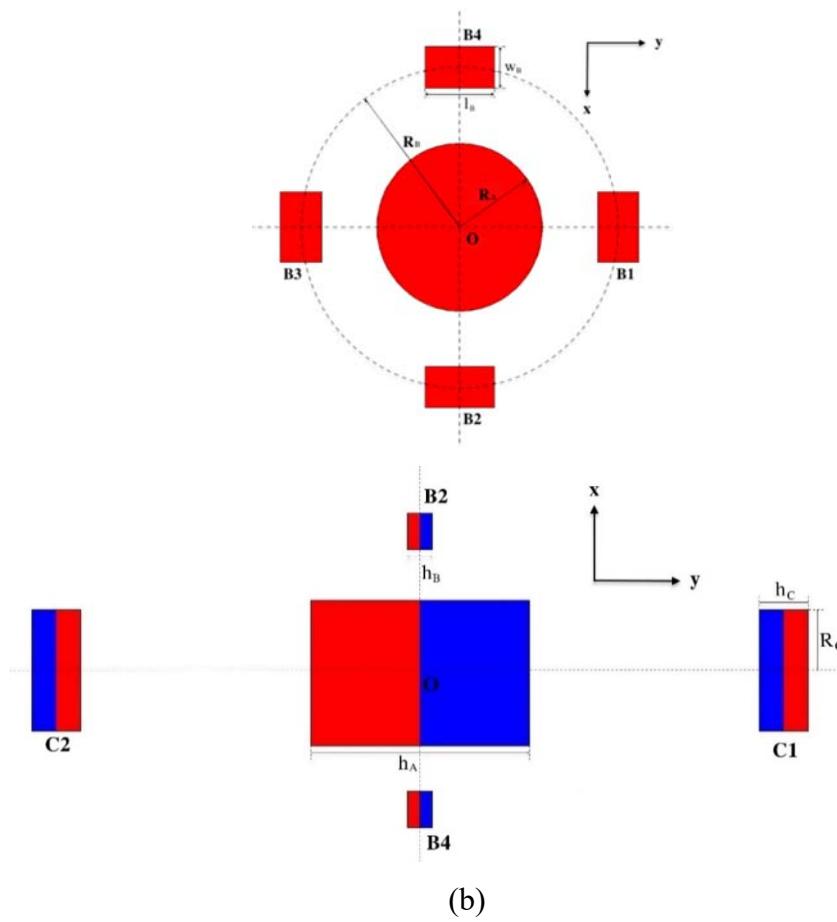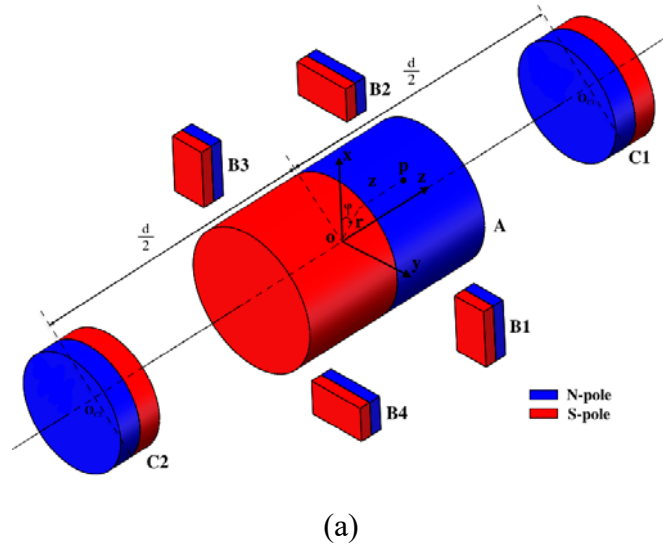where F is the Gaussian hypergeometric function.

(a)

(b)

Fig. 6.4: (a) Geometric diagram of the magnet model; and (b) cross-sectional views of the magnet model.

Substituting Eqs. (6.4)–(6.7) into Eqs. (6.1) and (6.2) with the cylindrical coordinate system given in Fig. 6.4 yields,

$$F_{B-z}(s) = -4\mu[\int_{-\frac{h_A}{2}+s}^{\frac{h_A}{2}+s}\int_0^{2\pi}\vec{K}_m\cdot\vec{H}_{B-x}(R_A\cos\theta-R_B,R_A\sin\theta,z)\cos\theta\cdot R_A d\theta dz$$
$$+\int_{-\frac{h_A}{2}+s}^{\frac{h_A}{2}+s}\int_0^{2\pi}\vec{K}_m\cdot\vec{H}_{B-y}(R_A\cos\theta-R_B,R_A\sin\theta,z)\sin\theta\cdot R_A d\theta dz] \qquad (6.8)$$

$$F_{C-z}(s) = \mu\int_{-\frac{h_A}{2}+s}^{\frac{h_A}{2}+s}\int_0^{2\pi}\vec{K}_m\cdot\left(\vec{H}_{C-r}(R_A,\theta,d/2-z)-\vec{H}_{C-r}(R_A,\theta,d/2+z)\right)\cdot R_A d\theta dz \qquad (6.9)$$

where s is the relative displacement between the slider and the tube. We observe that the proposed energy harvester performs symmetric oscillations in a horizontal position due to the magnetic forces. While the proposed energy harvester is placed in a vertical position, under the magnetic interaction and the effect of gravity, the oscillating system becomes asymmetric. These two conditions are given below:

(a) *Symmetric system*

In this condition, the restoring force (F_r) is written as

$$F_r(s) = F_{B-z}(s) + F_{C-z}(s) \qquad (6.10)$$

(b) *Asymmetric system*

In this case, the restoring force (F_r) becomes

$$F_r(s) = F_{B-z}(s) + F_{C-z}(s) + F_g \qquad (6.11)$$

where F_{B-z} and F_{C-z} are given in Eqs. (6.8) and (6.9), and F_g is the force of gravity.

In the theoretical analysis, a bifurcation study around the equilibrium states of the nonlinear system is performed to examine the existence of a triple-well behavior based on the restoring forces given in Eqs. (6.10) and (6.11). Relevant parameters and values of the hybrid energy harvester are listed in Tables 6.1 and 6.2. Figure 6.5 depicts the bifurcation behavior for the equilibrium states of the symmetric system with various distance values R_B = 10 mm, 11.5 mm, and 16 mm, where R_B is the distance between the centers of the four outer magnets (B1, B2, B3, and B4) and the coordinate origin. In the figure, d is the distance between the centers of both cylindrical magnets (C1 and C2). The solid and dashed lines denote the stable and unstable equilibria, respectively. When R_B is relatively small (R_B = 10 mm and 11.5 mm), the oscillator exhibits a mono-stable system with one stable trivial equilibrium only when $d <$ d_A (distance at point A). Increasing the value of d, a pair of saddle-node bifurcation points (at point A) occur to form a tri-stable oscillator with two unstable non-trivial equilibria and three

(non-)trivial stable equilibria. Further increasing the value of d leads the system to a bi-stable oscillator when it passes through the pitchfork bifurcation point B where the trivial stable equilibria become unstable. When R_B reaches to 16 mm, as depicted in Fig. 6.5(c), a pair of pitchfork bifurcation points disappear and the tri-stable region vanishes as well.

Table 6.1: Material properties of magnets.

Item	Material	Remanence Br (T)	Normal coercivity Hcb (kA/m)	Intrinsic coercivity Hcj (kA/m)	Mass energy product BH (kJ/m^3)
Magnets	NdFeB N35	1.17	868	955	279

Table 6.2: Material parameters and geometry of the hybrid energy harvester.

Parameters	Values
Radius (R_A) and height (h_A) of the moving magnet A	6 mm, 18 mm
Length (l_B), width (w_B) and height (h_B) of the four outer magnets (B1, B2, B3 and B4)	5 mm, 3 mm, 2 mm
Radius (R_C) and height (h_C) of the cylindrical magnets (C1 and C2)	5 mm, 4mm
Distance (R_B) between the center of the four outer magnets (B1, B2, B3 and B4) and the coordinate origin	11.5 mm
Proof mass (m_p)	0.0146 kg
Gravitational constant (g)	9.81 m/s^2
Magnetic permeability (μ_0)	$4\pi \times 10^{-7}$ H/m

Potential energy diagrams under different values of d are presented for $R_B = 10$ mm, 11.5 mm, and 16 mm in Fig. 6.6. As d increases, the oscillator, with $R_B = 10$ mm or 11.5 mm, changes from a mono-stable state to a tri-stable state, and further to a bi-stable state. In the tri-stable state, the depth of the outmost two symmetric potential wells decreases as d increases, which makes the large-amplitude inter-well motion harder to achieve since it is more difficult to escape from the outmost wells. At $R_B = 16$ mm, when d increases, the oscillator changes from a mono-stable state to a bi-stable state and the depth of the two symmetric potential wells goes deeper in the bi-stable state. Especially, when $d = 53.2$ mm in Fig. 6.5(a) and $d = 58.5$ mm in Fig. 6.5(b), the potential depth is more uniform with a lower potential barrier when comparing to other cases. Such potential shapes make the system achieve a large-amplitude inter-well motion more easily. A comparison of a tri-stable system and a mono-stable state (without the magnets B1, B2, B3, and B4) is given in Fig. 6.7. It is obvious that the potential with $R_B = 11.5$ mm and $d = 58.5$ mm requires less kinetic energy to excite a large displacement

motion. In the experimental test (horizontal orientation), this configuration of the system is employed for the proposed energy harvester to harness energy under low-level excitations.

(a)

(b)

(c)

Fig. 6.5: Bifurcation diagrams of the equilibrium solutions for $R_B =$ (a) 10 mm; (b) 11.5 mm; and (c) 16 mm.

(a)

(b)

(c)
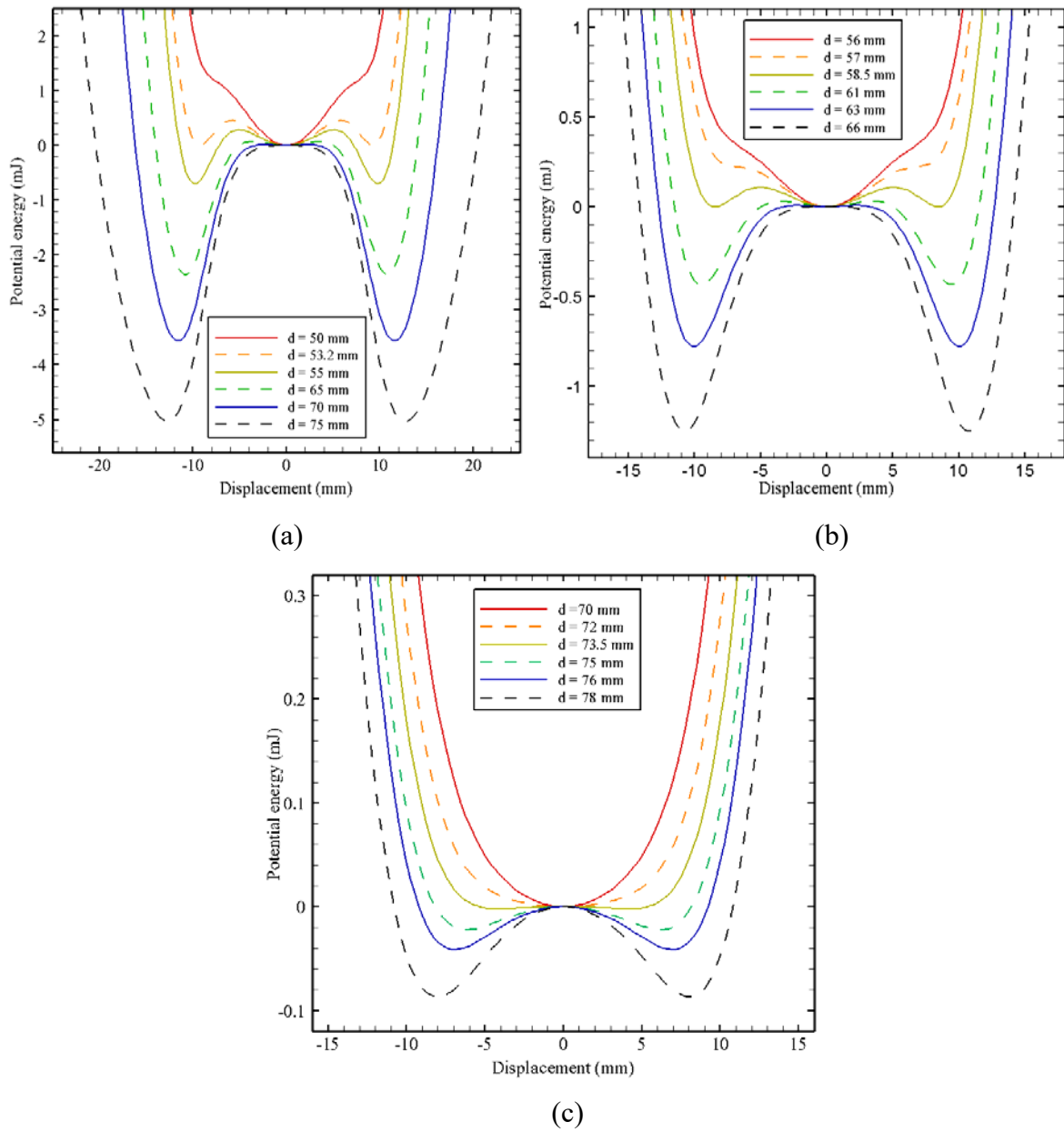
Fig. 6.6: Variation of potential energy of the symmetric tri-stable system for R_B = (a) 10 mm; (b) 11.5 mm; and (c) 16 mm.
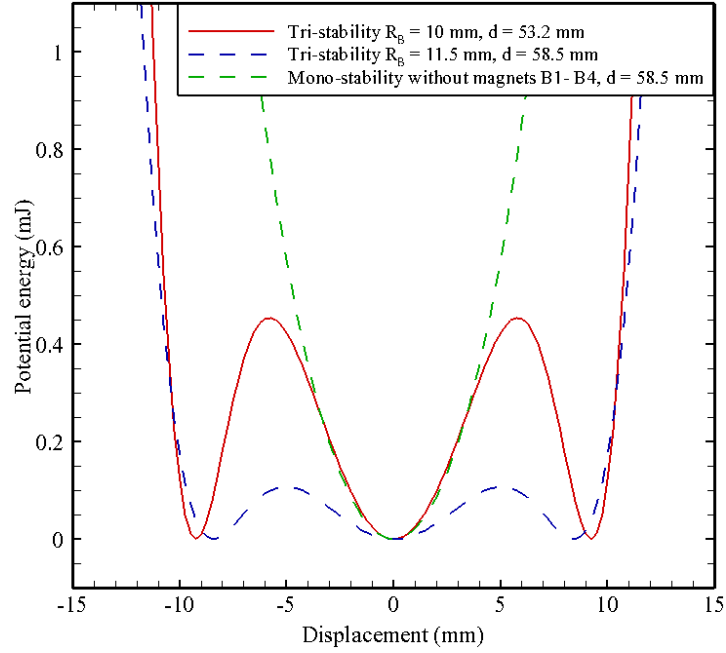
Fig. 6.7: Potential energy of the tri-stable and mono-stable configurations.

In Fig. 6.8(a), the bifurcation behavior for the equilibrium states of the asymmetric system for $R_B = 10$ mm is plotted. The solid and dashed lines denote the stable and unstable equilibria, respectively. The oscillator exhibits a mono-stable system with one stable equilibrium when $d < d_A$. Increasing the value of d, a saddle-node bifurcation point (at point A) occurs to form a bistable oscillator with one unstable equilibrium and two stable equilibria. Further increasing the value of d leads the system to a tri-stable oscillator when a saddle-node bifurcation point B occurs. The generator finally becomes a bistable system at a saddle-node bifurcation point C.

In Fig. 6.8(b), the potential energy diagram under different values of d for $R_B = 10$ mm is presented. As d increases, the oscillator changes in the sequence of: a mono-stable state → a bi-stable state → a tri-stable state. In the tri-stable state (when $d = 52.5$ mm), it is quite difficult for the system to escape from the middle well to the left well due to a higher potential barrier. The twofold-well potential (when $d = 50.5$ mm) has a uniform depth and a lower potential barrier, resulting in a much lower excitation threshold for inter-well motions. Therefore, in the following experimental test (vertical alignment), this bi-stable configuration of the system is employed for the proposed energy harvester to harness energy under low-level excitations.
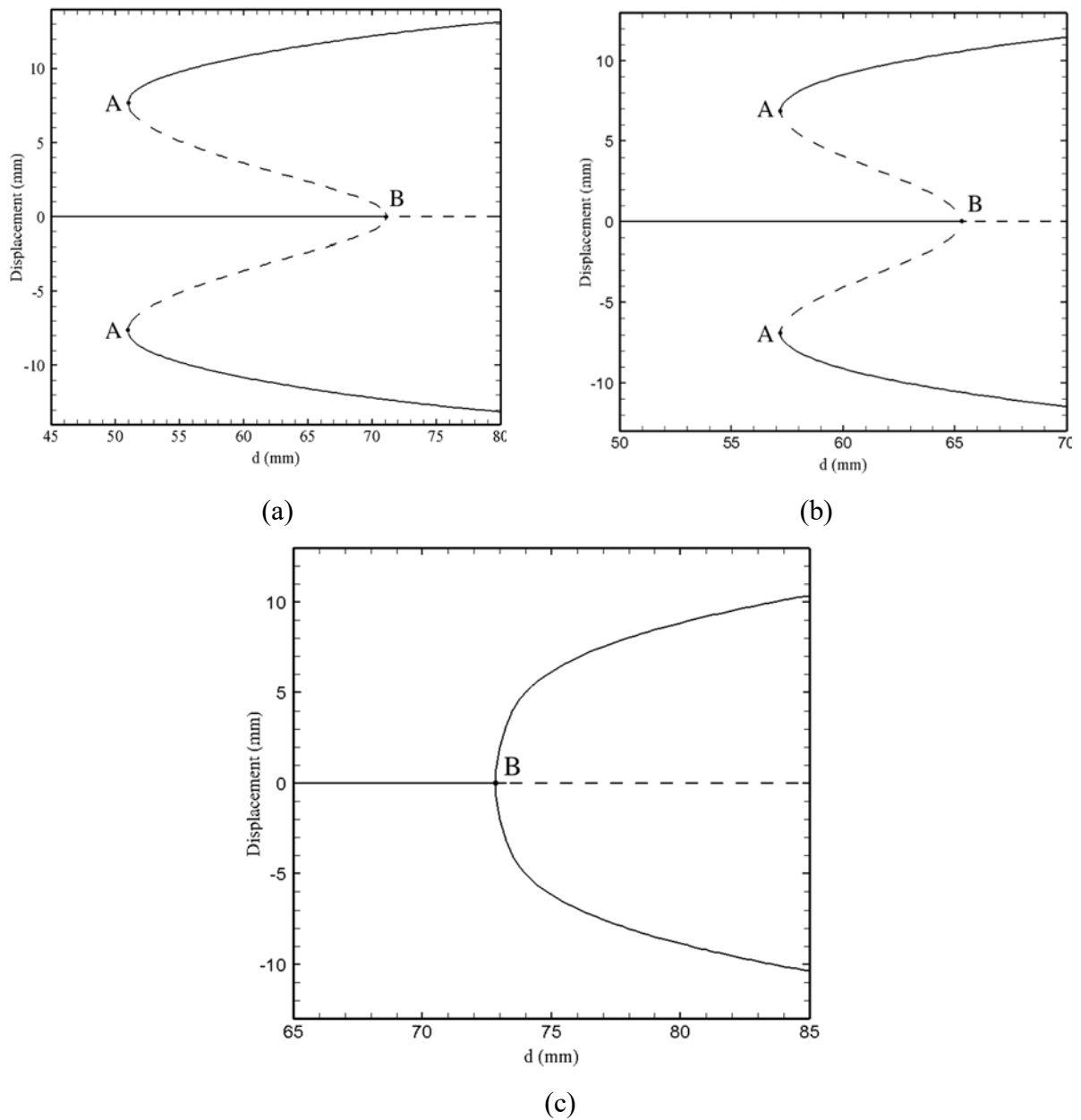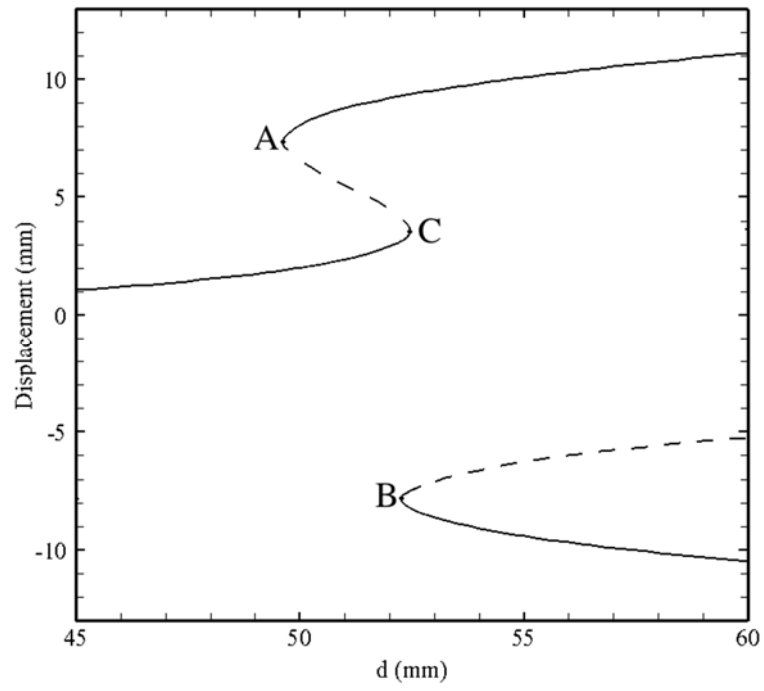
(a)
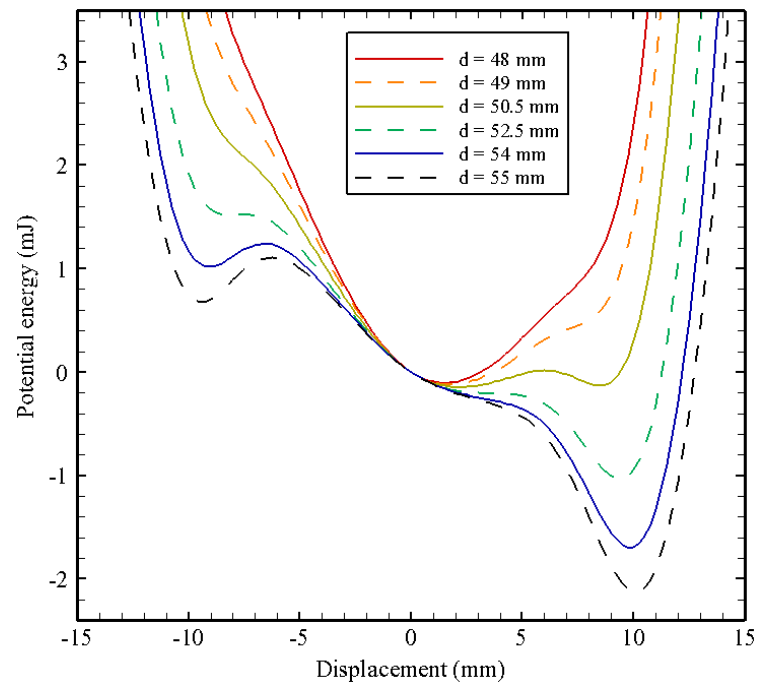
(b)

Fig. 6.8 (a) Bifurcation diagram of the equilibrium solutions for $R_B = 10$ mm; and (b) variation of potential energy of the asymmetric tri-stable system for $R_B = 10$ mm.

6.2.4 Theoretical Modeling of the Proposed System

A lumped parameter mechanical model of the hybrid energy harvester under a base excitation along the axial direction is shown in Fig. 6.9(a). The governing equation of the system is expressed by

$$m\ddot{x} + c\dot{x} + F_r(x) + f_d = -m\ddot{z}_b \tag{6.12}$$

where m is the proof mass, c is the total damping coefficient (including mechanical and electrical damping), f_d is the dry friction between the Al and PTFE films, $\ddot{z}_b$ is the input base acceleration, x is the relative displacement of the moving magnet, and $F_r(x)$ is the nonlinear restoring force of the proposed energy harvester that can be calculated by either Eq. (6.10) or Eq. (6.11). A schematic electronic circuit for power management is presented in Fig. 6.9(b).

(a)   (b)
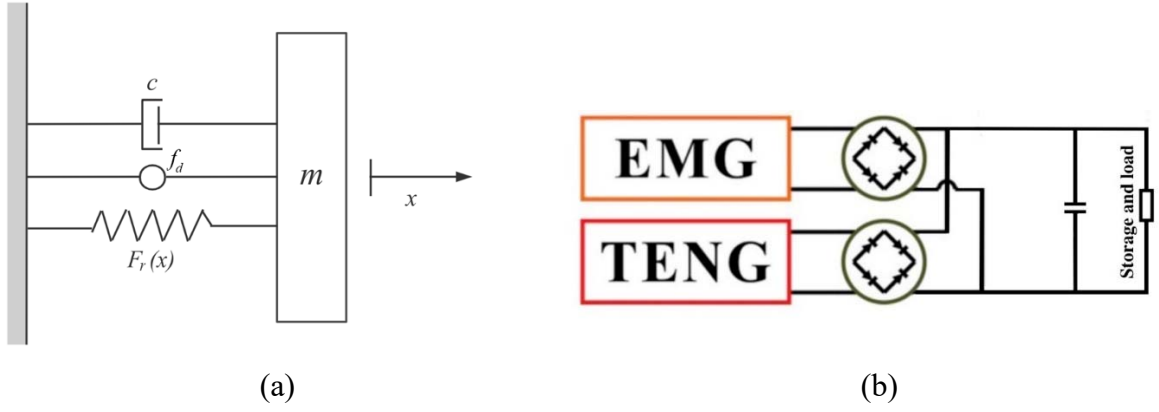
Fig. 6.9: (a) A lumped parameter model of the hybrid energy harvester; and (b) a schematic circuit of the hybrid energy harvester.

For the EMG unit, according to Faraday's Law, the open-circuit voltage V_{oc-EMG} and the short-circuit current I_{sc-EMG} are expressed as

$$V_{oc-EMG} = -Nd\phi / dt \tag{6.13}$$

$$I_{sc-EMG} = V_{oc} / R_l \tag{6.14}$$

where N, ϕ and R_l are the number of coil turns, the magnetic flux through the area enclosed by the coils, and the total internal coil resistance of the coils, respectively.

For the TENG unit, the open-circuit voltage $V_{oc-TENG}$ and the short-circuit current $I_{sc-TENG}$ are given by

$$V_{oc-TENG} = Q_{sc} / C = \Delta S \cdot \sigma / C \tag{6.15}$$

$$I_{sc-TENG} = dQ_{sc}/dt \qquad (6.16)$$

where Q_{sc}, C and σ are the short-circuit transferred charge, the capacitance between two electrodes, and the surface charge density on the slider, respectively. Because the transferred charge is induced by the triboelectric charge on the slider, the potential difference between the two electrodes is proportional to the change of the contact area, ΔS.

The EMG and TENG units naturally differ in internal resistance. When their outputs after rectifications are connected together to a load, the hybrid output is lower than the algebraic sum of the generators' outputs due to the impedance mismatch. To circumvent the problem of internal power consumption, full-wave rectifier bridges are cascaded to each of the generators to rectify the output voltage from AC to DC. This can avoid the output voltages in opposite phases that can distort the overall performance. The DC outputs will be connected in parallel to a capacitor. Although output impedance and voltage matching will affect the efficiency of energy storage in this case, phase delay may not. A standard charging circuit of the hybrid energy harvester is presented in Fig. 6.9(b). The EMG unit has low internal impedance and high current output, whereas the TENG unit has high internal impedance and it can generate much larger voltage than the EMG unit. Two full-wave bridge rectifiers are separately connected to the generators (EMG and TENG) to rectify the voltage outputs from AC to DC. The resultant DC outputs are then connected to a capacitor/load in parallel. Additional power management circuits can be utilized to match the output impedance of different working mechanisms and to achieve a better power output performance (Cao et al., 2007).

6.3 Experimental Studies

6.3.1 Shaker Test Setup

An experimental setup for the vibration test of the hybrid energy harvester is shown in Fig. 6.10. A waveform generator (KEYSIGHT 33500B) was used to generate signals to a power amplifier (APS 125) that can activate a long stroke vibration shaker (APS 113). Various excitation levels were measured by an accelerometer (DPO4104B) mounted on the shaking plate. All sampling signals were recorded and displayed on a digital oscilloscope (KEYSIGHT DSOX3014T). The hybrid energy harvester was mounted onto the shaking plate and the oscillation study was conducted in both horizontal and vertical directions, this can either eliminate or incorporate the effect of gravity.
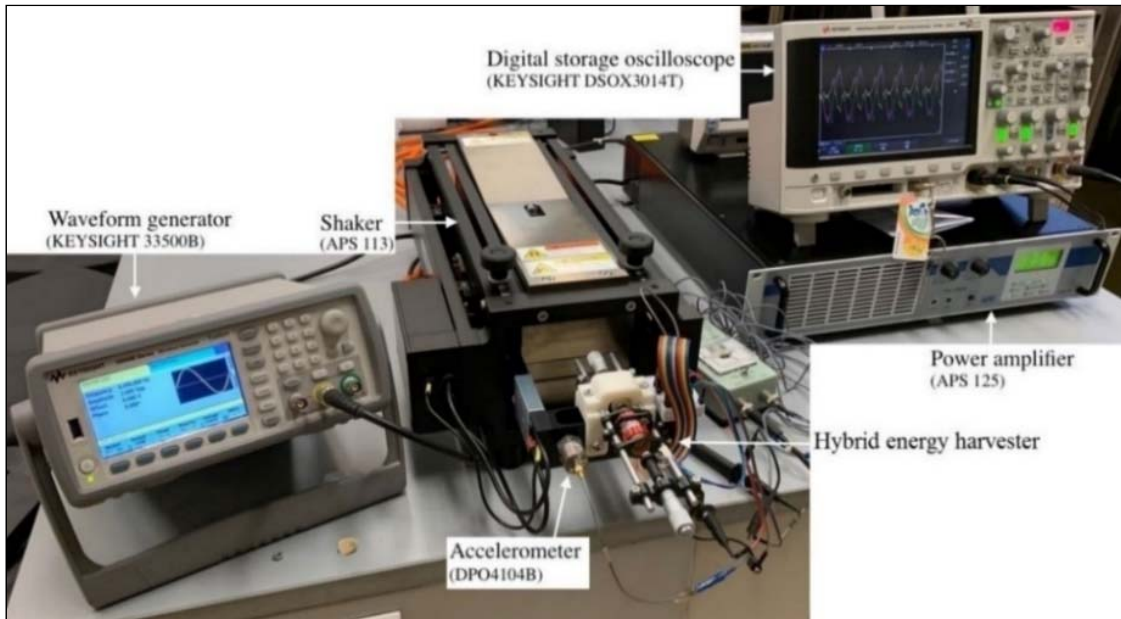
(a)
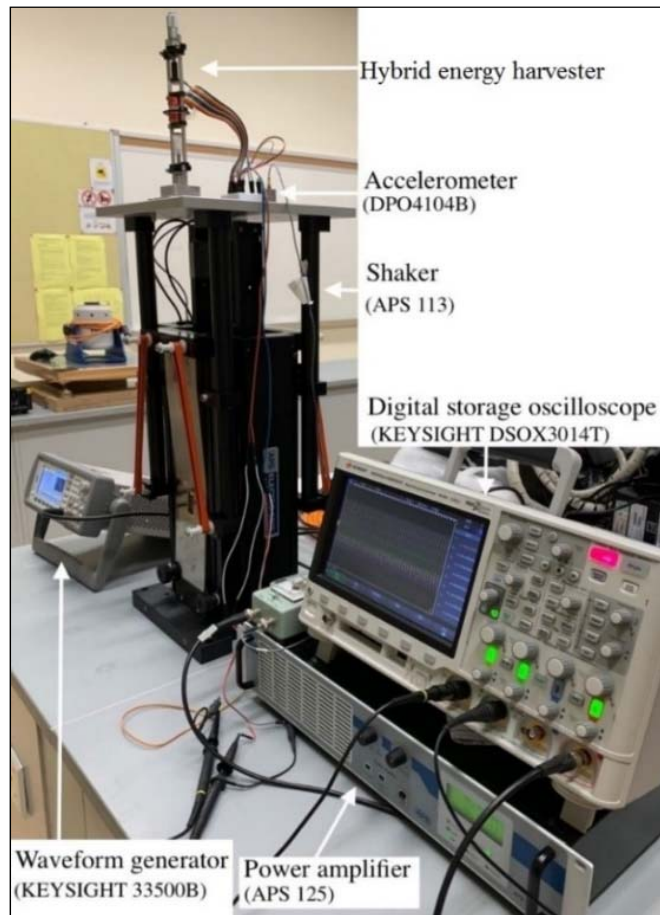
(b)

Fig. 6.10: Experimental platforms for vibration tests in (a) horizontal direction; and (b) vertical position.

6.3.2 Results and Discussion

(a) Experimental Results in a Horizontal Direction

To characterize the output performance of the fabricated prototype, we measured the open-circuit peak-to-peak voltage of each unit (EMG and TENG) in the frequency range of 3–20 Hz under various excitation levels (0.3g, 0.6g and 1g), as shown in Fig. 6.11. At 0.3g, both generators can produce a large peak-to-peak open-circuit voltage at low frequencies around 4 Hz due to the resonant inter-well oscillations. Increasing the excitation frequency, the output voltage would drop at around 5 Hz and the generators exhibit a non-resonant behavior. When the excitation amplitude increases to 0.6g, the effect of frictional damping results in a small decrease in the voltage response at low frequencies. The generators can cover a continuous bandwidth of 3–7 Hz. When the excitation amplitude further is tuned to 1g, the frequency range of the resonant inter-well oscillations can work under 3–8 Hz.

On the other hand, the measured open-circuit peak-to-peak voltage of the mono-stable counterpart without the magnets (B1, B2, B3 and B4) is shown in Fig. 6.12. The peak-to-peak open-circuit voltage can reach the highest values at about 12 Hz due to the effect of resonant oscillations, but the voltage would sharply drop at both sides of the resonant frequency. Hence, the tri-stable system can provide a wider operating bandwidth under low frequencies. In Fig. 6.13, the open-circuit voltage values of the EMG and TENG units under two excitation levels (7 Hz at 0.6g and 8 Hz at 1g) are presented. The results show that the peak-to-peak open-circuit voltage values of the EMG unit were 4.02 and 4.5 V, respectively. While for the TENG unit, the peak-to-peak open-circuit voltage values are 32.6 V and 35.4 V, respectively. In addition, to investigating the open-circuit voltage for electro-mechanical characterization, we also measured the maximum output power values of the EMG and TENG units across different external loads at 8 Hz under 1g acceleration. As depicted in Fig. 6.14, for the EMG unit, maximum power of 6.9 mW can be obtained under an optimum load resistance of 42 Ω. By contrary, the TENG unit can produce a much higher open-circuit voltage and a lower output power than those of the EMG unit due to a high internal impedance. The corresponding maximum power is 2.27 μW under a matching load resistance of 15 MΩ.
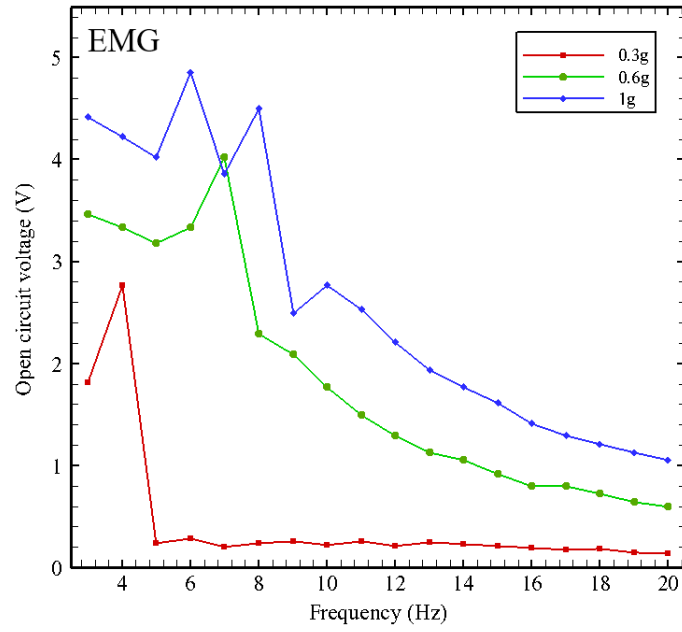
(a)
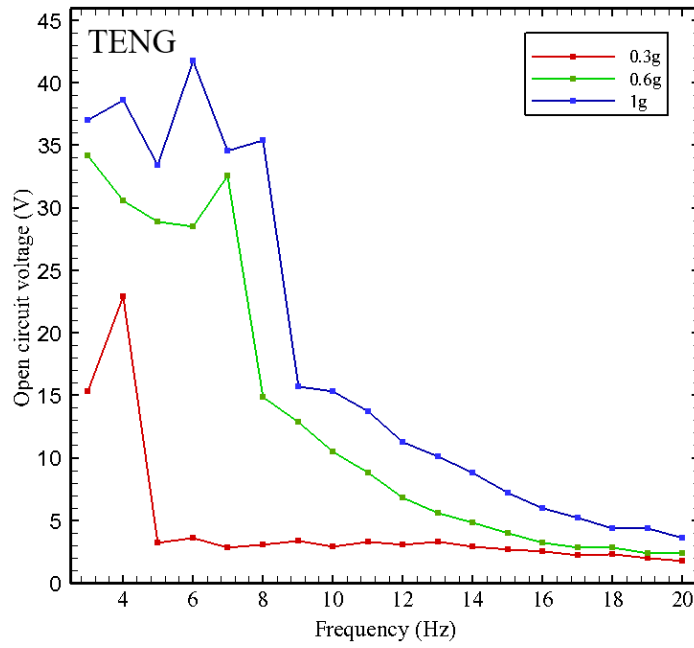
(b)

Fig. 6.11: Measured open-circuit voltages of the tri-stable system under various acceleration levels (0.3g, 0.6g, and 1g): (a) EMG and (b) TENG.

(a)

(b)

Fig. 6.12: Measured open-circuit voltages of the mono-stable system under various acceleration levels (0.3g, 0.6g, and 1g): (a) EMG and (b) TENG.

(a)

(b)
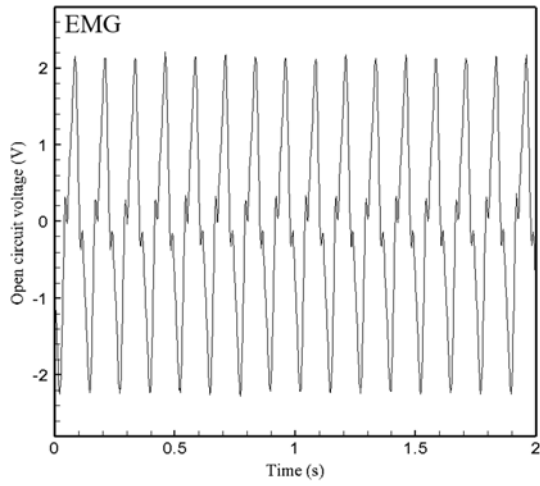
(c)
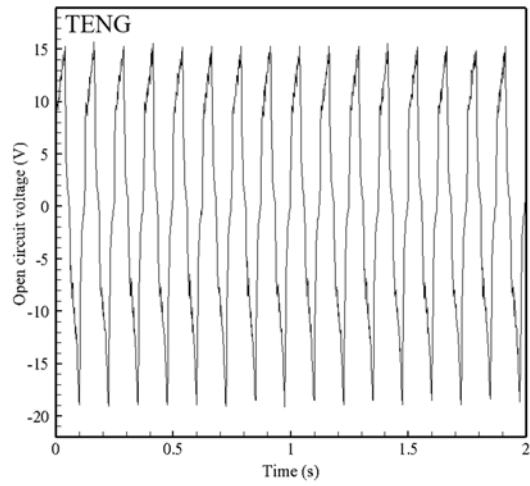
(d)

Fig. 6.13: Measured peak-to-peak open-circuit voltage curves of the tri-stable system: (a) EMG under 7 Hz at 0.6g; (b) TENG under 7 Hz at 0.6g; (c) EMG under 8 Hz at 1g; and (d) TENG under 8 Hz at 1g

.
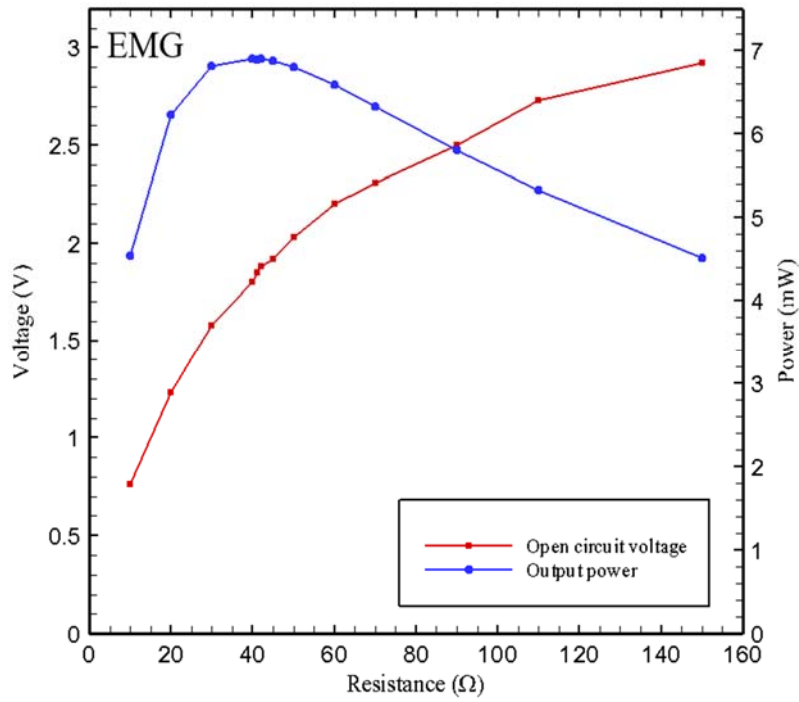
(a)
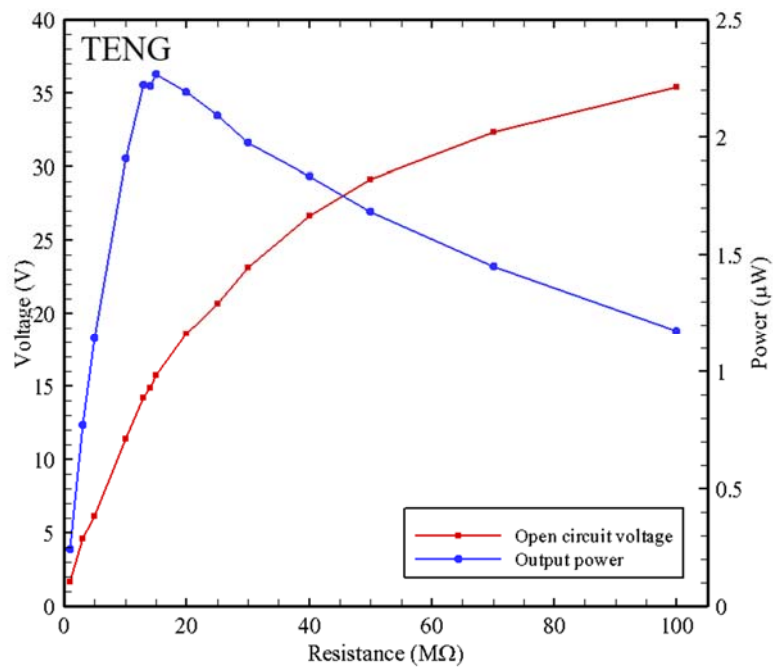
(b)

Fig. 6.14: Dependence of the open circuit voltage and peak output power on the external load resistance in the tri-stable system: (a) EMG and (b) TENG.

(b) Experimental Results in a Vertical Position

To study the effect of gravity on the prototype, the measured peak-to-peak open-circuit voltages of each unit in the frequency range of 3–20 Hz under various acceleration levels (0.3g, 0.6g, and 1g) are shown in Fig. 6.15. At 0.3g, the generators can produce a large peak-to-peak open-circuit voltage at low frequencies around 4 Hz, this is mainly caused by the resonant inter-well oscillations. With the increase of excitation frequency, the output voltage would drop at around 5 Hz due to the effect of frictional damping and the occurrence of chaotic behavior at around 9 Hz. When the excitation amplitude increases to 0.6g and 1g, the effect of frictional damping only results in a decrease of the voltage responses at around 7 Hz. In these two cases, careful observations found that the occurrence of chaotic behavior is at 10–15 Hz. The device can cover the frequency range of 3–6 Hz. Figure 6.15 also shows the existence of chaotic regions (i.e., the vertical dots in red, blue, and green colors) under various excitation levels.

In Fig. 6.16, the results show that the peak-to-peak open-circuit voltages of the EMG and TENG units are about 3.82 V and 24.1 V, respectively, under 8 Hz and 1g. In this bi-stable system, the maximum output power values of the EMG and TENG units across different external load resistance at 8 Hz under 1g are shown in Fig. 6.17. The open-circuit voltage is proportional to the load resistance. For the EMG unit, maximum power of 6.44 mW can be obtained under a matching load resistance of 41 Ω. For the TENG unit, the maximum power is 1.14 μW under a matching load resistance of 15 MΩ.

Coupling the tri-stable nonlinear behavior to the system not only can provide a wider operating bandwidth under low-frequency excitation levels, and also increase the output performance via resonant inter-well oscillations. The focus of this research mainly undertakes the dynamic characterization of the proposed system to show the existence of tri-stable potential wells, which can broaden the operating bandwidth of the hybrid energy harvester under low frequencies. The power output of this design can be enhanced by optimizing the governing parameters. To further improve the energy conversion efficiency of harvesters, a dedicated circuit design may be required to extract more power from the generators and improve the impedance match.
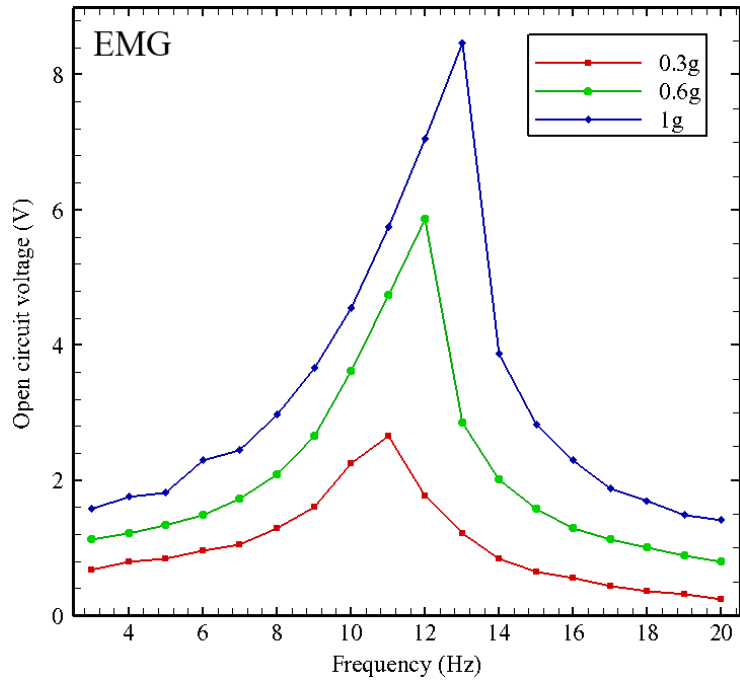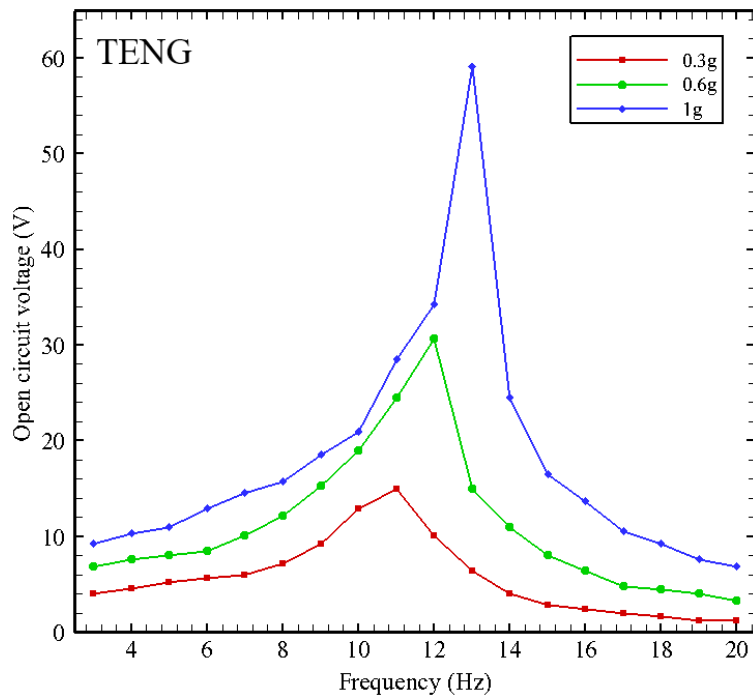
(a)
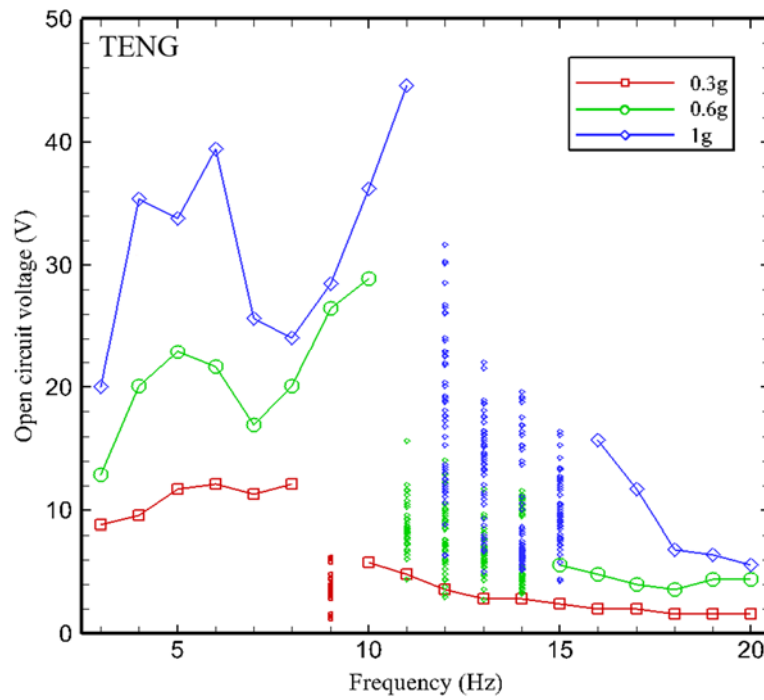
(b)

Fig. 6.15: Measured open-circuit voltages of the bi-stable system under various acceleration levels (0.3g, 0.6g, and 1g): (a) EMG and (b) TENG.
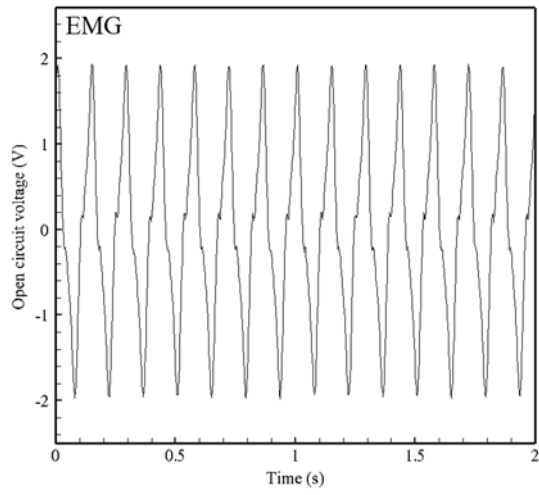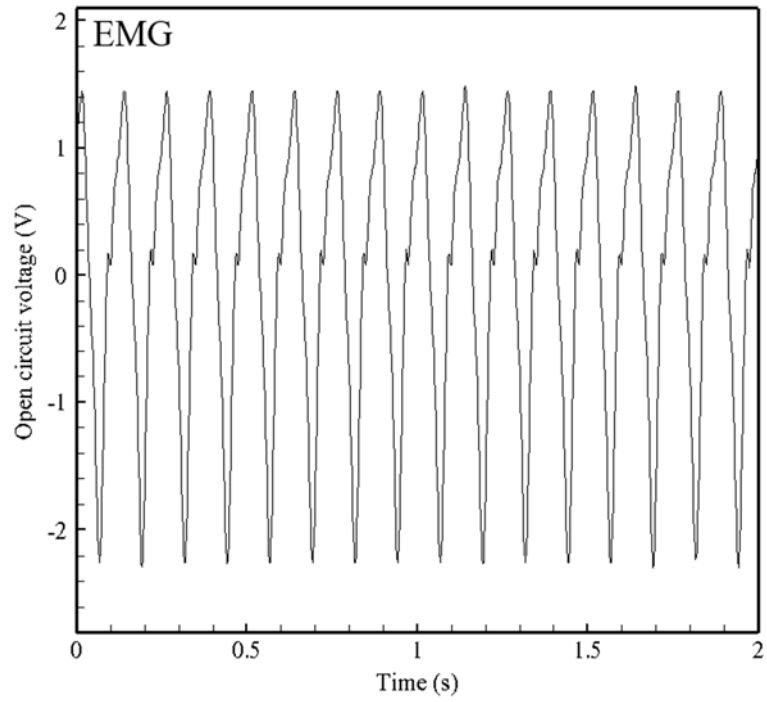
(a)
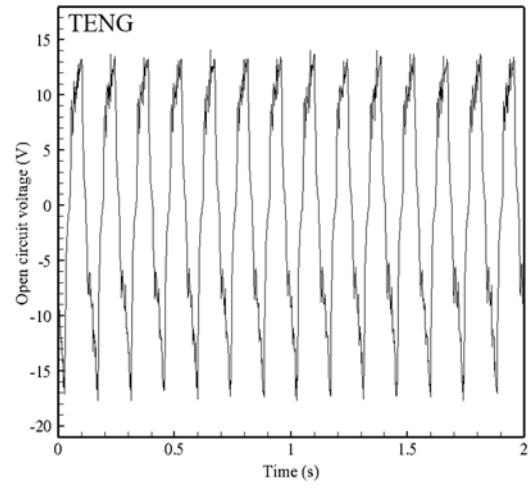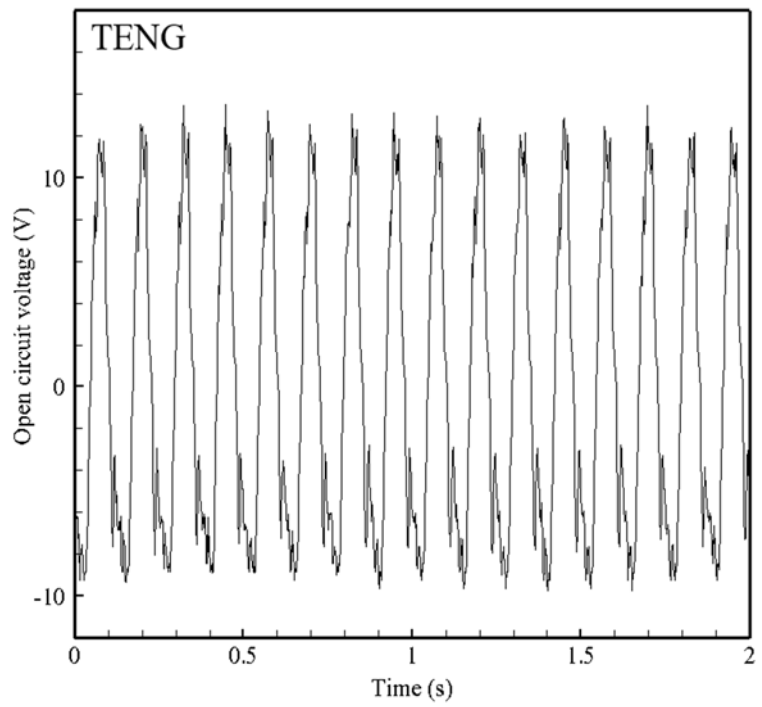

(b)

Fig. 6.16: Measured peak-to-peak open-circuit voltages of the bi-stable system under 8 Hz at 1g: (a) EMG and (b) TENG.
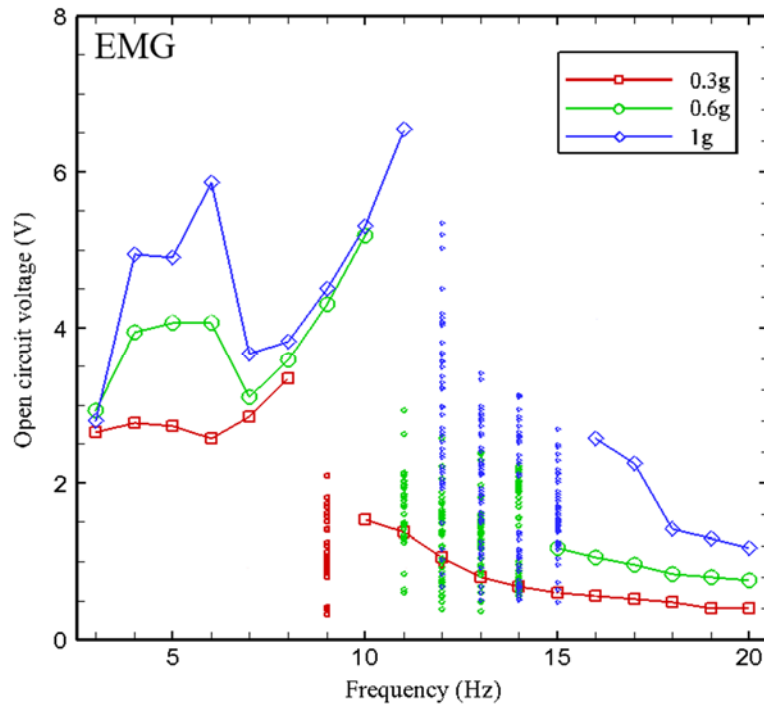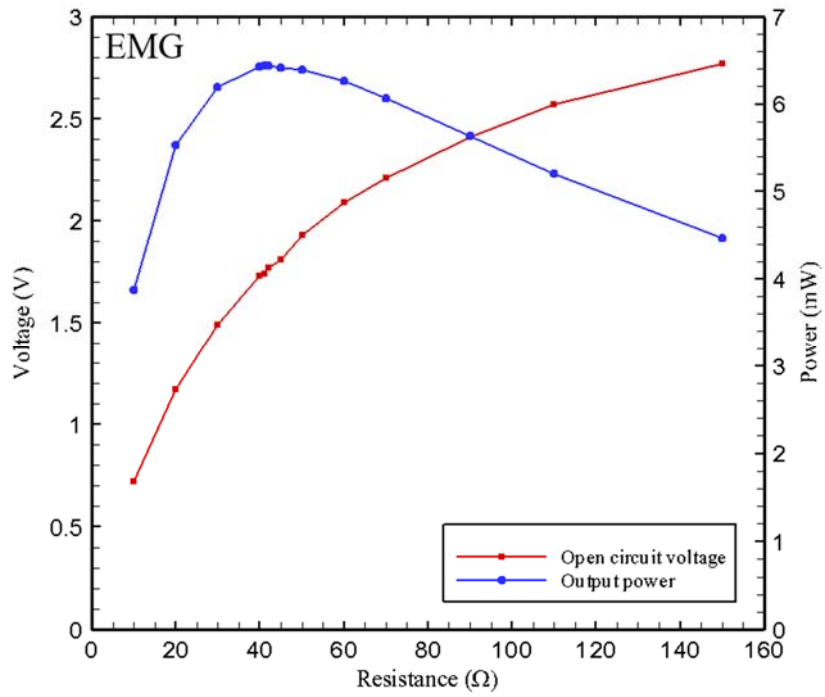
(a)
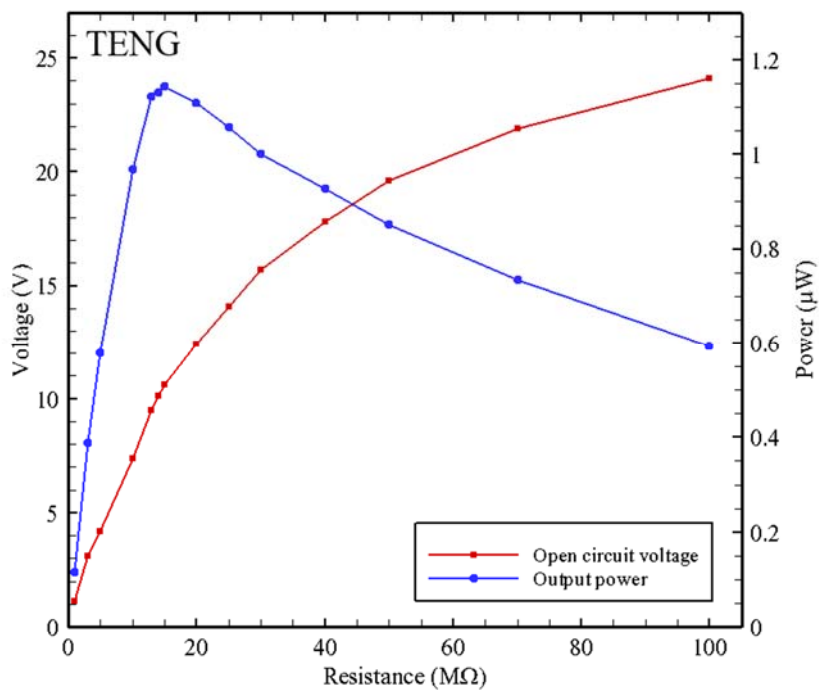
(b)

Fig. 6.17: Dependence of the open circuit voltage and peak output power on the external load resistance in the bi-stable system: (a) EMG and (b) TENG.

(c) Performance Comparison

A performance comparison between the present energy harvester and the recently proposed electromagnetic-triboelectric energy harvesters (Jin et al, 2016; Seol et al., 2016; Gupta et al., 2017; Zhu et al., 2017b; Salauddin et al., 2018; Saadatnia et al., 2018) is presented in Table 6.3. The comparison shows that the proposed hybrid energy harvester exhibits good performance in terms of the operating bandwidth and power density. In Fig. 6.18, simple demonstrations were also carried out to show that the present device can power three portable electronic humidity/temperature meters simultaneously in both horizontal and vertical orientations under 8 Hz and 1g.

Table 6.3: Performance comparison of various electromagnetic-triboelectric energy harvesters.

Approach	Acceleration	Excited frequency	Bandwidth	Peak power	Power density
Double-deck sandwiched structure for 4 TENG and 2 EMG units (Jin et al, 2016)	/	22 Hz	/	19.8 mW	167.22 W/m^3
Floating oscillator-embedded structure (Seol et al., 2016)	1.7g	7.5 Hz	8–12 Hz	/	130W/kg m^3 (TENG) 128W/kg m^3 (EMG)
Multimodal + Nonlinear stiffening (Gupta et al., 2017)	2g	80 Hz	46–114 Hz	50.2 μW	0.8 W/m^3
Cantilever structure (Zhu et al., 2017b)	2g	20 Hz	10–45 Hz	53 μW (EMG) 30 μW/ m^2 (TENG)	/
Magnetically floated type (Salauddin et al., 2018)	0.6g	4.5 Hz	3–5 Hz	10.07 mW	344 W/m^3
Linear tubular EMG unit in conjunction with grating structured freestanding mode TENG (Saadatnia et al., 2018)	2.5g	5 Hz	1–6 Hz	/	120 W/m^3
Present work (Magnetic levitation + Tri-stable nonlinearity)	1g	8 Hz	3–8 Hz	6.9 mW (Horizontal orientation)	132 W/m^3
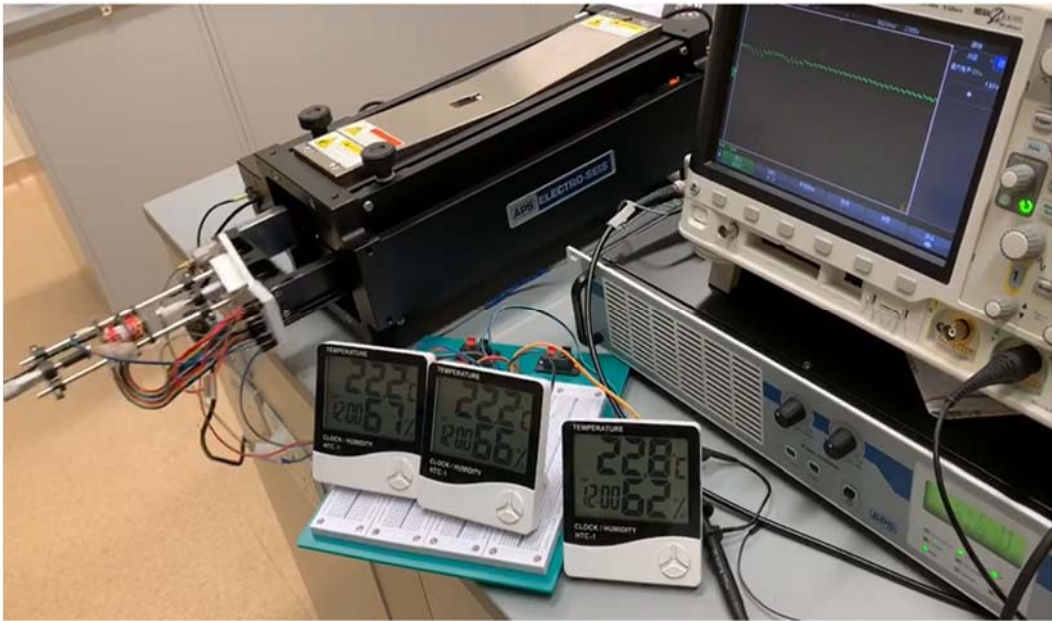
(a)
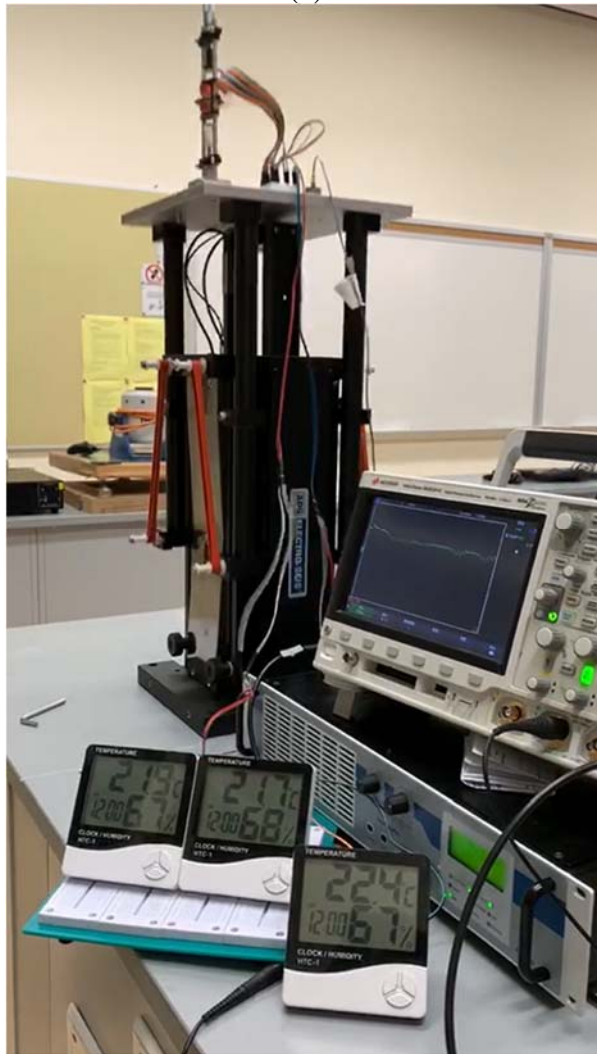
(b)

Fig. 6.18: Demonstration of the hybrid energy harvester for powering three electronic meters simultaneously in (a) horizontal and (b) vertical positions under 8 Hz and 1g.

6.4 Concluding Remarks

In this chapter, we designed a novel magnetic levitation-based hybrid energy harvester that can perform well under low-intensity and low-frequency sources. To facilitate the energy transfer, a tri-stable nonlinearity-enhanced mechanism was implemented. The tri-stable nonlinear behavior can be realized by using four outer static magnets on the same plane. Besides, a bifurcation analysis was conducted to identify the stable regime of the present system. The magnetizing current method is useful to analytically calculate the magnetic forces of this model to reveal the triple-well nonlinear phenomenon. To examine the working performance of the proposed design, experiments were carried out to demonstrate that the fabricated prototype can work well under a broadband range at 3−8 Hz. In the horizontal setup (without the effect of gravity), under 8 Hz and 1g, the EMG unit can deliver a peak output power of 6.9 mW across a loading resistance of 42 Ω, while the TENG unit can produce an output power of 2.27 μW across a loading resistance of 15 MΩ. In the vertical situation (under the effect of gravity), the fabricated prototype can produce a total power output of 6.44 mW under 8 Hz and 1g. Under low excitation levels, simple demonstrations were also carried out to demonstrate that the prototype can power up parallel-connected electronic devices.

Chapter 7
CONCLUSIONS AND RECOMMENDATIONS

7.1 Conclusions

This project has been devoted to investigating the nonlinear dynamics of MEMS resonators and vibration-based energy harvesting techniques, both of them play a critical role in the increasing demand for IoT systems. In the analysis of MEMS resonators, the NHB method has been used to construct lower-order analytical approximate solutions for both free and forced vibrations of doubly clamped MEMS resonators under electrostatic forces. The beauty of the NHB method helps understand the nature of systems in response to changes in geometrical and material parameters that affect the nonlinearity. Since micro-/nano-scale structures are involved in the design of MEMS/NEMS resonators, the nonlocal dynamic effect of micro-/nano-scale structures is also investigated in the present work. The new findings of this research are summarized as follows:

- An accurate dynamic model for the nonlinear free vibration of a doubly clamped microbeam with a one-sided electrode subjected to a suddenly applied DC voltage is derived by considering the effects of mid-plane stretching, axial residual stress, electric actuation, linear damping, and fringing field. The resultant nonlinear equation can then be solved by the NHB method. The analytical solutions are in good agreement with the numerical results obtained by the standard Runge–Kutta method for the whole stable regime. The results show that the vibration amplitude increases as the frequency decreases.

- An engineering model for the nonlinear forced vibration of a doubly clamped microbeam with a two-sided symmetric electrostatic actuation is established. Accurate frequency-amplitude responses near the first natural frequency of the system are derived by a modified NHB approach. The relationship between the vibration amplitude and natural freqeuncy of the microbeam is established and it is found that a softening effect due to the nonlinear electrostatic force is dominant in this case.

- A simple and easy approach for the determination of a size-dependent range in micro-/nano-scale structures is proposed. Three nanostructure models are investigated herein, i.e., the axial vibration of nanorods, transverse vibration of nanobeams, and free vibration of nanoplates, in accordance with the nonlocal partial-differential constitutive framework. According to this approach, the range of "e_0a" for studying the nonlocal scale effect in the

dynamical behavior of nanostructures can be taken as 0~0.8 nm. The results are compared with the available solutions to confirm its validity.

Unlike many vibration energy harvesters that can only operate over a narrow frequency bandwidth, a new electromagnetic-triboelectric tri-stable energy harvester is developed to work well under low-amplitude and low-frequency sources. A tri-stable nonlinear mechanism is adopted to enhance the working performance. The use of this device enables us to realize a self-autonomous and wireless power system. To gain deeper insights into the tri-stable nonlinear behavior, a triple-well non-natural system that exhibits both heteroclinic and homoclinic orbits under different equilibrium states has been investigated. The new findings of this work are as follows:

- A global analysis to investigate a triple-well non-natural system is presented. In qualitative analysis, the equilibrium points and its trajectories of the nonlinear system due to the influence of various governing parameters are classified, including the effect of negative linear stiffness. The intrinsic behavior of such a system, from a mono-stable mode to a tri-stable state, can be controlled by the governing parameters. The interchange of heteroclinic and homoclinic orbits under different equilibrium states are also presented. In addition, the NHB method is applied to construct accurate lower-order analytical approximations for symmetric and asymmetric oscillations around different equilibrium points of the nonlinear system. The analytical approximation results that are valid for large amplitudes of oscillation and governing parameters show good agreement with the exact solution.

- A novel magnetic levitation-based hybrid energy harvester with a tri-stable nonlinearity-enhanced mechanism is proposed. A bifurcation analysis is conducted to identify the stable regime of the present system. Besides, a prototype is also fabricated and tested to examine the performance of the proposed design. In the horizontal setup (without the effect of gravity), under 8 Hz and 1g, the EMG unit can deliver a peak output power of 6.9 mW across a loading resistance of 42 Ω, while the TENG unit can produce an output power of 2.27 μW across a loading resistance of 15 MΩ. Under the effect of gravity (i.e., in the vertical setup), the fabricated prototype can produce a total power output of 6.44 mW under 8 Hz and 1g. Using the present technique, sufficient power can be generated to support portable and wearable electronic devices.

- This research is of importance in terms of both theoretical analysis and practical implication. The implementation of a magnetic levitation approach in the present technique

can reduce the possibility of mechanical contact and impact damage, thereby ensuring long-term durability for practical use. The compact design of this battery-shaped device will foster many spin-off engineering applications and realize self-powered structural monitoring systems, because it can scavenge energy from low-frequency as well as low acceleration vibration sources, e.g., automobile transportation, railway vehicles, highway bridges, and building motions. Moreover, a series of packs (Tan et al., 2019), similar to a battery pack with an identical number of batteries, can be used to support various power levels of self-sustained low-energy electronics for structural monitoring.

7.2 Limitations and Recommendations for Future Work

In this project, we intend to provide an in-depth understanding of the complex dynamical behavior of MEMS resonators and vibration-based energy harvesters. Although relevant research studies have been well completed, there is still ample room to conduct further investigations among these problems. The following issues should be considered in future research work.

In this research, we only considered the symmetric oscillation of a doubly clamped MEMS resonator under an external harmonic force. In the case of asymmetric oscillations, a doubly clamped microbeam, subjected to a one-sided electrostatic actuation and a harmonic electrostatic load, is not investigated herein. This problem needs to be further addressed by using the recently proposed HB method (Zhou et al., 2020). In addition, further analysis of the nonlinear dynamics of complex MEMS resonators subjected to various mixed boundary supports and external excitation levels (e.g., random and constant excitations) is yet to be studied analytically. In fact, there is always an inherent mechanism to provoke bifurcations and instabilities of nonlinear dynamical systems. Instabilities and bifurcations may induce unpredictable dynamical responses, thereby causing the malfunction of MEMS devices. Furthermore, the effect of Casimir forces is significant at sub-micron scales in MEMS and NEMS, where attractive Casimir forces can cause the movable components (e.g., beams or plates) to stick together (Batra et al., 2008; Farrokhabadi et al., 2014; Stange et al., 2019). Not only the attractive interaction but the investigation of repulsive Casimir forces on such devices is also the main content of research (Munday et al., 2009), because many fundamental problems in switchable micro-/nano-scale devices remain to be resolved.

On the other hand, although this study has investigated the dynamic behavior of micro-/nano-scale structures by means of the nonlocal elasticity theory, the work only focused on the linear vibration analysis of homogeneous structures, i.e., nanorods, nanobeams, and nanoplates. Under the large deformation of such structures, the relationship of nonlinear behavior and surface stress becomes more pronounced and complicated in nature. Moreover, inhomogeneous materials, e.g., functionally gradient and carbon nanotube reinforced materials, have shown great potential in various engineering fields. The nonlinear oscillation of inhomogeneous nanostructures under different external forces is thus an emerging area for further research. With the advancement of equipment facilities and computing abilities, experiments at the nanoscale can also be used to verify the available theoretical results.

In the analysis of the vibration-based energy harvesting technique, the present design combines a slider-driven electromagnetic generator and a sliding-mode triboelectric nanogenerator into a single hub. To improve the current design, piezoelectric generators or other generator types can be combined in a smart way to harness more energy from vibration motions, resulting in a higher power density. Using the concept of multi-stable nonlinear behavior, shallower potential wells (e.g., quintuple-well potential) can be created by adjusting the arrangement of outer magnets to further improve the working performance under a low excitation threshold. Moreover, the mechanism of the inter-well jumping phenomenon under different external excitations and parameter turning strategies are still required to be investigated and refined. Although the prime concern of this project is on the exploration of nonlinearities in energy harvesting, the electromechanical coupling between mechanical transducers and adaptive electronic circuits for maximizing power output and minimizing energy loss during the power management is another key topic in future work.

To further enhance the energy conversion efficiency, the design of a dedicated circuit can extract more power from the hybrid generator. In contrast to the standard electronic circuit with rectifiers and filter capacitors, the synchronous switching circuit is viewed as an effective solution for achieving higher performance and providing better adaptability under the variation of loads. The synchronous switching harvesting on inductor (SSHI) (Guyomar et al., 2005) was first introduced to utilize the voltage inversion process to avoid the energy return phenomenon in a standard circuit. Subsequently, several improved circuits based on SSHI have been proposed, such as SSHI with magnetic rectifiers (Garbuio et al., 2009), double synchronized switch harvesting (Lallart et al., 2008), and enhanced synchronized switch harvesting (Shen et

al., 2010a). In addition, the synchronous electric charge extraction (SECE) technique (Lefeuvre et al., 2005) was raised to solve the impedance matching problem. Furthermore, an optimized SECE approach was applied to improve the working performance of SECE while keeping a low-load dependence (Wu et al., 2012). Nevertheless, all these circuit techniques are generally used for linear energy harvesters. How to optimize the design of synchronous switching circuits for wideband vibration-based energy harvesters is still a crucial problem to harness energy from ambient sources.

REFERENCES

Abdelkefi, A., Nayfeh, A. and Hajj, M. (2012) Effects of nonlinear piezoelectric coupling on energy harvesters under direct excitation, Nonlinear Dynamics, 67, 1221–1232.

Abdolvand, R., Johari, H., Ho, G.K., Erbil, A. and Ayazi, F. (2006) Quality factor in trench-refilled polysilicon beam resonators, Journal of Microelectromechanical Systems, 15(3), 471–478.

Abdoun, F., Azara, L., Daya, E.M., Potier-Ferry, M. (2009) Forced harmonic response of viscoelastic structures by an asymptotic-numerical method, Computers and Structures, 87, 91–100.

Abdulaziz, O., Noor, N.F.M. and Hashim, I. (2009) Homotopy analysis method for fully developed mhd micropolar fluid flow between vertical porous plates. International Journal for Numerical Methods in Engineering, 78(7), 817–827.

Agashe, J.S. and Arnold, D.P. (2008) A study of scaling and geometry effects on the forces between cuboidal and cylindrical magnets using analytical force solutions, Journal of Physics D: Applied Physics, 41, 105001.

Aghababaei, R. and Reddy, J.N. (2009) Nonlocal third-order shear deformation plate theory with application to bending and vibration of plates, Journal of Sound and Vibration, 326, 277–289.

Akoun, G. and Yonnet, J.P. (1984) 3D analytical calculation of the forces exerted between two cuboidal magnets, IEEE Transactions on Magnetics, 20, 1962–1964.

Algaba, A., Fernandez-Sanchez, F. and Merino, M. (2013) On Shilnikov analysis of homoclinic and heteroclinic orbits of the T-system, Journal of Computational and Nonlinear Dynamics, 8, 027001.

Ali, S.F., Adhikari, S., Friswell, M.I. and Narayanan, S. (2011) The Analysis of Piezomagnetoelastic Energy Harvesters Under Broadband Random Excitations, Journal of Applied Physics, 109(7), 074904.

Alijani, F., Amabili, M. and Bakhtiari-Nejad, F. (2011) On the accuracy of the multiple scales method for non-linear vibrations of doubly curved shallow shells, International Journal of Non-Linear Mechanics, 46(1), 170–179.

Alsaleem, F.M., Younis, M.I. and Ouakad, H.M. (2009) On the nonlinear resonances and dynamic pull-in of electrostatically actuated resonators. Journal of Micromechanics & Microengineering, 19(4), 045013.

Alsaleem, F.M., Younis, M.I. and Ruzziconi, L. (2010) An experimental and theoretical investigation of dynamic pull-In in MEMS resonators actuated electrostatically. Microelectromechanical Systems, Journal of, 19(4), 794–806.

Ando, B., Baglio, S., Trigona, C., Dumas, N., Latorre, L. and Nouet, P. (2010) Nonlinear mechanism in MEMS devices for energy harvesting applications, Journal of Micromechanics and Microengineering, 20(12), 125020.

Anjomshoa, A., Shahidi, A.R., Hassani, B. and Jomehzadeh, E. (2014) Finite element buckling analysis of multi-layered graphene sheets on elastic substrate based on nonlocal elasticity theory, Applied Mathematical Modelling, 38, 5934–5955.

Ansari, R., Fouhi, S. and Sahmani S. (2011) Calibration of the analytical nonlocal shell model for vibrations of double-walled carbon nanotubes with arbitrary boundary conditions using molecular dynamics, International Journal of Mechanical Seiences, 53, 786–792.

Ansari, R., Oskouie, M.F., Gholami, R. and Sadeghi, F. (2016) Thermo-electro-mechanical vibration of postbuckled piezoelectric Timoshenko nanobeams based on the nonlocal elasticity theory, Composites, Part B. Engineering, 89, 316–327.

Ansari, R., Sahmani, S. and Arash, B. (2010) Nonlocal plate model for free vibrations of single-layered graphene sheets, Physics Letters A, 375, 53–62.

Antaki, J.F., Bertocci, G.E., Green, E.C., Nadeem, A., Rintoul, T., Kormos, R.L. and Griffith B.P. (1995) A gait-powered autologous battery charging system for artificial organs, ASAIO Journal, 41(3), M588–M595.

Arash, B., Wang, Q., A review on the application of nonlocal elastic models in modeling of carbon nanotubes and graphenes, Comp. Mater. Sci. 51 (2012) 303–313.

Arefi, M., Mohammad-Rezaei Bidgoli, E., Dimitri, R., Bacciocchi, M. and Tornabene, F. (2019) Nonlocal bending analysis of curved nanobeams reinforced by graphene nanoplatelets. Composites Part B: Engineering, 166, 1–12.

Arietta, A.F., Hagedorn, P., Erturk, A. and Inman, D.J. (2010) A piezoelectric bistable plate for nonlinear broadband energy harvesting, Applied Physics Letters, 97(10), 104102.

Artan, R. and Lehmann, L. (2009) Initial values method for symmetric bending of micro/nano annular circular plates based on nonlocal plate theory, Journal of Computational and Theoretical Nanoscience, 6, 1125–1130.

Asfar, O.R. and Nayfeh, A.H. (1983) The application of the method of multiple scales to wave propagation in periodic structures, SIAM Review, 25(4), 455–480.

Aslanov, V. (2017) Rigid Body Dynamics for Space Applications, Butterworth-Heinemann.

Assadi, A. and Farshi, B. (2011) Stability analysis of graphene based laminated composite sheets under non-uniform inplane loading by nonlocal elasticity, Applied Mathematical Modelling, 35, 4541–4549.

Avramov, K.V. (2008) Analysis of forced vibrations by nonlinear modes, Nonlinear Dynamics, 53, 117–127.

Aya, S.A. and Tufekci, E. (2017) Modeling and analysis of out-of-plane behavior of curved nanobeams based on nonlocal elasticity, Composites Part B Engineering, 119, 184–195.

Aydogdu, M. (2009) Axial vibration of the nanorods with the nonlocal continuum rod model, Physica E, 41(5), 861–864.

Ayela, F. and Fournier, T. (1998) An experimental study of anharmonic micromachined silicon resonators. Measurement Science and Technology, 9, 1821–1830.

Azrar, L., Boutyour, E.H. and Potier-Ferry, M. (2002) Non-linear forced vibrations of plates by an asymptotic-numerical method, Journal of Sound and Vibration, 252, 657–674.

Bai, P., Zhu, G., Lin, Z.H., Jing, Q.S., Chen, J., zhang, G., Ma, J.S. and Wang. Z.l. (2013a) Integrated multilayered triboelectric nanogenerator for harvesting biomechanical energy from human motions. ACS Nano, 7(4), 3713–3719.

Bai, P., Zhu, G., Liu,Y., Chen, J., Jing, W.Q., Ma, J.S., Zhang, G. and Wang, Z.L. (2013b), Cylindrical rotating triboelectric nanogenerator. ACS Nano, 7(7), 6361–6366.

Baker, J., Roundy, S. and Wright, P. (2005) Alternative geometries for increasing power density in vibration energy scavenging for wireless sensor networks, 3rd International Energy Conversion Engineering Conference, 2, 959–970.

Barton, D.A.W., Burrow, S.G. and Clare, L.R. (2010) Energy Harvesting From Vibrations With a Nonlinear Oscillator, Journal of Vibration & Acoustics, 132(2), 021009.

Batra, R.C., Porfiri, M. and Spinello, D. (2006) Capacitance estimate for electrostatically actuated narrow microbeams, Micro & Nano Letters, 1(2), 71–73.

Batra, R.C., Porfiri, M. and Spinello, D. (2008) Reduced-order models for microelectromechanical rectangular and circular plates incorporating the Casimir force, International Journal of Solids and Structures, 45, 3558–3583.

Batra, R.C., Porfiri, M. and Spinello, D. (2008) Vibrations of narrow microbeams predeformed by an electric field, Journal of Sound and Vibration, vol. 309, 600–612, 2008.

Bayat, M., Pakar, I. and Bayat, M. (2013) Analytical solution for nonlinear vibration of an eccentrically reinforced cylindrical shell, Steel and Composite Structures, 14, 511–521.

Bayat, M., Pakar, I. and Cveticanin, L. (2014) Nonlinear vibration of stringer shell by means of extended Hamiltonian approach, Archive of Applied Mechanics, 84, 43–50.

Beeby, S.P., Torah, R.N., Tudor, M.J., Glynne-Jones, P., O'Donnell, T., Saha, C.R. and Roy, S. (2007) A micro electromagnetic generator for vibration energy harvesting, Journal of Micromechanics and Microengineering, 17(7), 1257.

Bekhoucha, F., Rechak, S., Duigou, L. and Cadou, J-M. (2013) Nonlinear forced vibrations of rotating anisotropic beams, Nonlinear Dynamics, 74, 1281–1296.

Berdy, D.F., Srisungsitthisunti, P., Xu, X. and Rhoads, J.F. (2009) Compact low frequency meandred piezoelectric energy harvester. PowerMEMS, 71–74.

Bin Yang, Chengkuo Lee, Wenfeng Xiang, Jin Xie, Johnny Han He, Rama Krishna Kotlanka, Siew Ping Low and Hanhua Feng (2009) Electromagnetic energy harvesting from

vibrations of multiple freuquencies. Journal of Micromechanics and Microengineering, 19(3), 035001.

Burrow, S.G. and Clare, L.R. (2007). A resonant generator with non- linear compliance for energy harvesting in high vibrational environments, IEEE International Electric Machines & Drives Conference, 715–720.

Burton, T.D. (1984) A perturbation method for certain non-linear oscillators, International Journal of Nonlinear Mechanics, 19(5), 397–407.

Burton, T.D. and Rahman, Z. (1986) On the multi-scale analysis of strongly non-linear forced oscillators, International Journal of Non-Linear Mechanics, 21, 135–146.

Cammarano, A., Burrow, S.G. and Barton, D.A.W. (2011) Modelling and experimental characterization of an energy harvester with bi-stable compliance characteristics, Proceedings of the Institution of Mechanical Engineers, Part I, 225(4), 475–484.

Cao, X., Chiang, W.J., King, Y.C. and Lee Y.K. (2007) Electromagnetic energy harvesting circuit with feedforward and feedback DC-DC PWM boost converter for vibration power generator system, Trans. Power Electron, 22(2), 679–685.

Caruntu D.I. and Taylor, K.N. (2014) Bifurcation type change of AC electrostatically actuated MEMS resonators due to DC bias, Shock and Vibration, 542023.

Caruntu, D.I. and Knecht, M. (2011) On nonlinear response near-half natural frequency of electrostatically actuated microresonators, International Journal of Structural Stability and Dynamics, 11, 641–672.

Chakraverty, S. and Mall, S. (2017) Artificial Neural Networks for Engineers and Scientists, Solving Ordinary Differential Equations. CRC Press, Boca Raton.

Challamel, N. and Wang, C.M. (2008) The small length scale effect for a non-local cantilever beam: a paradox solved, Nanotechnology, 19, 345703.

Chang, W.H. (1976) Analytic IC-metal-line capacitance formulas, IEEE Transactions on Microwave Theory Techniques, MTT-24, 608–611.

Chang, W.H. (1977) Correction to "Analytic IC-metal-line capacitance formulas", IEEE Transactions on Microwave Theory Techniques, MTT-25, 712.

Chen, J., Zhu, G., Yang, W., Jing, Q., Bai, P., Yang, Y., Hou, T.C. and Wang, Z.L. (2013) Harmonic-resonator-based triboelectric nanogenerator as a sustainable power source and a self- powered active vibration sensor, Advanced Materials, 25, 6094–6099.

Chen, S.H. and Cheung, Y.K. (1996) A modified Lindstedt–Poincaré method for a strongly nonlinear system with quadratic and cubic nonlinearities. Shock and Vibration, 3, 279–285.

Chen, Y.M. and Liu, J.K. (2008) Homotopy analysis method for limit cycle flutter of airfoils, Applied Mathematics and Computation, 203(2), 854–863.

Cheng, S., Wang, N. and Arnold, D.P. (2007) Modeling of magnetic vibrational energy harvesters using equivalent circuit representations, Journal of Micromechanics and Microengineering, 17(11), 2328–2335.

Cheung, Y.K., Chen, S.H. and Lau, S.L. (1991) A modified Lindstedt–Poincaré method for certain strongly non-linear oscillators. International Journal of Non-Linear Mechanics, 26, 367–378.

Chia, C.Y. (1980) Nonlinear analysis of plates, McGraw-Hill, New York.

Ching, N.N.H., Wong, H.Y., Li, W.J., Leong, P.H.W. and Wen, Z. (2002) A laser-micromachined multi-modal resonating power transducer for wireless sensing system. Sensors & Actuators A, 97–98, 685–690.

Cho, J., Anderson, M., Richards, R., Bahr, D. and Richards, C. (2005) Optimization of electromechanical coupling for a thin-film PZT membrane: II. Experiment, Journal of Micromechanics and Microengineering, 15(10), 1804–1809.

Choudhary, V. and Iniewski, K. (2017) MEMS - Fundamental Technology and Applications, CRC Press.

Civalek, Ö. and Akgöz, B. (2010) Free vibration analysis of microtubules as cytoskeleton components: nonlocal Euler–Bernoulli beam modeling, Transaction B: Mechanical Engineering, 17, 367–375.

Civalek, Ö. and Demir, C. (2011) Buckling and bending analyses of cantilever carbon nanotubes using the Euler–Bernoulli beam theory based on non-local continuum model, Asian Journal of Civil Engineering, 12(5), 651–661.

Comi, C., Zega, V. and Corigliano, A. (2020) Nonlinear mechanics in resonant inertial micro sensors, International Journal of Non-Linear Mechanics, 120, 103386.

Constable, R.T., Kenneth, R.P., Ella, B.W., Einar, M., Michael, W., Weijia, N. and Donald, S. (2004) Sentence complexity and input modality effects in sentence comprehension: an FMRI study. Neuroimage, 22(1), 11–21.

Cook-Chennault, K.A., Thambi, N. and Sastry, A.M. (2008) Powering MEMS portable devices-A review of non-regenerative and regenerative power supply systems with special emphasis on piezoelectric energy harvesting systems, Smart Materials and Structures, 17, 043001.

Cottone, F., Vocca, H. and Gammaitoni, L. (2009) Nonlinear Energy Harvesting, Physical Review Letters, 102, 080601.

Dantas, W.G. and Gusso, A. (2018) Analysis of the chaotic dynamics of MEMS/NEMS doubly clamped beam resonators with two-sided electrodes, International Journal of Bifurcation and Chaos, vol. 28, 1850122.

Daqaq, M.F. (2010) Response of uni-modal Duffing type harvesters to random forced excitations, Journal of Sound and Vibration, 329(18), 3621–3631.

Daqaq, M.F. (2011) Transduction of a bistable inductive generator driven by white and exponentially correlated Gaussian noise, Journal of Sound and Vibration, 330(11), 2554–2564.

Daqaq, M. F. and Bode, D. (2011) Exploring the parametric amplification phenomenon for energy harvesting, Proceedings of the Institution of Mechanical Engineers, Part I, 225(4), 456–466.

Daqaq, M.F., Masana, R., Erturk, A. and Quinn, D.D. (2014) On the role of nonlinearities in vibratory energy harvesting: A critical review and discussion, Applied Mechanics Reviews, 66, 040801.

Daqaq, M.F., Stabler, C., Qaroush, Y. and Seuaciuc-Osorio, T. (2009) Investigation of power harvesting via parametric excitations, Journal of Intelligent Material Systems and Structures, 20(5), 545–557.

De Boer, M.P. and Michalske, T.A. (1999) Accurate method for determining adhesion of cantilever beams, Journal of Applied Physics, 86, 817–827.

Dehrouyeh-Semnani, A.M., Nikkhah-Bahrami, M. and Yazdi, M.R.H. (2017a) On nonlinear stability of fluid-conveying imperfect micropipes. International Journal of Engineering Science, 120, 254–271.

Dehrouyeh-Semnani, A.M., Nikkhah-Bahrami, M. and Yazdi, M.R.H. (2017b) On nonlinear vibrations of micropipes conveying fluid, International Journal of Engineering Science, 117, 20–33.

Denhoff, M.W. (2003) A measurement of young's modulus and residual stress in mems bridges using a surface profiler, Journal of Micromechanics & Microengineering, 13(5), 686–692.

Domme, D.J. (2008) Experimental and analytical characterization of a transducer for energy harvesting through electromagnetic induction, Master book, Virginia State University, Petersburg.

Duan, W.H. and Wang, C.M. (2007) Exact solutions for axisymmetric bending of micro/nanoscale circular plates based on nonlocal plate theory, Nanotechnology, 18, 385704.

Duan, W.H., Wang, C.M. and Zhang, Y.Y. (2007) Calibration of nonlocal scaling effect parameter for free vibration of carbon nanotubes by molecular dynamics, Journal of Applied Physics, 101, 024305.

Ebrahimi, F. and Barati, M.R. (2017) Buckling analysis of nonlocal third-order shear deformable functionally graded piezoelectric nanobeams embedded in elastic medium, Journal of the Brazilian Society of Mechanical Sciences & Engineering, 39(3), 937–952.

Ebrahimi, F. and Barati, M.R. (2018) Vibration analysis of smart piezoelectrically actuated nanobeams subjected to magneto-electrical field in thermal environment, Journal of Vibration and Control, 24, 549–564.

Edelen, D.G.B. (1976) Nonlocal Field Theories, In: Eringe (Ed.), Continuum Physics (IV), Academic Press, New York, 75–204.

Elshurafa, A.M., Khirallah, K., Tawfik, H.H., Emira, A., Abdel Aziz, A.K.S. and Sedky, S.M.(2011) Nonlinear dynamics of spring softening and hardening in folded-MEMS comb drive resonators, Journal of Microelectromechanical Systems, 20, 943–958.

Elvin, N. and Erturk A. (2013) Advances in Energy Harvesting Methods, Springer.

Eringen, A.C. (1972). Nonlocal polar elastic continua. International Journal of Engineering Science, 10(1), 1–16.

Eringen, A.C. (1983) On differential equations of nonlocal elasticity and solutions of screw dislocation and surface waves, Journal of Applied Physics, 54, 4703–4710.

Eringen, A.C. (2002) Nonlocal Continuum Field Theories. Springer Science & Business Media.

Eringen, A.C. and Edelen, D.G.B. (1972) On nonlocal elasticity, International Journal of Engineering Science, 10(3), 233–248.

Erturk, A. and Inman, D.J. (2011) Broadband piezoelectric power generation on high-energy orbits of the bistable Duffing oscillator with electromechanical coupling, Journal of Sound and Vibration, 330, 2339–2353.

Erturk, A., Hoffmann, J., and Inman, D.J. (2009) A piezomagnetoelastic structure for broadband vibration energy harvesting, Applied Physics Letters, 94(25), 254102.

Fan, F., Tian, Z. and Wang, Z.L. (2012) Flexible triboelectric generator, Nano Energy, 1, 328–334.

Fan, K.Q., Liu, S.H., Liu, H.Y., Zhu, Y.M., Wang, W.D. and Zhang, D.X. (2018) Scavenging energy from ultra-low frequency mechanical excitations through a bi-directional hybrid energy harvester, Applied Energy, 216, 8–20.

Fang, Y. and Li, P. (2013). A new approach and model for accurate determination of the dynamic pull-in parameters of microbeams actuated by a step voltage, Journal of Micromechanics & Microengineering, 23(4), 045010.

Farokhi, H., Ghayesh, M.H., Gholipour, A. and Tavallaeinejad, M. (2018a) Stability and nonlinear dynamical analysis of functionally graded microplates, Microsystem Technologies, 24, 2109–2121.

Farokhi, H. and Ghayesh, M.H. (2018b) Supercritical nonlinear parametric dynamics of Timoshenko microbeams, Communications in Nonlinear Science and Numerical Simulation, 59, 592–605.

Farrokhabadi, A., Abadian, N., Rach, R. and Abadyan, M. (2014) Theoretical modeling of the Casimir force-induced instability in freestanding nanowires with circular cross-section, Physica E, 63, 67–80.

Ferrari, M., Bau, M., Guizzetti, M. and Ferrari, V. (2011) A single-magnet nonlinear piezoelectric converter for enhanced energy harvesting from random vibrations, Sensors and Actuators A, 172(1), 287–292.

Ferrari, M., Ferrari, V., Guizzetti, M., Ando, B., Baglio, S. and Trigona, C. (2010) Improved energy harvesting from wideband vibrations by nonlinear piezoelectric converters, Sensors and Actuators A, 162(2), 425–431.

Fu, Y.F., Zhang, J. and Jiang, Y.J. (2010) Influences of the surface energies on the nonlinear static and dynamic behaviors of nanobeams, Physica E: Low-Dimensional Systems and Nanostructures, 42, 2268–2273.

Gammaitoni, L., Cottone, F., Neri, I. and Vocca, H. (2009) Noise Harvesting, AIP Conference American Institute of Procics, 1129(1), 651–654.

Ganapathi, M. and Polit, O. (2017) Dynamic characteristics of curved nanobeams using nonlocal higher-order curved beam theory, Physica E Low Dimensional Systems & Nanostructures, S1386947716314345.

Gao, M.Y., Wang, Y., Wang, Y.T. and Wang, P. (2018). Experimental investigation of non-linear multi-stable electromagnetic-induction energy harvesting mechanism by magnetic levitation oscillation, Applied Energy, 220, 856–876.

Garbuio, L., Lallart, M., Guyomar, D., Richard, C. and Audigier, D. (2009) Mechanical energy harvester with ultralow threshold rectification based on SSHI nonlinear technique, IEEE Transactions on Industrial Electronics, 56, 1048–1056

Garbuio, L., Lallart, M., Guyomar, D., Richard, C. and Audigier, D. (2009) Mechanical energy harvester with ultralow threshold rectification based on SSHI nonlinear technique, IEEE Transactions on Industrial Electronics, 56, 1048–1056.

Ghayesh, M.H. (2018) Dynamics of functionally graded viscoelastic microbeams, International Journal of Engineering Science, 124, 115–131.

Ghayesh, M.H. (2019) Viscoelastic mechanics of Timoshenko functionally graded imperfect microbeams, Composite Structures, 225, 110974.

Ghayesh, M.H. and Amabili, M. (2012) Internal resonance and nonlinear response of an axially moving beam: Two numerical techniques, Coupled Systems Mechanics, 1, 235–245.

Ghayesh, M.H. and Farokhi, H. (2017) Nonlinear mechanics of doubly curved shallow microshells, International Journal of Engineering Science, 119, 288–304.

Ghayesh, M.H. and Farokhi, H. (2018) Nonlinear dynamics of doubly curved shallow microshells, Nonlinear Dynamics, 92, 803–814.

Ghayesh, M.H., Farokhi, H. and Amabili, M. (2013) Nonlinear behavior of electrically actuated MEMS resonators, International Journal of Engineering Science, 71, 137–155.

Goh, K.B., Li, H. and Lam, K.Y. (2018) Modeling the urea-actuated osmotic pressure response of urease-loaded hydrogel for osmotic urea biosensor, Sensors and Actuators: Chemical, B., 268, 465–474.

Goh, K.B., Li, H. and Lam, K.Y. (2019) Modeling the dual oxygen- and pH-stimulated response of hemoglobin-loaded polyampholyte hydrogel for oxygen-pH coupled biosensor platform, Sensors & Actuators: Chemical, B., 286, 421–428.

Green, P. L., Worden, K., Atalla, K. and Sims, N. D. (2012) The benefits of Duffing-Type nonlinearities and electrical optimization of a mono-stable energy harvester under white Gaussian excitations, Journal of Sound and Vibrations, 331, 4504–4517.

Gu, L. and Livermore, C. (2011) Impact-driven, frequency up-converting coupled vibration energy harvesting device for low frequency operation, Smart Materials and Structures, 20, 045004.

Guo, H.Y., Chen, J., Tian, L., Leng, Q., Xi, Y., Hu, C.G (2014) Airflow-induced triboelectric nanogenerator as a self-powered sensor for detecting humidity and airflow rate, ACS Applied Materials & Interfaces, 6(19), 17184–17189.

Guo, H.Y., Chen, J., Leng, Q., Xi, Y., Wang, M.J., He, X.M. and Hu, C.G. (2015a) Spiral-interdigital-electrode-based multifunctional device: dual-functional triboelectric generator and dual-functional self-powered sensor, Nano Energy, 12, 626–635.

Guo, H.Y., Leng, Q., He, X.M., Wang, M.J., Chen, J., Hu, C.G. and Xi, Y. (2015b), A triboelectric generator based on checker-like interdigital electrodes with a sandwiched pet thin film for harvesting sliding energy in all directions. Advanced Energy Materials, 5(1), 1–9.

Guo, S.Q. and Yang, S.P. (2012) Axial vibration analysis of nanocones based on nonlocal elasticity theory, Acta Mechanica Sinica, 28, 801–807.

Guo, Y.B., Zhang, X.S., Wang, Y., Gong, W., Zhang, Q.H., Wang, H.Z., Brugger, J. (2018a) All-fiber hybrid piezoelectric-enhanced triboelectric nanogenerator for wearable gesture monitoring, Nano Energy, 48, 152–160.

Guo, Z. and Zhang, W. (2016) The spreading residue harmonic balance study on the vibration frequencies of tapered beams, Applied Mathematical Modeling, 40, 7195–7203.

Gupta, R.K., Shu, Q., Dhakar, L., Wang, T., Heng, C.H. and Lee, C. (2017) Broadband energy harvester using non-linear polymer spring and electromagnetic/triboelectric hybrid mechanism, Scientific Reports, 7, 41396.

Guyomar, D., Badel, A., Lefeuvre, E. and Richard, C. (2005) Toward energy harvesting using active materials and conversion improvement by nonlinear processing, IEEE Transactions on Ultrasonics, Ferroelectrics, and Frequency Control, 52, 584–595.

Hadas, Z., Ondrusek, C. and Singule, V. (2010) Power sensitivity of vibration energy harvester, Microsystem Technologies, 16(5), 691–702.

Hajati, A. and Lim, S.G. (2011) Ultra-wide bandwidth piezoelectric energy harvesting, Applied Physics Letters, 99, 083105.

Halim, M.A., Cho, H., Salauddin, M. and Park, J.Y. (2016) A miniaturized electromagnetic vibration energy harvester using flux-guided magnet stacks for human-body-induced motion, Sensors and Actuators A: Physical, 249, 23–31.

Halvorsen, E. (2013) Fundamental Issues in Nonlinear Wide-Band Vibration Energy Harvesting, Physical Review E, 87, 042129.

Hamdan, M.N. and Shabaneh, N.H. (1997) On the large amplitude free vibrations of a restrained uniform beam carrying an intermediate lumped mass, Journal of Sound and Vibrations, 199, 711–736.

Hamdan, M.N., and Dado, M.H. (1997) Large amplitude free vibrations of a uniform cantilever beam carrying an intermediate lumped mass and rotary inertia, Journal of Sound and Vibrations, 206, 151–168.

Han, J.X., Zhang, Q.C. and Wang, W. (2015a) Design considerations on large amplitude vibration of a doubly clamped microresonator with two symmetrically located electrodes, Communications in Nonlinear Science and Numerical Simulation, 22, 492–510.

Han, J.X., Zhang, Q.C. and Wang, W. (2015b) Static bifurcation and primary resonance analysis of a MEMS resonator actuated by two symmetrical electrodes, Nonlinear Dynamics, 80, 1585–1599.

Hanagud, S.V., Meyyappa, M. and Craig, J.I. (1985) Method of multiple scales and identification of nonlinear structural dynamic systems. AIAA Journal, 23(5), 802–807.

Harne, R.L. and Wang, K.W. (2013) A review of the recent research on vibration energy harvesting via bistable systems, Smart Materials and Structures, 22(2), 023001.

Hassan, A. (1994a) Use of transformations with the higher order method of multiple scales to determine the steady state periodic response of harmonically excited non-linear oscillators, Part I: Transformation of derivative, Journal of Sound and Vibration, 178, 1–19.

Hassan, A. (1994b) Use of transformations with the higher order method of multiple scales periodic response of harmonically excited non-linear oscillators, Part II: Transformation of detuning, Journal of Sound and Vibration, 178, 21–40.

Hatipoglu, G. and Urey, H. (2010) FR4–based electromagnetic energy harvester for wireless sensor node. Smart Materials and Structures, 19(1), 015022.

He, Q. and Daqaq, M.F. (2013) Load optimization of a nonlinear mono-stable Duffing-type harvester operating in a white noise environment, American society of Mechanical Engineers, V008T13A086.

He, X., Wen, Q., Sun, Y. and Wen, Z. (2017) A low-frequency piezoelectric-electromagnetic-triboelectric hybrid broadband vibration energy harvester, Nano Energy, S2211285517305001.

Henry A. Sodano, Gyuhae Park, Donald J. Leo and Daniel J. Inman. (2003) Model of piezoelectronic power harvesting beam, Proceedings of IMECE'03, 1–10.

Hoffmann, D., Kallenbach, C., Dobmaier, M., Folkmer, B. and Manoli, Y. (2009) Flexible polyimide film technology for vibration energy harvesting, in Proceedings of Power MEMS, Washington, DC, USA, 455–458.

Hou, T.C., Yang, Y., Zhang, H., Chen, J., Chen, L.J. and Lin Wang, Z. (2013) Triboelectric nanogenerator built inside shoe insole for harvesting walking energy, Nano Energy, 2(5), 856–862.

Hu, Y., Xue, H., Yang, J. and Jiang, Q. (2006) Nonlinear behavior of a piezoelectric power harvester near resonance, IEEE Transactions on Ultrasonics, Ferroelectrics, and Frequency Control, 53(7), 1387–1391.

Hu, Y.G., Liew, K.M., Wang, Q., He, X.Q. and Yakobson, B.I. (2008) Nonlocal shell model for elastic wave propagation in single- and double-walled carbon nanotubes, Journal of the Mechanics and Physics of Solids, 56, 3475–3485.

Huang, Z. (2012) Nonlocal effects of longitudinal vibration in nanorod with internal long-range interactions, International Journal of Solids and Structures, 49, 2150–2154.

Hui, C.K., Lee, Y.Y. and Reddy, J.N. (2011) Approximate elliptical integral solution for the large amplitude free vibration of a rectangular single mode plate backed by a multi-acoustic mode cavity, Thin-Walled Structures, 49, 1191–1194.

Janowicz, M. (2003) Method of multiple scales in quantum optics. Physics Reports, 375(5), 327–410.

Jarrar, F.S.M. and Hamdan, M.N. (2007) Nonlinear vibrations and buckling of a flexible rotating beam: A prescribed torque approach, Mechanism and Machine Theory, 42, 919–939.

Javed, U. and Abdelkefi, A. (2018) Role of the galloping force and moment of inertia of inclined square cylinders on the performance of hybrid galloping energy harvesters, Applied Energy, 231, 259–276.

Jawhar, I., Mohamed, N. and Al-Jaroodi, J. (2018) Networking architectures and protocols for smart city systems, Journal of Internet Services and Applications, 9, 26.

Jayakumar, H., Lee, K., Lee, W. S., Raha, A., Kim, Y. and Raghunathan, V. (2014) Powering the Internet of Things, in Proceedings International Symposium Low Power Electronical Design, 375–380.

Jeon, Y., Sood, R., Steyn, L. and Kim, S.G. (2003) Energy Harvesting MEMS Devices based on d33 Mode Piezoelectric Pb(Zr,Ti)O3 Thin Film Cantilever, CIRP Seminar on Micro and Nano Technology.

Jeon, Y.B., Sood, R., Jeong, J.H. and Kim, S.G. (2005) MEMS power generator with transverse mode thin film PZT. Sensors and Actuators A, 122(1), 16–22.

Jia, X.L., Yang, J., Kitipornchai, S. and Lim C.W. (2012) Pull-in instability and free vibration of electrically-actuated poly-SiGe graded micro-beams with a curved ground electrode. Applied Mathematical Modelling, 36, 1875–1884.

Jia, X.L., Yang, J., Kitipornchai, S. and Lim, C.W. (2010) Free vibration of geometrically nonlinear micro-switches under electrostatic and Casimir forces, Smart Materials and Structures, 19, 115028.

Jiang, W., Zhang, G. and Chen, L. (2015), Forced response of quadratic nonlinear oscillator: comparison of various approaches, Applied Mathematics and Mechanics, 36(11), 1403–1416.

Jin, L., Chen, J., Zhang, B.B., Deng, W.L., Zhang, L., Zhang, H.T., Huang, X., Zhu, M.H., Yang, W.Q. and Wang, L. (2016) Self-powered safety helmet based on hybridized nanogenerator for emergency, ACS Nano, 10, 7874–7881.

Jing, Q., Zhu, G., Bai, P., Xie, Y., Chen, J., Han, R.P.S. and Wang, Z.L. (2014) Case-encapsulated triboelectric nanogenerator for harvesting energy from reciprocating sliding motion, ACS Nano, 8(4), 3836–3842.

Jomehzadeh, E. and Saidi, A.R. (2011) Decoupling the nonlocal elasticity equations for three dimensional vibration analysis of nano-plates, Composite Structures, 93, 1015–1020.

Ju, P.J. (2015) Global residue harmonic balance method for Helmholtz-Duffing oscillator, Applied Mathematical Modelling, 39(5), 2172–2179.

Ju. P.J. and Xue, X. (2015) Global residue harmonic balance method for large-amplitude oscillations of a nonlinear system, Applied Mathematical Modelling, 39(2), 449–454.

Kacem, N., Hentz, S., Pinto, D., Reig, B. and Nguyen, V. (2009) Nonlinear dynamics of nanomechanical beam resonators: Improving the performance of NEMS-based sensors. Nanotechnology, 20, 275501.

Karami, B., Janghorban, M., and Tounsi, A. (2020) Novel study on functionally graded anisotropic doubly-curved nanoshells, The European Physical Journal Plus, 135, 103.

Karami, B., Shahsavari, D., Janghorban, M. and Li, L. (2019) Influence of homogenization schemes on vibration of functionally graded curved microbeams, Composite Structures, 216, 67–79.

Karumuthil, S.C., Rajeev, S.P. and Varghese, S. (2017) Piezo-tribo nanoenergy harvester using hybrid polydimethyl siloxane based nanocomposite, Nano Energy, 40, 487–494.

Ke, L.L., Liu, C. and Wang, Y.S. (2015) Free vibration of nonlocal piezoelectric nanoplates under various boundary conditions, Physica E Low Dimensional Systems & Nanostructures, 66, 93–106.

Kelley, C.T. and Mukundan, L. (1993) Convergence analysis for the harmonic balance method, Nonlinear Analysis: Theory, Methods & Applications, 20(4), 365–380.

Kiani, K. and Mehri, B. (2010) Assessment of nanotube structures under a moving nanoparticle using nonlocal beam theories, Journal of Sound and Vibration, 329, 2241–2264.

Kim, H.W., Batra, A., Priya, S., Uchino, K., Markley, D., Newnham, R.E., Hofmann, H.F. (2004). Energy harvesting using a piezoelectric "cymbal" transducer in dynamic environment, Japanese Journal of Applied Physics, 43, 6178–6183.

Kim, M.K., Kim, M.S., Jo, S.E. and Kim, Y.J. (2016) Triboelectric-thermoelectric hybrid nanogenerator for harvesting frictional energy, Smart Materials and Structures, 25, 125007.

Kim, P. and Seok, J. (2014) A multi-stable energy harvester: dynamic modeling and bifurcation analysis, Journal of Sound and Vibration, 333, 5525–5547.

Kim, P. and Seok, J. (2015) Dynamic and energetic characteristics of a tri-stable magnetopiezoelastic energy harvester, Mechanism & Machine Theory, 94, 41–63.

Kim, S. (2002) Low Power Energy Harvesting with Piezoelectric Generators, PhD Dissertation, University of Pittsburgh, USA.

Kok, S.L., White, N.M.and Harris, N.R. (2008) A free standing thick film piezoelectric energy harvester, Sensors IEEE, 589–592.

Koukharenko E., Beeby, S.P., Tudor, M.J., White, N.M., O'Donnell, T., Saha, C., Kulkarni, S. and Roy, S. (2006) Microelectromechanical systems vibration powered electromagnetic generator for wireless sensor applications, Microsystem Technologies, 12, 1071–1077.

Kovacic, I. and Brennan, M.J. (2011) The Duffing Equation: Nonlinear Oscillators and Their Behavior, Wiley.

Krylov, N.M. andBogolyubov, N.N. (1937) Introduction to Non-linear Mechanics (in Russian). Kiev: Izd-vo AN SSSR.

Krylov, S. (2007) Lyapunov exponents as a criterion for the dynamic pull-in instability of electrostatically actuated microstructures. International Journal of Non-Linear Mechanics, 42(4), 626–642.

Kuang J.H. and Chen, C.J. (2004) Dynamic characteristics of shaped micro-actuators solved using the differential quadrature method, Journal of Micromechanics and Microengineering, 14, 647–655.

Lai, S.K. (2007) Accurate Higher-order Analytical Approximations to Nonlinear Oscillation Systems, PhD Dissertation, City University of Hong Kong.

Lai, S.K. and Chow, K.W. (2012) Exact solutions for oscillators with quadratic damping and mixed-parity nonlinearity, Physica Scripta, 85, 045006.

Lai, S.K., Lim, C.W., Lin, Z. and Zhang, W. (2011) Analytical analysis for large-amplitude oscillation of a rotational pendulum system, Applied Mathematics Computation, 217, 6115–6124.

Lai, S.K., Lim, C.W., Wu, B.S., Wang, C., Zeng, Q.C. and He, X. F. (2009a) Newton–harmonic balancing approach for accurate solutions to nonlinear cubic–quintic duffing oscillators, Applied Mathematical Modelling, 33(2), 852–866.

Lai, S.K., Lim, C.W., Xiang, Y. and Zhang, W. (2009b) On asymptotic analysis for large amplitude nonlinear free vibration of simply supported laminated plates, Journal of Vibration and Acoustics, 131, 051010.

Lai, S.K., Wang, C. and Zhang, L.H. (2019) A nonlinear multi-stable piezomagnetoelastic harvester array for low-intensity, low-frequency, and broadband vibrations, Mechanical Systems and Signal Processing, 122, 87–102.

Lai, S.K., Wu, B.S. and Lee, Y.Y. (2017) Free vibration analysis of a structural system with a pair of irrational nonlinearities, Applied Mathematical Modelling, 45, 997–1007.

Lai, S.K., Xiang, Y., Lim, C.W., He, X.F. and Zeng, Q.C. (2008) Higher-order approximate solutions for nonlinear vibration of a constant-tension string, Journal of Sound and Vibration, 317(3-5), 440–448.

Lai, S.K., Yang, X. and Gao, F.B. (2019) Analysis of large-amplitude oscillations in triple-well non-natural systems, Journal of Computational and Nonlinear Dynamics, 14, 091002.

Lai, T., Huang, C. and Tsou, C. (2008) Design and fabrication of acoustic wave actuated microgenerator for portable electronic devices, in Symposium on Design, Test, Integration and Packaging of MEMS/MOEMS, Nice, April 2008, 28–33.

Lakrad, F. and Belhaq, M. (2010) Suppression of pull-in instability in MEMS using a high-frequency actuation. Communications in Nonlinear Science and Numerical Simulation, 15(11), 3640–3646.

Lallart, M., Garbuio, L., Petit, L., Richard, C. and Guyomar, D. (2008) Double synchronized switch harvesting (DSSH): a new energy harvesting scheme for efficient energy extraction, IEEE Transactions on Ultrasonics, Ferroelectrics, and Frequency Control, 55, 2119–2130.

Lau, S.L. and Cheung, Y.K. (1981) Amplitude incremental variational principle for nonlinear vibration of elastic systems, Journal of Applied Mechanics, 48(4), 959–964.

Le Van Quyen, M., Staba, R., Bragin, A., Dickson, C, Valderrama, M., Fried, I. and Engel, J. (2010) Large-scale microelectrode recordings of high-frequency gamma oscillations in human cortex during sleep, The Journal of Neuroscience,7770–7782.

Lee, C., Stamp, D., Kapania, N.R. and MurMiranda, J.O. (2010) Harvesting vibration energy using nonlinear oscillations of an electromagnetic inductor, Proceedings of the 2010 SPIE Conference on Smart Structures/ NDE, San Diego, CA.

Lefeuvre, E., Badel, A., Richard, C. and Guyomar, D. (2005) Piezoelectric energy harvesting device optimization by synchronous electric charge extraction, Journal of Intelligent Material Systems and Structures, 16, 865–876.

Lenci, S., Menditto, G. and Tarantino, A.M. (1999) Homoclinic and heteroclinic bifurcations in the nonlinear dynamics of a beam resting on an elastic substrate, International Journal of Non-Linear Mechanics, 34, 615–632.

Leng, Y.G., Tan, D., Liu, J.J., Zhang, Y.Y. and Fan, S.B. (2017) Magnetic force analysis and performance of a tri-stable piezoelectric energy harvester under random excitation, Journal of Sound and Vibration, 406, 146–160.

Leung, A.Y.T. and Zhang, Q.C. (1998) Higher order normal form and period averaging, Journal of Sound and Vibration 217, 795–806.

Leung, A.Y.T. and Guo, Z.G. (2011a) Forward residue harmonic balance for autonomous and non-autonomous systems with fractional derivative damping. Communications in Nonlinear Science and Numerical Simulation, 16, 2169–2183.

Leung, A.Y.T. and Guo, Z.G. (2011b) Residue harmonic balance approach to limit cycles of non-linear jerk equations. International Journal of Non-Linear Mechanics 46, 898–906, 2011.

Leung, A.Y.T., Guo, Z.G. and Fung, T.C. (2010) The multi-parameter homotopy harmonic balance method for steady state problems, International Journal of Computer Mathematics, 87(5), 1158–1177.

Leus V. and Elata D. (2004) Fringing Field Effect in Electrostatic Actuators, Technical Report ETR-2004-2, Israel Institute of Technology.

Li, C. (2014a) A nonlocal analytical approach for torsion of cylindrical nanostructures and the existence of higher-order stress and geometric boundaries, Composite Structures, 118, 607–621.

Li, C. (2014b) Torsional vibration of carbon nanotubes: comparison of two nonlocal models and a semi-continuum model, International Journal of Mechanical Sciences, 82, 25–31.

Li, C., Lai, S.K. and Yang, X. (2019) On the nano-structural dependence of nonlocal dynamics and its relationship to the upper limit of nonlocal scale parameter, Applied Mathematical Modelling, 69, 127–141.

Li, C., Li, S., Yao, L.Q. and Zhu, Z.K. (2015) Nonlocal theoretical approaches and atomistic simulations for longitudinal free vibration of nanorods/nanotubes and verification of different nonlocal models, Applied Mathematical Modelling, 39, 4570–4585.

Li, C., Lim, C.W. and Yu, J.L. (2011a) Twisting statics and dynamics for circular elastic nanosolids by nonlocal elasticity theory. Acta Mechanica Solida Sinica, 24(6), 484–494.

Li, C., Lim, C.W. and Yu, J.L. (2011c) Dynamics and stability of transverse vibrations of nonlocal nanobeams with a variable axial load, Smart Materials and Structures, 20, 015023.

Li, C., Liu, J.J., Cheng, M. and Fan, X.L. (2017c) Nonlocal vibrations and stabilities in parametric resonance of axially moving viscoelastic piezoelectric nanoplate subjected to thermo-electro-mechanical forces, Composites Part B: Engineering, 116, 153–169.

Li, C., Zheng, Z.J. , Yu, J.L. and Lim, C.W. (2011b) Static analysis of ultra-thin beams based on a semi-continuum model, Acta Mechanica Sinica, 27, 713–719.

Li, G.G., Zhu, Z.Y. and Cheng, C.J. (2001) Dynamical stability of viscoelastic column with fractional derivative constitutive relation, Applied Mathematics and Mechanics, 22(3), 294–303.

Li, H., Qin, W., Lan, C., Deng, W. and Zhou, Z. (2016) Dynamics and coherence resonance of tri-stable energy harvesting system, Smart Materials and Structures, 25, 015001.

Li, H., Yew, Y.K., Lam, K.Y. and Ng, T.Y. (2003) Numerical simulation of hydrogel-based pH-responsive biosensors in BioMEMS, Symposium on Design, Test, Integration and Packaging of MEMS/MOEMS symposium, 218–222, Cannes, France.

Li, L. and Zhang, Q.C. (2017) Nonlinear dynamic analysis of electrically actuated viscoelastic bi-stable microbeam system. Nonlinear Dynamics, 87, 587–604.

Li, R. and Kardomatas, G.A. (2007) Thermal buckling of multi-walled carbon nanotubes by nonlocal elasticity, Journal of Applied Mechanics, 74 (3), 399–405.

Li, R. and Kardomateas, G.A. (2007). Thermal buckling of multi-walled carbon nanotubes by nonlocal elasticity, Journal of Applied Mechanics, 74(3), 399–405.

Li, X., Li, L., Hu, Y., Ding, Z. and Deng, W. (2017a) Bending, buckling and vibration of axially functionally graded beams based on nonlocal strain gradient theory, Composite Structures, 165, 250–265.

Li, Z., Feng, K., Yang, J.S., Tan, L. and Lin, H. (2010) Collective buckling of nonuniform nanobeams interacting through an elastic substrate, Acta Mechanica, 209, 285–293.

Li, Z.J., Saadatnia, Z., Yang, Z.B., Naguib, H. (2018) A hybrid piezoelectric-triboelectric generator for low-frequency and broad-bandwidth energy harvesting, Energy Conversion and Management, 174, 188–197.

Liang, F., Yang, X.D., Qian, Y.J. and Zhang, W. (2018) Forced response analysis of pipes conveying fluid by nonlinear normal modes method and iterative approach, Journal of Computational and Nonlinear Dynamics, 13(1), 014502.

Liang, Q., Yan, X., Gu, Y., Zhang, K., Liang, M., Lu, S., Zheng, X. and Zhang, Y. (2015) Highly transparent triboelectric nanogenerator for harvesting water-related energy reinforced by antireflection coating, Scientific Reports, 5, 9080.

Liang, Y. and Han, Q. (2014) Prediction of the nonlocal scaling parameter for graphene sheet, European Journal of Mechanics A-Solid, 45, 153–160.

Liao, S.J. (1992) The Proposed Homotopy Analysis Technique for the Solutions of Non-linear Problems, PhD Dissertation, Shanghai Jiao Tong University.

Liao, S.J. (2003) Beyond Perturbation - Introduction to the Homotopy Analysis Method, CRC, New York.

Lim, C.W. (2008) A discussion on the nonlocal elastic stress field theory for nanobeams, The Eleventh East Asia-Pacific Conference on Structural Engineering & Construction (EASEC-11), Taipei, Taiwan.

Lim, C.W. (2009) Equilibrium and static deflection for bending of a nonlocal nanobeam, Advances in Vibration Engineering, 8, 277–300.

Lim, C.W. (2010a) On the truth of nanoscale for nanobeams based on nonlocal elastic stress field theory: equilibrium, governing equation and static deflection, Applied Mathematics and Mechanics, 31, 37–54.

Lim, C.W. (2010b) Is a nanorod (or nanotube) with a lower Young's modulus is stiffer? Is not Young's modulus a stiffness indicator? Science in China Series G: Physics, Mechanics & Astronomy, 53, 712–724.

Lim, C.W. and Yang, Y. (2010) Wave propagation in carbon nanotubes: nonlocal elasticity induced stiffness and velocity enhancement effects, Journal of Mechanics of Materials and Structures, 5 (3), 459–476.

Lim, C.W., Li, C. and Yu, J.L. (2009) The effects of stiffness strengthening nonlocal stress and axial tension on free vibration of cantilever nanobeams, Interaction and Multiscale Mechanics, 2, 223–233.

Lim, C.W., Li, C. and Yu, J. L. (2010a) Dynamic behavior of axially moving nanobeams based on nonlocal elasticity approach, Acta Mechanica Sinica, 26(5), 755–765.

Lim, C.W., Li, C. and Yu, J.L. (2010b) Free vibration of pre-tensioned nanobeams based on nonlocal stress theory, Journal of Zhejiang University Science A, 11, 34–42.

Lim, C.W., Yang, Q. and Zhang, J.B. (2012) Thermal buckling of nanorod based on non-local elasticity theory, International Journal of Non-Linear Mechanics, 47(5), 496–505.

Lim, C.W., Zhang, G. and Reddy, J.N. (2015) A higher-order nonlocal elasticity and strain gradient theory and its applications in wave propagation, Journal of the Mechanics and Physics of Solids, 78, 298–313.

Litak, G., Friswell, M. I. and Adhikari, S. (2010) Magnetopiezoelastic energy harvesting driven by random excitations, Applied Physics Letters, 96(21), 214103.

Liu, C. and Rajapakse, R.K.N.D. (2010) Continuum models incorporating surface energy for static and dynamic response of nanoscale beams, IEEE Transactions on Nanotechnology, 9, 422–431.

Liu, C., Ke, L.L. and Yang, J., Kitipornchai, S. and Wang, Y.S. (2018) Nonlinear vibration of piezoelectric nanoplates using nonlocal mindlin plate theory, Mechanics of Advanced Materials and Structures, 25, 1252–1264.

Liu, J.J., Chen, L., Xie, F., Fan, X.L. and Li, C. (2016) On bending, buckling and vibration of graphene nanosheets based on the nonlocal theory, Smart Structures and Systems, 17, 257–274.

Liu, J.J., Li, C., Fan, X.L. and Tong, L.H. (2017b) Transverse free vibration and stability of axially moving nanoplates based on nonlocal elasticity theory, Applied Mathematical Modelling, 45, 65–84.

Liu, T., Hai, M. and Zhao, M.H. (2008) Delaminating buckling model based on nonlocal Timoshenko beam theory for microwedge indentation of a film/substrate system, Engineering Fracture Mechanics, 75, 4909–4919.

Liu, W., Wu, B. and Lim, C.W. (2017a) Linear and nonlinear free vibrations of electrostatically actuated micro-/nanomechanical resonators, Microsystem Technologies, 23(1), 113–123.

Liu, W., Wu, B., Chen, X. and Zhu, W.D. (2019) Analytical approximate solutions for asymmetric conservative oscillators, Archive of Applied Mechanics, 89, 2265–2279.

Lu, P. (2007) Dynamic analysis of axially prestressed micro/nanobeam structures based on nonlocal beam theory, Journal of Applied Physics, 101, 073504.

Lu, P., Lee, H.P., Lu, C. and Zhang, P.Q. (2006). Dynamic properties of flexural beams using a nonlocal elasticity model, Journal of Applied Physics, 99, 073510.

Lu, P., Lee, H.P., Lu, C. and Zhang, P.Q. (2007) Application of nonlocal beam models for carbon nanotubes, International Journal of Solids and Structures, 44, 5289–5300.

Lu, Y., Cottone, F. and Boisseau, S. (2015) A nonlinear MEMS electrostatic kinetic energy harvester for human-powered biomedical devices, Applied Physics Letters, 107, 253902.

Luongo, A. and Egidio, D.A. (2005) Bifurcation equations through multiple-scales analysis for a continuous model of a planar beam, Nonlinear Dynamics, 41, 171–190.

Ma, T., Xu, N. and Zhang, H. (2010) A Nonlinear Method for Harvesting Mechanical Energy From Vibrations, Proceedings of the 12th Biennial International Conference on Engineering, Construction, and Operations in Challenging Environments and Fourth NASA/ARO/ASCE Workshop on Granular Materials in Lunar and Martian Exploration, Honolulu, HI, 14–17.

Madou, M.J. (1997) Fundamentals of Microfabrication: The Science of Miniaturization.

Mann, B. P. and Sims, N. D. (2008) Energy harvesting from the nonlinear oscillations of magnetic levitation, Journal of Sound and Vibration, 319, 515–530.

Mann, B.P. and Owens, B.A. (2010) Investigations of a nonlinear energy harvester with a bistable potential well, Journal of Sound and Vibration, 329, 1215–1226.

Mann, B.P. and Sims, N.D. (2009). Energy harvesting from the nonlinear oscillations of magnetic levitation, Journal of Sound and Vibration, 319, 515–530.

Mao, J.J., Lu, H.M., Zhang, W., and Lai, S.K. (2020) Vibrations of graphene nanoplatelet reinforced functionally gradient piezoelectric composite microplate based on nonlocal theory, Composite Structures, 236, 111813.

Maranganti, R. and Sharma, P. (2007) Length scales at which classical elasticity breaks down for various materials, Physical Review Letters, 98, 195504.

Marinkovic, B. and Koser, H. (2009) Smart sand-a wide bandwidth vibration energy harvesting platform, Applied Physics letters, 94(10), 307–309.

Masana, R. and Daqaq, M.F. (2009) Relative Performance of a Vibratory Energy Harvester in Mono- and Bi-stable Potentials, Journal of Sound and Vibration, 330(24), 6036–6052.

Masana, R. and Daqaq, M.F. (2011) Electromechanical Modeling and Non- linear Analysis of Axially Loaded Energy Harvesters, ASME Journal of Vibration and Acoustics, 133(1), 011007.

Masana, R. and Daqaq, M.F. (2012) Energy Harvesting in the Super- harmonic Frequency Region of a Twin-well Oscillator, Journal of Applied Physics, 111(4), 044501.

McInnes, C., Gorman, D. and Cartmell, M. (2008) Enhanced Vibrational Energy Harvesting Using Nonlinear Stochastic Resonance, Journal of Sound and Vibration, 318, 655–662.

McNicoll, G. (2005) United Nations, Department of Economic and Social Affairs: World Economic and Social Survey 2004: International Migration, Population and Development Review, 31, 183–185.

Mei, X., Zhou, S., Yang, Z., Kaizuka, T. and Nakano, K. (2020) A tri-stable energy harvester in rotational motion: Modeling, theoretical analyses and experiments, Journal of Sound and Vibration, 469, 115142.

Meirovitch, L. (1970) Methods of Analytical Dynamics, McGraw-Hill, New York.

Mestrom, R.M.C., Fey, R.H.B., J.T.M. Van Beek, K.L. Phan and Nijmeijer, H. (2008) Modelling the dynamics of a MEMS resonator: simulations and experiments. Sensors and Actuators A: Physical, 142, 306–315.

Miki, D., Honzumi, M., Suzuki, Y. and Kasagi, N. (2010) Large-Amplitude MEMS electret generator with nonlinear springs, 2010 IEEE 23rd International Conference on Micro Electro Mechanical Systems (MEMS), 176–179.

Moghimi M. and Ahmadian, M.T. (2009) Application of homotopy analysis method in studying dynamic pull-in instability of microsystems, Mechanics Research Communications, 36, 851–858.

Mohanasubha, R. and Senthilvelan, M. (2017) On the symmetries of a non-polynomial oscillator, Communictions in Nonlinear Science and Numerical Simulation, 43, 111–117.

Munday, J.N., Capasso, F. and Adrian Parsegian, V. (2009) Measured long-range repulsive Casimir-Lifshitz forces, Nature, 457, 170–173.

Murmu, T. and Adhikari, S. (2010) Nonlocal transverse vibration of double-nanobeam-systems, Journal of Applied Physics, 108, 083514.

Murmu, T. and Pradhan, S.C. (2009a) Buckling of biaxially compressed orthotropic plates at small scales, Mechanics Research Communications, 36, 933–938.

Murmu, T. and Pradhan, S.C. (2009b) Vibration analysis of nanoplates under uniaxial prestressed conditions via nonlocal elasticity, Journal of Applied Physics, 106, 104301.

Murmu, T. and Pradhan, S.C. (2009c) Small-scale effect on the free in-plane vibration of nanoplates by nonlocal continuum model, Physica E-Low-Dimensional Systems and Nanostructures, 41, 1628–1633.

Murmu, T. and Pradhan, S.C. (2009d) Vibration analysis of nano-single-layered graphene sheets embedded in elastic medium based on nonlocal elasticity theory, Journal of Applied Physics, 105, 064319.

Murmu, T., Sienz, J., Adhikari, S. and Arnold, C. (2013) Nonlocal buckling of double-nanoplate-systems under biaxial compression, Composites Part B-Engineering, 44, 84–94.

Nathanson, H.C., Newell, W.E., Wickstrom, W.E., Davis, R.A. and JR Jr (1967) The resonant gate transistor, IEEE Transelectron Devices, 14(3), 117–133.

Naumann, G. (2003) Energiewandlersystem für den Betrieb von autarken Sensoren in Fahrzeugen, PhD Dissertation, Technische Universität Dresden, Dresden (in German).

Nayfeh, A.H. and Mook, D.T. (1995) Nonlinear Oscillations, Wiley.

Nayfeh, A.H. and Lacarbonara, W. (1997) On the discretization of distributed-parameter systems with quadratic and cubic nonlinearities, Nonlinear Dynamics, 13, 203–220.

Nayfeh, A.H., Younis, M.I. and Abdel-Rahman, E.M. (2007) Dynamic pull-in phenomenon in MEMS resonators, Nonlinear Dynamics, 48, 153–163.

Nayfeh, A.H., and Hassan, S.D. (1971) The method of multiple scales and non-linear dispersive waves, Journal of Fluid Mechanics, 48, 463–475.

Neamaty, A., Agheli, B. and Darzi, R. (2015) Numerical solution of high-order fractional Volterra integro-differential equations by variational homotopy perturbation iteration method, Journal of Computational and Nonlinear Dynamics, 10, 061023.

Ng, T.Y., Li, H., Lam, K.Y., Pan, L.S. and Xu, D. (2008) Book Chapter 4 on "New Approaches for the Simulation of Micro-Fluidics in MEMS", Advances in Multiphysics Simulation and Experimental Testing of MEMS, Imperial College Press, 121–152.

Nguyen, D. S., Halvorsen, E., Jensen, G. U., and Vogl, A. (2010) Fabrication and characterization of a wideband MEMS energy harvester utilizing nonlinear springs, Journal of Micromechanics and Microengineering, 20(12), 125009.

Nguyen, S.D. and Halvorsen, E. (2011) Nonlinear springs for bandwidth-tolerant vibration energy harvesting, Journal of Microelectromechal Systems, 20(6), 1225–1227.

Nguyen, S.D., Halvorsen, E. and Paprotny, I. (2013) Bistable springs for wideband microelectromechanical energy harvesters, Applied Physics Letters, 102(2), 023904.

Niu, J.C., Lim, C.W. and Leung, A.Y.T. (2009) Third-order non-local beam theories for the analysis of symmetrical nanobeams, Journal of Mechanical Engineering Science, 223, 2451–2463.

Niu, J.C., Lim, C.W. and Leung, A.Y.T. (2010) Analytical model of unconstrained non local higher-order nano-plates for bending analysis, Manufacturing Science and Engineering, 97–101, 4193-4196.

Niu, P., Chapman, P., DiBerardino, L. and Hsiao-Wecksler, E. (2008) Design and optimization of a biomechanical energy harvesting device, in Power Electronics Specialists Conference PESC, Rhodes, 4062–4069.

Osterberg, P.M. and Senturia, S.D. (1997) M-test: A test strip for MEMS material property measurement using electrostatically actuated test structures, Journal of Microelectromechanical Systems, 6, 107–118.

Oumbé, G.T., Tékam, Kitio, C.A., Kwuimy and Woafo, P. (2015) Analysis of tristable energy harvesting system having fractional order viscoelastic material, Chaos, 25, 013112.

Pakar, I. and Bayat, M. (2015) Nonlinear vibration of stringer shell: An analytical approach, Proceedings of the Institution of Mechanical Engineers, Part E: Journal of Process Mechanical Engineering, 229, 44–51.

Palmer H.B. (1937) Capacitance of a parallel-plate capacitor by the Schwartz-Christoffel transformation, Transactions on AIEE, 56(3), 363–366.

Pandey, A., Ghose-Choudhury, A. and Guha, P. (2017) Chiellini integrability and quadratically damped oscillators, International Journal of Non-Linear Mechanics, 92, 153–159.

Pankaj, W. and Anindya, C. (2004) Averaging oscillations with small fractional damping and delayed terms, Nonlinear Dynamics, 38, 3–22.

Panyam, M. and Daqaq, M.F. (2017) Characterizing the effective bandwidth of tri-stable energy harvesters, Journal of Sound and Vibration, 386, 336–358.

Park, J.Y., Salauddin Md. and Salauddin Rasel, M. (2019) Nanogenerator for scavenging low frequency vibrations, Journal of Micromechanics and Microengineering, 29, 053001.

Park, S. and Lee, K.C. (2002) Design and analysis of a microelectromagnetic vibration transducer used as an implantable middle ear hearing aid, Journal of Micromechanics and Microengineering, 12(5), 505–511.

Peddieson, J., Buchanan, G.G. and McNitt, R.P. (2003) Application of nonlocal continuum models to nanotechnology, International Journal of Engineering Science, 41, 305–312.

Pelesko J.A. and Bernstein D.H. (2003) Modeling MEMS and NEMS, Boca Raton, CRC.

Pellegrini, S.P., Tolou, N., Schenk, M. and Herder, J.L. (2013) Bistable vibration energy harvesters: A review, Journal of Intelligent Material Systems and Structures, 24, 1303–1312.

Perko, L.M. (1968) Higher order averaging and related methods for perturbed periodic and quasi-periodic systems, SIAM Journal of Applied Mathematics, 17(4), 469–724.

Phadikar, J.K. and Pradhan, S.C. (2010) Variational formulation and finite element analysis for nonlocal elastic nanobeams and nanoplates, Computational Materials Science, 49, 492–499.

Poincaré, H. (1892) Les Méthodes Nouvelles de la Mécanique Céleste, Vol. 1. Gauthier-Villars, Paris.

Polit, O., Merzouki, T. and Ganapathi, M. (2018) Elastic stability of curved nanobeam based on higher-order shear deformation theory and nonlocal analysis by finite element approach, Finite Elements in Analysis and Design, 146, 1–15.

Pradhan, S.C. (2009) Buckling of single layer graphene sheet based on nonlocal elasticity and higher order shear deformation theory, Physics Letters A, 373, 4182–4188.

Pradhan, S.C. and Kumar, A. (2010) Vibration analysis of orthotropic graphene sheets embedded in Pasternak elastic medium using nonlocal elasticity theory and differential quadrature method, Computational Materials Science, 50, 239–245.

Pradhan, S.C. and Kumar, A. (2011) Vibration analysis of orthotropic graphene sheets using nonlocal elasticity theory and differential quadrature method, Composite Structures, 93, 774–779.

Pradhan, S.C. and Murmu, T. (2009) Small scale effect on the buckling of single-layered graphene sheets under biaxial compression via nonlocal continuum mechanics, Computational Materials Science, 47, 268–274.

Pradhan, S.C. and Phadikar, J.K. (2009) Nonlocal elasticity theory for vibration of nanoplates, Journal of Sound and Vibration, 325, 206–223.

Priya, S. and Inman, D.J. (2009) Energy Harvesting Technologies, Springer.

Qian, Y.H., Lai, S.K., Zhang, W. and Xiang, Y. (2011) Study on asymptotic analytical solutions using HAM for strongly nonlinear vibrations of a restrained cantilever beam with an intermediate lumped mass, Numerical Algorithms, 58, 293–314.

Qian, Y. H., Pan, J.L., Chen, S.P. and Yao, M.H. (2017) The spreading residue harmonic balance method for strongly nonlinear vibrations of a restrained cantilever beam, Advances in Mathematical Physics, 1–8.

Qian, Y.H., Ren, D.X., Lai, S.K. and Chen, S.M. (2012) Analytical approximations to nonlinear vibration of an electrostatically actuated microbeam, Communications in Nonlinear Science and Numerical Simulation, 17, 1947–1955.

Quan, T., Wang, X., Wang, Z.L. and Yang, Y. (2015) Hybridized electromagnetic–triboelectric nanogenerator for a self-powered electronic watch, ACS Nano, 9(12), 12301–12310.

Quinn, D., Vakakis, D., Alexander, F. and Bergman, L.A. (2007) Vibration-based energy harvesting with essential nonlinearities, 2007 Proceedings of the ASME International Design Engineering Technical Conferences and Computers and Information in Engineering Conference, DETC2007, 779–786.

Quinn, D.D., Triplett, A.L., Bergman, L.A. and Vakakis. A.F. (2011) Comparing linear and essentially nonlinear vibration-based energy harvesting, ASME Conference on Smart Materials, 133, 011001.

Quinn, D.D., Triplett, A.L., Vakakis, A.F. and Bergman, L.A. (2011) Energy harvesting from impulsive loads using intentional essential nonlinearities, Journal of Vibration and Acoustics, 133(1), 011004.

Rahmani, O. and Pedram, O. (2014) Analysis and modeling the size effect on vibration of functionally graded nanobeams based on nonlocal Timoshenko beam theory, International Symposium on Aircraft Materials ACMA, 77, 55–70.

Ramesh, K.T. (2009) Nanomaterials: Mechanics and Mechanisms, Springer.

Rao, G.V. (2003) Large amplitude vibrations of slender uniform beams on elastic foundation, Indian Journal of Engineering and Materials Sciences, 10, 87–91.

Rahman, Z. and Burton, T.D. (1986) Large amplitude primary and superharmonic resonances in the Duffing oscillator, Journal of Sound and Vibration, 110, 363–380.

Rahman, Z. and Burton, T.D. (1989) On high order methods of multiple scales in non-linear oscillations-periodic steady state response, Journal of Sound and Vibration, 133, 369–379.

Rawnak, H. and Mehmet, R.Y. (2017) A wearable energy harvester unit using piezoelectric-electromagnetic hybrid technique, Sensors and Actuators, 257, 198–207.

Reddy, J.N. (2007) Nonlocal theories for bending, buckling and vibration of beams, International Journal of Engineering Science, 45, 288–307.

Reddy, J.N. (2008) Nonlocal continuum theories of beams for the analysis of carbon nanotubes, Journal of Applied Physics, 103, 023511.

Reddy, J.N. (2010) Nonlocal nonlinear formulations for bending of classical and shear deformation theories of beams and plates. International Journal of Engineering Science, 48(11), 1507–1518.

Renaud M. (2007) Piezoelectric harvesters and MEMS technology: fabrication, modeling and measurements solid-state sensors, Actuators and Microsystems Conference, 89, 1–894.

Renaud, M., Fiorini, P. and Hoof, C.V. (2007) Optimization of a piezoelectric unimorph for shock and impact energy harvesting, Smart Materials and Structures, 16, 1125–1135.

Rezazadeh, G., Madinei, H. and Shabani, R. (2012) Study of parametric oscillation of an electrostatically actuated microbeam using variational iteration method, Applied Mathematical Modelling, 36, 430–443.

Rhoads, J.F., Shaw, S.W. and Turner, K.L. (2010) Nonlinear dynamics and its applications in micro-and nanoresonators. Journal of Dynamic Systems, Measurement and Control, 132, 034001.

Roundy, S., Wright, P.K. and Rabaey, J. (2003) A study of low level vibrations as a power source for wireless sensor nodes, Computer Communications, 26, 113l–1144.

Roundy, S. and Wright, P.K. (2004) A piezoelectric vibration based generator for wireless electronics, Smart Materials and Structures, 13, 1131–1142.

Ruellan, M.,Turri, S., Ahmed, H.B. and Multon, B. (2005) Electromagnetic resonant generator, in Proceedings of 40th Industry Applications Conference Annual Meeting, Hong Kong, 1540–1547.

Saadatm, M. and Shooshtari, A. (2018) Nonlinear vibration analysis of a circular micro-plate in two-sided NEMS/MEMS capacitive system by using harmonic balance method, Acta Mechanica Sinica, 35, 129–143.

Saadatnia, Z., Esmailzadeh, E. and Naguib, H.E. (2018) Design, simulation, and experimental characterization of a heaving triboelectric-electromagnetic wave energy harvester, Nano Energy, 50, 281–290.

Saenz, A.W. (1991) Higher-order averaging for nonperiodic systems, Journal of Mathematical Physics, 32(10), 2679–2694.

Saha, C.R., O'Donnel, T., Wang, N. and Mc Closkey, P. (2008) Electromagnetic generator for harvesting energy from human motion. Sensors and Actuators A 147, 248–253.

Sahmani, S. and Aghdam, M.M. (2017) Nonlinear instability of axially loaded functionally graded multilayer graphene platelet-reinforced nanoshells based on nonlocal strain gradient elasticity theory, International Journal of Mechanical Sciences, 131-132, 95–106.

Sahmani, S. and Aghdam, M.M. (2018) Boundary layer modeling of nonlinear axial buckling behavior of functionally graded cylindrical nanoshells based on the surface elasticity theory, Iranian Journal of Science & Technology Transactions of Mechanical Engineering, 42(3), 229–245.

Salauddin, M., Cho, H. and Park, J.Y. (2017) A hybrid electromagnetic-triboelectric energy harvester using a dual halbach magnet array powered by human-body-induced motion, Advanced Materials Technologies, 1700240.

Salauddin, Md, Toyabur, R.M., Maharjan, P., Rasel, M.S., Kim, J.W., Cho, H. and Park, J.Y. (2018) High performance human-induced vibration driven hybrid energy harvester for powering portable electronics, Nano Energy, 45, 236–246.

Samih, H. (2019) Smart cities and internet of things, Journal of Information Technology Case and Application Research, 21, 3–12.

Sanders, J.A. and Verhulst, F. (1985) Averaging methods in nonlinear dynamical systems, Springer, New York.

Sebald, G., Kuwano, H., Guyomar, D., and Ducharne, B. (2011a) Experimental Duffing oscillator for broadband piezoelectric energy harvesting, Smart Materials and Structures, 20(10), 102001.

Sebald, G., Kuwano, H., Guyomar, D., and Ducharne, B. (2011b) Simulation of a Duffing oscillator for broadband piezoelectric energy harvesting, Smart Materials and Structures, 20(7), 075022.

Seleim, A., Towfighian, S., Delande, E., Abdel-Rahman, E. and Heppler, G. (2012) Dynamics of a close-loop controlled mems resonator. Nonlinear Dynamics, 69, 615–633.

Seol, M.L., Han, J.W. and Park, S.J. (2016) Hybrid energy harvester with simultaneous triboelectric and electromagnetic generation from an embedded floating oscillator in a single package, Nano Energy, 23, 50–59.

Seol, M.L., Jeon, S.B., Han, J.W. and Choi, Y.K. (2017) Ferrofluid-based triboelectric-electromagnetic hybrid generator for sensitive and sustainable vibration energy harvesting, Nano Energy, 31, 233–238.

Serre, C., Perez-Rodriguez, A., Fondevilla N., Martincic, E., Martinez S., Morante, J.R., Monteserrat, J. and Esteve, J. (2008) Design and implementation of mechanical resonators for optimized inertial electromagnetic microgenerators. Microsystem Technologies, 14, 653–658.

Serre, C., Perez-Rodriguez, A., Fondevilla, N., Martincic, E., Martinez, S., Morante, J.R. (2008) Design and implementation of mechanical resonators for optimized inertial electromagnetic microgenerators. Microsystem Technologies, 14, 653–658.

Serry, F.M., Walliser, D. and Maclay, G.J. (1998) The role of the Casimir effect in the static deflection and stiction of membrane strips in microelectromechanical systems (MEMS), Journal of Applied Physics, 84, 2501–2506.

Shen, H., Qiu, J., Ji, H., Zhu, K. and Balsi, M. (2010a) Enhanced synchronized switch harvesting: a new energy harvesting scheme for efficient energy extraction, Smart Materials and Structures, 19, 115017.

Shen, H., Zhang, C. and Xiang, Y. (2010b) Nonlocal shear deformable shell model for thermal postbuckling of axially compressed double-walled carbon nanotubes, Philosophical Magazine, 90, 3189–3214.

Shen, Y.J., Yang, S.P., Xing, H.J. and Gao, G.S. (2012a) Primary resonance of Duffing oscillator with fractional-order derivative, Communications in Nonlinear Science and numerical Simulation 17(7), 3092–3100.

Shen, Z.B., Tang, H.L., Li, D.K. and Tang, G.J. (2012b) Vibration of single-layered graphene sheet-based nanomechanical sensor via nonlocal Kirchhoff plate theory, Computational Materials Science, 61, 200–205.

Shenck, N.S. and Paradiso, J.A. (2001) Energy scavenging with shoe-mounted piezoelectrics, IEEE Micro, 21(3), 30–42.

She, G.L., Ren, Y.R. and Yan, K.M. (2019a) On snap-buckling of porous FG curved nanobeams, Acta Astronautica, 161, 475–484.

She, G.L., Yuan, F.G., Karami, B., Ren, Y.R. and Xiao, W.S. (2019b) On nonlinear bending behavior of FG porous curved nanotubes, International Journal of Engineering Science, 135, 58–74.

Shirvanimoghaddam, M., Shirvanimoghaddam, K., Abolhasani, M.M. and Farhangi, M. (2019) Towards a green and self-powered Internet of Things using piezoelectric energy harvesting, IEEE Access, 7, 94533–94556.

Shivamoggi, B. (2003) Method of Multiple Scales, Perturbation Methods for Differential Equations, Birkhäuser Boston.

Sneller, A.J., Cette, P. and Mann, B.P. (2011) Experimental investigation of a post-buckled piezoelectric beam with an attached central mass used to harvest energy, Archive Proceedings of the Institution of Mechanical Engineers, Part I, 225(4), 497–509.

Soares dos Santos, M.P., Ferreira, J.A.F., Simões, J.A.O., Pascoal, R., Torrão, J., Xue, X. and Furlani, E.P. (2016) Magnetic levitation-based electromagnetic energy harvesting: A semi-analytical nonlinear model for energy transduction, Scientific Reports, 6, 18579.

Sobhy, M. and Abazid, M.A. (2019) Dynamic and instability analyses of FG graphene-reinforced sandwich deep curved nanobeams with viscoelastic core under magnetic field effect, Composites Part B: Engineering, 174, 106966.

Sodano, H. A., Park, G. and Inman, D.J. (2004) An investigation into the performance of macro-fiber composites for sensing and structural vibration applications, Mechanical systems and signal processing, 18(3), 683–697.

Soliman, M.S.M., Abdel–Rahman, E.M., El–Saadany, E.F. and Mansour, R.R. (2008) A wideband vibration–based energy harvester. Journal of Micromechanics and Microengineering, 18(11), 115021.

Spreemann D. and Manoli, Y. (2012) Electromagnetic Vibration Energy Harvesting Devices–Architectures, Design, Modeling and Optimization, Springer.

Sriramdas, R. and Pratap, R. (2018) An experimentally validated lumped circuit model for piezoelectric and electrodynamic hybrid harvesters, IEEE Sensors Journal, 18, 2377–2384.

Stange, A., Imboden, M., Javor, J., Barrett, L.K. and Bishop, D.J. (2019) Building a Casimir metrology platform with a commercial MEMS sensor, Microsystems & Nonoengineering, 5, 14.

Stanton, S.C., Erturk, A., Mann, B.P., and Inman, D. J. (2010a) Nonlinear Piezoelectricity in Electroelastic Energy Harvesters: Modeling and Experimental Identification, Journal of Applied Physics, 108(7), 074903.

Stanton, S.C., McGehee, C.C., and Mann, B.P. (2010b) Nonlinear Dynamics for Broadband Energy Harvesting: Investigation of a Bistable Piezoelectric Inertial Generator, Phys. D, 239, 640–653.

Sudak, L.J. (2003) Column buckling of multiwalled carbon nanotubes using nonlocal continuum mechanics, Journal of Applied Physics, 94, 7281–7287.

Sun, Y.H., Yu, Y.P. and Liu, B.C. (2015) Closed form solutions for predicting static and dynamic buckling behaviors of a drillstring in a horizontal wel, European Journal of Mechanics-A/Solids, 49, 362–372.

Sun, W.P., Lim, C.W., Wu, B.S. and Wang, C. (2009) Analytical approximate solutions to oscillation of a current-carrying wire in a magnetic field, Nonlinear Analysis Real World Applications, 10(3), 1882–1890.

Sun, W.P. and Wu, B.S. (2008) Accurate analytical approximate solutions to general strong nonlinear oscillators, Nonlinear Dynamics, 51, 277–287.

Sun, W.P., Wu, B.S. and Lim, C.W. (2007) Approximate analytical solutions for oscillation of a mass attached to a stretched elastic wire, Journal of Sound and Vibration, 300, 1042–1047.

Sun, W.P., and Wu, B.S. (2008) Accurate analytical approximate solutions to general strong nonlinear oscillators, Nonlinear Dynamics, 51, 277–287.

Sze, K.Y., Chen, S.H. and Huang, J.L. (2005) The incremental harmonic balance method for nonlinear vibration of axially moving beams, Journal of Sound and Vibration, 281, 611–626.

Taati, Ehsan, Sina and Nima (2018) Static pull-in analysis of electrostatically actuated functionally graded micro-beams based on the modified strain gradient theory, International Journal of Applied Mechanics, 10, 1850031.

Takahara, K., Ohsaki, S., Kawaguchi, H. and Itoh, Y. (2004) Development of linear power generator: conversion of vibration energy of a vehicle to electric power, Journal of Asian Electric Vehicles, 2, 639–643.

Talookolaei, R.A., Salarieh, H. and Kargarnovin, M.H. (2011) Analysis of large amplitude free vibrations of unsymmetrically laminated composite beams on a nonlinear elastic foundation, Acta Mechanica, 219, 65–75.

Tajaddodianfar, F., Pishkenari, H.N., Yazdi, M.R.H. and Miandoab, E.M. (2015), On the dynamics of bistable micro/nano resonators: Analytical solution and nonlinear behavior, Communications in Nonlinear Science and Numerical Simulation, 20, 1078–1089.

Tajaddodianfar, F., Yazdi, M.R.H. and Pishkenari, H.N. (2017), Nonlinear dynamics of MEMS/NEMS resonators: analytical solution by the homotopy analysis method, Microsystem Technologies, 23, 1913–1926.

Tan, D., Leng, Y.G. and Gao, Y.J. (2015) Magnetic force of piezoelectric cantilever energy harvesters with external magnetic field, The European Physical Journal Special Topics, 224, 2839–2853.

Tan, P. , Zheng, Q., Zou, Y., Shi, B., Jiang, D., Qu, X., Ouyang, H., Zhao, C., Cao, Y., Fan, Y., Wang, Z.L. and Li, Z. (2019) A battery-like self-charge universal module for motional energy harvest, Advanced Energy Materials, 9, 1901875.

Tang, D.F., Lim, C.W., Hong, L., Jiang, J. and Lai, S.K. (2017) Analytical asymptotic approximations for large amplitude nonlinear free vibration of a dielectric elastomer balloon, Nonlinear Dyn, 88:2255–2264.

Tang, D.F., Lim, C.W., Hong, L., Jiang, J., and Lai, S.K. Lai (2018) Dynamic response and stability analysis with Newton harmonic balance method for nonlinear oscillating dielectric elastomer balloons, International Journal of Structural Stability and Dynamics, 18, 1850152.

Tang, Y., and Yang, T. (2018) Post-buckling behavior and nonlinear vibration analysis of a fluid-conveying pipe composed of functionally grade material, Composite Structures, 185, 393–400.

Tao, K., Yi, H., Tang, L., Wu, J., Wang, P., Wang, N. and Chang, H. (2019) Piezoelectric ZnO thin films for 2DOF MEMS vibrational energy harvesting, Surface & Coatings Technology, 359, 289–295.

Thorby, D (2008) Structural Dynamics and Vibration in Practice, Butterworth-Heinemann.

Tilmans, H.A.C. and Legtenberg, R. (1994) Electrostatically driven vacuum-encapsulated polysilicon resonators: Part II. Theory and performance, Sensors and Actuators A: Physical, 45, 67–84.

Tong, L.H., Lai, S.K., Zeng, L.L., Xu, C.J. and Yang, J. (2018) Nonlocal scale effect on Rayleigh wave propagation in porous fluid-saturated materials, International Journal of Mechanical Sciences, 148, 459–466.

Tounsi, A., Heireche, H., Beerabah, H.M., Benzair, A. and Boumia, L. (2007) Effect of small size on wave propagation in double-walled carbon nanotubes under temperature field, Journal of Applied Physics, 104(10), 104301.

Toyabur, R.M., Salauddin, M., Cho, H. and Park, J.Y. (2018) A multimodal hybrid energy harvester based on piezoelectric-electromagnetic mechanisms for low-frequency ambient vibrations, Energy Convers, Manag, 168, 454–466.

Tvedt, L.G.W., Nguyen, D.S. and Halvorsen, E. (2010) Nonlinear behavior of an electrostatic energy harvester under wide- and narrowband excitation, Journal of Microelectromechanical Systems, 19, 305–316.

Urabe, M. (1965) Galerkin procedure for nonlinear periodic systems, Archive for Rational Mechanics and Analysis 20(2), 120–152.

Urabe, M. and Reiter, A. (1966) Numerical computation of nonlinear forced oscillations by Galerkin's procedure, Journal of Mathematical Analysis and Applications, 14(1), 107-140.

Vakakis, A.F., Gendelman, O.V., Bergman, L.A., McFarland, D.M., Kerschen, G., and Lee, Y.S. (2009) Nonlinear Targeted Energy Transfer in Mechanical and Structural Systems I & II, Springer.

van der Meijs, N.P. and Fokkema, J.T. (1984) VLSI circuit reconstruction from mask topology, Integration, 2: 85–119.

Waluya, S.B. and van Horssen, W.T. (2003) On approximations of first integrals for a strongly nonlinear forced oscillator, Nonlinear Dynamics, 33, 225–252.

Wang, C. and Pop, I. (2006) Analysis of the flow of a power-law fluid film on an unsteady stretching surface by means of homotopy analysis method. Journal of Non Newtonian Fluid Mechanics, 138, 161–172.

Wang, C., Lai, S.K., Wang, Z.C., Wang, J.M., Yang, W.Q. and Ni, Y.Q. (2019a) A low-frequency, broadband and tri-hybrid energy harvester with septuple-stable nonlinearity-enhanced mechanical frequency up-conversion mechanism for powering portable electronics, Nano Energy, 64, 103943.

Wang, C., Zhang, Q., Wang, W. and Feng, J. (2018) A low-frequency, wideband quad-stable energy harvester using combined nonlinearity and frequency un-conversion by cantilever-surface contact, Mechanical Systems and Signal Processing, 112, 305–318.

Wang, C., Zhang, Q.C., Wang, W. (2017a) Low-frequency wideband vibration energy harvesting by using frequency-up conversion and quin-stable nonlinearity, Journal of Sound and Vibration, 399, 169–181.

Wang, C.M., Duan, W.H. (2008) Free vibration of nanorings/arches based on nonlocal elasticity, Journal of Applied Physics, 104, 014303.

Wang, C.M., Kitipornchai, S., Lim, C.W. and Eisenberger, M. (2008) Beam bending solutions based on nonlocal Timoshenko beam theory, Journal of Engineering Mechanics-ASCE, 134, 475–481.

Wang, C.M., Xiang, Y. and Kitipornchai, S. (2009) Postbuckling of nano rods/tubes based on nonlocal beam theory, International Journal of Applied Mechanics, 1, 259–266.

Wang, C.M., Xiang, Yang, Y., J. and Kitipornchai, S. (2012a) Buckling of nano-rings/arches based on nonlocal elasticity, International Journal of Applied Mechanics, 4, 1250025.

Wang, C.M, Zhang, H., Challamel, N. and Xiang, Y. (2016b), Buckling of nonlocal columns with allowance for selfweight, Journal of Engineering Mechanics, 142, 04016037.

Wang, C.M., Zhang, Y.Y. and He, X.Q. (2007a) Vibration of nonlocal of Timoshenko beams, Nanotechnology, 18, 105401.

Wang, C.Y., Murmu, T. and Adhikari, S. (2011) Mechanisms of nonlocal effect on the vibration of nanoplates, Applied Physics Letters, 98, 153101.

Wang, G., Zhao, Z., Liao, W.H., Tan, J., Ju, Y. and Li, Y. (2020) Characteristics of a tri-stable piezoelectric vibration energy harvester by considering geometric nonlinearity and gravitation effects, Mechanical Systems and Signal Processing, 138, 106571.

Wang, H.F., Chen, S.H., Cai, B., Ge, L.H. and Chen, Q.R. (2014a) Study on the dynamics of tribocharged coal and mineral particles in free-fall triboelectric separator, Separation Science & Technology, 49(18), 2990–2998.

Wang, J., Shen, H., Zhang, B., Liu, J. and Zhang, Y. (2018) Complex modal analysis of transverse free vibrations for axially moving nanobeams based on the nonlocal strain gradient theory, Physica E, 101, 85–93.

Wang, L. (2009) Vibration and instability analysis of tubular nano- and micro-beams conveying fluid using nonlocal elastic theory, Physica E-Low-Dimensional Systems and Nanostructures, 41, 1835–1840.

Wang, L. and Hu, H. (2005) Flexural wave propagation in single-walled carbon nanotubes, Physical review, B, Condensed Matter And Materials Physics, 71(19), 195412.

Wang, N. and Arnold, D.P. (2009) Fully batch–fabricated MEMS magnetic vibrational energy harvesters, in Proceedings of PowerMEMS 2009, Washington, DC, 348–351.

Wang, P., Dai, X., Zhao, X. and Ding, G. (2009b) A micro electromagnetic low level vibration energy harvester based on MEMS technology, Microsyst, Technol, 15(6), 941–951.

Wang Q. (2005) Wave Propagation in carbon nanotubes via nonlocal continuum mechanics, Journal of Applied Physics, 98, 124301.

Wang, Q. and Varadan, V.K. (2006) Vibration of carbon nanotubes studied using nonlocal continuum mechanics, Smart Materials and Structures, 15, 659–666.

Wang, Q.X., Li, H. and Lam, K.Y. (2007b) Analysis of microelectromechanical systems (MEMS) devices by the meshless point weighted least-squares method, Computational Mechanics, 40, 1-11.

Wang, Q., Han Q.K. and Wen B.C. (2008) Estimate of material property of carbon nanotubes vis nonlocal elasticity. Advances in Theoretical and applied Mechanics, 1, 1–10.

Wang, S., Lin, L. and Wang, Z.L. (2012a) Nanoscale triboelectric-effect-enabled energy conversion for sustainably powering portable electronics. Nano Letters, 12(12), 6339–6346.

Wang, S., Lin, L. and Wang, Z.L. (2012b) Nanoscale triboelectric-effect-enabled energy conversion for sustainably powering portable electronics, Nano Letters, 12(12), 6339–6346.

Wang, Z.L., Zhu, G., Yang, Y., Wang, S. and Pan, C. (2012c) Progress in nanogenerators for self-powered mobile/portable electronics, Materials Today, 15, 532–543.

Wang, S., Lin, L., Xie, Y., Jing, Q., Niu, S., Wang, Z.L. (2013) Sliding-triboelectric nanogenerators based on in-plane charge-separation mechanism, Nano Letters, 13, 2226–2233.

Wang, S.H., Xie, Y.N., Niu, S.M., Lin, L. and Wang, Z.L. (2014b), Freestanding triboelectric-layer-based nanogenerators for harvesting energy from a moving object or human motion in contact and non-contact modes, Advanced Materials, 26(18), 2818–2824.

Wang, Z., Feng, H., Ding, H. and Chen, L. (2019b) Parametric influence on energy harvesting of magnetic levitation using harmonic balance method, Journal of Vibration Engineering & Technologies, 7, 543–549.

Wang, Z.L. (2013) Triboelectric nanogenerators as new energy technology for self-powered systems and as active mechanical and chemical sensors, ACS Nano, 7, 9533–9557.

Wang, Z.L. (2017) On Maxwell's displacement current for energy and sensors: The origin of nanogenerators, Materials Today, 20, 74–82.

Wang, Z.L. (2020) Triboelectric nanogenator (TENG) – Sparking an energy and sensor revolution, Advanced Energy Materials, 2000137.

Wang, Z.L., Jiang, T., Xu, L. (2017b) Toward the blue energy dream by triboelectric nanogenerator networks, Nano Energy, 39, 9–23.

Wang, Z.L., Lin L., Chen Niu, J., S. and Zi, Y.L. (2016a) Triboelectric nanogenerators, Springer.

Wong, E., Sheehan, P.E. and Lieber, C. M. (1997) Nanobeam mechanics: Elasticity, strength, and toughness of nanorods and nanotubes, Science, 277, 1971–1975.

Williams C.B. and Yates R.B. (1996) Analysis of a micro-electric generator for microsystems, Sensors and Actuators, 52, 8–11.

Wu, B.S., Lim, C.W. and He, L.H. (2003) A new method for approximate analytical solutions to nonlinear oscillations of nonnatural systems, Nonlinear Dynamics, 32, 1–13.

Wu, B.S., and Lim, C.W. (2004) Large amplitude nonlinear oscillations of a general conservative system, International Journal of Non Linear Mechanics, 39, 859–870.

Wu, B.S., Liu, W.J., Chen, X. and Lim, C.W. (2017) Asymptotic analysis and accurate approximate solutions for strongly nonlinear conservative symmetric oscillators, Applied Mathematical Modelling, 49, 243–254.

Wu, B.S., Sun, W.P. and Lim, C.W. (2006) An analytical approximate technique for a class of strongly non-linear oscillators, International Journal of Non Linear Mechanics, 41, 766–774.

Wu, B., Yu, Y. and Li, Z. (2007a) Analytical approximations to large post-buckling deformation of elastic rings under uniform hydrostatic pressure, International Journal of Mechanical Sciences, 49(6), 661–668.

Wu, B.S., Sun, W.P. and Lim, C.W. (2007b) Analytical approximations to the double-well duffing oscillator in large amplitude oscillations, Journal of Sound and Vibration, 307, 953–960.

Wu, B.S. and Sun, W.P. (2011) Construction of approximate analytical solutions to strongly nonlinear damped oscillators, Archive of Applied Mechanics, 81(8), 1017–1030.

Wu, B.S., Yang, Z., Lim, C.W., and Sun, W.P. (2018b) Analytical approximations to resonance response of harmonically forced strongly odd nonlinear oscillators, Archive of Applied Mechanics, 88, 2123–2134.

Wu, C, Wang, A.C., Ding, W., Guo, Wang and H., Z.L. (2019) Triboelectric nanogenerator: A foundation of the energy for the new era, Advanced Energy Materials, 9, 1802906.

Wu, R.Q., Zhang, W. and Yao, M.H. (2018) Nonlinear dynamics near resonances of a rotor-active magnetic bearings system with 16-pole legs and time varying stiffness, Mechanical Systems and Signal Processing, 100, 113–134.

Wu, Y., Badel, A., Formosa, F., Liu, W. and Agbossou, A.E. (2012) Piezoelectric vibration energy harvesting by optimized synchronous electric charge extraction, Journal of Intelligent Material Systems and Structures, 24, 1445–1458.

Wu, Y., Kuang, S., Li, H., Wang, H., Yang, R., Zhai, Y., Zhu, G. and Wang, Z.L. (2018a) Triboelectric-thermoelectric hybrid nanogenerator for harvesting energy from ambient environments, Advanced Materials Technologies, 3, 1800166.

Xiang, Y., Wang, C.M., Kitipornchai, S. and Wang, Q. (2010) Dynamic instability of nanorods/nanotubes subjected to an end follower force, Journal of Engineering Mechanics, 136, 1054–1058.

Xie, Y.N., Wang, S.H, Niu, S.M, Lin, L., Jing, Q.S., Yang, J., Wu, Z.Y. and Wang, Z.L. (2014) Grating-structured freestanding triboelectric-layer nanogenerator for harvesting mechanical energy at 85% total conversion efficiency, Advanced Materials, 26(38), 6599–6607.

Xu, M.T. (2006) Free transverse vibrations of nano-to-micron scale beams, Proceedings of the royal society A-Mathematical Physical and Engineering Sciences, 462, 2977–2995.

Xu, X.J., Wang, X.C., Zheng, M.L., Ma, Z. (2017) Bending and buckling of nonlocal strain gradient elastic beams, Composite Structures, 160, 366–377.

Xu, Z., Cheung, Y.K. (1994) Averaging method using generalized harmonic functions for strongly nonlinear oscillators, Journal of Sound and Vibration, 174, 563–576.

Yan, B., Zhou, S., Zhao, C., Wang, K. and Wu, C. (2019) Electromagnetic energy harvester for vibration control of space rack: modeling, optimization, and analysis. Journal of Aerospace Engineering, 32(1), 04018126.

Yan, J.W., Zhang, L.W., Liew, K.M. and He, L.H. (2014) A higher-order gradient theory for modeling of the vibration behavior of single-wall carbon nanocones, Applied Mathematical Modelling, 38(11-12), 2946–2960.

Yang, F., Chong, A.C.M., Lam, D.C.C. and Tong, P. (2002) Couple stress based strain gradient theory for elasticity. International Journal of Solids and Structures, 39(10), 2731–2743.

Yang, W., Chen, J., Zhu, G., Wen, X., Bai, P., Su, Y., Lin, Y. and Wang, Z. (2013a) Harvesting vibration energy by a triple- cantilever based triboelectric nanogenerator, Nano Research, 6, 880–886.

Yang, W., Chen, J., Zhu, G., Yang, J., Bai, P., Su, Y., Jing, Q., Cao, X. and Wang, Z.L. (2013b) Harvesting energy from the natural vibration of human walking, ACS Nano, 7, 11317–11324.

Yang, X.D. and Chen, L.Q. (2006) Non-linear forced vibration of axially moving viscoelastic beams, Acta Mechanica Solida Sinica, 19, 365–373.

Yang, Y., Tang, L.H. and Li, H.Y. (2009a) Vibration energy harvesting using macro-fiber composites, Smart Material structure, 18, 5025–5033.

Yang, Y., Zhu, G., Zhang, H.L., Chen, J., Zhong,X.D., Lin, Z.H., Su, Y.J., Bai, P., Wen, X.N. and Wang, Z.L. (2003c) Triboelectric nanogenerator for harvesting wind energy and as self-powered wind vector sensor system, ACS Nano, 7, 9461–9468.

Yang, Z., Erturk, A. and Zu, J. (2017) On the efficiency of piezoelectric energy harvesters. Extreme Mechanics Letters, 15, 26–37.

Yao, M.H. and Zhang, W. (2007) Shilnikov-type multipulse orbits and chaotic dynamics of a parametrically and externally excited rectangular thin plate, International Journal of Bifurcation and Chaos 17, 851–875.

Yew, Y.K., Ng, T.Y., Li, H. and Lam, K.Y. (2007) Analysis of pH and electrically controlled swelling of hydrogel-based micro-sensors/actuators, Biomedical Microdevices, 9, 487–499.

Younis, M.I. and Alsaleem, F.M. (2009) Exploration of new concepts for mass detection in electrostatically-actuated structures based on nonlinear phenomena, Journal of Computational and Nonlinear Dynamics, 4, 021010.

Younis, M.I. and Nayfeh, A.H. (2003) A study of the nonlinear response of a resonant microbeam to an electric actuation, Nonlinear Dynamics, 31, 91–117.

Younis, M.I. and Alsaleem, F.M. (2009) Exploration of new concepts for mass detection in electrostatically-actuated structures based on nonlinear phenomena, Journal of Computational and Nonlinear Dynamics, 4, 021010.

Yu, Y.P., Lim, C.W. and Wu, B.S. (2008) Analytical approximations to large hygrothermal buckling deformation of a beam. Journal of Structural Engineering, 134(4), 602–607.

Yu, Y.P., Wu, B.S. and Lim, C.W. (2012) Numerical and analytical approximations to large post-buckling deformation of MEMS. International Journal of Mechanical Sciences, 55, 95–103.

Yu, Y.P., Wu, B.S., Sun, Y.H. and Zang, L. (2013a) Analytical approximate solutions to large amplitude vibration of a spring-hinged beam, Meccanica, 48, 2569–2575.

Yu, Y., Sun, Y. and Zang, L. (2013b) Analytical solution for initial postbuckling deformation of the sandwich beams including transverse shear. Journal of Engineering Mechanics, 139(8), 1084–1090.

Yu, Y.P., Zhang, H.Z., Sun, Y.H. and Sun. W.P. (2017) Predicting dynamic response of large amplitude free vibrations of cantilever tapered beams on a nonlinear elastic foundation. Archive of Applied Mechanics, 87, 751–765.

Zand, M.M. (2012) The dynamic pull-in instability and snap-through behavior of initially curved microbeams, Mechanics of Advanced Materials and Structures, 19, 485–491.

Zhang, C., Zhou, T., Tang, W., Han, C., Zhang, L. and Wang, Z.L. (2014a), Rotating-disk-based direct-current triboelectric nanogenerator. Advanced energy materials, 4(9), 1–7.

Zhang, H.L., Yang, Y., Zhong, X.D., Su, Y.J., Zhou, Y.S., Hu, C.G. and Wang, Z.L. (2014b) Single-electrode-based rotating triboelectric nanogenerator for harvesting energy from tires, ACS Nano, 8(1), 680–689.

Zhang, W.M. and Meng, G. (2007) Nonlinear dynamic analysis of electrostatically actuated resonant MEMS sensors under parametric excitation. IEEE Sensors Journal, 7, 370–380.

Zhang, X.S., Han, M.D., Wang, R.X., Zhu, F.Y., Li, Z.H., Wang, W. and Zhang, H.X. (2013) Frequency-multiplication high-output triboelectric nanogenerator for sustainably powering biomedical microsystems, Nano Letters, 13, 1168–1172.

Zhang, Y., Lei, Z.X., Zhang, L.W., Liew, K.M. and Yu, J. L. (2015b) Nonlocal continuum model for vibration of single-layered graphene sheets based on the element-free kp-Ritz method. Engineering analysis with boundary elements, 56, 90–97.

Zhang, Y., Zhang, L.W., Liew, K.M. and Yu, J.L. (2015a) Transient analysis of single-layered graphene sheet using the kp-ritz method and nonlocal elasticity theory. Applied Mathematics & Computation, 258, 489–501.

Zhang, Y., Zhang, L.W., Liew, K.M. and Yu, J.L. (2016a) Nonlocal continuum model for large deformation analysis of SLGSs using the kp-Ritz element-free method. International Journal of Non-Linear Mechanics, 79, 1–9.

Zhang, Y., Zhang, L.W., Liew, K.M. and Yu, J.L. (2016b) Buckling analysis of graphene sheets embedded in an elastic medium based on the kp-Ritz method and non-local elasticity theory, Engineering Analysis with Boundary Elements, 70, 31–39.

Zhang, Y.Q., Liu, G.R. and Xie, X.Y. (2005) Free transverse vibrations of double-walled carbon nanotubes using a theory of nonlocal elasticity, Physical Review B, 71, 195404.

Zhao, J.H., Yu, S.J., Li, K., Dong, Y., Zhou, Q. and You, Z. (2009) Improvement of a micro-beam in a smart gas sensor with resonating mechanism, Proceedings of the 4th IEEE International Conference on Nano/Micro Engineered and Molecular Systems, 371–375.

Zhong, J., Zhong, Q., Fan, F., Zhang, Y., Wang, S., Hu, B., Wang, Z.L. and Zhou, J. (2013a) Finger typing driven triboelectric nanogenerator and its use for instantaneously lighting up LEDs, Nano Energy, 2, 491–497.

Zhong, Q., Zhong, J., Hu, B., Hu, Q., Zhou, J. and Wang, Z.L. (2013b) A paper-based nanogenerator as a power source and active sensorf, Energy & Environmental Science, 6(6), 1779–1784.

Zhou, S. and Zuo, L. (2018) Nonlinear dynamic analysis of asymmetric tristable energy harvesters for enhanced energy harvesting, Communications in Nonlinear Science and Numerical Simulation, 61, 274–284.

Zhou, S., Cao, J., Inman, D.J., Lin, J., Liu, S.S. and Wang, Z.Z. (2014) Broadband tristable energy harvester: Modeling and experiment verification, Applied Energy, 133, 33–39.

Zhou, S., Cao, J., Inman, D.J., Liu, S., Wang, W. and Lin, J. (2015) Impact-induced high-energy orbits of nonlinear energy harvesters, Applied Physics Letters, 106 (9), 093901.

Zhou, S., Cao, J., Lin, J. and Wang, Z. (2014) Exploitation of a tristable nonlinear oscillator for improving broadband vibration energy harvesting. The European Physical Journal Applied Physics, 67(3), 30902.

Zhou, S.X., Cao, J.Y., Inman, D.J., Lin, J. and Li, D. (2016) Harmonic balance analysis of nonlinear tristable energy harvesters for performance enhancement, Journal of Sound and Vibration, 373, 223–235.

Zhou, Y., Wu, B.S., Lim, C.W. and Sun, W. (2020) Analytical approximations to primary resonance response of harmonically forced oscillators with strongly general nonlinearity, Applied Mathematical Modelling, 87, 534–545.

Zhou, Z.Y., Qin, W.Y. and Zhu, P. (2017) A broadband quad-stable energy harvester and its advantages over bi-stable harvester: simulation and experiment verification, Mechanical Systems & Signal Processing, 84, 158–168.

Zhou, Z.Y., Qin, W.Y., Lan, C.B., Li, H.T. and Deng W.Z. (2016) Dynamics and coherence resonance of tri-stable energy harvesting system, Smart Materials and Structures, 25, 015001.

Zhu, D., Roberts, S., Tudor, J. and Beeby, S. (2010) Design and experimental characterization of a tunable vibration-based electromagnetic micro-generator, Sensors and Actuators A, 158(2), 284–293.

Zhu, G., Lin, Z.H., Jing, Q., Bai, P., Pan, C., Yang, Y., Zhou, Y. and Wang, Z.L. (2013) Toward large-scale energy harvesting by a nanoparticle-enhanced triboelectric nanogenerator, Nano Letters, 13, 847–853.

Zhu, G., Pan, C.F., Guo, W.X., Chen, C.Y., Zhou, Y.S., Yu, R.M. and Wang, Z.L. (2012) Triboelectric-generator-driven pulse electrodeposition for micropatterning, Nano Letters, 12(9), 4960–4965.

Zhu, J.X., Wang, A.C., Hu, H.B. and Zhu, H. (2017b) Hybrid electromagnetic and triboelectric nanogenerators with multi-impact for wideband frequency energy harvesting, Energies 10, 2024.

Zhu, J., Liu, X., Shi, Q., He, T., Sun, Z., Guo, X., Liu, W., Sulaiman, O.B., Dong, B. and Lee, C. (2020) Development trends and perspectives of future sensors and MEMS/NEMS, Micromachines, 11, 7.

Zhu, P., Ren, X., Qin, W. and Zhou, Z. (2017a) Improving energy harvesting in a tri-stable piezomagnetoelastic beam with two attractive external magnets subjected to random excitation, Archive of Applied Mechanics, 87, 45–57.

Zhu, S., Shen, W.A. and Xu, Y.L. (2012) Linear electromagnetic devices for vibration damping and energy harvesting: Modelling and testing, Engineering Structures, 34, 198–212.

Zhu, Y. and Zu, J.W. (2012) A magneto electric generator for energy harvesting from the vibration of magnetic levitation, IEEE Transactions on Magnetics, 48, 3344–3347.

Ziebart, V., Paul, O., Munch, U., Schwizer, J. and Baltes, H. (1998) Mechanical properties of thin films from the load deflection of long clamped plates, Journal of Microelectromechanical Systems, 7(3), 320–328.

Zook, J.D., Burns, D.W., Guckel, H., Sniegowski, J.J., Engelstad, R.L. and Feng, Z. (1992) Characteristics of polysilicon resonant microbeams. Sensors and Actuators A: Physical, 35, 51–59.

Zuo, L., Scully, B., Shestani, J. and Zhou, Y. (2010) Design and characterization of an electromagnetic energy harvester for vehicle suspensions, Smart Materials and Structures, 19(4), 045003.